Technical Report 32-1443

Analysis of Surveyor Data

JET PROPULSION LABORATORY
CALIFORNIA INSTITUTE OF TECHNOLOGY
PASADENA, CALIFORNIA

June 30, 1969

NATIONAL AERONAUTICS AND SPACE ADMINISTRATION

Technical Report 32-1443

Analysis of Surveyor Data

JET PROPULSION LABORATORY
CALIFORNIA INSTITUTE OF TECHNOLOGY
PASADENA, CALIFORNIA

June 30, 1969

Prepared Under Contract No. NAS 7-100
National Aeronautics and Space Administration

Preface

This publication presents some of the results obtained by extended postflight analysis of data returned by the *Surveyor* lunar spacecraft. The publication consists of a number of sections, each describing results obtained by one or more scientists. The work described in this report was performed by the *Surveyor* Science Data Analysis Project of the Jet Propulsion Laboratory during the period from July 1, 1968 to June 30, 1969.

Contents

Abstract

This report presents some of the results of the extended postflight analysis of *Surveyor* data for the thermal, physical, and mechanical properties of the lunar surface, the photometric and polarimetric properties of the earth, and the colorimetric measurements of the solar eclipse and earth. Also presented are the optical systems and alignment procedures used in the *Surveyor VII* Laser Pointing Test.

Revised Lunar Surface Temperatures and Thermal Characteristics From *Surveyor*

L. D. Stimpson, W. A. Hagemeyer, J. W. Lucas, and Z. Popinski
Jet Propulsion Laboratory
Pasadena, California

J. M. Saari
Boeing Scientific Research Laboratories
Seattle, Washington

I. Background

The *Surveyor* Project was managed by the Jet Propulsion Laboratory (JPL) for the National Aeronautics and Space Administration (NASA). The *Surveyor* spacecraft was designed, fabricated, and flown by the Hughes Aircraft Company under contract to JPL. The mission of *Surveyor* was to land unmanned on the lunar surface, to operate for a lunar day, and to investigate possible landing sites for the *Apollo* missions. Four spacecraft did land and operate successfully within the *Apollo* equatorial region, and the final spacecraft was sent to a region far to the south near the crater Tycho.

Each of the five successfully landed *Surveyor* spacecraft[1] transmitted data back to earth for at least 2 weeks. The *Surveyor* landing sites are shown in Fig. 1; Table 1 lists the selenographic location, time of landing, local slope, and sun elevation above the eastern horizon at landing. The landed orientations of the spacecraft are given in detail in Appendix A.

The local terrain upon which each of the spacecraft landed was different. *Surveyor I* landed on a relatively smooth, nearly level surface, encircled by hills and low mountains. *Surveyor III* landed about halfway down a 12½-deg slope of a crater about 200 m in diameter and 15 m deep. *Surveyor V* landed with one leg on the rimless edge of a 9- by 12-m crater that was 1.5 m deep, with the other two legs inside the crater, and was tilted about 20 deg from the lunar horizontal. *Surveyor VI* landed on a relatively smooth, flat surface. The local slope was less than 1 deg; after the hop made by the spacecraft, the local slope on the new site was about

[1]*Surveyor II* failed during a midcourse maneuver and *Surveyor IV* ceased to transmit data just before landing.

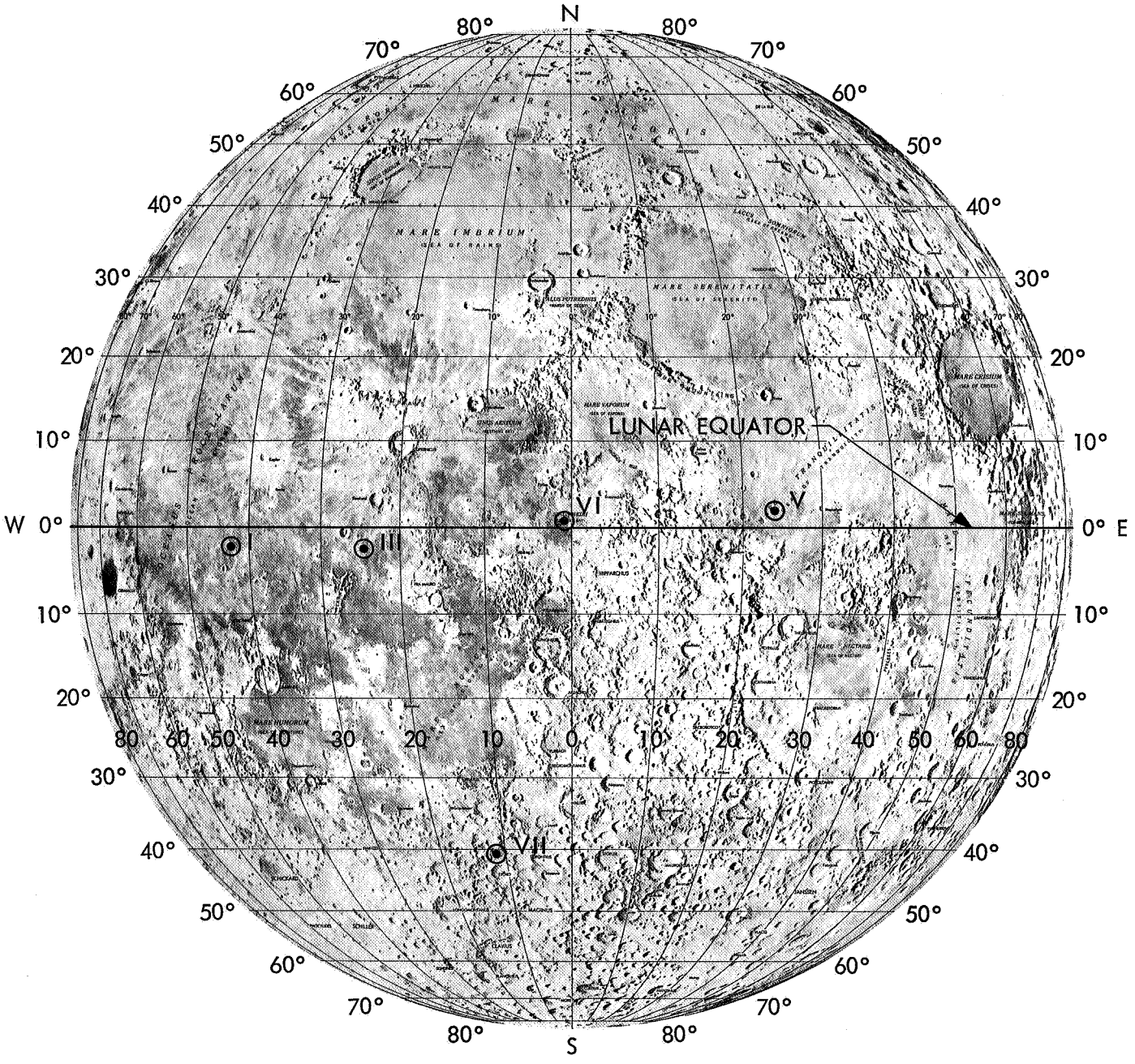

Fig. 1. *Surveyor* landing sites

Table 1. Positional characteristics of *Surveyor* spacecraft

Spacecraft	Selenographic coordinates *Atlas*/ACIC system		Selenographic location	Touchdown time		Sun elevation above eastern horizon at touchdown, deg	Approximate local slope, deg
	Latitude	Longitude		Date	GMT, h:min:s		
Surveyor I	2.46°S	43.23°W	Southwest part of Oceanus Procellarum (Ocean of Storms)	6/2/66	06:17:36	28.5	<1
Surveyor III	2.99°S	23.34°W	Southeast part of Oceanus Procellarum (Ocean of Storms)	4/20/67	00:04:17[a]	11.8	12.4
Surveyor V	1.4°N[b]	23.2°E[b]	Mare Tranquillitatis (Sea of Tranquillity)	9/11/67	00:46:42	16.4	20
Surveyor VI	0.51°N	1.39°W	Sinus Medii (Central Bay)	11/10/67	01:01:04	2.8	<1[c]
Surveyor VII	40.88°S	11.45°W	Ejecta blanket of crater Tycho	1/10/68	01:05:36	12.5	3

[a]Initial touchdown; second touchdown was at 00:04:41 GMT; final touchdown was at 00:04:53 GMT.

[b]Approximate.

[c]Before the hop; after the hop, the slope was about 4 deg.

4 deg. *Surveyor VII* landed in extremely rough terrain, but with a local slope of only about 3 deg.

The behavior of the various spacecraft on the lunar surface varied. *Surveyor I* gave excellent data for two successive lunar days, and partial data were obtained as late as the fifth and sixth lunar days. The spacecraft operated for 48 h into the first lunar night.

Surveyor III landed with the vernier propulsion system still at a thrust level almost equal to the lunar weight. It hopped twice down the crater slope after initial touchdown. On the second touchdown, all analog telemetry signals became erroneous. It was found that most of the analog data obtained in the lowest rate mode (17.2 bits/s) were fairly reliable and could be corrected with simple calibration factors. However, the overall accuracy of telemetered temperatures from *Surveyor III* was estimated at $\pm 6°K$ compared with that of $\pm 4°K$ for the other spacecraft. *Surveyor III* also experienced a solar eclipse (by the earth) during its first lunar day on April 24, 1967, offering the first opportunity to observe such an event from the moon. *Surveyor III* shutdown occurred almost immediately after sunset (2 h) on the first lunar day.

Surveyor V, which operated for about 115 h into the first lunar night, also experienced a solar eclipse (by the earth) on the second lunar day on October 18, 1967, and operated for about 215 h into the second lunar night. It operated for a short period of time during the fourth lunar day, transmitting 200-line television pictures.

The vernier rocket engines on *Surveyor VI* were fired on the lunar surface during the first lunar day, causing the spacecraft to lift off from the lunar surface and to hop 2.4 m. *Surveyor VI* operated for about 40 h into the lunar night; it was revived on the second lunar day, but gave thermal data for only a short time.

Surveyor VII, which operated for about 80 h into the first lunar night, was successfully revived on the second lunar day, giving good thermal data during the day. However, contact with the spacecraft was lost before sunset on the second lunar day.

Surveyor science investigation teams were formed earlier on the project to guide the experiments and analyze the data. Teams formed were for the television, alpha scattering, and soil mechanics surface sampler experiments. Over 65,000 television pictures were taken by the five spacecraft; the alpha scattering experiment determined the elemental constituents of the lunar soil; the surface sampler dug trenches and tested clods and rocks to determine the soil structure.

In addition, a number of working groups were formed. They were groups that studied the following subjects:

(1) astronomy, (2) laser tests, (3) lunar surface electromagnetic properties, (4) lunar surface mechanical properties, (5) lunar theory and processes, and (6) lunar surface thermal properties. The recent work of the lunar surface thermal properties working group is covered in detail in this paper.

Surveyor I presented the first opportunity to obtain *in situ* estimates of the lunar surface temperatures and thermophysical characteristics, in addition to engineering data on the thermal behavior of the spacecraft during operation on the lunar surface. It should be emphasized that none of the *Surveyor* spacecraft carried any instruments, as such, to measure lunar surface temperatures or surface thermal characteristics. For operational reasons, the spacecraft were thermally isolated from the lunar surface to the greatest extent possible.

Fortunately, for present purposes, there were temperature sensors on the outer surfaces of two electronic compartments, on the solar panel, and on the planar array. These surfaces were highly dependent on the local thermal radiation environment and only partially dependent on other spacecraft equipment. It was the objective of the lunar surface thermal properties group to use these spacecraft temperatures to estimate the average brightness temperature[2] of those portions of the surface viewed by each sensor.

The *Surveyor* spacecraft provided estimates of surface temperature out to about 18 m from the compartments. Compared with the best previous infrared earth-based telescopic observations, this *in situ* measurement is an improvement in ground resolution by a factor of ~1000. The derived temperatures after sunset, and during the two eclipses, were used to estimate the thermal characteristics of the lunar surface at each site. The maximum lunar surface temperature at noon and the minimum at night were found to be nearly 400°K (260°F) and 100°K (−280°F), respectively. The derived lunar surface temperatures after sunset and during eclipses suggest a highly insulating and particulate soil.

II. Introduction

This paper covers the work of the *Surveyor* lunar surface thermal properties group during the period from July 1968 to June 1969. The lunar surface temperatures and thermal characteristics derived from the *Surveyor* telemetry data were revised using more complete spacecraft models and more extensive computer utilization.

Earlier reports (Refs. 1–7) presented some preliminary results of lunar surface temperatures derived from temperature sensor data on the outboard faces of two electronic compartments. A radiative heat balance equation was used that took into account several effects such as direct solar illumination, indirect heating, shadowing from the spacecraft, and heat loss from the compartment interior. The lunar surface temperatures derived from the compartment data have been compared with theoretical Lambertian values and with temperatures determined from earth-based measurements described in Appendix B. Discrepancies in the results appeared during each of the periods: lunar day, lunar night, and solar eclipse. Generally, higher lunar surface temperatures were obtained from *Surveyor* compartment data than from earth-based measurements.

The earth-based resolution of about 18 km is about 1000 times less than the resolution obtained by the *Surveyor* spacecraft. Therefore, it would not be too surprising to find discrepancies between *Surveyor* and earth-based measurements due to detection of entirely different resolutions. However, a recent effort (Ref. 8) shows that lunar surface temperatures derived from a thermal sensor located on the solar panel are lower than from compartment data and are in better agreement with earth-based results.

Some of the discrepancies found among the compartment, solar panel, and earth-based lunar surface temperatures from earlier work (Refs. 1–7) are highlighted in the representative case shown in Fig. 2. During the morning, the lunar surface temperature derived from compartment B on *Surveyor V* was higher than from the Lambertian predictions. This peak could be explained by the presence of directional emission. The compartment was viewing west and could be expected to detect a greater thermal emission from the lunar surface with the morning sun over its "shoulder." The agreement with Lambertian results during the afternoon was excellent. However, some cases from other missions of higher than normal temperature could not be attributed to the presence of directional emission.

After sunset, the lunar soil cooling behavior is dependent upon the lunar soil characteristics. This correlation

[2]In this paper, brightness temperature is used in the usual sense; that is, the experimentally observed temperature a surface with unit emissivity must have to produce the measured response.

is represented theoretically by the two different γ curves[3] shown in Fig. 2. The early results from *Surveyor V* compartment data suggested a γ of about 400, whereas some preliminary results derived from solar panel data suggested a value greater than 800. Further confusion existed previously because the earth-based post-sunset measurements indicated a γ of about 850, whereas the earth-based eclipse measurements indicated a γ of about 1370.

The largest discrepancy between *Surveyor* and earth-based temperatures was noted for the eclipse measurements, shown on Fig. 3 from the *Surveyor III* eclipse data. The lunar surface eclipse temperatures obtained from the *Surveyors III* and *V* (second lunar day) compartment data were about 50 and 80°K, respectively, higher than earth-based eclipse measurements. A preliminary check using solar panel data resulted in lunar surface temperatures again nearer the earth-based results.

[3]Using $\gamma = (k\rho c)^{-1/2}$ in $cm^2\ s^{1/2}\ °K/g\text{-}cal$ units, where k = thermal conductivity, ρ = density, and c = heat capacity of the lunar soil. It should be emphasized that the γ representation assumes a uniform soil composition and properties with depth; however, it is convenient to use because of its familiarity and for comparison purposes.

Error analyses were performed to determine the significant sources of error in the lunar temperatures obtained from *Surveyor* thermal data. In the compartments, heat conducted from the other faces was found to be small but significant and has been included in the latest

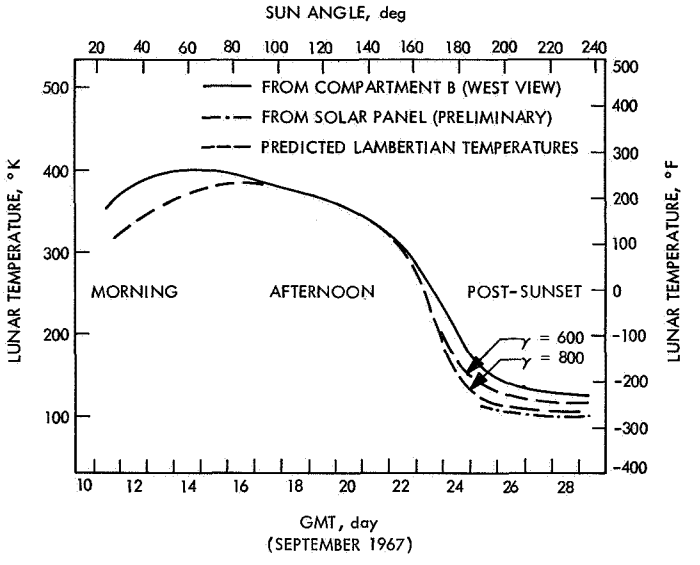

Fig. 2. Preliminary lunar surface temperatures for *Surveyor V* site

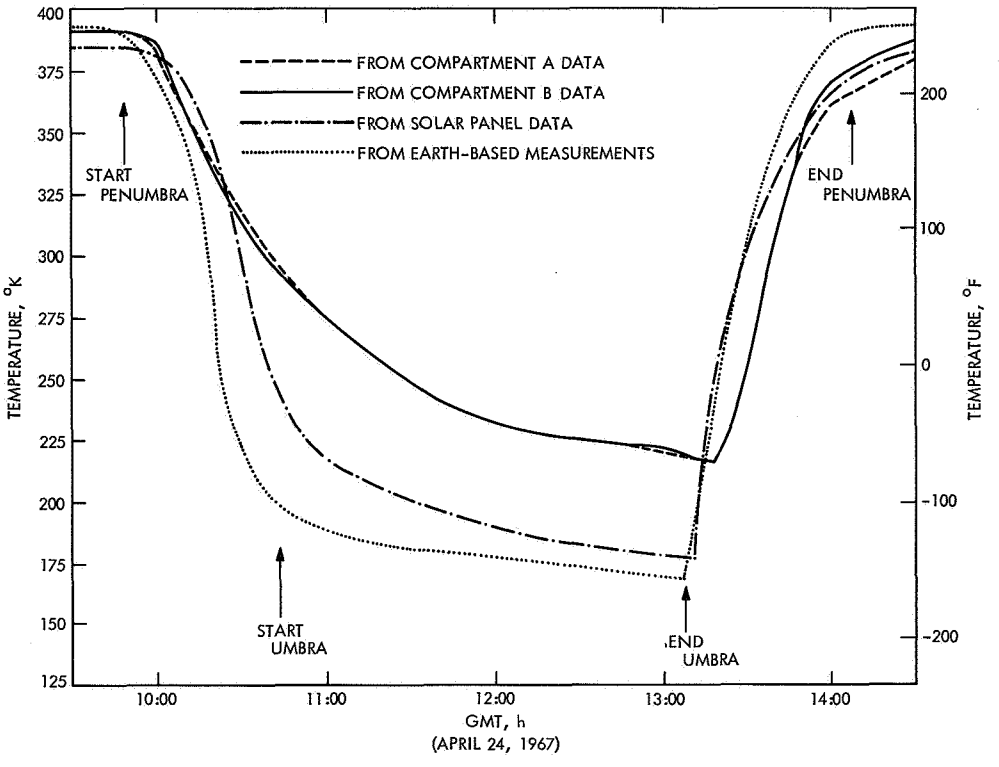

Fig. 3. Lunar surface temperatures during eclipse from *Surveyor III*

calculations. Derived post-sunset and eclipse temperatures from solar panel data were found to have total errors similar to those from the compartment thermal sensor data.

The actual temperature sensor measurement inaccuracies, uncertainties in view factors, and conduction effects have been shown to be the most significant sources of error from the *Surveyor* data. Other sources of error found to be of some significance resulted from uncertainties in internal heat loss, solar absorptance, and emissivity. Error bands have been established for these factors using *Surveyor V* data and are presented later. The overlapping of these error bands with each other and with the earth-based results illustrates the degree of agreement of the revised data from the different sources on the *Surveyor V* mission. They are expected to be similar for the other missions.

III. Spacecraft Description

The *Surveyor* spacecraft (Fig. 4) had a basic structural frame of tubular aluminum which served as a tetrahedral mounting structure for the electronic gear and propulsion system. The three spacecraft legs were attached at the three corners of the base. The planar array antenna and solar panel, mounted on a mast about 1 m above the apex of the structure, cast varying shadow patterns on the spacecraft and the lunar surface throughout the lunar day. Changes in shadow patterns occurred as a result of the commanded repositionings of the planar array antenna and solar panel and from the apparent movement of the sun (about 0.5 deg/h).

Generally, the spacecraft components in the sun-illuminated areas had white painted surfaces that provided a low-solar-absorptance and high-infrared-emittance thermal finish. The polished aluminum underside thermally isolated the spacecraft from the lunar surface.

The temperature data of various points in the spacecraft were provided by platinum resistance temperature sensors. Each sensor was calibrated individually to $\pm 2°K$; other nominal system inaccuracies degraded the overall accuracy to $\pm 4°K$.[4] Most of the 75 sensors measured internal spacecraft temperatures. Some, however, were externally located and were responsive to the lunar surface radiation; one each was located on the outside panels of the two main electronic components, on the solar panel, and on the planar array antenna.

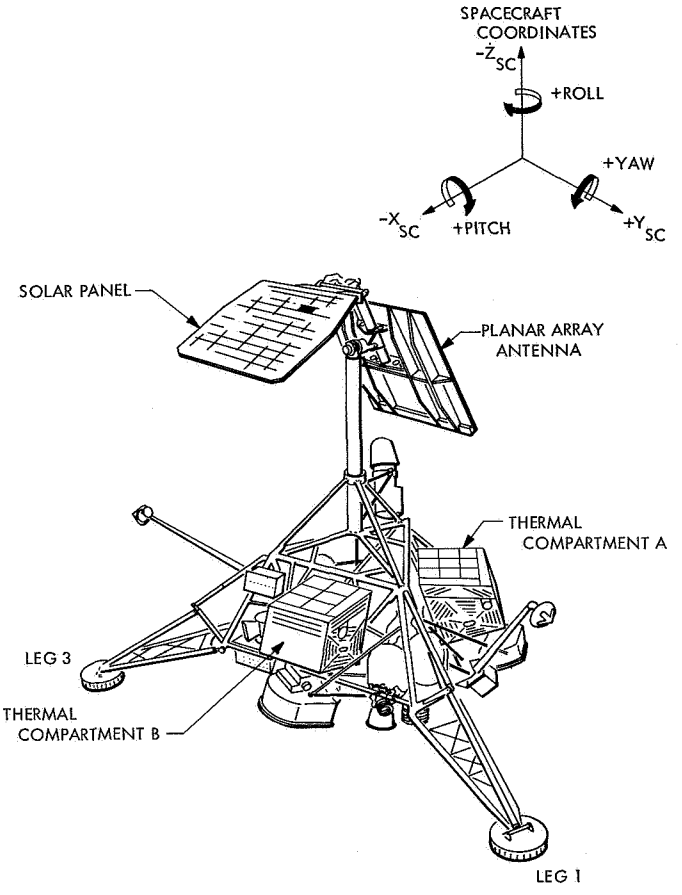

Fig. 4. *Surveyor* spacecraft configuration

A. Compartment Canisters

Compartments A and B housed the spacecraft electronics and battery. A thermal blanket of multilayer insulation surrounded the components in each compartment, which in turn was covered with an aluminum panel. Heat was rejected from the compartments during the hot lunar day through bimetal-actuated (semi-active) thermal switches connected to highly polished Vycor mirrors on the top of each compartment. At sunset, the thermal switches opened to isolate the interior from the exterior. Internal electrical heaters were available to warm the compartments.

A temperature sensor was bonded to the polished-aluminum inner surface of the outboard panel; i.e., the

[4]These temperature sensors were low resolution; other sensors, critical for spacecraft performance assessment, were calibrated to $\pm 1°K$ with an overall accuracy of $\pm 3°K$ over a narrow temperature range.

surface facing the blanket of each compartment (Fig. 5). A thermal sensor was located on compartment B in the same manner. The thermal blanket isolated the external panels from the inside of the compartments. Since the outboard panels of the compartments had a strong radiative coupling to the lunar surface, but were virtually shielded from view of other spacecraft components, an analysis of lunar surface brightness temperatures was possible. In the most recent model, the small heat conducted around from the side panels also has been included.

B. Solar Panel and Planar Array Antenna

The solar panel and planar array antenna (shown in Fig. 4) were relatively low-heat-capacity planar surfaces. Temperature data measured by these two surfaces also were used to derive lunar surface brightness temperatures. Each surface had a thermal sensor located on it, in addition to two other sensors on the upper part of the mast. Data from these four sensors have been used in the solar panel model described in more detail in Section IV-C.

The model is referred to as the solar panel model since it is the sensor on the solar panel that is considered most sensitive and is used as the primary sensor. That is, the lunar surface temperature in the model is adjusted until it produces a temperature equal to that actually sensed on the lunar surface by the solar panel. The planar array antenna and two stepping motor (mast) temperatures are held fixed at their actual measured values while the adjustment in lunar surface temperature is made.

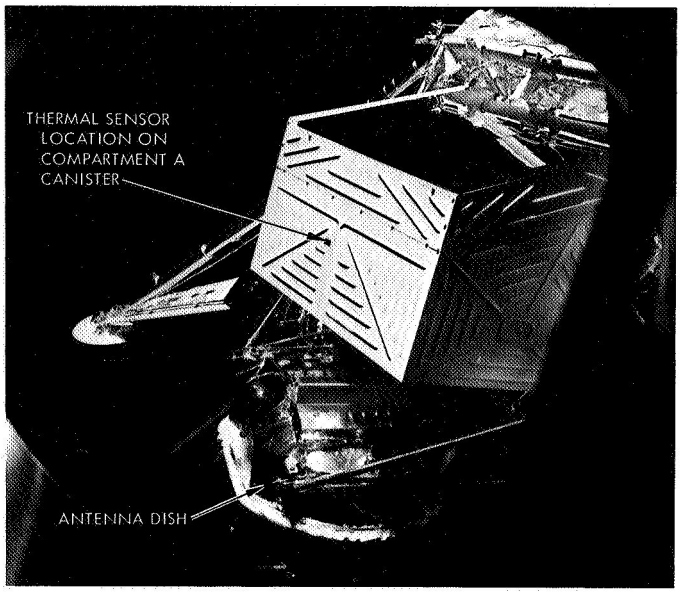

Fig. 5. Closeup view of compartment A

IV. Analytical Techniques

A. Earlier Calculations

The lunar surface brightness temperatures from *Surveyor* thermal sensor data (Refs. 1–7) were based upon the simplified radiation heat balance equation depicted in Fig. 6. An outboard compartment face was assumed to be thermally isolated from the remainder of the spacecraft except for a small conductive heat loss from the interior of a compartment.

The energy radiated by a unit area of a compartment was $\epsilon_1\sigma T_1^4$. This was balanced by five energy inputs:

(1) Infrared (IR) radiation from the sunlit lunar surface $\epsilon_1 F_{12}(\epsilon_2\sigma T_2^4)$.

(2) Infrared radiation from the shaded lunar surface $\epsilon_1 F_{13}(\epsilon_3\sigma T_3^4)$.

(3) Direct solar radiation $\alpha_{1s}\, S \cos\beta$.

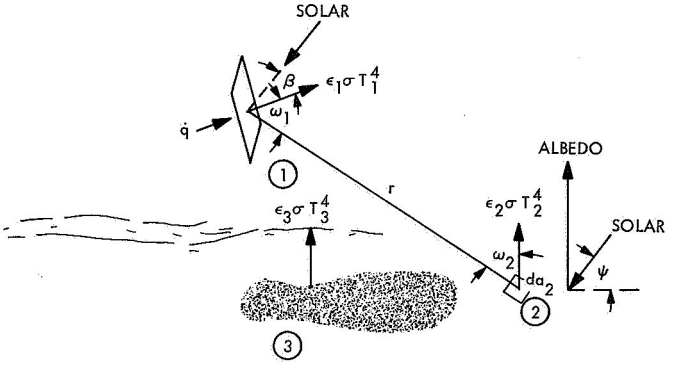

HEAT BALANCE

$\epsilon_1\sigma T_1^4 = \alpha_{1s}\, S \cos\beta$	SOLAR RADIATION
$+\epsilon_1 F_{12}\left(\epsilon_2\sigma T_2^4\right)$	RADIATION FROM SUNLIT LUNAR SURFACE
$+\epsilon_1 F_{13}\left(\epsilon_3\sigma T_3^4\right)$	RADIATION FROM SHADED LUNAR SURFACE
$+\alpha_{1s} F_{12}\left(\rho_2\, S \sin\psi\right)$	ALBEDO FROM LUNAR SURFACE
$+\dot{q}$	HEAT FLOW OUT OF COMPARTMENT

VIEW FACTOR

$$F_{1i} = \int_{a_i} \frac{\cos\omega_1 \cos\omega_1}{\pi r^2}\, da_i;\ i = 2,\ 3$$

Fig. 6. Heat transfer for a compartment outboard face

(4) Reflected solar radiation (albedo) from the lunar surface $\alpha_{1s}F_{12}(\rho_2 S \sin\psi)$.

(5) Heat flux $\dot{q}$ from inside the compartment.

An assumed value of 200°K (−100°F) was used for the shaded lunar surface. This assumed value was adequate since the shadow heat input term was only of minor significance due to the small view factor values involved and then only during a small part of the lunar day. An approximate value of 3.5 W/m², found from cold chamber tests, was used for the heat flux $\dot{q}$ from inside the compartments. This heat conduction term was important after sunset and during the totality of the eclipse.

The heat flux density balance equation used to derive the lunar surface temperature T_2 was:

$$\sigma T_2^4 = \frac{\sigma T_1^4}{\epsilon_2 F_{12}} - \frac{F_{13}}{F_{12}}\sigma T_3^4 - \frac{\alpha_{1s}S}{\epsilon_1\epsilon_2 F_{12}}(F_{12}\rho_2 \sin\psi + \cos\beta) - \frac{\dot{q}}{\epsilon_1\epsilon_2 F_{12}} \quad (1)$$

where

T_1 = compartment surface temperature, °K

T_2 = sunlit lunar surface brightness temperature, °K

T_3 = shaded lunar surface brightness temperature, assumed = 200°K

$S = S_0 I$ = solar radiation during penumbral stage of eclipse with S_0 as given in Table 2, W/m²

I = fraction of solar radiation during penumbral stage of eclipse

F_{12} = view factor from compartment to sunlit lunar surface (given in Table 2)

F_{13} = view factor from compartment to shaded lunar surface

$\dot{q}$ = conduction heat flux from inside of compartment to outboard face, 3.5 W/m²

σ = Stefan–Boltzmann constant, 5.675×10^{-8} W/m² − °K⁴

ϵ_1 = compartment surface emittance, dimensionless = 0.87 ±0.02 (inorganic white paint)

ϵ_2 = lunar surface emittance, dimensionless = 1.0 (brightness assumption)

α_{1s} = compartment surface solar absorptance, dimensionless = 0.20 ±0.02 (inorganic white paint)

β = angle between direction of sun and normal to compartment surface, deg

ψ = sun elevation angle above lunar horizon, deg

ρ_2 = lunar albedo, lunar reflectance to solar irradiation (earth-based), dimensionless

Table 2. Solar constant and view factors

Surveyor	Time	S_0, W/m²	ρ_2	Compartment	
				A, F_{12}	B, F_{13}
I	Landing	1352	0.052	0.28	0.29
III	Landing	1386	0.076	0.31	0.41
V	Landing	1375	0.077	0.247	0.255
V	Eclipse	1408	0.077	0.234	0.267
VI	Landing	1423	0.084	0.321	0.318
VI	After hop	1430	0.084	0.350	0.316
VII	Landing	1442	0.17	0.337	0.333

Table 2 shows some of the parameter values used in the lunar surface temperature calculations for each mission. Other parameters used, such as sun angles, are given in Refs. 1–5.

B. Revised Calculations

The error analysis (Ref. 8), also given later in Section V, indicated that a small but significant amount of heat was conducted around from the other faces of the compartments. Therefore, recent calculations using *Surveyor* compartment thermal sensor data have included this effect. Each of the faces has its own heat balance equation like that shown in Fig. 6; however, heat conduction terms coupling adjacent sides have been appended. Thus,

$$\epsilon_1\sigma T_1^4 = \epsilon_1\epsilon_2 F_{12}\sigma T_2^4 + \epsilon_1\epsilon_3 F_{13}\sigma T_3^4 + \alpha_{1s}S(\cos\beta + \rho_2 F_{12}\sin\phi) + \dot{q} + K_{41}(T_4 - T_1) + K_{51}(T_5 - T_1) + K_{71}(T_7 - T_1) + K_{81}(T_8 - T_1) \quad (2)$$

where subscripts

4 and 5 refer to vertical sides of the compartment (inorganic white paint)

7 refers to the bottom (polished aluminum)

8 refers to the top (exclusive of thermally isolated mirrors)

and parameters

$K = kA_c/LA_1$ = conductivity coefficient

k = thermal conductivity of aluminum, W/°K-m

A_c = thin sheet cross-sectional area of two adjoining sides, m²

L = conduction length between centers of two adjoining sides, m

A_1 = area of side 1, m²

The equations for the remaining five sides are similar in form to Eq. (2). It should be noted that the inboard surface, 6, was polished aluminum.

C. Solar Panel Model

A predominately radiative heat-balance equation was used for determining the lunar surface temperature from *Surveyor* solar panel thermal sensor data as depicted in Fig. 7. The thermal sensor was nearly centrally located on the illuminated side of *Surveyors I–IV* and on the shaded side of *Surveyors V–VII*. Both sides of the solar

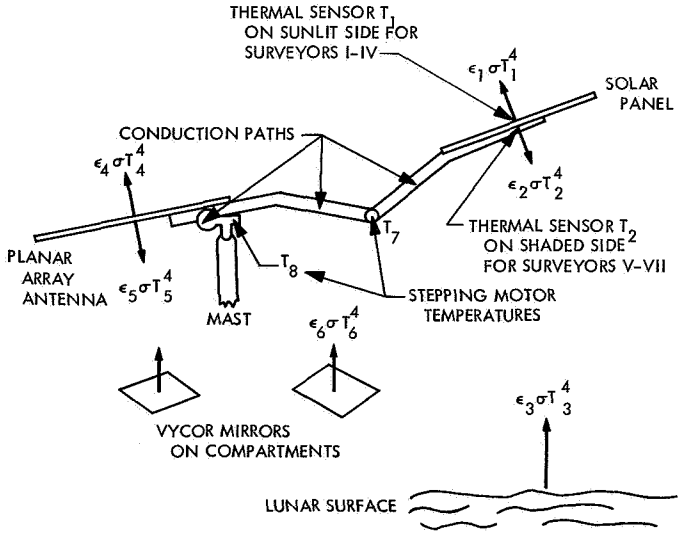

Fig. 7. Solar panel heat transfer model

panel emitted heat and also viewed the lunar surface, space, and other spacecraft components. Those components of primary influence were the planar array, the mast, and the Vycor mirror surfaces on top of the compartments. Also included was the heat conduction through the mast. The heat flux density balance equation for the solar panel, after sunset or during total eclipse, is

$$\epsilon_1\sigma T_1^4 + \epsilon_2\sigma T_2^4 = (\epsilon_1 F_{13} + \epsilon_2 F_{23})\epsilon_3\sigma T_3^4 + \epsilon_1\epsilon_4 F_{14}\sigma T_4^4 + \epsilon_2\epsilon_5 F_{25}\sigma T_5^4 + \epsilon_2\epsilon_6 F_{26}\sigma T_6^4 + K_{71}(T_7 - T_1) - C\dot{T}_2 \quad (3)$$

where subscripts

1 and 2 = sunlit and shaded solar panel sides, respectively; $\epsilon_1 = 0.8$ (solar cells) and $\epsilon_2 = 0.84$ (organic white)

3 = lunar surface

4 and 5 = front and back of planar array antenna, respectively; $\epsilon_4 = \epsilon_5 = 0.88$ (black)

6 = compartment mirror surfaces; $\epsilon_6 = 0.79$

7 = solar stepping motor; $\epsilon_7 = 0.86$ (organic white, 3M)

and parameters

$K = kA_c/LA_1$ = conductivity coefficient

$C = mC_p/A_1$ = heat capacity coefficient

and the remaining terms have been defined analogous to the earlier definitions for terms in Eq. (1). A similar equation exists for the planar array antenna.

D. Computer Programs

A JPL steady-state thermal analyzer program, TAS-1B, was used to determine the lunar day and post-sunset results from both compartment and solar panel thermal sensor data. This is a relaxation program that computes the heat flow at each node except where specified as constant, and the program includes radiative, conductive, and radiosity (inter-reflection) effects. The lunar surface, solar flux, and space normally dominate the situation compared with the relatively small spacecraft. Telemetered thermal-sensor data from the spacecraft were used as a radiometric measure of the lunar surface temperature.

The analysis was accomplished, using the computer, by assuming different values of the lunar surface temperature at selected time points and calculating the sensor measurements that would have been obtained. When these values were compared with the actual telemetered data at these same time points, convergence to the appropriate lunar surface temperature was achieved.

A North American Aviation computer program, CONFAC II, was used to obtain the view factors F_{ij}. A Chrysler dynamic thermal analyzer program, CINDA, was used to determine the eclipse results from compartment and solar panel data. CINDA required a considerable effort, since it required the programming of a variety of available subroutines. Initial efforts were directed toward achieving stability in addition to feeding in data. The next phase necessitated matching the telemetered data by iterating the lunar surface temperature at each time point. Finally, the input (telemetered) data and output data were smoothed, since the scatter in the earlier results would have been too great for interpreting the γ trends.

Coordinate transformations described in Appendix C were readily solved using a Tymshare computer terminal.

V. Error Analyses

Early efforts were made during the mission operations time period to explain the discrepancies in lunar surface temperatures derived from compartment, solar panel, and earth-based data. These discrepancies included the possible effects that could result from dust, paint degradation, crater cavities, heat capacity of rocks, and directional emission. Of these, only the last two effects were found to be of significance; rocks may have had the effect of maintaining a higher post-sunset temperature for compartment B on *Surveyor VII*, and directional emission partially explained some of the higher morning or afternoon temperatures.

Efforts subsequent to the mission operations time period were devoted to searching for other possible errors and determining their influence upon the calculated lunar surface temperatures. The first errors investigated were those within Eq. (1), in which it was confirmed that the temperature sensor inaccuracy and the view factor uncertainty were the significant error contributors during the lunar day; also, the uncertainty in compartment internal heat loss $\dot{q}$ was significant during an eclipse and after sunset. The inaccuracy in the sensor measurement was established as being the most significant error source with a possible error of $\pm 2°K$, and a possible error of $\pm 4°K$ when other telemetry system inaccuracies were included.

Attention was then given to the solar panel to see whether, by varying the initial errors, one could possibly make it more nearly match the compartment results. Heat conduction from the mast, where there were thermal sensors on two of the drive motors, increased the difference between the two spacecraft predictions of the lunar surface temperatures. Allowing for change of emittance of the back surface paint at cryogenic temperatures produced a slightly favorable reduction in this difference. Most of the other possible contributors increased the energy received by the solar panel, and further separated the two results.

Later, it was realized that, since the compartment side faces were nearly vertical, they would view approximately one-half lunar surface and one-half cold space, whereas an outboard face containing the temperature sensor was tilted back about 20 deg and would view more cold space than warm lunar surface. Also, at least one of the sides was illuminated by the sun during the day. In some missions, either early in the morning or late in the afternoon, the sun also heated the inboard face to rather high temperatures, since it was a polished aluminum (low emissivity) surface. These effects have been included in Eq. (2).

Figures 8–10 show the results obtained from a subsequent error analysis of *Surveyor V* data, performed by using a computer. Figure 8 shows the individual contributing error sources from compartment A data and Fig. 9 from compartment B on *Surveyor V*; the errors become magnified near sunset. (These error sources are

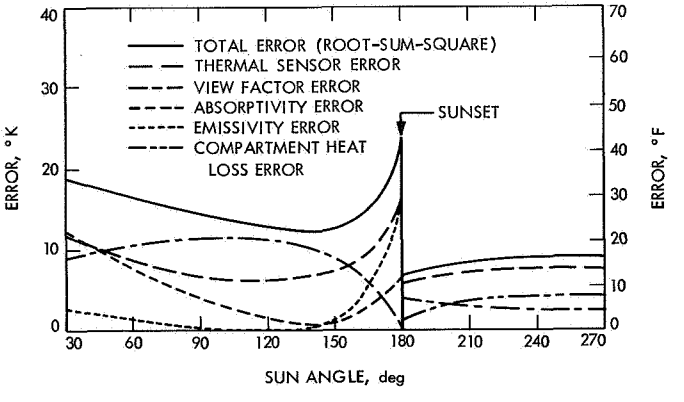

Fig. 8. Errors from *Surveyor V* compartment A data

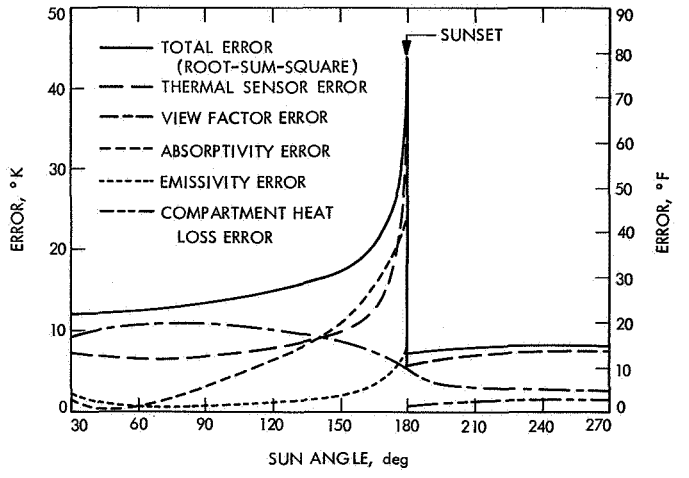

Fig. 9. Errors from *Surveyor V* compartment B data

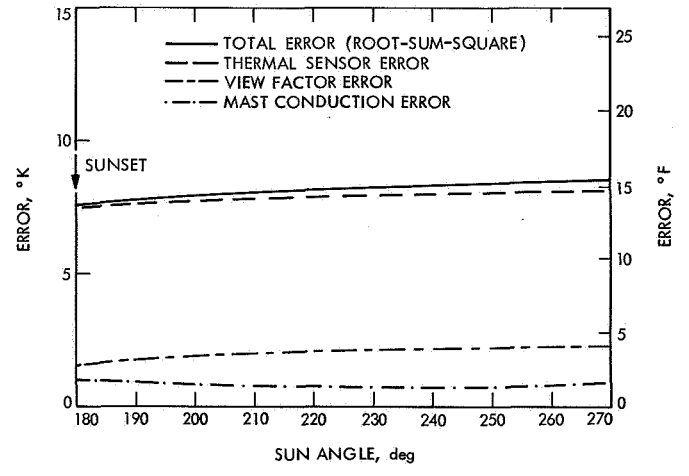

Fig. 10. Errors from *Surveyor V* solar panel data after sunset

reflected in subsequent figures as error bands placed about the results obtained.) The total errors, assumed to be independent from each other, are obtained by taking a root-sum-square of the individual errors.

Error sources from the *Surveyor* V solar panel post-sunset data are shown in Fig. 10. The total error is similar to that obtained from the compartments. The temperature sensor error is the predominant source in the three figures, especially after sunset. The mast conduction error shown in Fig. 10 is primarily due to uncertainties in temperature sensor measurements on the mast.

Use of the solar panel data to predict daytime lunar surface temperatures would result in rather large errors. This result is due to the higher sensitivity of the solar panel to the direct solar input (and less sensitivity to the lunar surface), and the uncertainty in temperature due to variable electrical power loading.

A good correlation exists between the error analysis results obtained from the computer and those obtained analytically from Eqs. (1) and (3). Thus, error sources previously found to have insignificant effects upon the total error have been omitted from Figs. 8–10.

The individually assumed errors for these analyses were

$$\Delta T_i = \pm 4°\text{C}\ (\pm 7.2°\text{F})$$

$$\Delta F_{ij} = \pm 10\%$$

$\Delta \epsilon_i = \pm 0.02$ for painted surfaces, and $+0.02, -0.01$ for polished aluminum

$$\Delta \alpha_i = \pm 0.02$$

$$\Delta \dot{q} = \pm 20\%$$

$$\Delta K_{ij} = \pm 10\%$$

VI. Results

A. Preliminary Results

The lunar surface temperatures derived from the *Surveyor I* compartment data using Eq. (1) differed from earth-based predictions. Higher morning temperatures were evident and lower values of γ resulted from *Surveyor*. Similar discrepancies occurred on the subsequent *Surveyor* missions, and especially large differences were noted during the eclipses on the *Surveyors III* and V missions. These *Surveyor* derived eclipse lunar surface temperatures were found to be higher than earth-based predictions by 50 and 80°K, respectively.

Another discrepancy also appeared when lunar surface temperatures derived from the solar panel temperature measurements were found to differ from the results obtained from compartment data. In fact, the solar panel results were closer to earth-based predictions. This comparison is shown in Fig. 3 during the *Surveyor III* eclipse.

Under the early conviction that compartment data were more reliable, efforts were concentrated upon reducing these data, as well as attempting to explain the above discrepancies. During some of the missions, the compartment results were as much as 25°K higher during

the daytime than earth-based predictions. At night, the compartment-based lunar surface temperatures also were higher, resulting in γ values near 500, compared with earth-based eclipse predictions for γ of about 1350. Recent earth-based measurements taken during the lunar night (Ref. 9) have resulted in γ values less than 1000, compared with the earlier earth-based measurements taken during eclipses (Refs. 10–12) with γ values averaging about 1350.

Several effects have been considered in modeling the lunar surface characteristics in order to explain the difference between eclipse and post-sunset measurements. Effects given serious consideration are directional thermal emission, variation of thermal conductivity with soil depth, and variation of density with depth. Winter and Saari (Ref. 13) have developed a "cube" model that varies thermal conductivity with depth, and they have been able to match the Wildey, Murray, and Westphal lunar post-sunset data as well as eclipse measurements with this model. Jones (Ref. 14) recently suggested a model that includes density variation with depth and conductivity as a function of depth and temperature.

B. Revised Daytime Results

The lunar surface daytime temperatures obtained from *Surveyor V* compartment data are compared in Figs. 11 and 12 with the Lambertian prediction based upon the solar insulation and bolometric albedo. (Sufficient time was not available to correct daytime results from the other missions, where revisions would have a similar effect.) The revised results using Eq. (2) and including side conduction effects, compares more favorably with the Lambertian curve.

Some evidence of directionality exists in the curves shown in Figs. 11 and 12. The *Surveyor V* compartment B (Fig. 12) viewed the west; therefore, a directional effect (temperature increase) would be expected during the lunar morning. The error band that is shown in Fig. 12 for compartment B (from Fig. 9) during the lunar morning suggests that a directional trend exists.

A similar trend is not as clearly indicated in Fig. 11. Compartment A viewed the southeast and would be expected to show a directional effect in the lunar after-

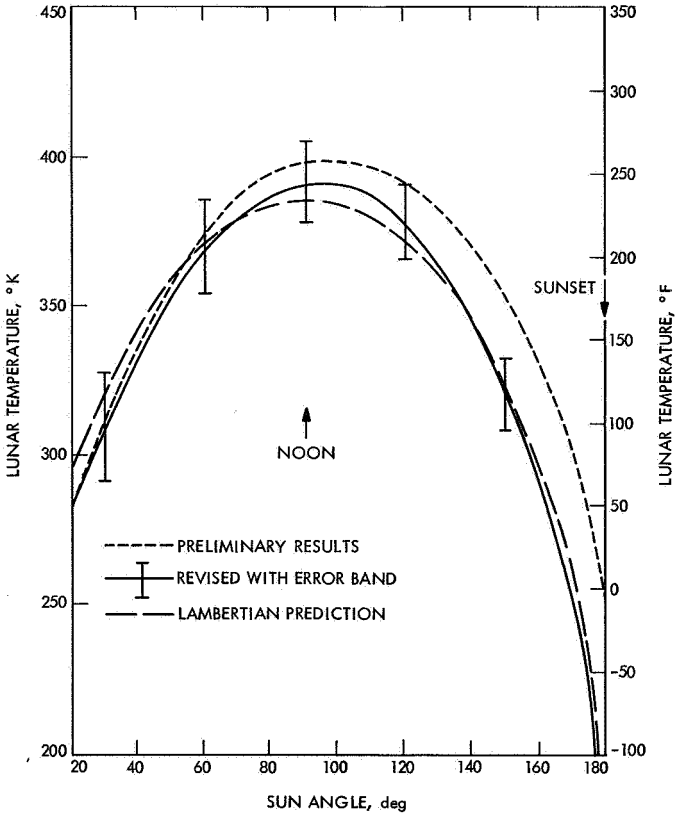

Fig. 11. Daytime lunar surface temperatures from *Surveyor V* compartment A data

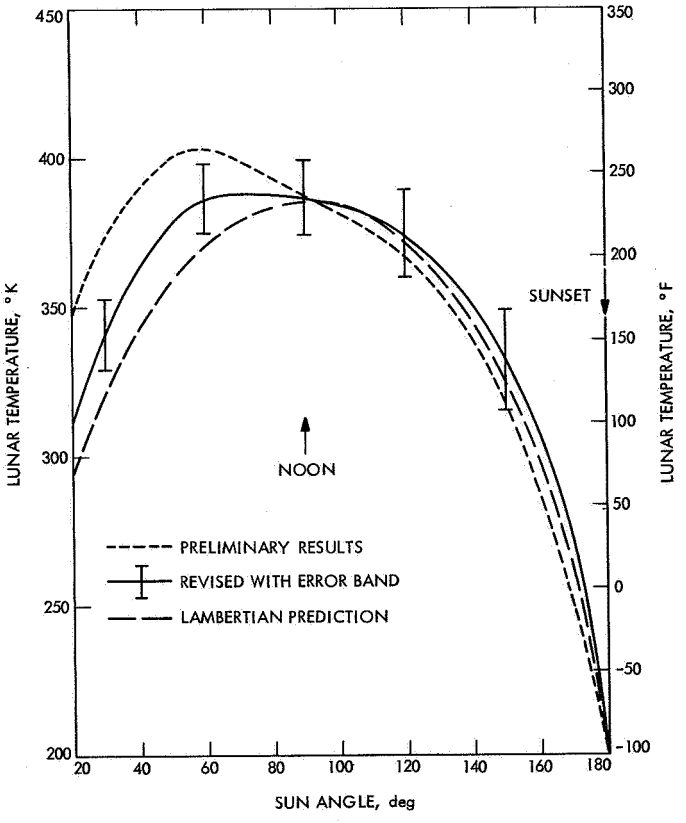

Fig. 12. Daytime lunar surface temperatures from *Surveyor V* compartment B data

noon. These figures also indicate that the earlier predicted directional trend has been reduced by about one-half in intensity.

In the earlier *Surveyor V* work (Refs. 3 and 6), the Lambertian curves were shifted to the right 10 deg for compartment A and to the left 15 deg for compartment B, to account for the local lunar surface slope. A more detailed study of the crater profile indicated that the local slope seen by the compartments was less than 5 deg. Therefore, shifting of the Lambertian curve cannot account fully for the directional effect; it must, in part, be due to the roughness of the lunar surface.

C. Revised Post-Sunset Results

The post-sunset lunar surface temperatures derived from compartment data have been revised for all the missions, except for the data from *Surveyor III*, which transmitted only 2 h after sunset. Lunar surface temperatures derived from *Surveyor V* post-sunset data during the second lunar night also were revised, since the transmission lasted the longest of any mission (9 earth days). In addition, lunar surface temperatures have been derived from solar panel post-sunset temperature data.

The principal effect included in the revised compartment results was the small but significant heat flow around the outside of the compartments from the sides, bottom, and inboard compartment faces. The two sides were warmer than the outboard face (where the temperature sensor was located), since they were vertical and viewed more of the warm lunar surface. The outboard face was tilted back 20 deg and viewed more cold space.

The compartment model, described by Eq. (2), included similar equations for the remaining faces. The actual computer program utilized eight nodes that included the six faces, the lunar surface, and cold space. Other possible nodes were considered, but were found to be negligible, such as the RADVS antenna located just under each compartment. The solar panel model, described by Eq. (3) in conjunction with Fig. 7, used nine nodes, including space.

Figures 13–16 compare the post-sunset lunar surface temperatures from the revised compartment model, Eq. (2), with the preliminary compartment model, Eq. (1), and with theoretical γ curves. In Fig. 13, the revised γ value for *Surveyor I* increases from about 600 to 800 ($cm^2\ s^{1/2}$ °K/g-cal). The revised trend appears to follow more closely the theoretical constant γ trend, particularly later into the night (transmission lasted 48 h). The γ curves assume a lunar surface having thermal characteristics that are constant. Actually, the lunar surface properties are expected to vary with depth of soil and with temperature (Refs. 13 and 14). Thus, a difference in behavior between the γ curves and the compartment band shortly after sunset is to be expected.

The revised γ curves from *Surveyor V* compartment data, shown in Fig. 14, increase from 400 to 600. Only data from the first lunar night are presented in the preliminary results. Four compartment curves (both compartments on two successive nights) are presented in the revised results as a band, since they fall close to each other.

The revised γ curves from *Surveyor VI* compartment data, shown in Fig. 15, increase from 600 to an average value of about 750. The upper curve of the revised results is from the compartment A data and the lower curve from the compartment B data. The bandwidth again has increased as it did from the *Surveyor I* data.

The revised γ values from *Surveyor VII*, shown in Fig. 16, also have increased to larger γ values. However, the results from compartments A and B are sufficiently different from each other, before and after revision, so that they should be treated individually. In Ref. 5, this difference in behavior from the two compartments was attributed to compartment B viewing what appears to

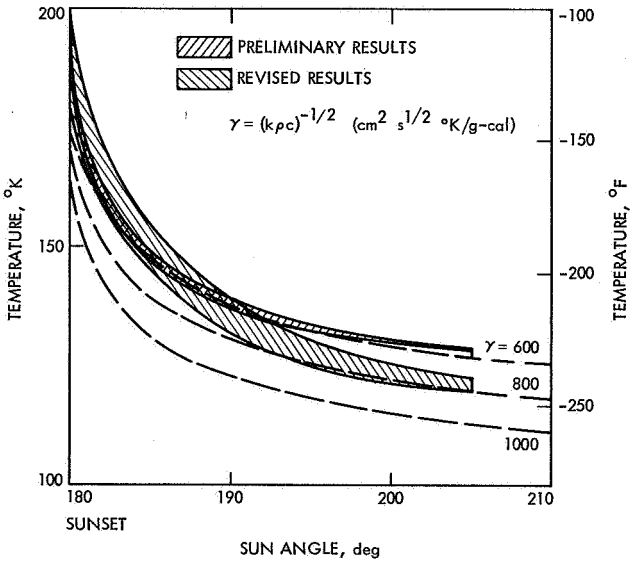

Fig. 13. Post-sunset lunar surface temperatures from *Surveyor I* compartment data

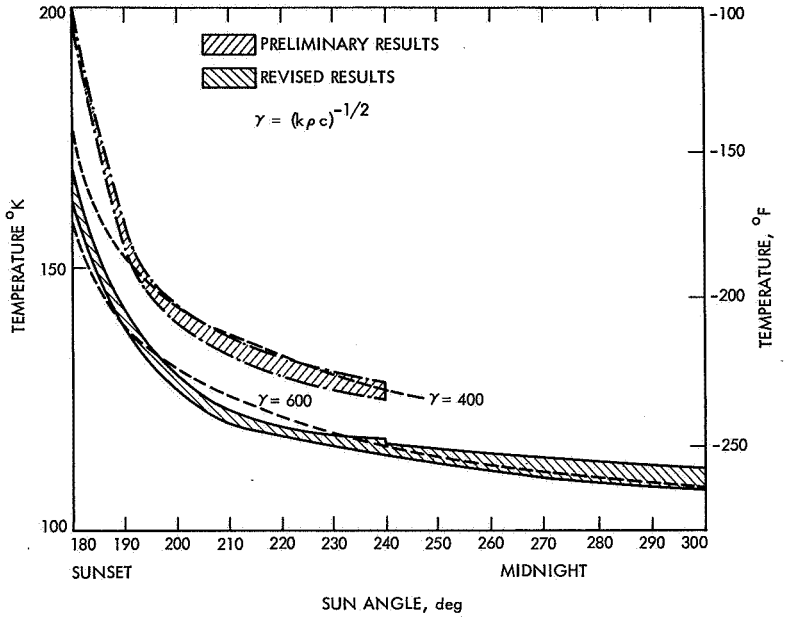

Fig. 14. Post-sunset lunar surface temperatures from *Surveyor V* compartment data

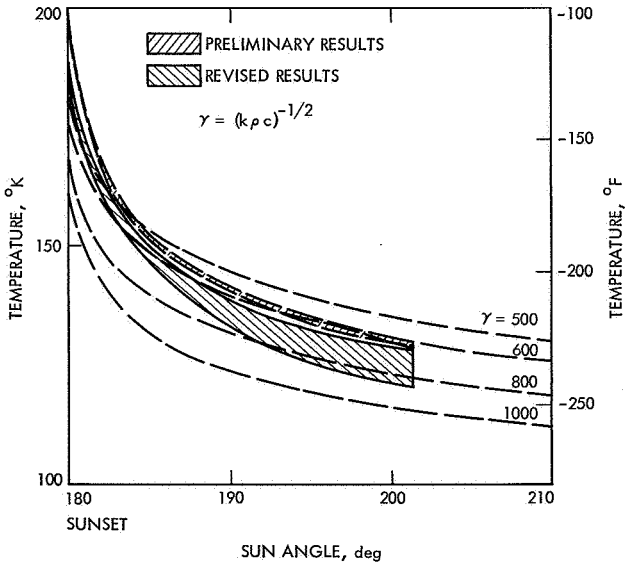

Fig. 15. Post-sunset lunar surface temperatures from *Surveyor VI* compartment data

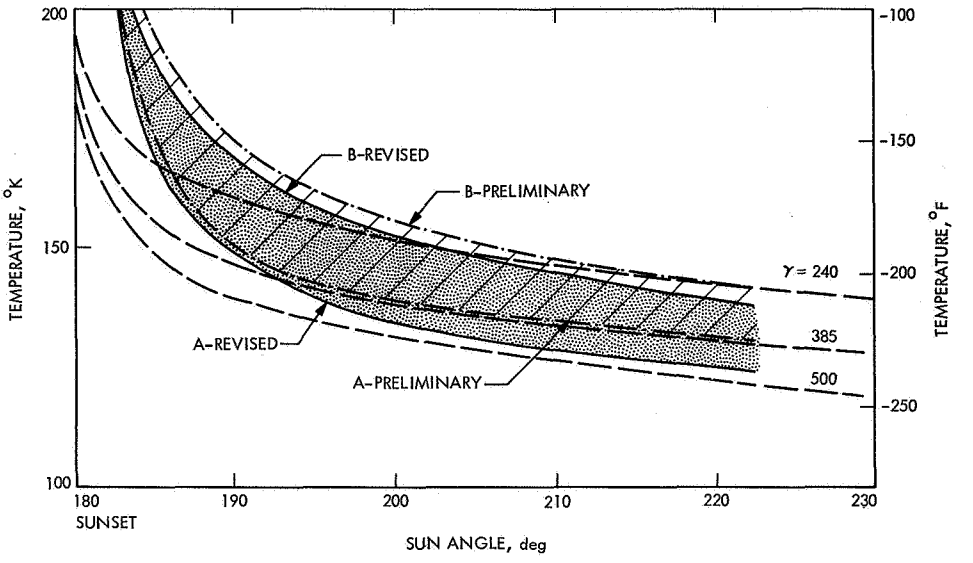

Fig. 16. Post-sunset lunar surface temperatures from *Surveyor VII* compartment data

be a much more rocky terrain than did compartment A. This difference has been preserved in the revised results. Thus the γ value for compartment A has increased from 385 to 450 and for compartment B from 240 to 300.

The post-sunset lunar surface temperatures from the compartment data previously shown (Figs. 13–16) are now compared with results from solar panel data and earth-based measurements. These comparisons are given in Figs. 17–21. The earth-based post-sunset measurements by Wildey, Murray, and Westphal (Ref. 9) are shown for comparison.

Figure 17 shows a close agreement of *Surveyor I* compartment results with earth-based measurements having a γ value of about 800. The solar panel data produce a γ value of about 1200.

The post-sunset lunar surface temperatures from various *Surveyor V* sources are compared in Fig. 18, the compartment band is from Fig. 14. The solar panel band, which is from the first and second lunar nights, has a behavior similar to the compartment band.

Error bands are shown in Fig. 18 for the *Surveyor V* compartment and solar panel based results. The earth-based measurement error band is unspecified. These error bands were presented in more detail in Figs. 8–10, where the individual uncertainties were root-sum-squared to get the total bands. A small degree of error band overlap between compartment and solar-panel based results is evident. The regions of most likely occurrence that fall centrally within the error bands are apparent from the compartments where the four cases were available. If one assumes a normal (gaussian) distribution as shown in Fig. 18 for the distribution within the error bands, then the degree of overlap is seen to be weak.

Terminal theoretical curves are included on the right-hand edge in Fig. 18 for values of γ equal to 600, 800, and 1000. The compartment trend fits a γ value of about

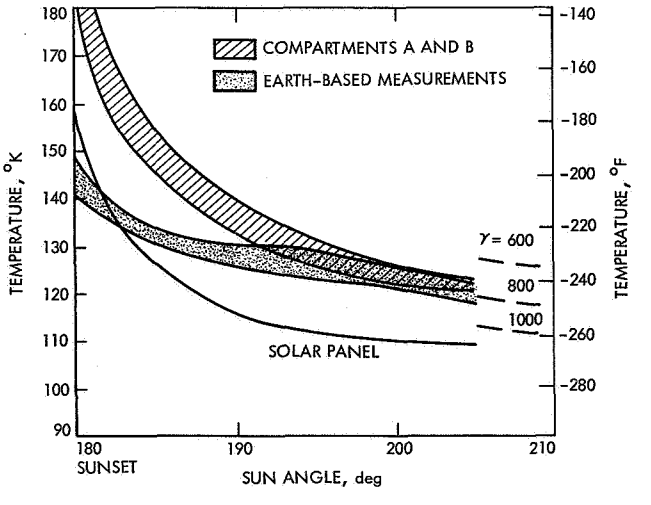

Fig. 17. Post-sunset lunar surface temperatures from various sources for *Surveyor I*

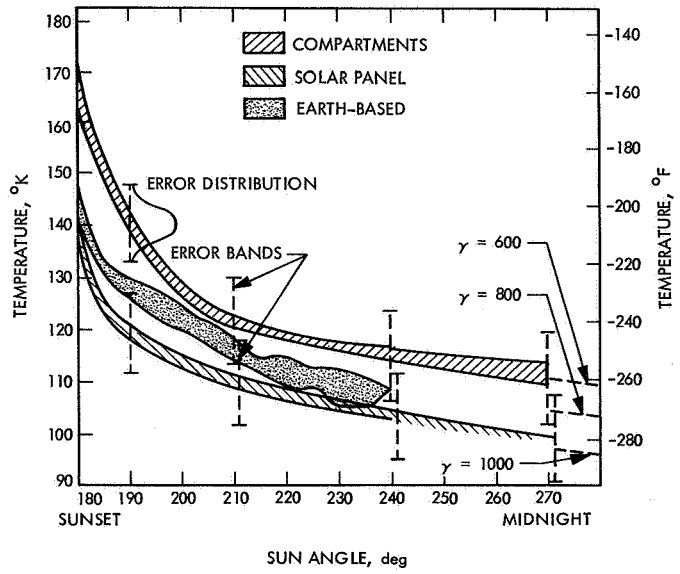

Fig. 18. Post-sunset lunar surface temperatures from various sources for *Surveyor V*

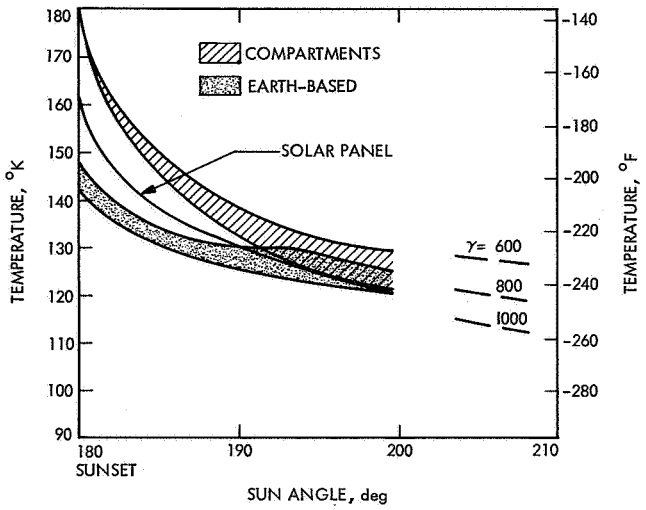

Fig. 19. Post-sunset lunar surface temperatures from various sources for *Surveyor VI*

600, the earth trend fits an average γ value of about 850, and the solar panel trend fits a γ value of about 1000.

Figure 19 shows that the results from the three sources all fall close to each other for *Surveyor VI* with an average γ value of about 800. However, Fig. 20 shows that the lunar surface temperatures measured by the *Surveyor VII* compartments is considerably higher at Tycho than the earth-based measurements that were averaged in a sense, since they were taken over about half of the visible surface of the moon. There is no post-sunset curve for the solar panel, since its thermal sensor failed at sunset. Figure 21 consolidates the results from the three spacecraft in lunar maria; the spacecraft transmitted data well into the night. The compartments consistently result in higher lunar surface post-sunset temperatures (and lower γ values) than do the solar panel data, while the earth-based post-sunset data fall in the intermediate region.

D. Revised Eclipse Results

The sun was eclipsed by the earth at the *Surveyor III* site on the first lunar day and at the *Surveyor V* site on the second lunar day. The preliminary lunar surface temperatures derived from the *Surveyor III* compartment

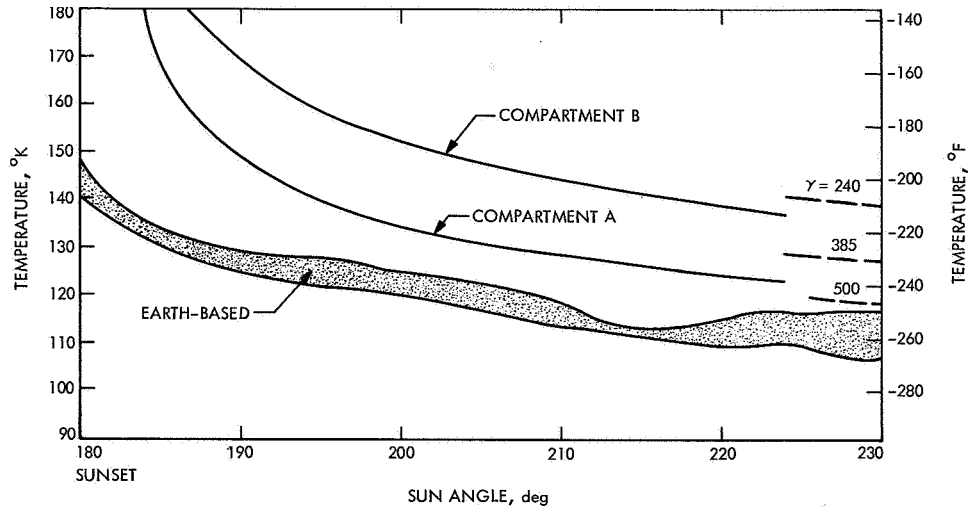

Fig. 20. Post-sunset lunar surface temperature from *Surveyor VII* compartments compared with earth-based measurements

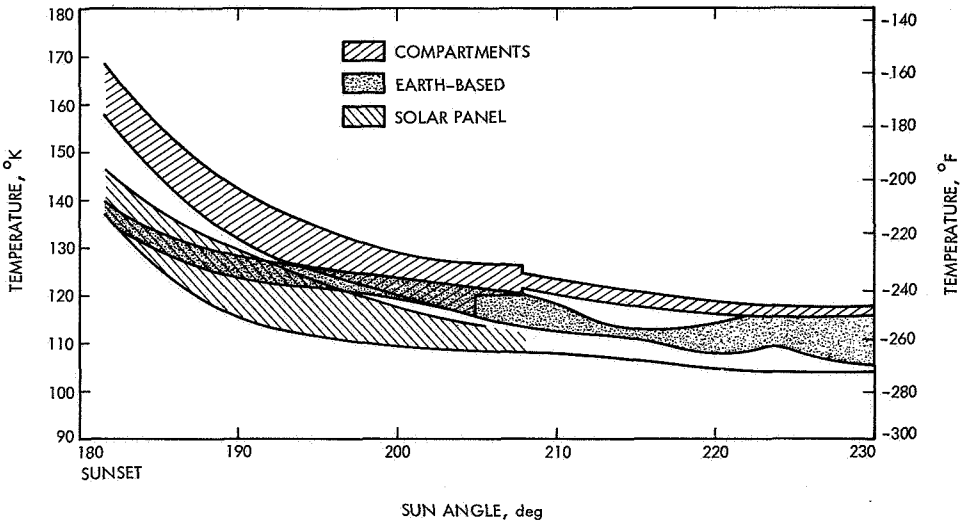

Fig. 21. Post-sunset lunar surface temperatures from *Surveyors I, V,* and *VI*

data during the eclipse were presented earlier in Fig. 3 and were compared with a theoretical prediction based on earth-based measurements and Lambertian theory.

The *Surveyor III* results from the revised compartment model [Eq. (2)], shown in Fig. 22, compare very closely with the preliminary results and a γ trend of 400. The *Surveyor III* results also are compared in Fig. 23 with temperatures from solar panel data and the earth-based measurements. The lunar surface temperatures derived from the solar panel data are close to the earth-based measurements, whereas the compartments predict higher temperatures as they did after sunset. The γ values from the two compartments A and B, the solar panel, and the earth-based prediction are 450, 400, ~1000, and 1420,[5] respectively.

Preliminary and revised lunar surface temperatures from the *Surveyor V* compartments during the eclipse are compared in Fig. 24 along with γ trends. In Fig. 25, the revised compartment results are compared with results from the solar panel and the earth-based prediction. Similar trends exist; namely, higher compartment temperatures. The γ values from the two compartments A and B, the solar panel, and the earth-based prediction are 425, 385, 1000, and 1350,[5] respectively.

The error bands also are shown in Fig. 25 for compartment and solar panel derived lunar surface temperatures. They definitely do not overlap.

[5]Comparison made at start of umbra phase for earth-based measurements.

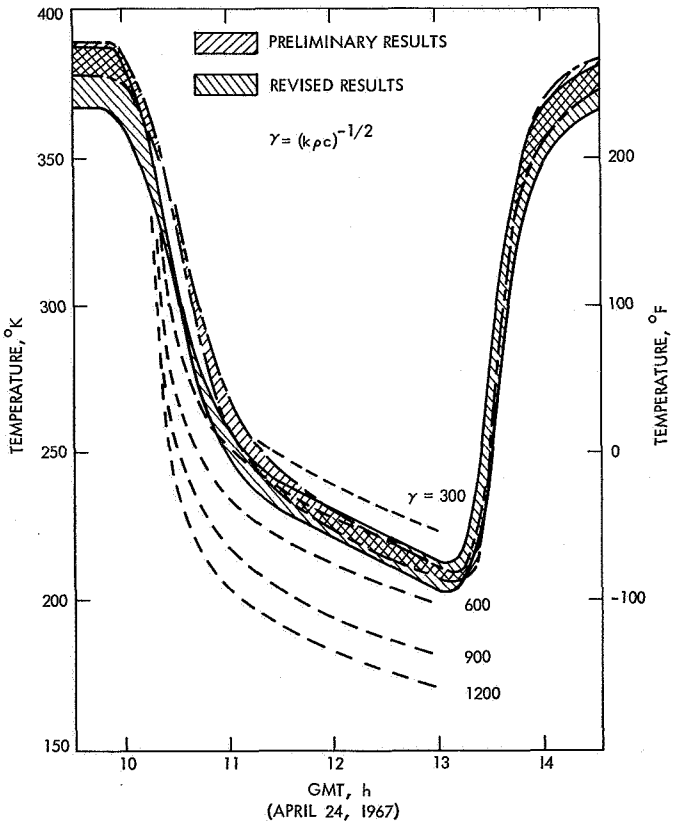

Fig. 22. Eclipse lunar surface temperatures from *Surveyor III* compartment data

VII. Conclusions

The revised daytime lunar surface temperatures derived from the *Surveyor V* compartment data still show

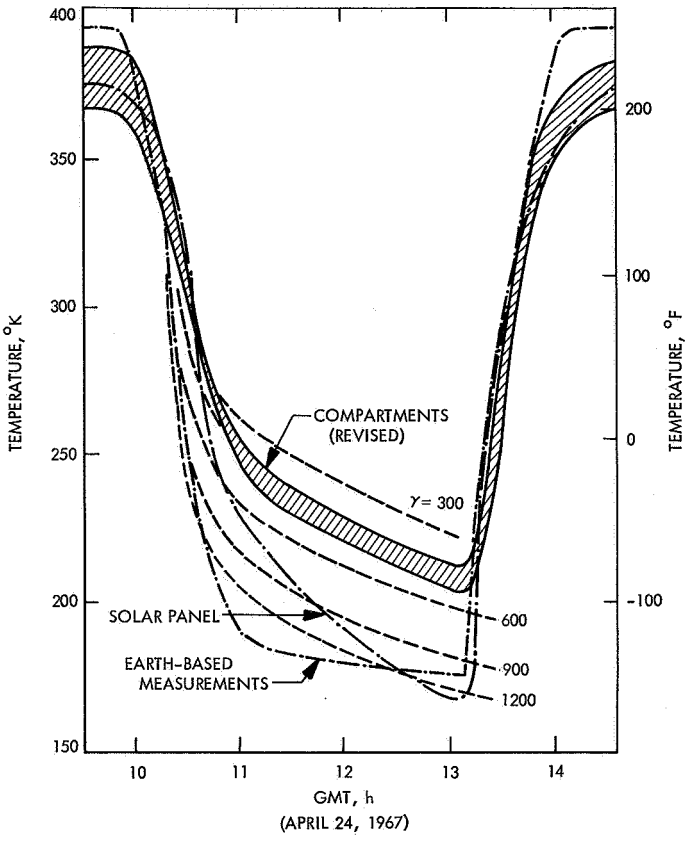

Fig. 23. Eclipse lunar surface temperatures from various sources for *Surveyor III*

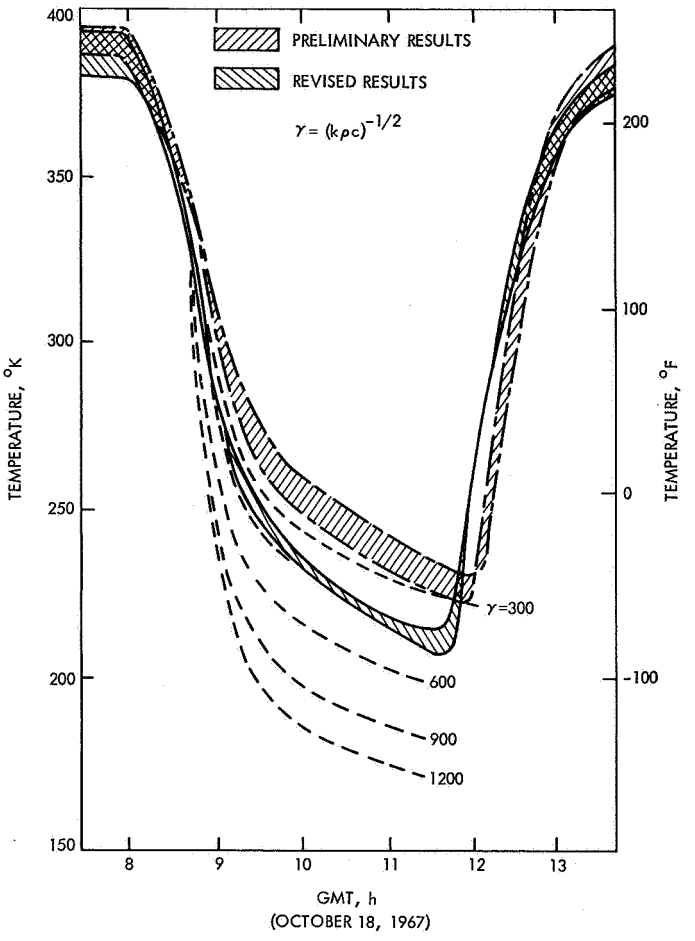

Fig. 24. Eclipse lunar surface temperatures from *Surveyor V* compartment data

the presence of directionality but with about one-half the intensity previously given. It is believed that the directional trends reported earlier from the other *Surveyor* missions would be preserved to a similar degree.

The correlation of post-sunset results from compartment, solar panel and earth-based data is improved over past correlations. This improvement is due to using a revised compartment model (which includes side conduction effects) and earth-based measurements from post-sunset rather than eclipse measurements. The most probable post-sunset lunar surface temperature corresponds closely to the earth-based measurements.

A summary comparison of post-sunset results from the *Surveyor* compartments and solar panel, together with earth-based results for each landing site, is given in Table 3. For all the *Surveyor* sites for which there are post-sunset data (i.e., *Surveyors I, V, VI,* and *VII*), there is essential agreement between the compartment and the earth-based values of gamma; the value from compartment B on *Surveyor VII* was low, which is believed to be due to the presence of rock-like debris near the compartment (also supported by photographic evidence). The value of gamma from the solar panel data is higher for *Surveyors I* and *V*, but about the same for *Surveyor VI*. In other words, the values from the solar panel are not in as good agreement.

These results indicate that the lunar soil is a finely particulate, highly insulating material (the γ values for

Table 3. Intercomparison of constant gamma post-sunset values from *Surveyor* and earth-based data

Surveyor	From compartments	From solar panel	Earth based
I	800	1200	800
V	600	1000	850
VI	750	900	800
VII	450 (A) 300 (B)	—	550

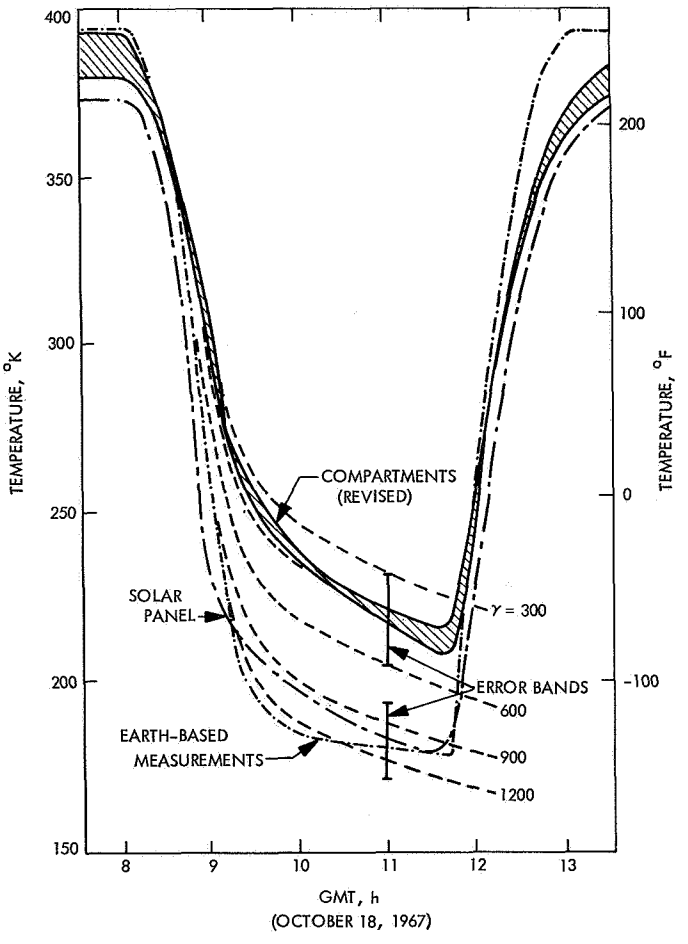

Fig. 25. Eclipse lunar surface temperatures from various sources for *Surveyor V*

rock, beach sand, and dust are 20, 100, and 1000 +, respectively). No dust layer is apparent on any of the spacecraft, since it would have had an appreciable thermal effect and would have been detected by the thermal sensors.

A comparison of eclipse results from the *Surveyor* compartments and solar panel, together with earth-based results for the landing sites (*Surveyors III* and *V*), is given in Table 4. The values of gamma from the three sources are significantly different. Values from the compartments are the lowest, values from the solar panel are intermediate, and earth-based values are highest. It is suggested that the uppermost layer of the lunar soil was modified during the *Surveyor* landings. This may have removed a low-conductivity, low-heat capacity layer from underneath and closely surrounding the spacecraft and would cause the compartments to sense higher temperatures during the eclipse than expected. Since the solar panel views terrain farther from the spacecraft, the panel could be expected to provide an intermediate value. Additional analysis would be required to investigate this possibility further. The suggestion of fine particles being blown from the landing site has further weight because of the dust cloud observed during *Apollo 11* and *12* landings.

In conclusion, a fundamental effect or combination of effects caused the inferred lunar surface temperatures from the compartments, solar panels, and earth-based measurements to be different. This may have also been due to the inferential technique used in this analysis.

Finally, it would be highly desirable for future missions to have an instrument especially designed and tested to make direct thermal measurements of the unknown environment.

Table 4. Intercomparison of constant gamma eclipse values from Surveyor and earth-based data

Surveyor	From compartments	From solar panel	Earth based
III	450 (A) 400 (B)	1000	1420
V	425 (A) 385 (B)	1000	1350

Appendix A

Spacecraft Landed Orientations

The landed orientations for the different *Surveyor* spacecraft are compared in Fig. A-1. The surface views from compartments A and B are depicted along with local downslope tilt. The values used for calculation purposes, as shown in Fig. A-1, were based on solar panel and planar array antenna positional data.

The lunar surface temperatures were found to be dependent primarily on the sun elevation angle to the local lunar surface slope. Thus, for *Surveyors III* and *V*, which landed on sloping surfaces, simple time translations of the lunar noon to a normal from the local surface resulted in improved temperature distributions. The lunar surface temperature measured by each compartment sensor also was influenced by terrain features and shadowing of the lunar surface by the spacecraft.

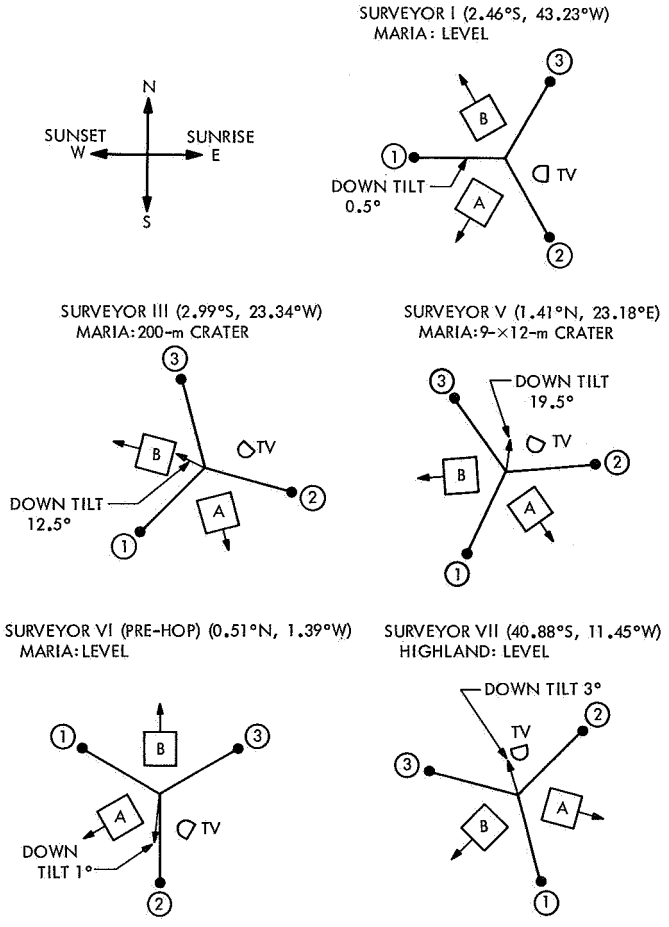

Fig. A-1. *Surveyor* spacecraft landed orientations

I. *Surveyor I*

The landed orientation of *Surveyor I* is shown in Fig. A-2. The azimuth of leg 1, the *Y* axis, is given as 1 deg south of west; the spacecraft $-Z$ (vertical) axis is taken to be tilted 0.5 deg toward the west. To ensure early morning coverage, the science bay (television camera) was directed eastward, which resulted in compartment A viewing southwest and compartment B viewing northwest. The normal to the outer canister face of each compartment made an angle of 69 ± 1 deg with the spacecraft $-Z$ axis. The view factors from compartments A and B to the lunar surface were approximately 0.28 and 0.29, respectively. The temperature data measured by thermal sensors on the outboard faces of the compartments are given in Ref. 1.

The solar panel was stepped throughout the lunar day so that it would be nearly normal to the sun vector. The solar panel temperature data are presented in Ref. 6.

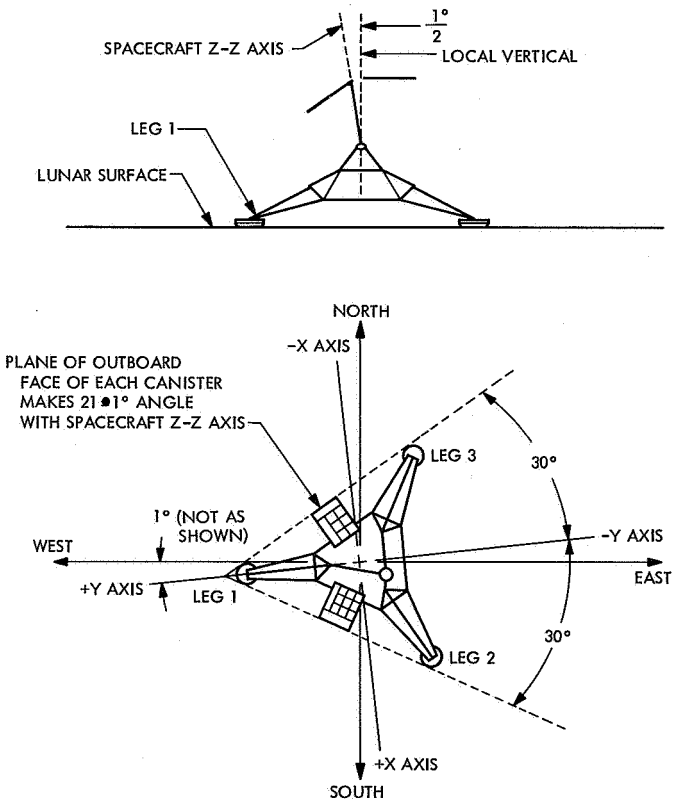

Fig. A-2. *Surveyor I* landed orientation

II. *Surveyor III*

The assumed orientation of *Surveyor III* with respect to lunar coordinates is given in Fig. A-3. The normal to the compartment A outer canister face was lying in a vertical plane of azimuth 9 deg east of south and was inclined at an angle of 65 deg to the local vertical. The normal to the compartment B outer canister face had an azimuth 16 deg north of west and was inclined at an angle of 81 deg to the local vertical. The spacecraft $-Z$ axis approximated the direction of the local surface normal; both compartment normals were inclined at 69 deg to this direction.

The *Surveyor III* landing site (about 45 m southeast of the crater center) is shown in Fig. A-4. The surface area viewed by each compartment was limited by the

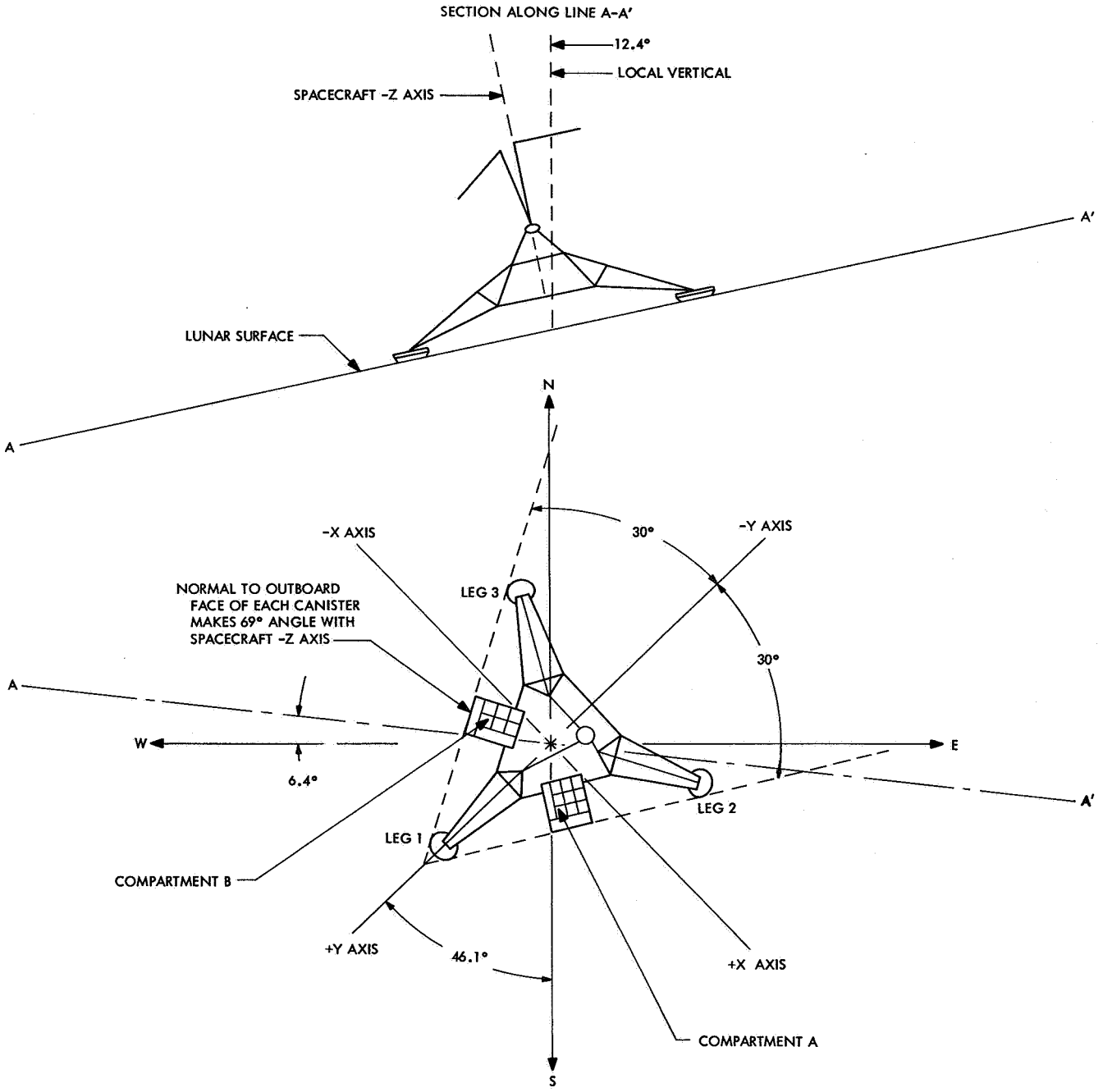

Fig. A-3. *Surveyor III* landed orientation

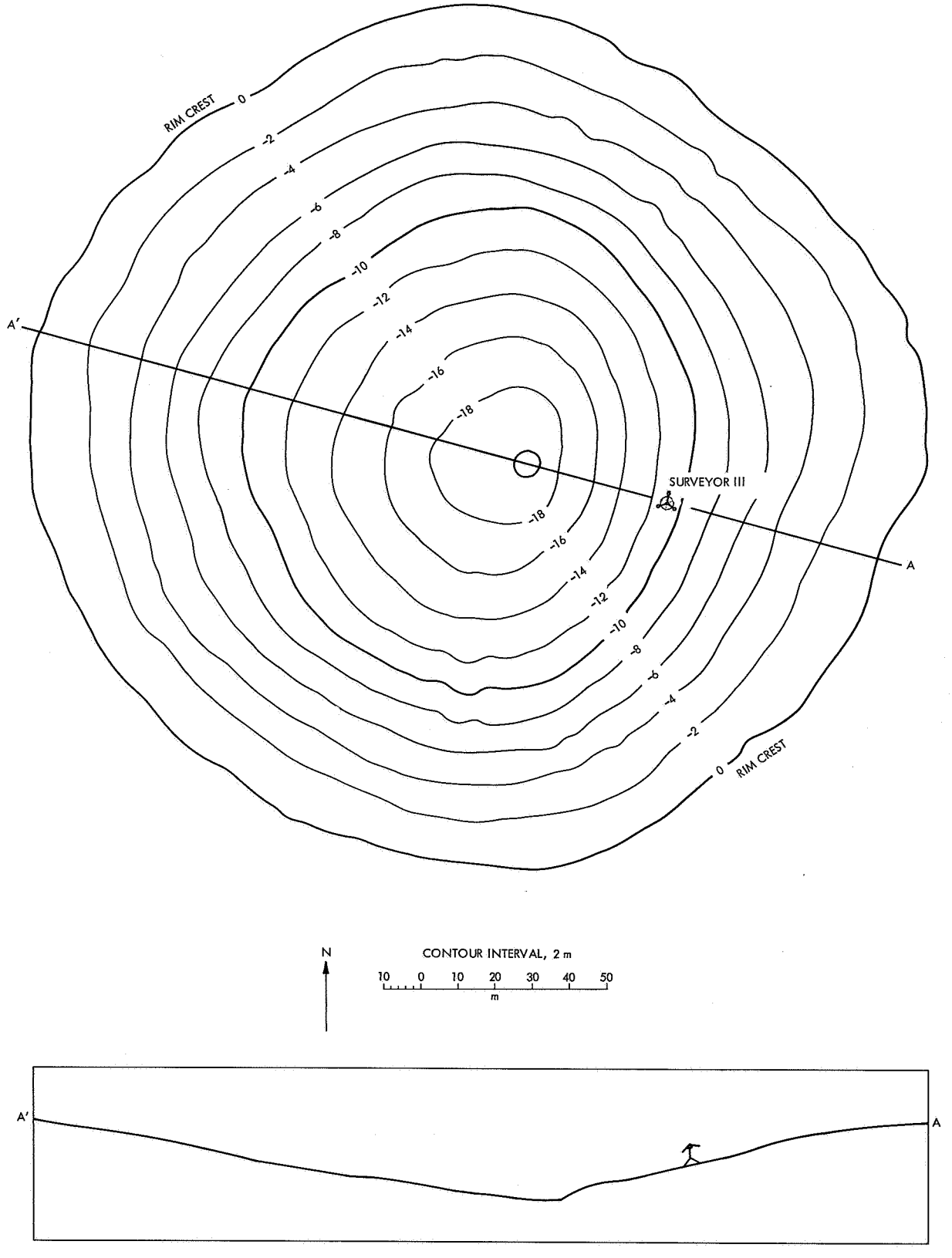

Fig. A-4. Contour map and profile of crater in which *Surveyor III* landed

canister face orientation and crater rim. On this basis, compartment A viewed a maximum projected surface area of 1.3×10^4 m², and compartment B an area of 2.6×10^4 m². The resulting view factors from compartments A and B to the lunar surface were 0.31 and 0.41, respectively. The compartment, solar panel, and planar array temperature data are given in Ref. 2.

III. *Surveyor V*

Surveyor V landed in a small (9- × 12-m) crater, with leg 1 positioned near the crater rim and legs 2 and 3 downslope on the southwest wall of the crater. Figure A-5 shows the assumed orientation of *Surveyor V* with respect to the lunar coordinates. At approximately sunset of the first lunar day, the shock absorbers on legs 2 and 3 compressed, placing the spacecraft even more downslope. During the second lunar day, the spacecraft nearly returned to the orientation it had during the first lunar day, and then at sunset one leg compressed. Table A-1 lists the different orientations.

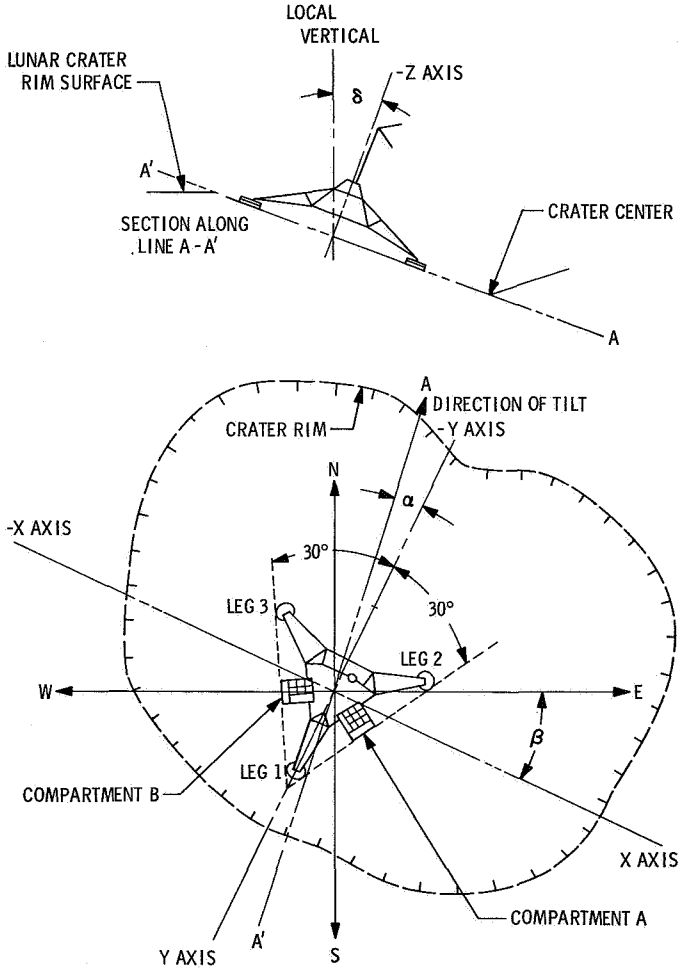

Fig. A-5. *Surveyor V* landed orientation

Table A-1. Orientation angles for *Surveyor V*

Period	Angle, deg			
	α	β	γ	δ
First day	97.6	−24.5	−16.9	19.5
First night	101.0	−25.0	−14.0	24.5
Second day	103.8	−25.4	−11.6	19.2
Second night	100.2	−25.6	−15.4	21.8

The location of the spacecraft within the crater profile is shown in Fig. A-6. Compartment A initially viewed the east side of the crater, the surface beyond the crater, and space, with an overall view factor of 0.247 to the lunar surface. Compartment B viewed the west side of the crater, the surface beyond the crater rim, and space, with an overall view factor of 0.255 to the lunar surface. The view factors for the second day are given in Table 2. The compartment, solar panel, and planar array temperature data are given in Ref. 3.

IV. *Surveyor VI*

Surveyor VI, after the initial landing and later after the hop, was situated on a generally level, flat surface. The hop occurred on November 17 when the vernier engines were fired for 2.5 s, causing the spacecraft to rise and to land 2.4 m from the original landing point.

The assumed orientations of the spacecraft with respect to the lunar coordinates are shown in Fig. A-7. Compartment A viewed the area to the southwest, with a view factor of 0.321 to the lunar surface after the initial landing and 0.350 after the hop. Compartment B viewed the area to the north, with a view factor of 0.318 to the lunar surface after the initial landing and 0.316 after the hop.

The compartment temperature data are given in Ref. 4. The solar panel temperature data are presented in Ref. 6.

V. *Surveyor VII*

Surveyor VII landed on a generally level surface in a highland area. The orientation of the spacecraft with

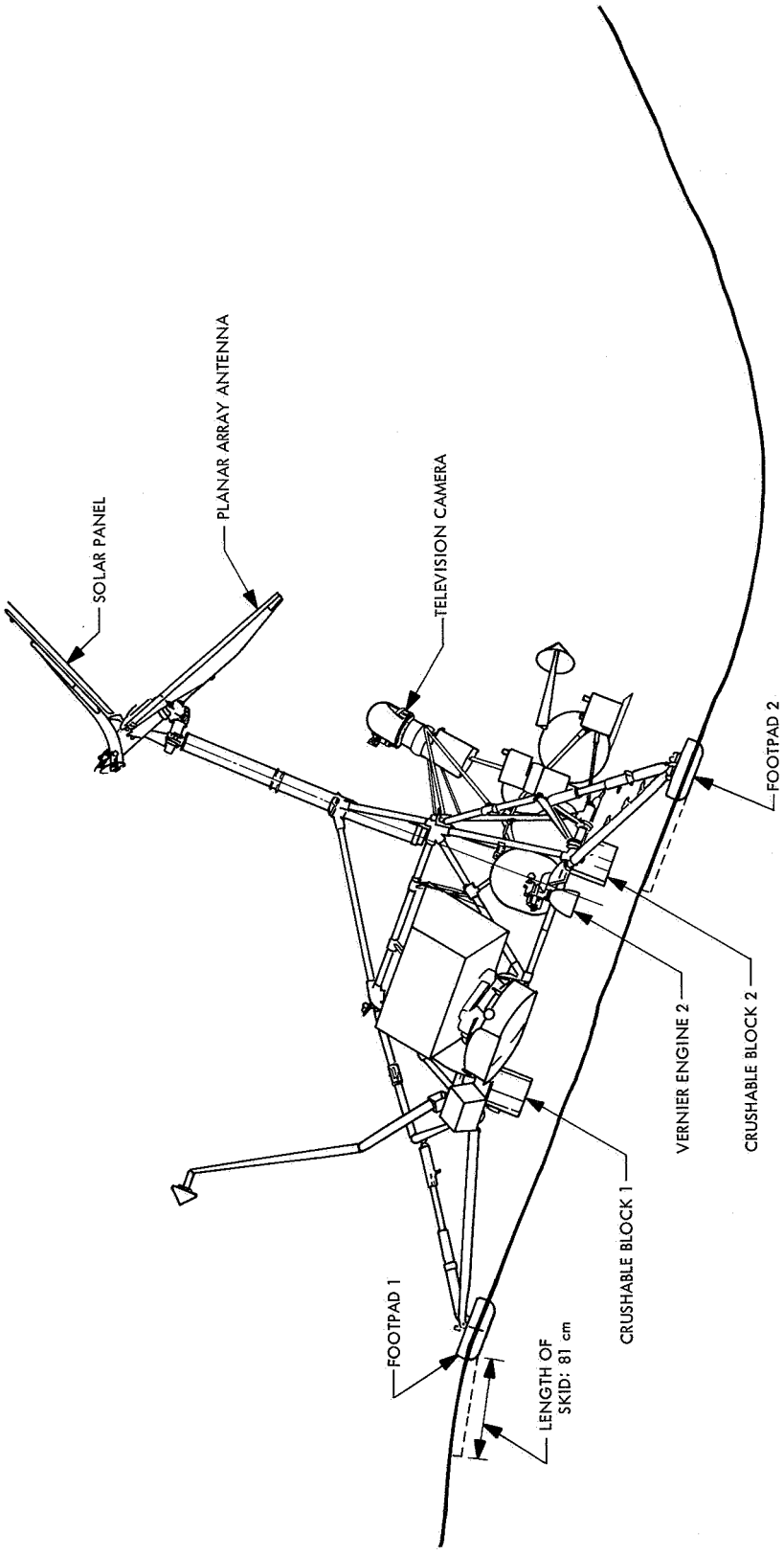

Fig. A-6. Profile of crater in which *Surveyor V* landed

respect to lunar coordinates is shown in Fig. A-8. Compartment A viewed the east, with a view factor of 0.337 to the lunar surface. Compartment B viewed the area to the southwest, with a view factor of 0.333 to the lunar surface. During the lunar night, shock absorber 2 compressed, resulting in a slope of the spacecraft vertical axis about 6 deg with respect to the local vertical during the second lunar day. The compartment, solar panel, and planar array temperature data are given in Ref. 5.

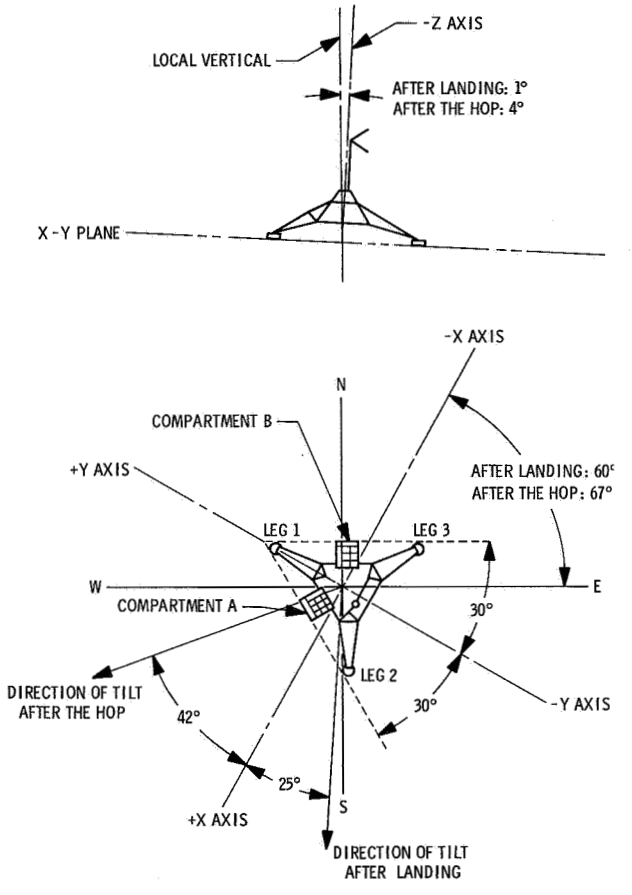

Fig. A-7. *Surveyor VI* landed orientations

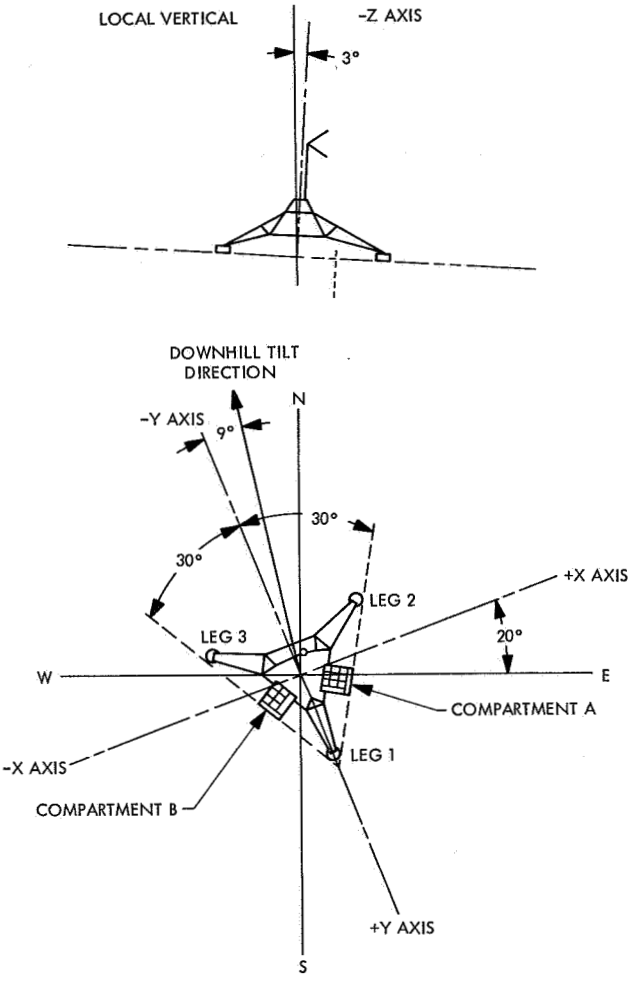

Fig. A-8. *Surveyor VII* landed orientation

Appendix B

Earth-Based Thermophysical Observations

The surface temperatures calculated from the spacecraft thermal data have been compared with earth-based measurements and theoretical thermophysical models. In the following paragraphs, a summary is given of the pertinent earth-based measurements of the various landing site regions.

I. Albedo

It is necessary to know the bolometric albedo so that, during illumination, the amount of solar radiation absorbed by the surface can be calculated. If the small amount of energy conducted in or out of the surface during illumination is ignored, then the Lambertian temperature T_L (with unit surface emissivity assumed) is defined by the expression

$$\sigma T_L^4 = (1 - A)\, S \sin \psi \qquad \text{(B-1)}$$

where

σ = Stefan–Boltzmann constant, W/m² °K⁴

A = bolometric or total solar albedo, dimensionless

S = solar irradiation, W/m²

ψ = elevation angle of sun to the surface, deg

By this definition, the Lambertian temperature is that which a perfectly diffuse blackbody surface would have to radiate the same energy as is absorbed. Actually, the lunar surface exhibits directional effects in its emission; however, it has been found that the Lambertian temperature provides a useful comparison to the spacecraft data.

To calculate T_L, the bolometric albedo of each site must be known. For this purpose, the simultaneous infrared and photometric scan data of Ref. 15 were used. Of particular interest was the scan at full moon (−2-deg phase angle) just prior to the December 19, 1964, eclipse. The data show the brightness[6] temperature changes with the photometric brightness on adjacent regions. This allows the calculation of the relationship between the photometric brightness on this scan and the bolometric albedo.

[6]With unit surface emissivity assumed.

Now, due to the directional emission of the lunar surface, the observed brightness temperature T_b differs from T_L because of the angle of view, so that

$$T_b(\psi) = D(\psi) T_L \qquad \text{(B-2)}$$

which defines the directional factor $D(\psi)$. For the full-moon scan, if the bolometric albedo A is assumed proportional to the measured photometric brightness B, then

$$A = KB \qquad \text{(B-3)}$$

where K is a constant that, if known, allows the determination of A for any point. To determine K, measurements were made on two areas (1 and 2) of differing brightness at the same ψ, so, from Eqs. (B-1) and (B-2),

$$\sigma \left[\frac{T_{b,1}}{D(\psi)}\right]^4 = (1 - KB_1)\, S \sin \psi \qquad \text{(B-4a)}$$

$$\sigma \left[\frac{T_{b,2}}{D(\psi)}\right]^4 = (1 - KB_2)\, S \sin \psi \qquad \text{(B-4b)}$$

Eliminating $D(\psi)$ between these two equations and solving for K, we find

$$K = \frac{T_{b,2}^4 - T_{b,1}^4}{B_1 T_{b,2}^4 - B_2 T_{b,1}^4} \qquad \text{(B-5)}$$

It was thought that K could possibly be a function of ψ, hence, many pairs of points of different brightness were measured over the disk. The results showed that K was essentially independent of ψ.

For each landing site region, B was measured from the scan data and the bolometric albedo calculated with the value of K determined above (see Table 2, where bolometric albedo = ρ_2). Because the measurements were made with a resolution of 10 arc-s (18 km at the center of the disk) and with a location accuracy of 4–8 km, the albedo of the region in the immediate vicinity of a spacecraft could depart considerably from the quoted values. The location of the *Surveyor* spacecraft, relative to nearby features on *Lunar Orbiter* photographs, is known to 1 m.

II. Thermophysical Properties of the *Surveyor* Landing Sites

The thermophysical properties can be determined only from post-sunset, eclipse, or lunation cooling curves. The most extensive eclipse measurements are those of Refs. 10 and 11 (made during the December 19, 1964, eclipse). Data on isotherms during totality for the equatorial region have been published (Ref. 12); the measurements revealed anomalous cooling of features of a wide range of sizes, varying from kilometer-sized craters to the entire maria. It would not, therefore, be surprising if thermal heterogeneity were found to dimensions much smaller than possible to measure by the earth-based eclipse measurements; for example, any local areas strewn with sizable boulders should cool more slowly than unstrewn areas.

The area in which *Surveyor I* landed is one with small horizontal thermal gradients; thus, it contains the highly insulating properties that typify the general lunar surface. The *Surveyor III, V,* and *VI* regions also appear to be relatively bland and at the limit of resolution of the earth-based measurements.

The crater Tycho is an outstanding thermal anomaly on the lunar surface from the standpoint of the temperature difference over its environs and the size of the area affected. Three maxima in the temperature distribution exist within the crater and the anomaly extends about one crater diameter beyond the rim. The *Surveyor VII* landing site is within the anomalous area surrounding the crater.

III. Earth-Based Predictions of Lunar Surface Temperatures of the *Surveyor* Landing Sites

The spacecraft data were compared with earth-based measurements of the illuminated lunar surface made during the December 19, 1964, eclipse. The latter measurements were influenced by the directional effects of infrared emission determined by the direction from which the site regions were observed on earth.

Lunation calculations (Ref. 16) of the homogeneous model were used assuming constant thermophysical properties. These properties are characterized by the thermal parameter $\gamma = (k\rho c)^{-1/2}$, where k is thermal conductivity, ρ is density, and c is specific heat. This constant γ model, however, cannot adequately represent the earth-based measurements during both eclipse and post-sunset, since the former requires a much larger constant γ than the latter. During illumination, the model predicts temperatures essentially in agreement with Eq. (B-1) when γ is greater than 500. Recently a particulate model of the lunar soil has been proposed (Ref. 13) which agrees with both the eclipse and post-sunset cooling.

The bolometric albedos used in the following calculations are those given in Table 2 for each landing site. The temperatures were corrected for the appropriate moon/sun distance. Also, the normal to each surface element was assumed coincident with the local vertical.

A γ value of 800 (Ref. 16) is typical for the lunation of the equatorial *Surveyor* sites and was derived from earth-based post-sunset measurements of mare areas in the eastern section (Ref. 9). The larger γ values given in the following paragraphs resulted from earth-based eclipse measurements. The difference in γ is thought to be a consequence of heat exchange from only the uppermost millimeters of soil during an eclipse, whereas a different type of soil at a lower depth is involved during the lunation warming and cooling phases.

The calculated lunar surface Lambertian temperatures (Ref. 16)[7] for the homogeneous model at the *Surveyor I* landing site are shown in Fig. B-1. The specific values for solar constant and lunar reflectivity (albedo) used for each mission are given in Table 2. The time scale was fixed assuming a flat moon surface at sunset. The $\gamma = 800$ intermediate curve in Fig. B-1 is considered most representative of the site. The lunar surface Lambertian temperatures for *Surveyors III, V,* and *VI* are nearly identical to that shown in figure for *Surveyor I.*

Thermal measurements were made of the *Surveyor III* site during the April 24, 1967, eclipse. Figure 3 shows a predicted cooling curve for the site from earth-based measurements obtained during the December 19, 1964, eclipse (Ref. 10). When this curve was compared with the theoretical eclipse cooling curves for a homogeneous model (Ref. 17), it was possible to infer a value for γ of 1400. Values of γ in this range, as determined from eclipse calculations, are representative of the insulating material that characterizes much of the lunar surface. The warming curve in Fig. 3 represents calculated equilibrium surface temperatures corresponding to the insolation at each time.

[7]B. P. Jones calculated the Lambertian curves for the different *Surveyor* sites including post-sunset where the differentiation due to γ is significant.

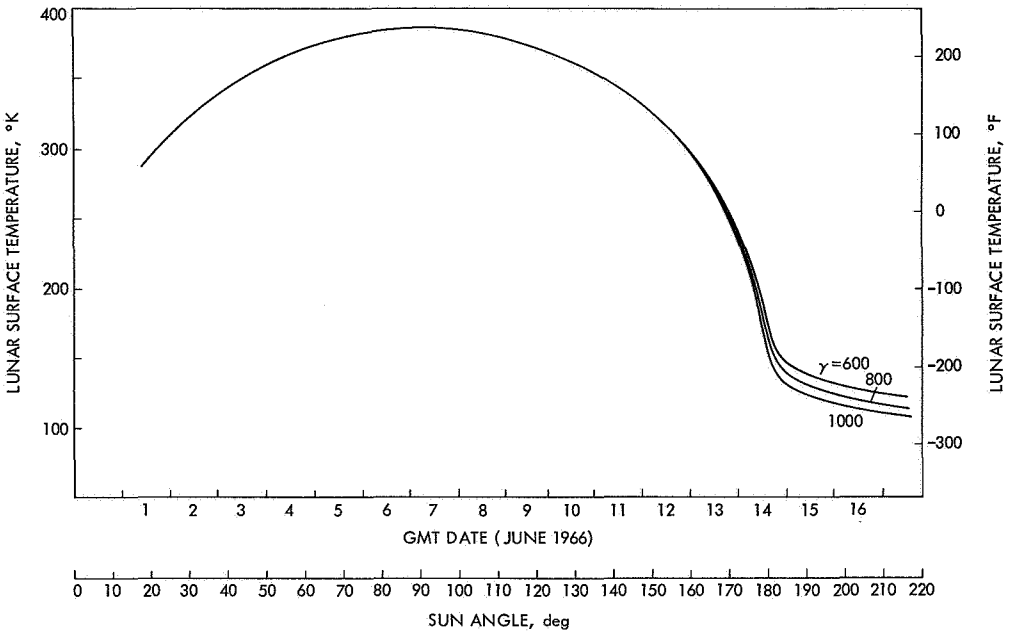

Fig. B-1. Calculated Lambertian temperature for *Surveyor I*

Figure B-2 is a predicted eclipse cooling curve for the *Surveyor V* site, from earth-based measurements. By using the theoretical eclipse cooling curves for a homogeneous model (Ref. 17), a γ of 1350 was obtained for the lunar surface material.

The calculated Lambertian temperatures and earth-based temperatures at the *Surveyor VI* landing site are shown in Fig. B-3. Each value has been plotted at that time in November 1967 when the elevation angle of the sun was the same as when the measurement was made. These earth-based measurements show the directionality of lunar infrared emission; near local noon, when the surface was observed from the same general direction as the sun (i.e., when the phase angle was small), the measured temperatures were higher than the calculated Lambertian temperatures. Earth-based eclipse observations show cooling during totality comparable to that for a homogeneous model with a γ of 1100.

The calculated Lambertian temperatures for the *Surveyor VII* landing site are shown in Fig. B-4. Also shown are the earth-based measured temperatures, which again show a directional effect distributed over a larger portion of the lunar day. During the December 19, 1964, eclipse, Ingrao, et al. (Ref. 18) made measurements of Tycho to a 9-arc-s resolution up to a few minutes before the end of totality. These eclipse observational data fit

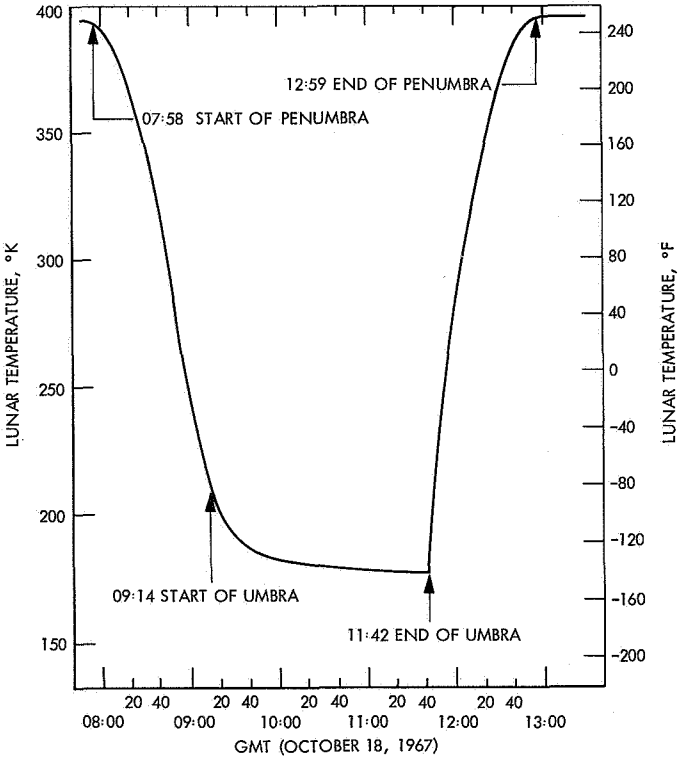

Fig. B-2. Calculated eclipse brightness temperature for *Surveyor V*

the cooling curve for a homogeneous model, with $\gamma = 450$ inside the crater and with $\gamma = 1100$ outside the crater by 30 arc-s.

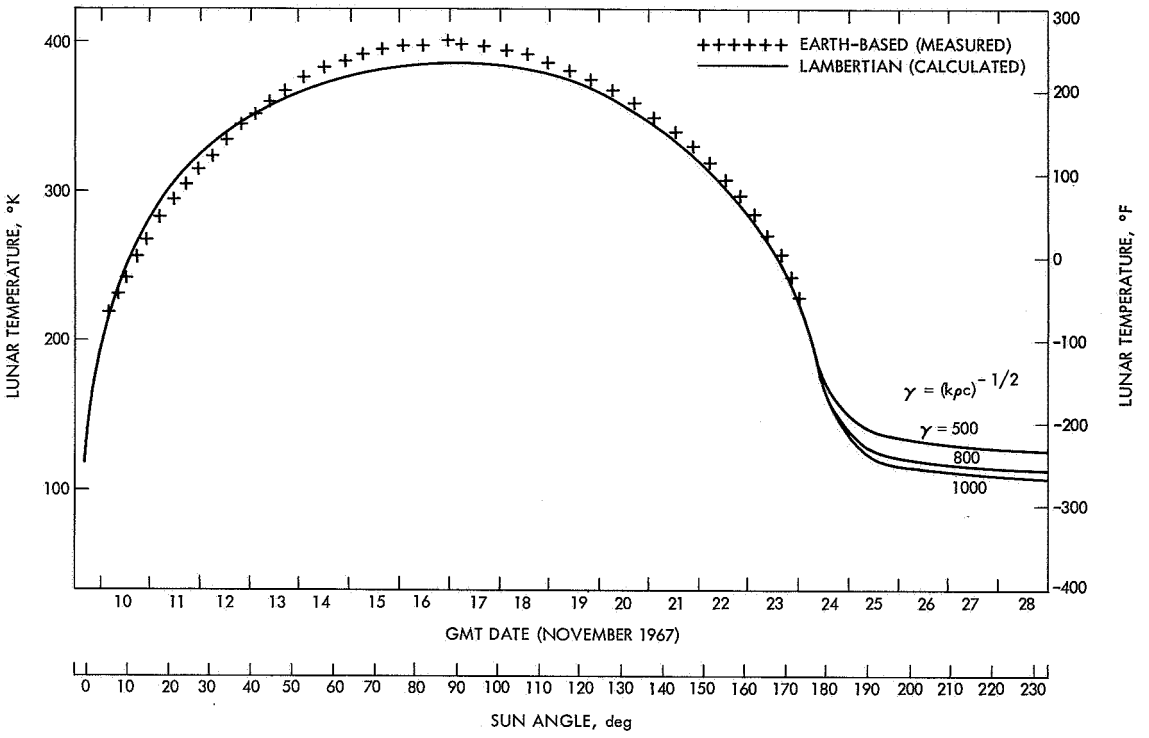

Fig. B-3. Earth-based and calculated brightness temperatures for *Surveyor VI*

Although no earth-based measurements of the *Surveyor VII* landing site region were made during the lunar night, it was possible to obtain a post-sunset cooling curve by interpolation in the following manner:

(1) Earth-based eclipse cooling curves were obtained from the data of Ref. 10 for the crater itself, the landing site region, and the environs outside the anomalous region surrounding the crater. These curves showed the landing site region had a temperature difference over the environs only 0.27 as large as that for the crater.

(2) Post-sunset cooling curves were available for the crater (Ref. 15); for the environs, a theoretical curve for the homogeneous model with $\gamma = 800$ was assumed.

(3) A post-sunset curve for the landing site region was determined by interpolating 0.27 of the way from the environs curve to the crater curve, resulting in the predicted X curve shown in Fig. B-4. This post-sunset curve corresponds to a γ of 550 for the landing site region.

IV. Directional Effects

It has been determined that, when the lunar surface is illuminated by the sun, the observed brightness temperature is not constant for different angles of observation; i.e., the surface does not behave like a Lambertian surface (Ref. 19). This effect, ascribed to surface roughness, causes the brightness temperature to be higher when the phase angle is small (i.e., when the sun/surface/observer angle is small) than when it is large. (Qualitatively, the emission is greater when viewing the lunar surface with the sun over one's shoulder.) Such directionality will have an effect on the radiation received by the compartments on the *Surveyor* spacecraft to a degree depending upon the scale of the local surface roughness.

To correct the calculations for directional effects, earth-based measurements over the entire lunar disk were used for three sun angles. For a sun elevation angle of 90 deg, the measurements of Sinton (Ref. 20) were taken and show the variation in radiance from the subsolar point as a function of the angle of observation. For two other sun angles of 30 and 60 deg, the infrared scan data for different phases made by Shorthill and Saari were used. The albedo corrections for each point were made from the full-moon photometric data. The

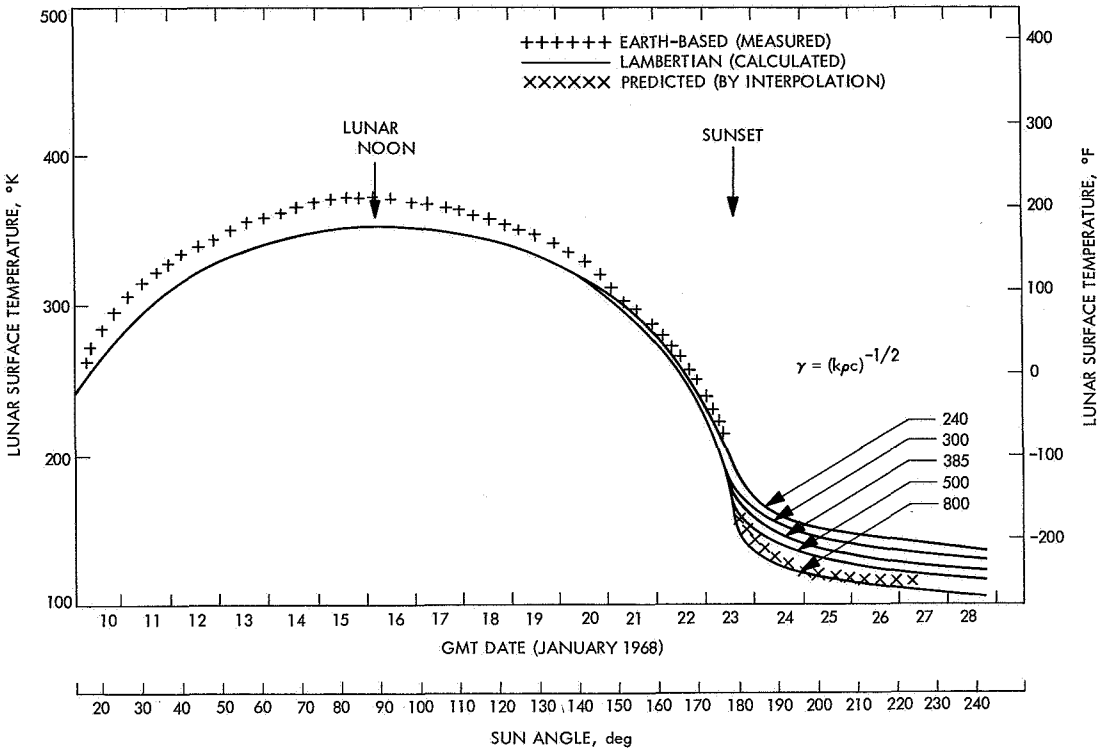

Fig. B-4. Earth-based, calculated, and predicted brightness temperatures for *Surveyor VII*

directional factor was determined from Eq. (B-2) by using a calculated Lambertian temperature at each point.

Directional factors obtained in this manner were referenced to a lunar surface element by a coordinate system with azimuth and elevation angles for the direction of observation defined as follows. Azimuth angles were measured from the normal projection of the sun direction onto the surface. Elevation angles were measured from the surface in the plane of observation. Directional factors obtained over the globe were referenced to this azimuth/elevation angle system. A least-squares spherical harmonic fit, symmetrical with respect to plus and minus azimuth angles, was then computed for the data. Directional factors were, of necessity, obtained from global measurements made on a variety of features. It is possible, therefore, for a small area such as a *Surveyor* landing site to have different directional effects than the average surface if the local roughness or surface configuration differed significantly from the average.

Appendix C

Coordinate Transformations

Certain coordinate transformations were required to determine the view factors and sun angles for each of the compartment faces, the solar panel, and the planar-array antenna. Each view factor required a vectorial description of the normal to the face (or panel) and to the local lunar surface. In the simplest case, the view factor was obtained (see Fig. C-1) by the equation

$$F_{ij} = \frac{1}{2}(1 + \cos\theta) \qquad \text{(C-1)}$$

To find the angle θ, the local lunar surface slope and the tilt of the face (or panel) from the local horizon were required. The cosine of the sun angle on a face was the scalar (dot) product of the normal vector and the sun vector, varying with the lunar day.

It was easier to express the vectors for the face normals first in terms of spacecraft coordinates, Fig. 4. The normals to the compartment faces (r_i) are:

(1) Compartment A faces:

$$\begin{aligned}
&\text{Outboard} && \mathbf{r}_1 = 0.813\,\mathbf{i}_{SC} + 0.470\,\mathbf{j}_{SC} - 0.342\,\mathbf{k}_{SC}\\
&\text{Sides} && \mathbf{r}_4 = 0.500\,\mathbf{i}_{SC} - 0.866\,\mathbf{j}_{SC} = -\mathbf{r}_5\\
&\text{Inboard} && \mathbf{r}_6 = -\mathbf{r}_1\\
&\text{Bottom} && \mathbf{r}_7 = 0.295\,\mathbf{i}_{SC} + 0.171\,\mathbf{j}_{SC} + 0.940\,\mathbf{k}_{SC}\\
&\text{Top} && \mathbf{r}_8 = -\mathbf{k}_{SC}
\end{aligned} \qquad \text{(C-2)}$$

(2) Compartment B faces:

$$\begin{aligned}
&\text{Outboard} && \mathbf{r}_1 = -0.813\,\mathbf{i}_{SC} + 0.470\,\mathbf{j}_{SC} - 0.342\,\mathbf{k}_{SC}\\
&\text{Sides} && \mathbf{r}_4 = 0.500\,\mathbf{i}_{SC} + 0.866\,\mathbf{j}_{SC} = -\mathbf{r}_5\\
&\text{Inboard} && \mathbf{r}_6 = -\mathbf{r}_1\\
&\text{Bottom} && \mathbf{r}_7 = -0.295\,\mathbf{i}_{SC} + 0.171\,\mathbf{j}_{SC} + 0.940\,\mathbf{k}_{SC}\\
&\text{Top} && \mathbf{r}_8 = -\mathbf{k}_{SC}
\end{aligned} \qquad \text{(C-3)}$$

where the $\mathbf{i}_{SC}$, $\mathbf{j}_{SC}$, and $\mathbf{k}_{SC}$ are unit vectors along the spacecraft axes in Fig. 4.

The normal to the sunlit side of the solar panel was expressed in terms of four angles, which were the solar (θ_S), polar (θ_P), elevation (θ_E), and roll (θ_R) angles shown in Fig. C-2. The solar panel normal in spacecraft coordinates is

$$\begin{aligned}
\mathbf{r}_1 = {} & [\cos(\theta_S + \theta_P)\cos\theta_R - \sin(\theta_S + \theta_P)\sin\theta_E \sin\theta_R]\,\mathbf{i}_{SC}\\
& + [\cos(\theta_S + \theta_P)\sin\theta_R + \sin(\theta_S + \theta_P)\sin\theta_E \cos\theta_R]\,\mathbf{j}_{SC}\\
& + [\sin(\theta_S + \theta_P)\cos\theta_E]\,\mathbf{k}_{SC}
\end{aligned} \qquad \text{(C-4)}$$

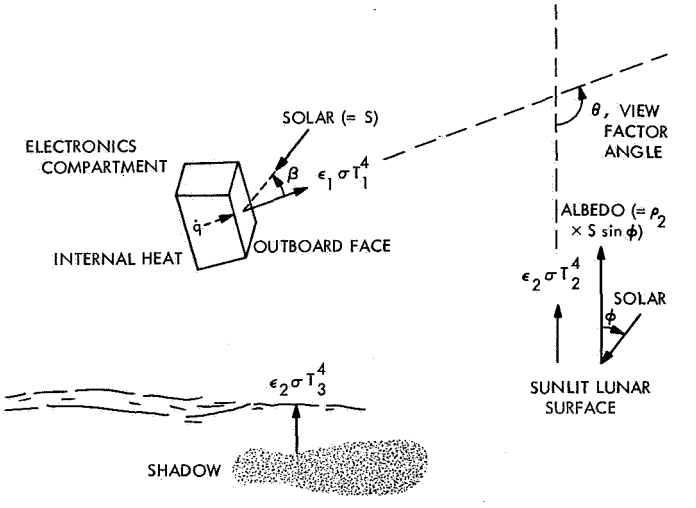

Fig. C-1. Heat exchange for a compartment face

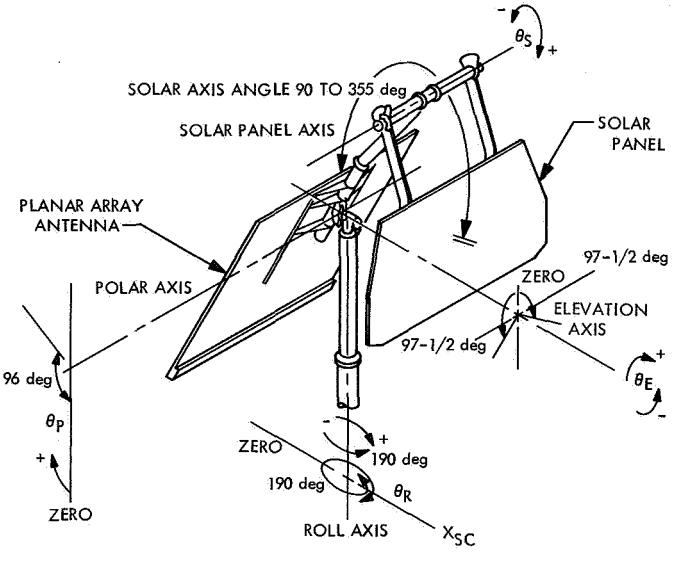

Fig. C-2. Solar panel coordinate system

The coordinate transformation required to change the previous vectors into local coordinates (i, j, k) corresponding to east, north, and local zenith, respectively, is

$$a = (a_{SC} \sin\alpha + b_{SC} \cos\alpha) \cos\gamma + [(-a_{SC} \cos\alpha + b_{SC} \sin\alpha) \cos\delta + c_{SC} \sin\delta] \sin\gamma \quad \text{(C-5a)}$$

$$b = (a_{SC} \sin\alpha + b_{SC} \cos\alpha) \sin\gamma - [(-a_{SC} \cos\alpha + b_{SC} \sin\alpha) \cos\delta + c_{SC} \sin\delta] \cos\gamma \quad \text{(C-5b)}$$

$$c = (-a_{SC} \cos\alpha + b_{SC} \sin\alpha) \sin\delta - c_{SC} \cos\delta \quad \text{(C-5c)}$$

where (a_{SC}, b_{SC}, c_{SC}) and (a, b, c) are coefficients of the vectors in Eqs. (C-2) and (C-3) expressed alternatively as

$$\mathbf{r}_i = a_{SC}\mathbf{i}_{SC} + b_{SC}\mathbf{j}_{SC} + c_{SC}\mathbf{k}_{SC} = a\mathbf{i} + b\mathbf{j} + c\mathbf{k} \quad \text{(C-6)}$$

with

$$i = 1, \cdots, 8$$

and the spacecraft orientation angles α, β, and δ are shown in Figs. A-2, A-3, A-5, A-7, and A-8, and

$$\gamma = \alpha + \beta - 90 \quad \text{(C-7)}$$

References

1. Lucas, J. W., et al., "Lunar Surface Thermal Characteristics," *Surveyor I Mission Report: Part II. Scientific Data and Results*, Technical Report 32-1023. Jet Propulsion Laboratory, Pasadena, Calif., Sept. 10, 1966.
2. Lucas, J. W., et al., "Lunar Temperatures and Thermal Characteristics," *Surveyor III Mission Report: Part II. Scientific Results*, Technical Report 32-1177. Jet Propulsion Laboratory, Pasadena, Calif., June 1, 1967.
3. Lucas, J. W., et al., "Lunar Surface Temperatures and Thermal Characteristics," *Surveyor V Mission Report: Part II. Science Results*, Technical Report 32-1246. Jet Propulsion Laboratory, Pasadena, Calif., Nov. 1, 1967.
4. Vitkus, G., et al., "Lunar Surface Temperatures and Thermal Characteristics," *Surveyor VI Mission Report: Part II. Science Results*, Technical Report 32-1262. Jet Propulsion Laboratory, Pasadena, Calif., Jan. 10, 1968.
5. Vitkus, G., et al., "Lunar Surface Temperatures and Thermal Characteristics," *Surveyor VII Mission Report: Part II. Science Results*, Technical Report 32-1264. Jet Propulsion Laboratory, Pasadena, Calif., Mar. 15, 1968.
6. Lucas, J. W., et al., "Lunar Surface Temperatures and Thermal Characteristics," *Surveyor Project Final Report: Part II. Science Results*, Technical Report 32-1265. Jet Propulsion Laboratory, Pasadena, Calif., June 1, 1968.
7. Vitkus, G., Lucas, J. W., and Saari, J. M., "Lunar Surface Thermal Characteristics During Eclipse From *Surveyors III, V*, and After Sunset From *Surveyor V*," in *Thermal Design Principles of Spacecraft and Entry Bodies, Vol. 21: AIAA Progr. Astronaut. and Aeronaut. Series*. Academic Press, New York, 1969.

References (contd)

8. Stimpson, L. D., and Lucas, J. W., "Revised Lunar Surface Thermal Characteristics Obtained From the *Surveyor V* Spacecraft," to be published in *J. Spacecraft Rockets.* (Also, presented at the AIAA Fourth Thermophysics Conference, San Francisco, Calif., June 16–18, 1969.)

9. Wildey, R. L., Murray, B. C., and Westphal, J. A., "Reconnaissance of Infrared Emission from the Lunar Nighttime Surface," *J. Geophys. Res.*, Vol. 72, No. 14, pp. 3743–3749, 1967.

10. Saari, J. M., and Shorthill, R. W., "Thermal Anomalies of the Totally Eclipsed Moon of December 19, 1964," *Nature*, Vol. 205, pp. 964–965, 1965.

11. Saari, J. M., and Shorthill, R. W., "Physics of the Moon," *Sci. Technol. Series*, Vol. 13, pp. 57–99, 1967.

12. Saari, J. M., and Shorthill, R. W., *Isotherms in the Equatorial Region of the Totally Eclipsed Moon*, Document D1-82-0530. Boeing Scientific Research Laboratories, Seattle, Wash., April 1966.

13. Winter, D. F., and Saari, J. M., *A New Thermophysical Model of the Lunar Soil*, Document DI-82-0725. Boeing Scientific Research Laboratories, Seattle, Wash., 1968. (Also, "A Particulate Thermophysical Model of the Lunar Soil," *Astrophys. J.*, Vol. 156, No. 3, pp. 1135–1151, June 1969.)

14. Jones, B. P., "Density-Depth Model for the Lunar Outermost Layer," *J. Geophys. Res.*, Vol. 73, No. 24, pp. 7631–7635, 1968.

15. Saari, J. M., and Shorthill, R. W., "Isothermal and Isophotic Atlas of the Moon," NASA Report CR-855. National Aeronautics and Space Administration, Washington, D.C., Sept. 1967.

16. Jones, B. P., "Diurnal Lunar Temperatures," Paper 67-289 presented at AIAA Thermophysics Specialist Conference, New Orleans, La., April 17–19, 1967.

17. Jaeger, J. L., "Surface Temperature of the Moon," *Austral. J. Phys.*, Vol. 6, No. 10, 1953.

18. Ingrao, H. C., Young, A. T., and Linsky, J. L., "A Critical Analysis of Lunar Temperature Measurements in the Infrared," in *The Nature of the Lunar Surface*, proceedings of the 1965 IAU-NASA Symposium. Johns Hopkins Press, Baltimore, Md., pp. 185–211, 1966.

19. Six, F., Montgomery, C., Saari, J. M., and Shorthill, R. W., "Directional Characteristics of the Lunar Thermal Emission," paper presented at AIAA Thermophysics Specialist Conference, New Orleans, La., April 17–19, 1967.

20. Sinton, W. M., "Temperatures of the Lunar Surface," *Physics and Astronomy of the Moon*, (S. Kopal, Ed.), Chapter 11. Academic Press, New York, 1962.

Lunar Soil Bulk Density as Determined From Surveyor Data and Laboratory Tests

R. Choate
Jet Propulsion Laboratory
Pasadena, California

I. Introduction

In study of *Surveyor* data during mission operations, it became apparent that many of the physical properties of the lunar soil were remarkably similar at the five *Surveyor* landing sites (Refs. 1–6). One such physical property was that of bearing strength. On earth, the bearing strength of a soil is normally sensitive to changes in other interrelated physical properties, especially, relative packing density, cohesion, and water content.

A series of laboratory tests was conducted on simulated soils to more accurately evaluate several of these physical properties; namely soil bulk density or relative packing density, and the coefficient of friction. Using soils similar to lunar soil composition, particle size distribution, and cohesion as determined from the *Surveyor* mission, the bulk density and coefficient of friction were evaluated by reproducing soils with the same force vs penetration characteristics (bearing strength) as demonstrated at the *Surveyor* landing sites. The determination of soil bulk density is presented in this paper; the soil coefficient of friction is treated separately in the next paper[1] of this report.

[1]Choate, R., "Lunar Soil Coefficient of Friction Determined From *Surveyor* Data and Laboratory Tests."

II. Soil Selection and Preparation

Two soil materials, crushed basalt and powdered aluminum, were chosen for testing. The crushed basalt was selected as the primary test material because, based on the chemical analyses performed by the alpha scattering instruments on *Surveyors V, VI,* and *VII,* it was considered analogous to lunar soil. The powdered aluminum was chosen as a secondary test material because it contained many of the physical properties observed for lunar soil and because it could be readily acquired in a large number of size distributions and in any amounts desired.

The basalt selected for use was crushed into three size ranges. The source rock was hand selected, dense, nonvesicular olivine basalt from the Little Lake lava flow, about ⅓ mi south of Little Lake, Inyo County, California. The soil was prepared by breaking basalt blocks with a hand sledge, then feeding and refeeding the resulting fragments through a small jaw crusher. Particle size distribution of the three basalt soils are shown in Fig. 1a. The particle size ranges from less than 1 μ to 200, 400, and 1000 μ for the three soils. Mean particle size is 12, 55, and 170 μ, respectively. The 55- and 170-μ basalt soils were prepared solely by crushing; the

12-μ basalt soil, in addition to crushing, was dry ground in a laboratory model disk grinder. Particle size for all three soils follows a natural distribution formed by the breaking processes involved. That is, the only screening involved in arriving at the approximate mean particle size desired was to remove all coarse material larger than some selected maximum particle size. Grain density of the basalt is 2.88 g/cm^3.

The four aluminum powder mixtures selected for use were Alcan MD-205B, MD-294, MD-44, and a mixture of equal amounts by mass of the above three powders. As shown by the particle size distribution curves in Fig. 1b, the particle size ranges for each of the three standard Alcan powders were very narrow. The mean particle sizes were 6.4, 26, and 82 μ for the three standard powders, respectively, and 22 μ for the mixture. Comparison of particle size distributions for the aluminum and basalt powders is given in Table 1.

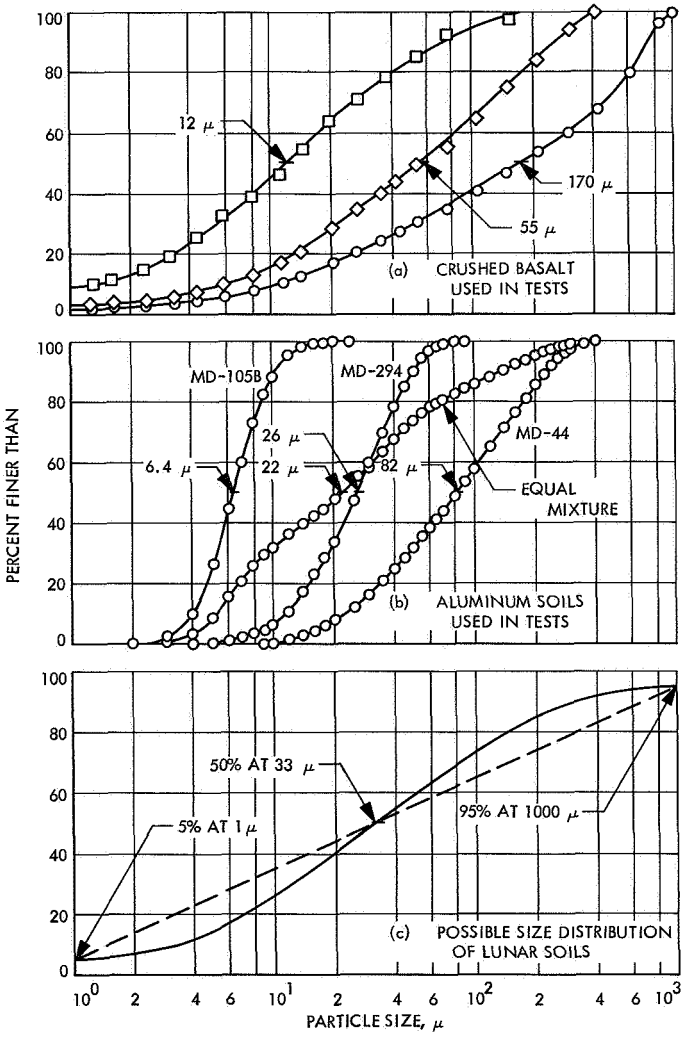

Fig. 1. Soil particle size distributions

A. Soil Particle Size Selection

Particle size distributions of the seven soils were chosen to bracket the size distribution thought to be most probable for lunar soil encountered at the landing sites. The *Surveyor* pictures of spacecraft footpad imprints show that the soil at all five sites was predominantly finer than the 1-mm resolution of the television cameras. Counts of rock and soil fragments lying on the undisturbed surface for all *Surveyor* landing sites made by E. Morris of the U. S. Geological Survey (Ref. 7) also indicate that 95% of the soil is finer than 1 mm.

The firing of the *Surveyor V* vernier engines onto the lunar surface resulted in gas erosion of the soil. Following the completion of the *Surveyor* missions, tests have been performed with the firing of the *Surveyor* vernier engines over soil beds of various particle size distributions in a large vacuum chamber. These tests indicated that soils coarser than about 60 μ did not reproduce craters similar to the craters formed by the firing of vernier engines on the lunar surface by *Surveyors V* and *VI*. It was possible to reproduce such craters with soils up to 60 μ in size (E. Christensen, JPL, oral communication). Laboratory simulations of the footpad imprint made by *Surveyor III* show that imprints using the same 12-μ basalt shown in Fig. 1a have too high a reflectivity and that this test soil is finer than the lunar soil.

To date, *Surveyor* data indicate that the lunar soil mean particle size (by mass) probably lies between approximately 20 and 60 μ. A closer estimate possibly

Table 1. Particle size distribution of soils used in force vs penetration measurements

Soil material	Mean particle size (by mass), μ	Particle size range, μ
Crushed basalt	12	<1–200
Crushed basalt	55	<1–400
Crushed basalt	170	<1–1000
Powdered aluminum, MD-205B	6	2–20
Powdered aluminum, MD-294	26	4–80
Powdered aluminum, MD-44	82	8–400
Powdered aluminum, equal mixture	22	2–400

can be made of the mean particle size by estimating two extended points on the hypothesized size distribution curve and then drawing any normal distribution curve through these two points. The upper point is provided by the 95% estimate finer than 1 mm determined by fragment counts. A lower point of 5% finer than 1 μ is selected as being reasonable, because it is smaller than the 9% value for the 12-μ basalt and is greater than the 3 and 1% values of the 55- and 170-μ basalts (Fig. 1a). A straight line drawn between these two points falls at 33 μ at the 50% point. A reasonable normal distribution curve that fits known *Surveyor* data at the coarser end and is symmetrical with the curves of the three crushed basalts at the finer end is shown in Fig. 1c. It is stressed that the size distributions of the three basalt soils used in these tests result from natural breakage caused by crushing or grinding processes; i.e., they do not represent a designed or arbitrarily selected mix.

B. Equipment Description

Soil bulk density tests were performed in association with coefficient of friction tests[2] of simulated lunar soils with different bulk densities, compositions, size distributions, and values of cohesion. To correlate test results more accurately, much of the same equipment and basalt soils in the same physical states were used in both series of tests.

Soil container size (45.7-cm diameter by 35.6-cm deep[3]) was controlled by the need for a sample large enough to eliminate or minimize bottom and sidewall effects and yet small enough for two men to be able to handle and run several tests per day. Container volume was 0.0579 m^3.

The penetrometers used for the tests were 15.2- and 7.6-cm diameter plates. These dimensions are ½ and ¼ the scale of *Surveyor* footpad diameters, respectively.

Continuous curves of normal force vs penetration were recorded on an X–Y recorder. Normal force was measured by the strain-gage bridge and penetration by the potentiometer shown in Fig. 2. Movement of the entire lead-screw support system was restricted to the vertical direction by four thin-wall flexures.

[2]Described in following paper (see footnote 1).

[3]Values are given in cm-g-s units; to convert to ft-lb-s units, the following factors apply: 1 cm = 0.394 in., 1 N (newton) = 10^5 dyn = 0.225 lb, and 1 μ (micron) = 1.0×10^{-4} cm = 3.94×10^{-6} in.

C. Test Procedure

It was desired to test the soils at loose, dense, and intermediate packing densities such that they would bracket the probable packing density of the lunar soil. Loose packing was accomplished by carefully pouring the selected soil through a coarse screen as it was slowly raised from the bottom of the soil container. The soil was then leveled even with the container top and weighed.

Dense packed soil was prepared by similar screening of the same amount of soil into the container, which was then vibrated on a rapid air vibrator until soil settlement ceased. The soil surface was continuously leveled with a scraper as settlement progressed.

In addition to determining the average density of the entire soil sample, density was also measured at the surface, both before and after each test. Density measurements were made by taking a sample of soil with a thin-wall plexiglass tube (1.60-cm inside diameter; soil sample length = 3.81 cm). Also, cohesion of the surface soil was measured before and after each test with a shear vane and torque meter.

III. Test Results and Discussion

A total of 58 force vs penetration tests were performed on the basalt and aluminum soils. Penetration tests were performed on each of the seven soil mixtures with the 7.6- and 15.2-cm diameter plates at approximately the four relative densities[4] of 5, 30, 60, and 100%. Relative densities of individual tests varied from the above stated goals because it was impractical to reproduce identical conditions in each test.

Exact values of the physical properties of the basalt and aluminum soils for each test are given in Tables 2 and 3, respectively. These values include relative density, absolute density, average porosity, surface porosity before and after each test, and surface cohesion before and after each test. Graphs for each test of soil relative density and surface cohesion, as measured with a 2.5-cm long shear vane, are shown in Figs. 3 and 4.

In Fig. 5, *Surveyor* lunar surface force vs penetration data are plotted for various sized penetrators, including

[4]Relative density is a measure of the degree of compaction of a soil aggregate and is a comparison of the porosity of a given soil with that of the same soil in its most loose and dense states.

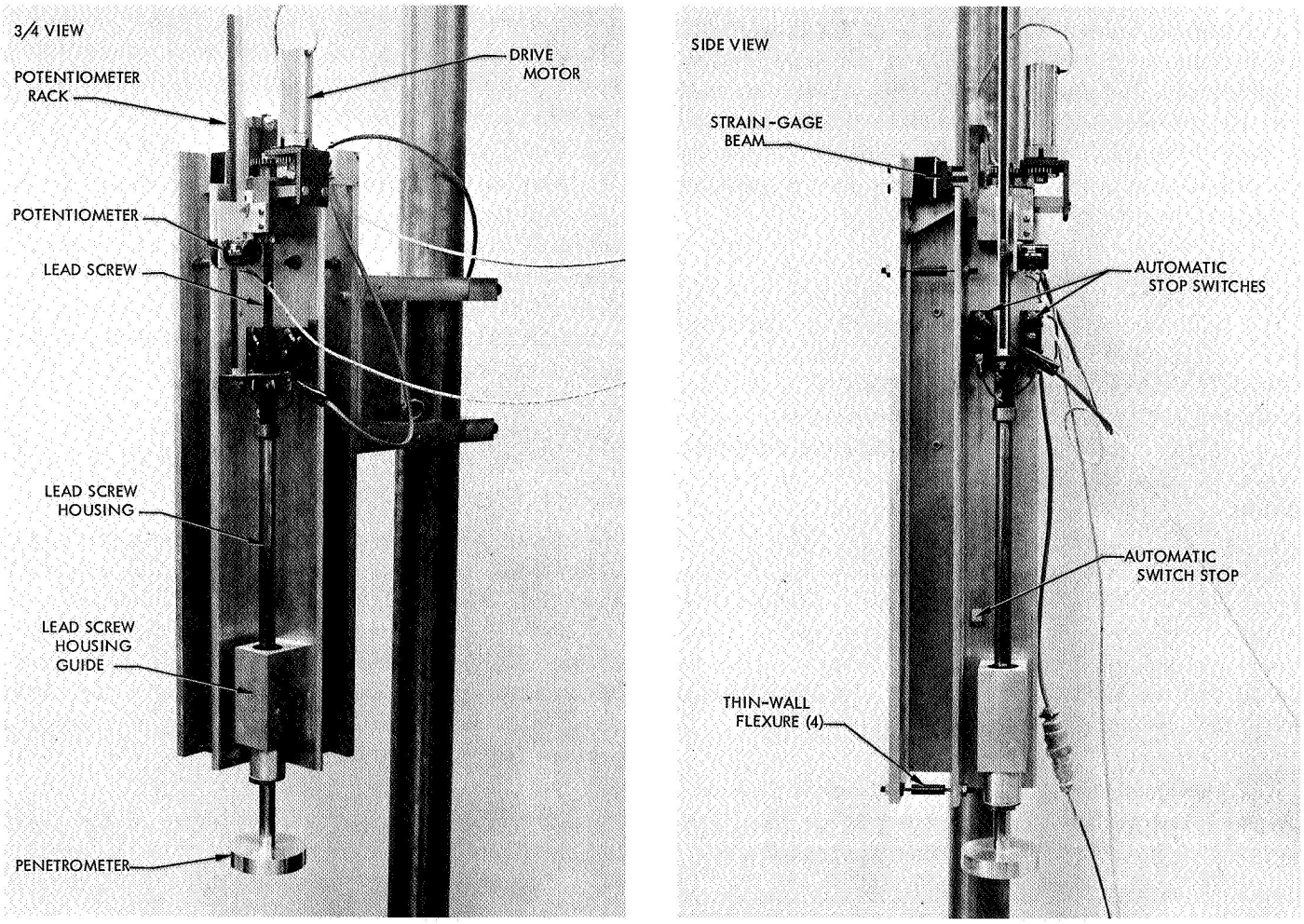

Fig. 2. Specially designed penetrometer used for soil tests

Table 2. Relative physical properties of basalt soils used in tests

Test	Material	Mean particle size, μ	Plate diam, cm	Relative density, %	Cohesion, N/cm^2		Density, g/cm^3			Porosity, %		
					Surface	Post-test	Average	Surface	Post-test	Average	Surface	Post-test
1	Basalt	12	7.6	88	0.36[a]	0.43[d]	1.51	—	1.70[c]	47.1	—	40.8[c]
2	Basalt	12	15.2	88	0.36[a]	0.45[c]	1.51	—	1.69[c]	47.1	—	41.0[c]
3	Basalt	12	7.6	56	0.23[a]	0.45[d]	1.36	—	1.65[c]	52.5	—	42.8[c]
4	Basalt	12	15.2	56	0.23[a]	0.36[d]	1.36	—	1.64[c]	52.5	—	42.9[c]
5	Basalt	12	7.6	48	0.10[a]	0.38[a]	1.32	1.33	1.67[d]	53.8	53.7[a]	41.6[d]
6	Basalt	12	15.2	48	0.10[a]	0.38[a]	1.32	1.38	1.70	53.8	52.0	40.8
7	Basalt	12	7.6	27	0.045	0.32[d]	1.22	1.18	1.63	57.3	59.1[a]	41.8[d]
8	Basalt	12	15.2	27	0.07[a]	0.27[d]	1.22	1.22	1.67[d]	57.4	57.6[a]	41.8[d]
9	Basalt	12	7.6	6	0.018[a]	0.22[d]	1.12	1.00	1.58	60.9	65.2[b]	45.1
10	Basalt	12	15.2	4	0.020	0.25	1.11	1.03	1.60[c]	61.2	64.3[c]	44.1[c]
11	Basalt	55	7.6	100	0.53[c]	0.53[c]	1.90	1.90	1.90	33.5	33.8	33.8
12	Basalt	55	15.2	100	0.53[c]	0.53[c]	1.90	1.90	1.90	33.5	33.8	33.8
13	Basalt	55	7.6	60	0.18[c]	0.25[b]	1.70	1.72[b]	1.77[c]	40.4	40.1[b]	38.3[c]
14	Basalt	55	15.2	60	0.18[c]	0.22[b]	1.70	1.72[b]	1.76[b]	40.4	40.1[b]	38.8[b]
15	Basalt	55	7.6	28	0.13[a]	0.24[d]	1.54	—	1.80[c]	46.2	—	37.3[c]
16	Basalt	55	15.2	28	0.13	0.20[b]	1.54	—	1.77[c]	46.2	—	38.3[c]
17	Basalt	55	7.6	14	0.058[a]	0.20[b]	1.47	1.49[a]	1.73[c]	48.5	48.2[a]	39.4[c]
18	Basalt	55	15.2	14	0.056[b]	0.18[b]	1.47	1.44[b]	1.75[a]	48.4	50.0[b]	39.3[a]
19	Basalt	55	7.6	4	0.034[c]	0.17[a]	1.42	1.33[c]	1.71[c]	50.5	53.8[c]	40.5[c]
20	Basalt	55	15.2	4	0.034[c]	0.16[b]	1.42	1.33	1.78[c]	50.2	53.7[c]	38.2[c]
21	Basalt	170	7.6	88	0.7+[d]	0.7+[d]	2.03	2.03	2.03	29.0	29.3	29.3
22	Basalt	170	15.2	88	0.7+[d]	0.7+[d]	2.03	2.03	2.03	29.0	29.3	29.3
23	Basalt	170	7.6	56	0.23[b]	0.29[b]	1.87	1.71[b]	1.80[b]	34.7	59.9[b]	37.3[b]
24	Basalt	170	15.2	56	0.23[b]	0.28[b]	1.87	1.71[b]	1.73[b]	34.7	59.9[b]	39.7[b]
25	Basalt	170	7.6	30	0.09[b]	0.20[c]	1.74	1.62[c]	1.86[c]	39.5	43.8[c]	35.4[c]
26	Basalt	170	15.2	30	0.09[b]	0.16[b]	1.74	1.62[c]	2.07[b]	39.5	43.8[c]	28.1[b]
27	Basalt	170	7.6	12	0.06[d]	0.23[b]	1.65	1.38[c]	1.68[b]	42.5	52.1[c]	41.6[b]
28	Basalt	170	15.2	10	0.05[c]	0.18[b]	1.64	1.31[c]	1.78[b]	42.7	54.6[c]	38.2[b]

[a]Degree of soil disturbance during sampling and shear vane tests: no disturbance.

[b]Degree of soil disturbance during sampling and shear vane tests: slight disturbance.

[c]Degree of soil disturbance during sampling and shear vane tests: moderate disturbance.

[d]Degree of soil disturbance during sampling and shear vane tests: substantial disturbance.

Table 3. Relative physical properties of aluminum soils used in tests

Test	Material	Mean particle size, μ	Plate diameter, cm	Relative density, %	Cohesion, N/cm^2		Density, g/cm^3			Porosity, %		
					Surface	Post-test	Average	Surface	Post-test	Average	Surface	Post-test
29	Aluminum	6.4	7.6	100	0.36[a]	0.45[d]	1.20	1.19[c]	1.28[d]	55.7	55.2[c]	52.7[d]
30	Aluminum	6.4	15.2	100	0.36[a]	0.38[c]	1.20	1.19[c]	1.31[d]	55.7	55.2[c]	51.7[d]
31	Aluminum	6.4	7.6	58	0.12[a]	0.49[d]	1.02	1.02[a]	—	62.4	62.3[a]	—
32	Aluminum	6.4	15.2	58	0.12[a]	0.33[c]	1.02	1.02[a]	1.18[d]	62.4	62.3[a]	56.5[d]
33	Aluminum	6.4	7.6	26	0.029[a]	0.27[d]	0.88	0.81[b]	1.29[c]	67.3	70.4[b]	52.4
34	Aluminum	6.4	15.2	26	0.029[a]	0.22[c]	0.88	0.81[b]	1.24[c]	67.3	70.4[b]	53.0[c]
35	Aluminum	6.4	7.6	12	0.027[a]	0.19[b]	0.82	0.82[a]	1.23[b]	69.7	69.6[a]	54.4[b]
36	Aluminum	6.4	15.2	5	0.018[a]	0.29[d]	0.79	0.72[b]	1.21[b]	69.7	73.6[b]	55.2[c]
37	Aluminum	26	7.6	100	0.27[c]	0.20[d]	1.57	1.51[b]	1.52[d]	41.9	44.0[b]	43.8[d]
38	Aluminum	26	15.2	100	0.27[c]	0.39[d]	1.57	1.51[b]	1.55[d]	41.9	44.0[b]	42.5[d]
39	Aluminum	26	7.6	59	0.17[a]	0.20[b]	1.40	—	1.49[c]	48.1	—	44.0[c]
40	Aluminum	26	15.2	59	0.17[a]	0.19[b]	1.40	—	1.49[c]	48.1	—	44.0[c]
41	Aluminum	26	7.6	24	0.067[a]	0.20[b]	1.26	1.24[a]	1.40[c]	53.3	54.2[a]	48.1[c]
42	Aluminum	26	15.2	24	0.067[a]	0.13[c]	1.26	1.24[a]	1.40[c]	53.3	54.2[a]	48.4[c]
43	Aluminum	26	7.6	2	0.020[d]	0.13[a]	1.17	1.06[d]	1.32[b]	56.7	60.8[d]	51.2[b]
44	Aluminum	26	15.2	5	0.024[b]	0.11[c]	1.18	1.14[d]	1.35[b]	56.5	57.8[d]	50.1[b]
45	Aluminum	82	7.6	100	—	—	1.66	1.66	1.66	38.6	38.6	38.6
46	Aluminum	82	15.2	100	—	—	1.66	1.66	1.66	38.6	38.6	38.6
47	Aluminum	82	7.6	31	0.067[b]	0.13[b]	1.41	1.35[d]	1.41[b]	47.7	50.0[d]	48.0[b]
48	Aluminum	82	15.2	31	0.067[b]	0.13[b]	1.41	1.35[d]	1.30[c]	47.7	50.0[d]	52.1[c]
49	Aluminum	82	7.6	3	0.040[b]	0.12[a]	1.31	1.34[c]	1.54[b]	51.4	50.3[c]	43.2[b]
50	Aluminum	82	15.2	3	0.045[b]	0.08[c]	1.31	1.32[b]	1.47	51.4	51.3[b]	45.7
51	Aluminum	22 (mixture)	7.6	100	0.39[b]	0.45[d]	1.54	1.55[a]	1.63[c]	43.0	—	—
52	Aluminum	22 (mixture)	15.2	100	0.39[b]	0.30[d]	1.54	1.55[a]	1.52[d]	43.0	—	—
53	Aluminum	22 (mixture)	7.6	60	0.09[c]	0.39[d]	1.37	1.25[b]	1.64[d]	49.5	—	—
54	Aluminum	22 (mixture)	15.2	60	11	0.24[d]	1.37	1.25[b]	1.50[d]	49.5	—	—
55	Aluminum	22 (mixture)	7.6	24	0.036[b]	0.35[d]	1.22	—	1.71	55.0	—	36.8
56	Aluminum	22 (mixture)	15.2	24	0.042[a]	0.27[d]	1.22	1.05[b]	1.58[c]	55.0	—	—
57	Aluminum	22 (mixture)	7.6	5	0.02	—	1.14	—	1.39	58.1	—	—
58	Aluminum	22 (mixture)	15.2	7	0.022	0.27	1.15	1.02[c]	1.65[c]	57.4	62.1[c]	38.8[c]

[a]Degree of soil disturbance during sampling and shear vane tests: no disturbance.

[b]Degree of soil disturbance during sampling and shear vane tests: slight disturbance.

[c]Degree of soil disturbance during sampling and shear vane tests: moderate disturbance.

[d]Degree of soil disturbance during sampling and shear vane tests: substantial disturbance.

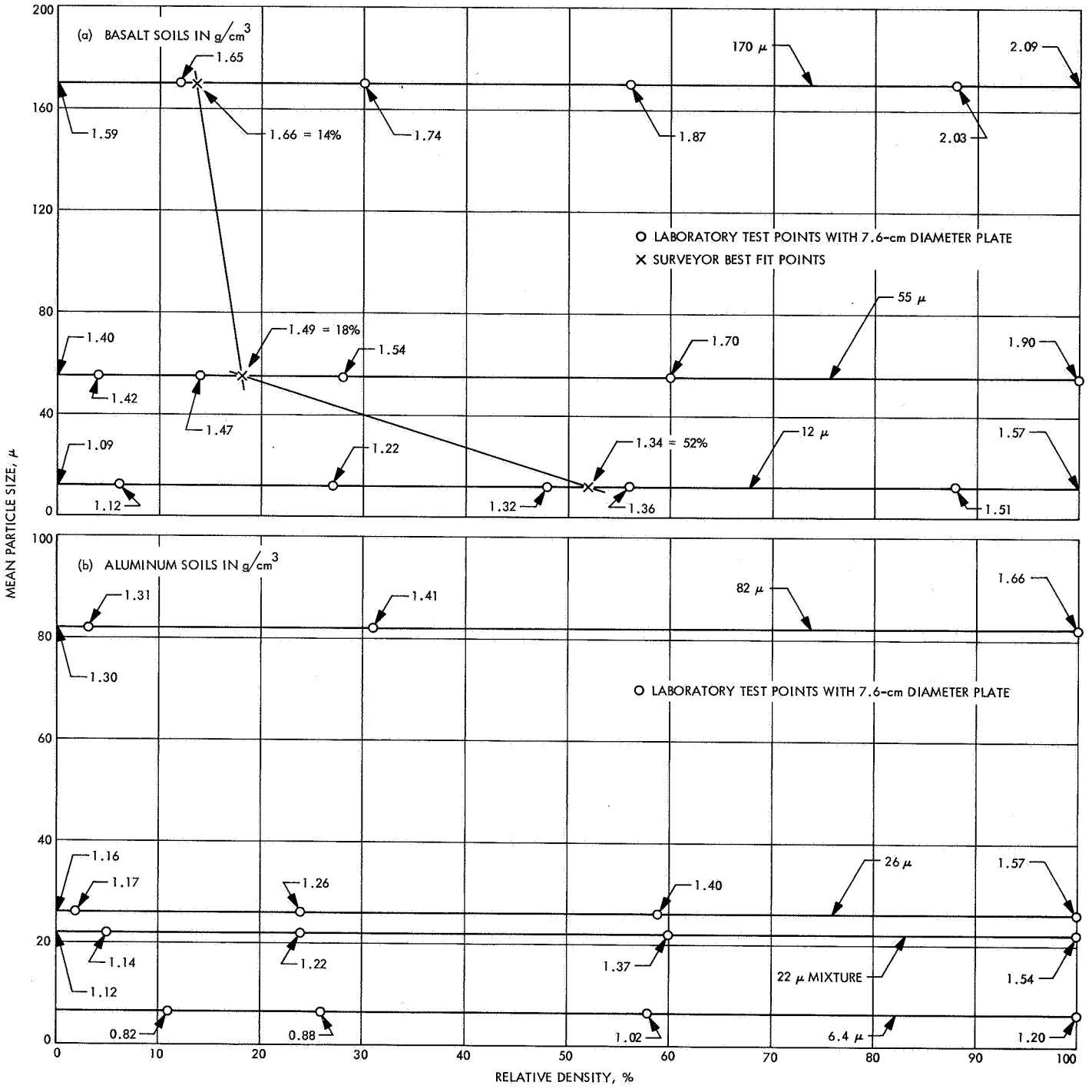

Fig. 3. Relative densities of soils used in tests

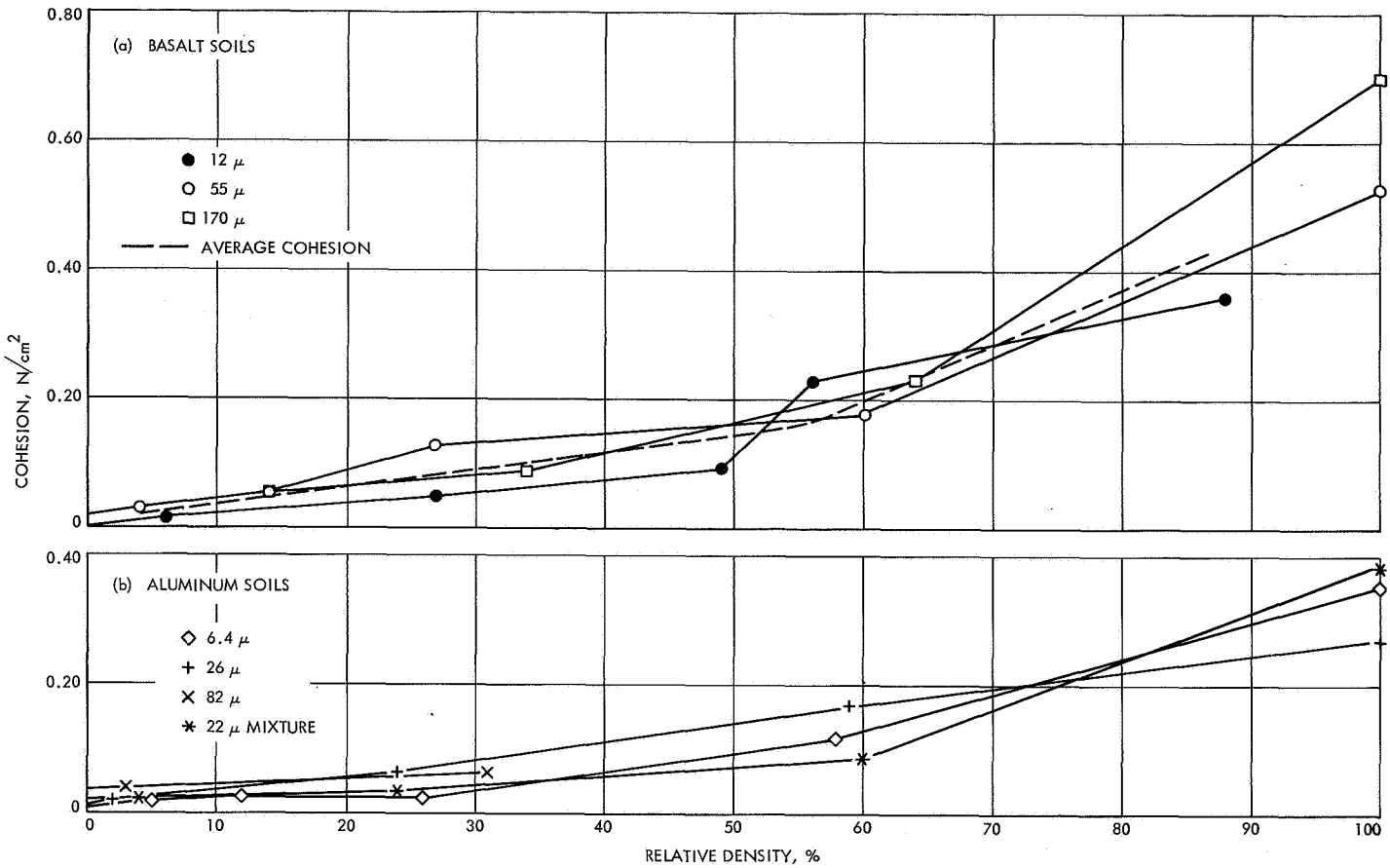

Fig. 4. Cohesion vs relative density of test soils

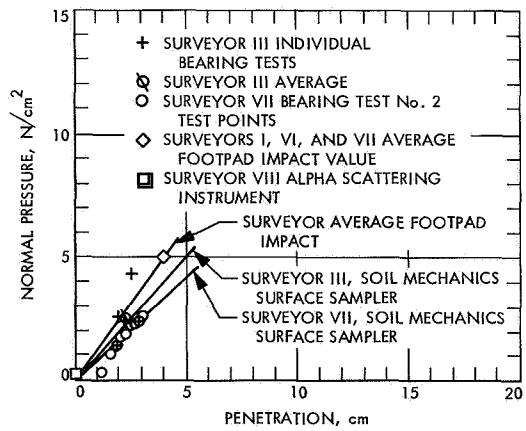

Fig. 5. Lunar surface force vs penetration curves for *Surveyor* footpads, surface sampler, and sensor head of the alpha scattering instrument

Surveyor footpads, the alpha scattering instrument, and the soil mechanics surface sampler. Static bearing capacity for a 30-cm diameter footpad is taken as 5 N/cm² at a depth of 4 cm as the average value for normal landings (Ref. 6).

During the *Surveyor VII* mission, values of 0.2 N/cm² at a depth of about 2 mm were obtained with two emplacements of the sensor head of the alpha scattering instrument (Ref. 5). For the *Surveyor III* mission, Scott and Roberson (Ref. 8) report depth of penetration and force of application data on six bearing tests with the surface sampler. They also report data (Refs. 9 and 10) on individual test points for bearing test number 2 for the *Surveyor VII* mission. Force vs penetration curves for these data are also plotted in Fig. 5.

Values of force reported by Scott and Roberson are increased 10%, because the force values are not applied perpendicular to the lunar surface but in a direction tangent to circles drawn through the instrument pivot point. These tangent directions formed angles with the lunar surface ranging from 58 to 67 deg and averaging 63 deg (sin 63 deg = 0.89 ≅ 0.90). It is assumed here that the lunar soil strength would follow approximately

a sine relationship for sloped surfaces (or for forces applied at an angle). The bearing plate on the surface sampler penetrated the soil at an angle; the plate was perpendicular to the forces shown in Fig. 5.

As seen from the data in Fig. 5, *Surveyor* penetration data for the footpad and surface sampler range from about 3.5 to 5 N/cm^2 for penetration depths of about 4 cm; the curve for *Surveyor III* data falls approximately at the midpoint between data from the *Surveyor VII* surface sampler and footpads. The value taken here that best defines the average *Surveyor* pressure vs penetration for various sized penetrators is the line passing through 4 N/cm^2 at a depth of 4 cm.

Figures 6 and 7 show continuous curves of pressure vs penetration for the 7.6- and 15.2-cm diameter plates in each of the basalt and aluminum soils at a minimum of four different packing densities. In Fig. 8, each of the four packing densities (5, 30, 60, and 90 to 100% relative densities) the continuous pressure vs penetration curves are shown for the 7.6-cm diameter plate used for all the soils. In all figures, *Surveyor* penetration data are also shown for comparison.

From Figs. 6 and 7, which show penetration curves for both sizes of plates, several general conclusions can be made:

(1) All curves pass through zero, indicating that the soil has zero bearing strength at the surface; i.e., it will not support load without penetration.

(2) Some curves, close to zero, are concave downward, probably because leveling of the soil surface during processing increased the surface soil density somewhat compared with the underlying soil.

(3) Most curves have a straight line portion for the first few centimeters of penetration in the loosely packed soil, and are essentially straight for the entire distance of penetration in the densely packed soil. The concave upward portion of the curves of the loosely packed soils is caused principally by the packing of the soil beneath the plate as it penetrates and by the bottom effect. Packing and bottom effects occur at shallower penetrations for the 15.2-cm plate than for the 7.6-cm plate.

(4) One of the most important features of these figures is that the curves for the 7.6- and 15.2-cm diameter plates are, for the most part, superimposed in their straight portions for loosely packed soils; i.e., where relative densities are approximately equal to or less than 50%. This indicates, then, that for soils with loose packing or relative densities less than 50%, their depth of penetration is directly proportional to pressure and is independent of size and shape of the penetrator.

In comparing *Surveyor* penetration data with the laboratory penetration data as shown at the four packing densities (Fig. 8), the most noticeable feature is that, for dense packing (Fig. 8d), all of the soils are much too dense to correlate with *Surveyor* data. At approximately 60% relative density, a good fit occurs for only the very fine cohesive 6.4-μ aluminum powder. At approximately 30% relative density, there is no fit to *Surveyor* data; all of the coarser soils are too dense and the finer soils (12-μ basalt, 6.4-μ aluminum, and 22-μ aluminum mixture) are too loosely packed. At the loosest packing with approximately 5–15% relative density, all of the soils except the coarsest grades (170-μ basalt and 82-μ aluminum) are too loosely packed.

Considering only the three basalt curves (Fig. 6), the best fit for the 170-μ basalt occurs at a porosity of 42.2 $\pm$0.6% and bulk density of 1.66 $\pm$0.02 g/cm^3. The tolerances listed are based on probable maximum and minimum ranges for porosity and on bulk densities from the limits of *Surveyor* footpad and surface sampler data as given in Table 3. For the 55-μ basalt, the best fit occurs at a porosity of 47.8 $\pm$0.8% and a bulk density of 1.49 $\pm$0.02 g/cm^3. For the 12-μ basalt, the best fit occurs at a porosity of 53.2 $\pm$0.4% and a bulk density of 1.34 $\pm$0.01 g/cm^3.

As discussed earlier, the mean particle size of lunar soil probably lies between the 12- and 55-μ size ranges at approximately 33 μ. Assuming that the value of 33 μ is the present best estimate for the lunar soil mean particle size and that the 12- and 55-μ basalts are reasonable limits, then the best estimate for lunar soil porosity is 50.5 $\pm$3.5% or, after rounding off, 51 $\pm$4%.

The grain density of the test soil was 2.88 g/cm^3, the average of measurements made on 10 specimens from Little Lake Basalt. This density agrees closely with the density of a lunar rock measured with the *Surveyor VII* surface sampler; Scott and Roberson (Ref. 9) report that "the density was in the range of 2.4–3.1 g/cm^3, with the most probable value about 2.8 to 2.9 g/cm^3."

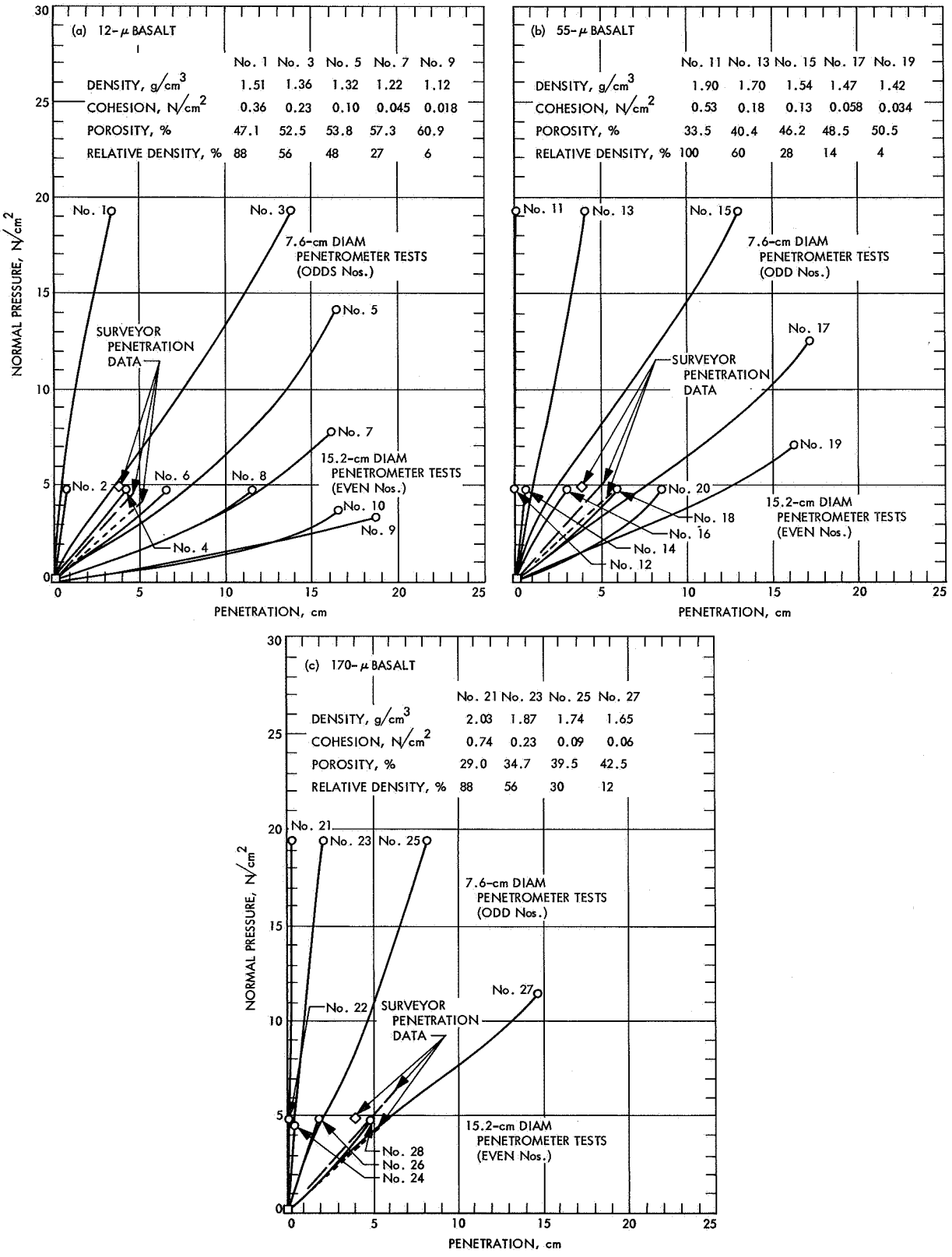

Fig. 6. Pressure vs penetration curves of basalt soils for 7.6- and 15.2-cm diameter plates and for *Surveyor* lunar data

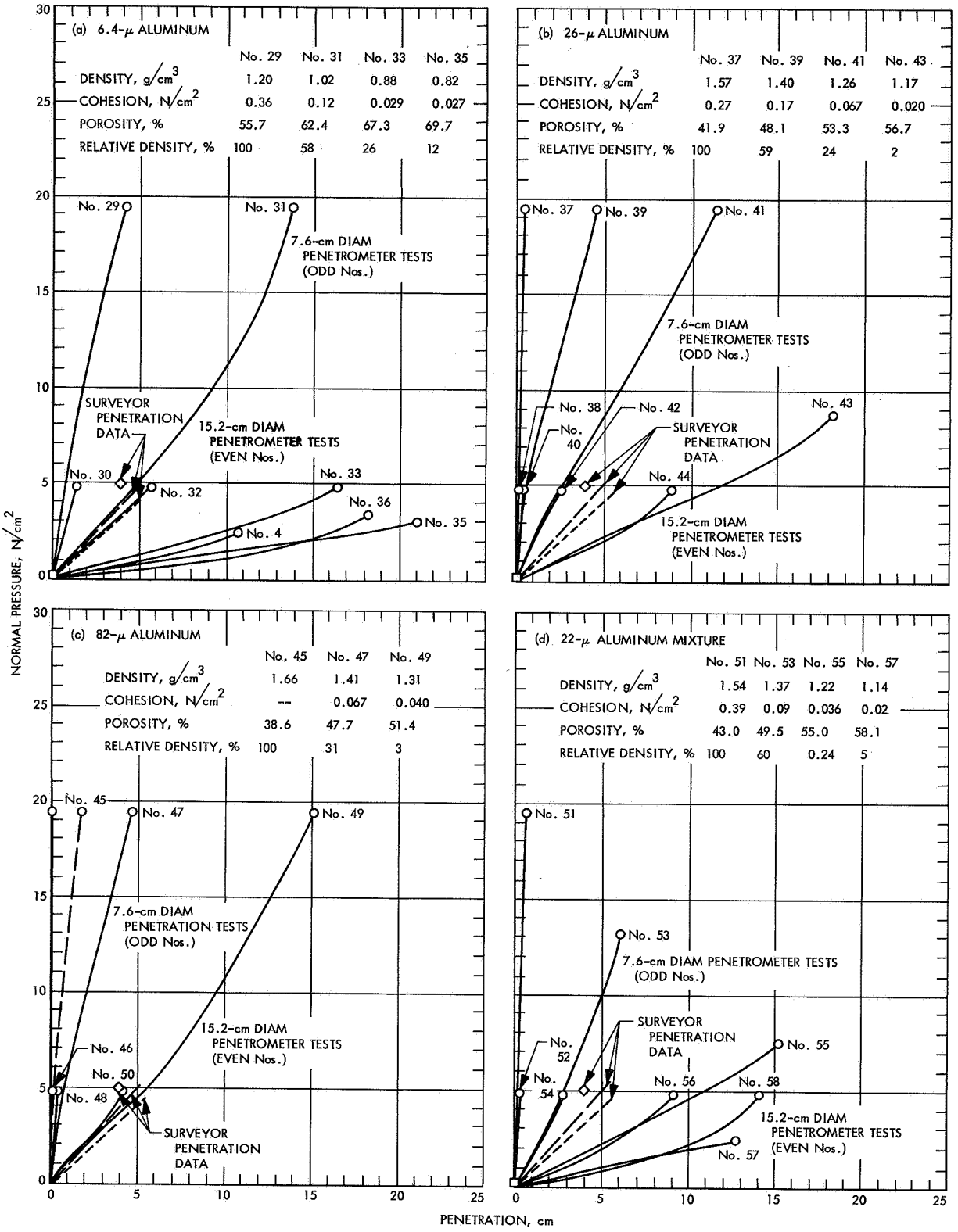

Fig. 7. Pressure vs penetration curves of aluminum soils for 7.6- and 15.2-cm diameter plates and for *Surveyor* lunar data

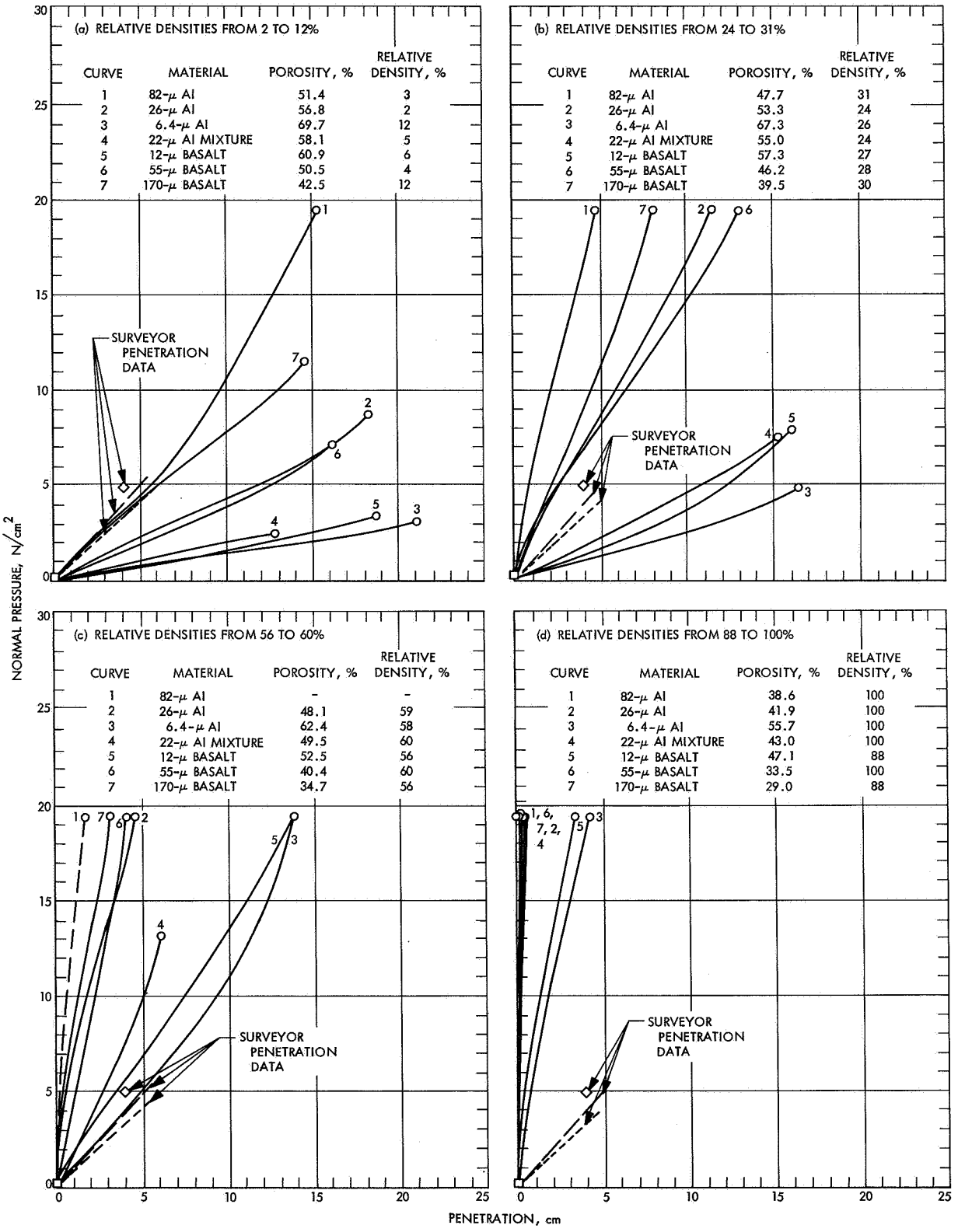

Fig. 8. Bearing strength vs penetration curves for basalt and aluminum soils at various packing densities, compared with *Surveyor* lunar data (7.6-cm diameter plate)

Assuming that the test basalt soil has the same grain density as lunar soil, which is also interpreted as being of basalt origin, then the best fit for laboratory and *Surveyor* penetration data occurs for soil bulk density of 1.42 $\pm$0.10 g/cm^3.

However, this value for bulk density is based on an average rock grain density of 2.88 g/cm^3. Gault, et al. (Ref. 11), state that rock grain density based on analyses of data from the alpha scattering instrument at the highland site is 3.0 $\pm$0.05 g/cm^3 and at the mare sites tested as 3.2 $\pm$0.3 g/cm^3. If these values are used for average rock grain density, the lunar soil bulk density is raised to 1.48 $\pm$0.10 g/cm^3 for the highland site and 1.58 $\pm$0.10 g/cm^3 for the mare sites.

These laboratory tests, in addition to providing a value within close limits for the lunar soil bulk density, have also provided valuable data on the size effects of bearing plates penetrating lunar soil. These tests indicate that lunar soils, within the depth range tested by *Surveyor* spacecraft, are loosely packed; i.e., the relative density is equal to or less than 50%. These tests indicate that, for such soils, the bearing strength is independent of bearing plate size and shape. That is, penetration is directly proportional to pressure and is independent of the bearing plate size.

IV. Comparison of *Surveyor* and Test Soil Failure Characteristics

Figures 9 through 15 show the results of the tests with the 15.2-cm diameter plate (½ scale of *Surveyor* footpad) in all seven of the basalt and aluminum soils. Except for some of the loosely packed soils, the normal soil pressure existing at which these photographs were taken was 4.8 N/cm^2. This pressure is only slightly lower than the peak landing pressures exerted by the average *Surveyor* footpad, which ranged from 4.2 to 5.9 N/cm^2 during impact. Failure characteristics of the soils can be studied in these photographs, where relative density ranged from 2–12% for the loosely packed soils to 88–100% for the densely packed soils. In general, the basalt and aluminum test soils had similar failure characteristics.

Possibly the most striking characteristic observable in the pictures of the penetration tests is that a well-developed system of peripheral fractures developed around all imprints made in the most loosely packed soils. No such system of peripheral fractures is observable in any *Surveyor* pictures of footpad and crushable block imprints, shown in Figs. 16 and 17, respectively.

The second characteristic readily observable is that, with all densely packed soils, penetration is much less than in the *Surveyor* footpad and crushable block penetration pictures. For example, in the tests on the densely packed 170-μ basalt (Fig. 11d), though the imprint is visible, the depth is too small to measure. In the densely packed 55-μ basalt, the imprint cannot be seen. The imprint with the 7.6-cm diameter plate, which exerted a pressure of 19 N/cm^2, can be seen; however, it is barely visible (Fig. 10).

In the laboratory tests, bearing strength vs penetration curves matched *Surveyor* data for the 170-μ basalt at the loose packing of 14% relative density, for the 55-μ basalt at 18% relative density, and for the 12-μ basalt at 52% relative density. Thus, the pictures with the closest match to *Surveyor* penetration data are Fig. 11a for the 170-μ basalt, Fig. 10b for the 55-μ basalt, and Fig. 9c for the 12-μ basalt. Table 4 provides a summary of the physical properties of these basalt soils that best fit the *Surveyor* bearing strength and cohesion soils.

The large number of peripheral fractures indicates that the 170-μ basalt does not fit *Surveyor* data. However, the general lack of fractures in Figs. 9c and 10b indicate that the 12- and 55-μ basalts are better fits to *Surveyor* data.

Table 4. Physical properties of basalt soils

Soil properties[a]	Best fit	Maximum	Minimum
170-μ basalt			
Density, g/cm^3	1.66	1.68	1.65
Relative density, %	14	17	12
Porosity, %	42.2	42.6	41.6
55-μ basalt			
Density, g/cm^3	1.49	1.51	1.48
Relative density, %	18	22	16
Porosity, %	47.8	48.2	47.0
12-μ basalt			
Density, g/cm^3	1.34	1.35	1.33
Relative density, %	52	54	50
Porosity, %	53.2	53.5	52.8

[a]Little Lake Basalt, Inyo County, Calif.; grain density = 2.88 g/cm^3.

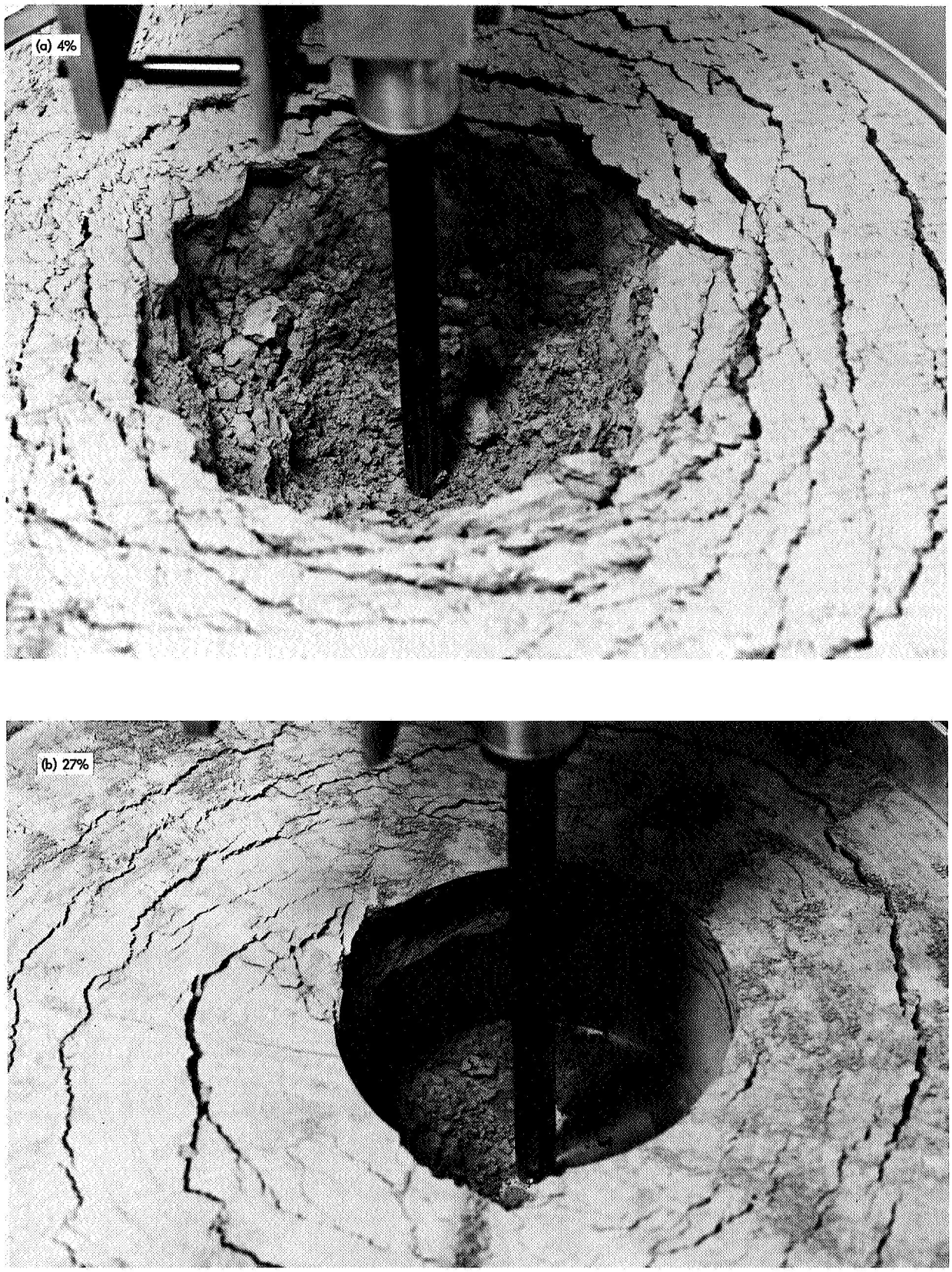

Fig. 9. Penetration test with 12-μ basalt at various relative densities

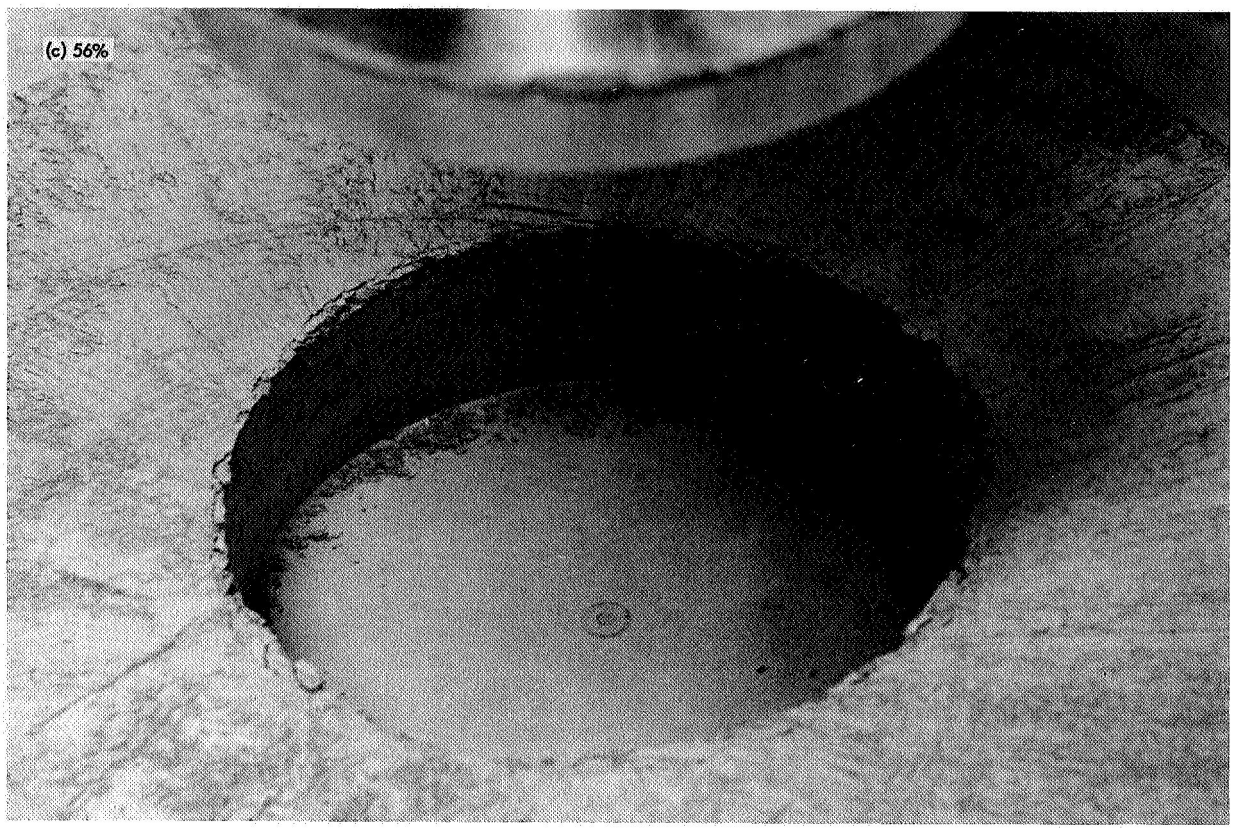

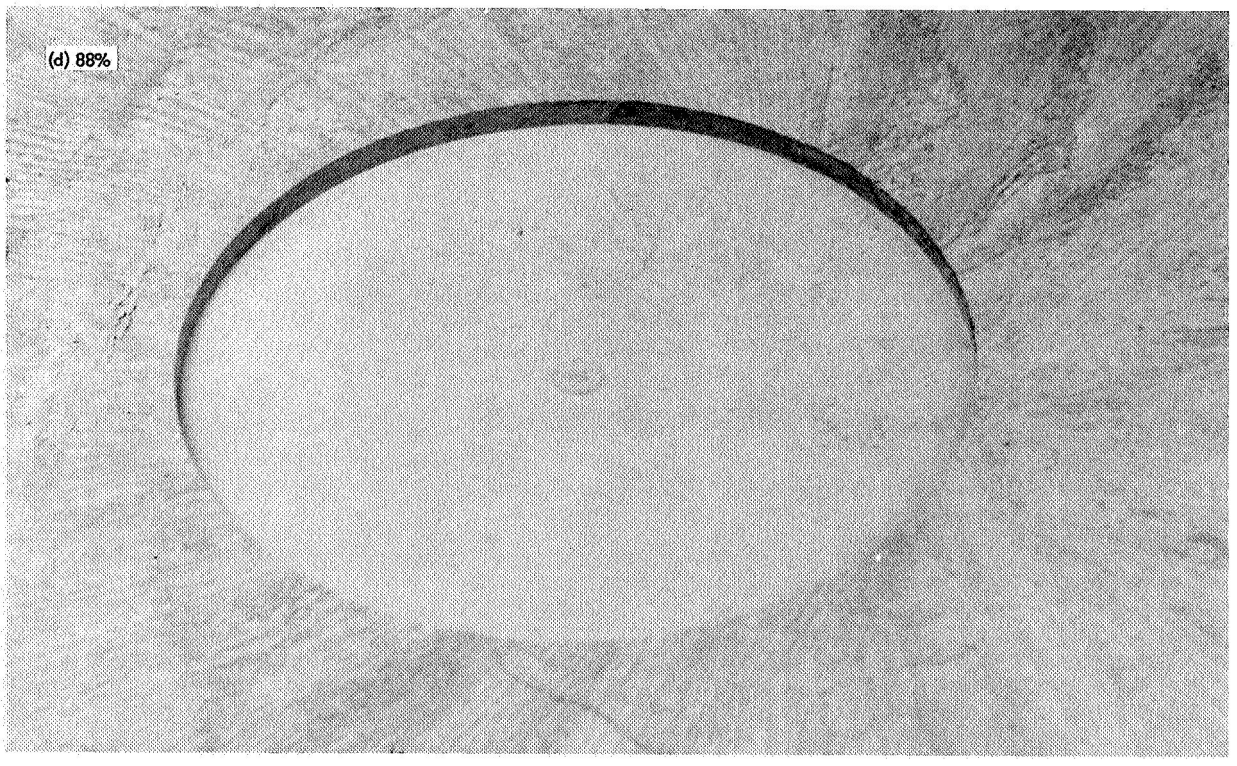

Fig. 9 (contd)

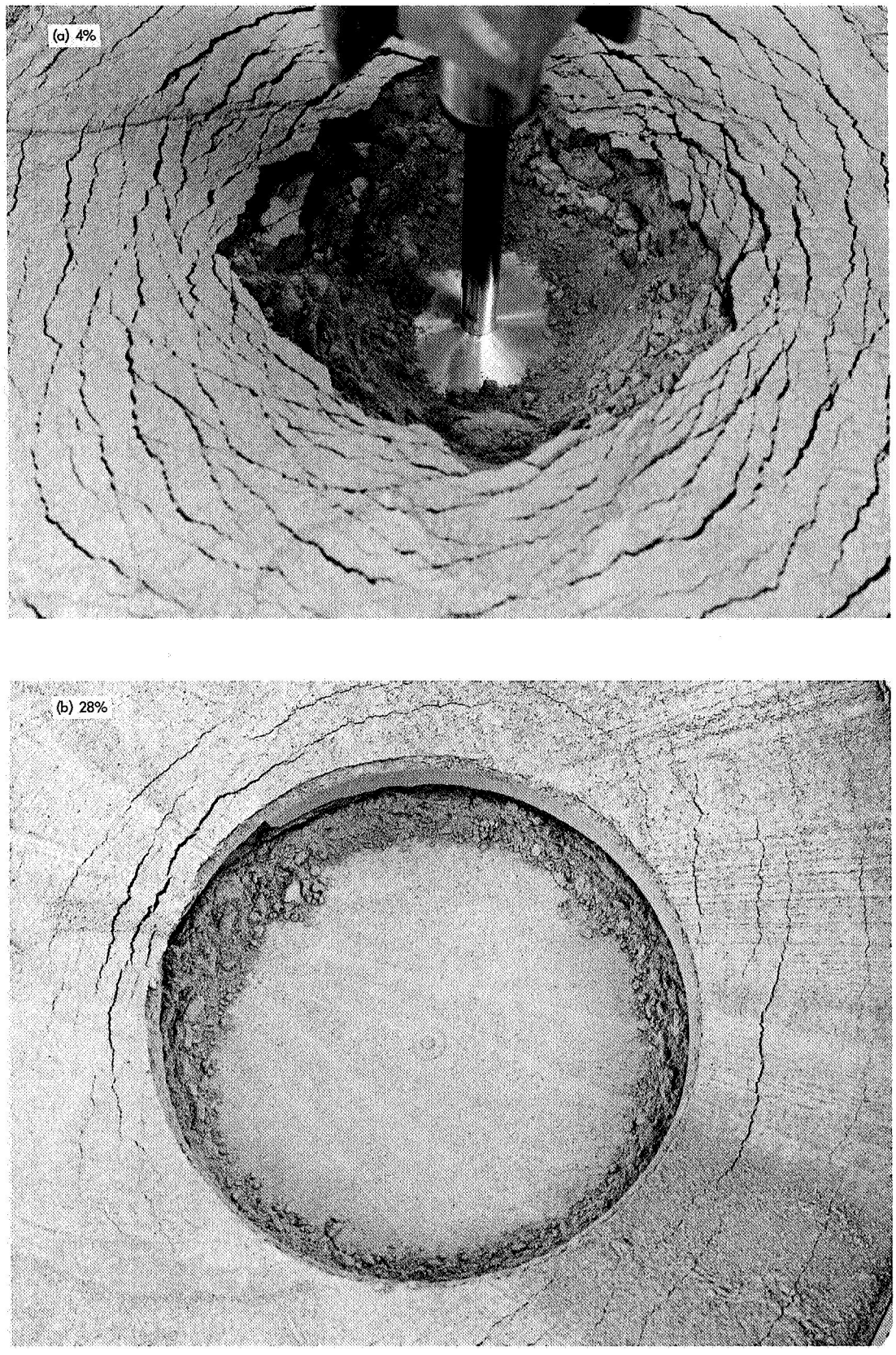

Fig. 10. Penetration test with 55-μ basalt at various relative densities

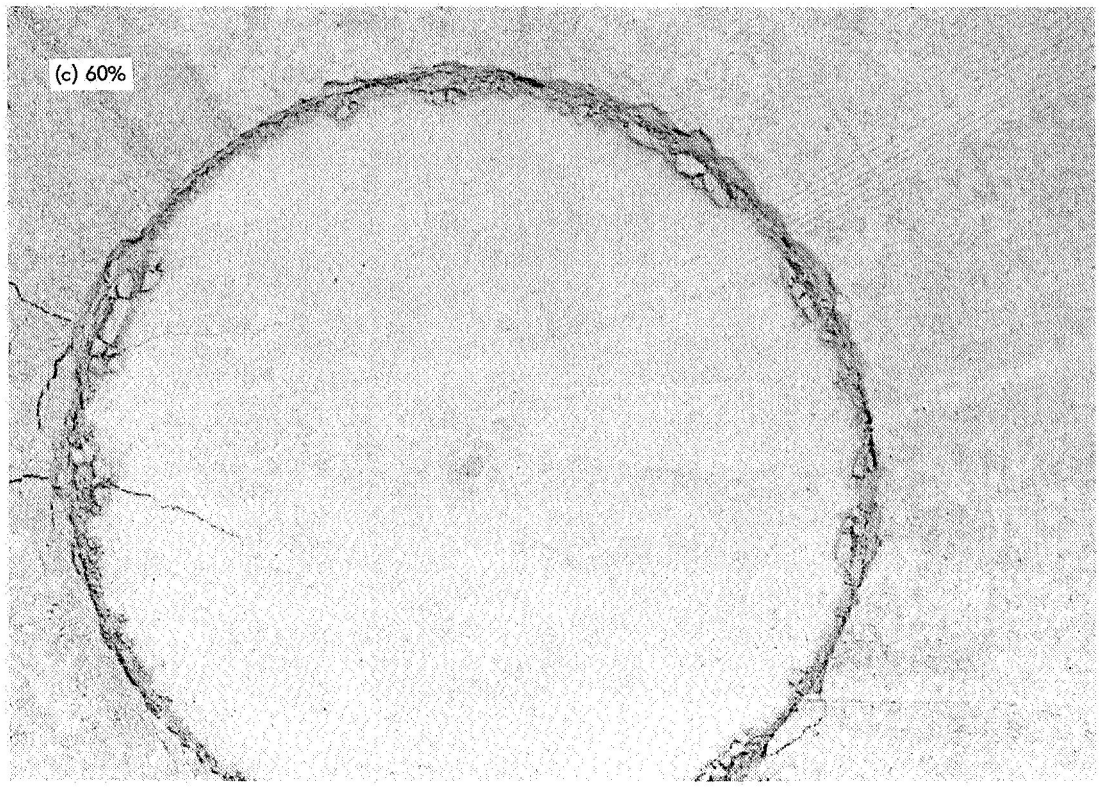

Fig. 10 (contd)

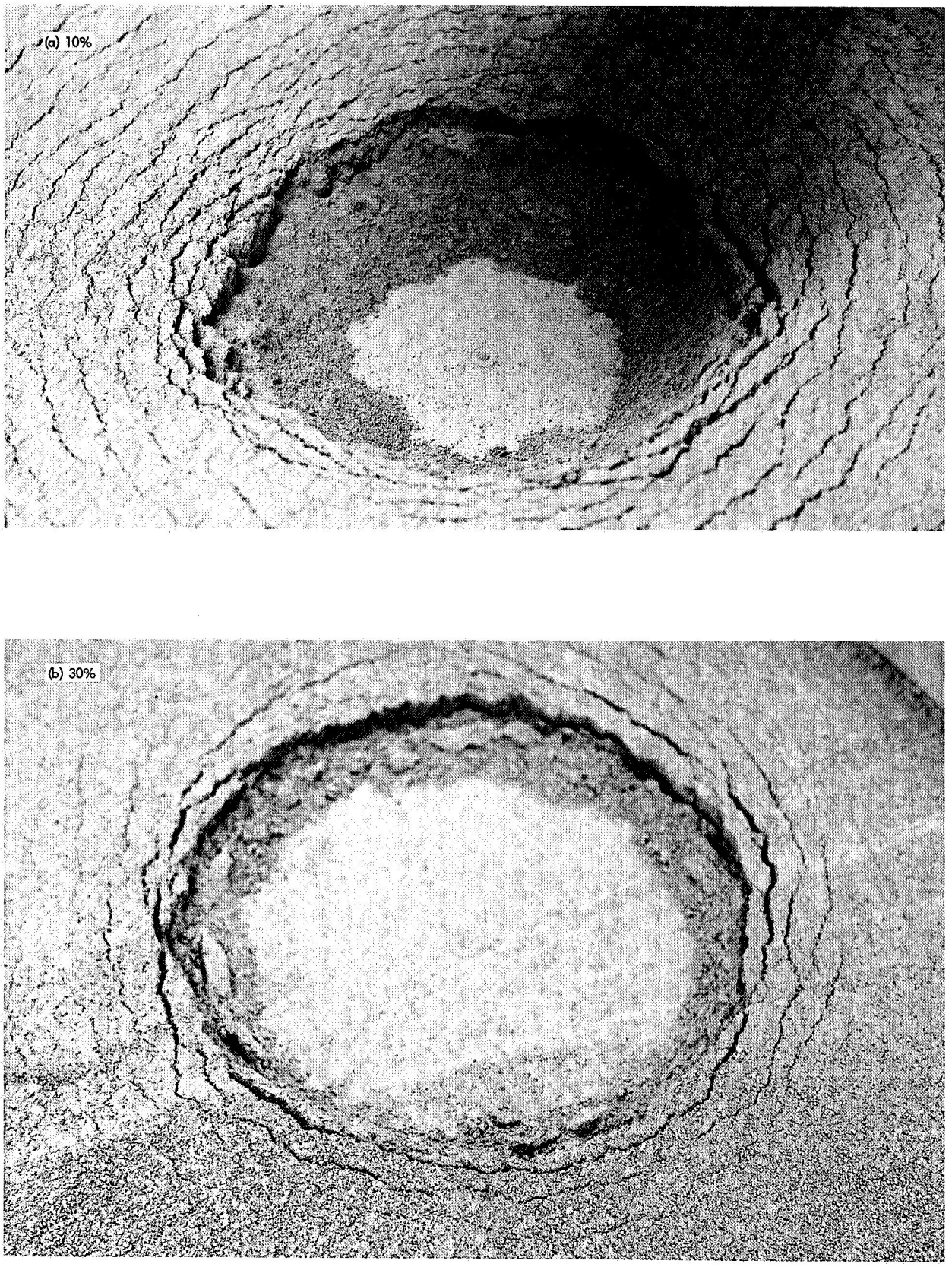

Fig. 11. Penetration test with 170-μ basalt at various relative densities

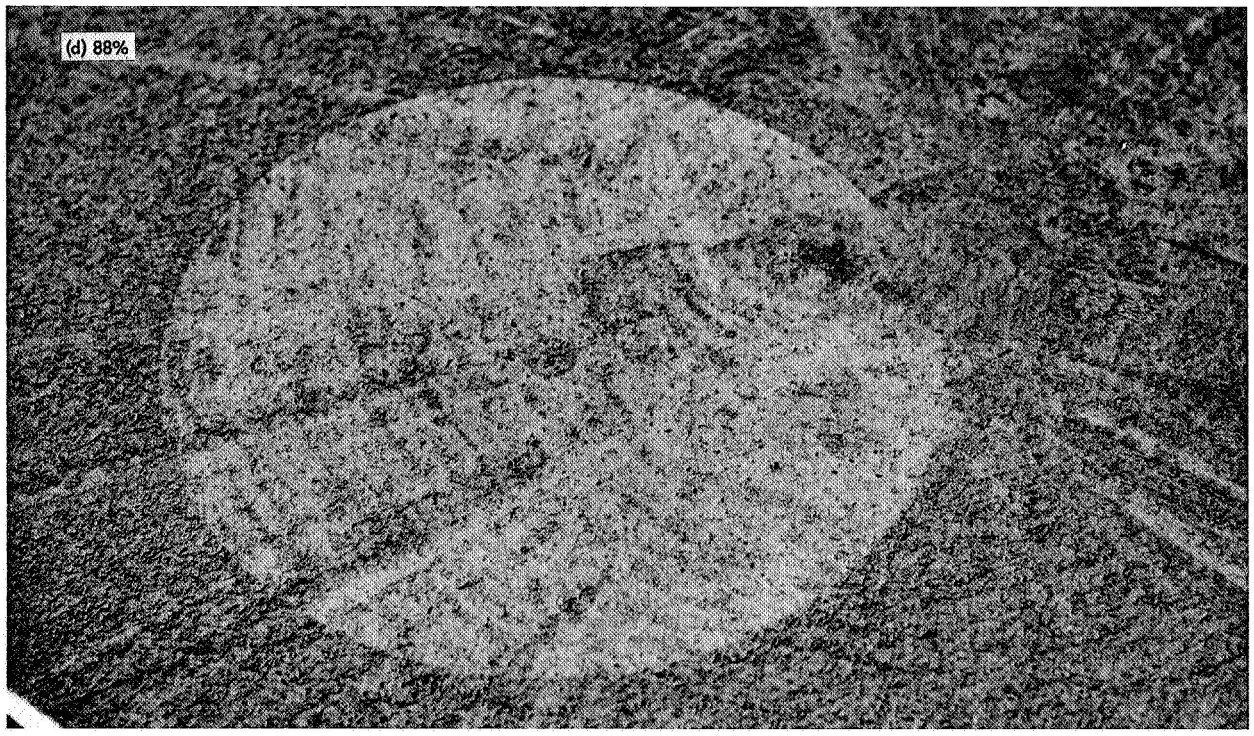

Fig. 11 (contd)

Fig. 12. Penetration test with 6.4-μ aluminum at various relative densities

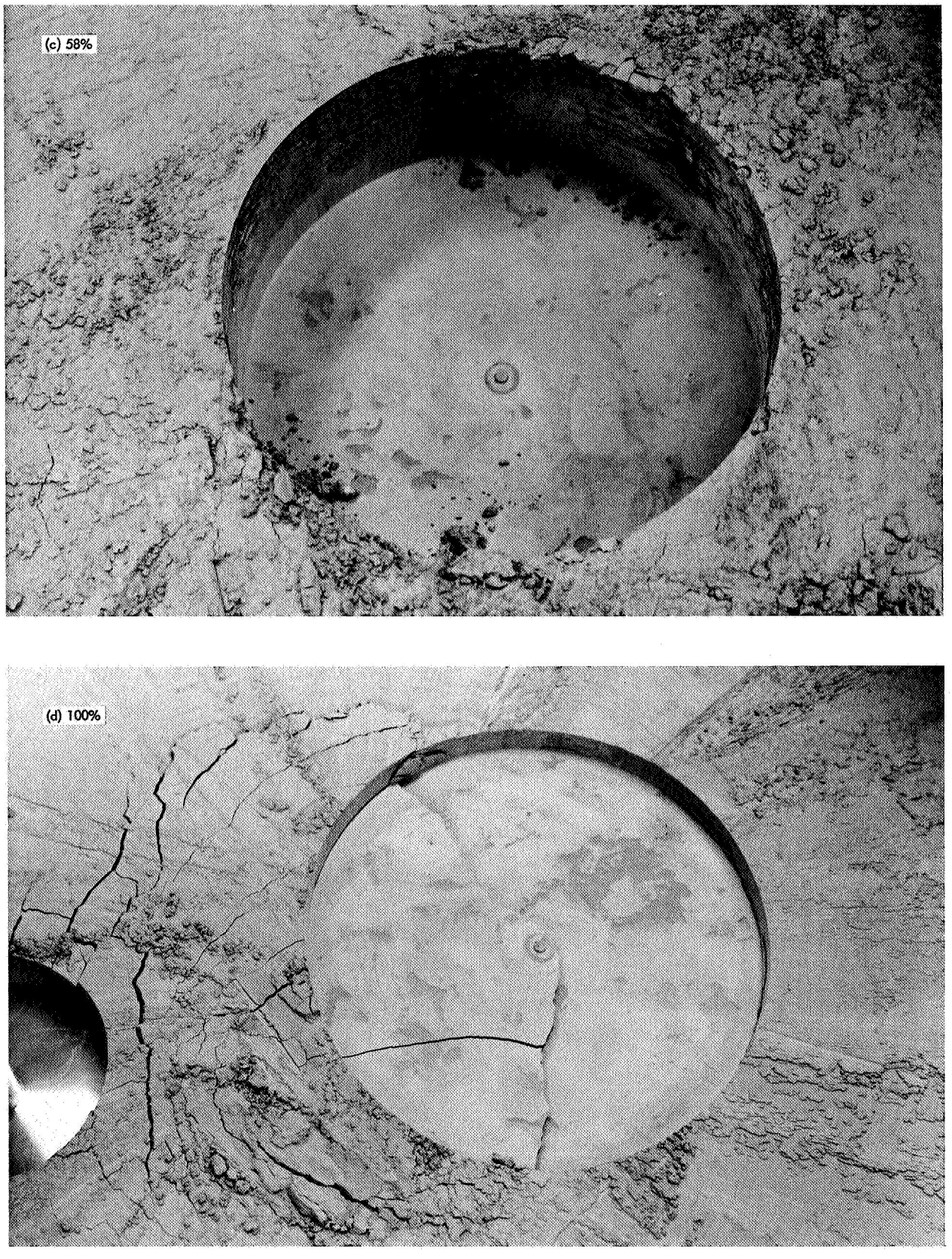

Fig. 12 (contd)

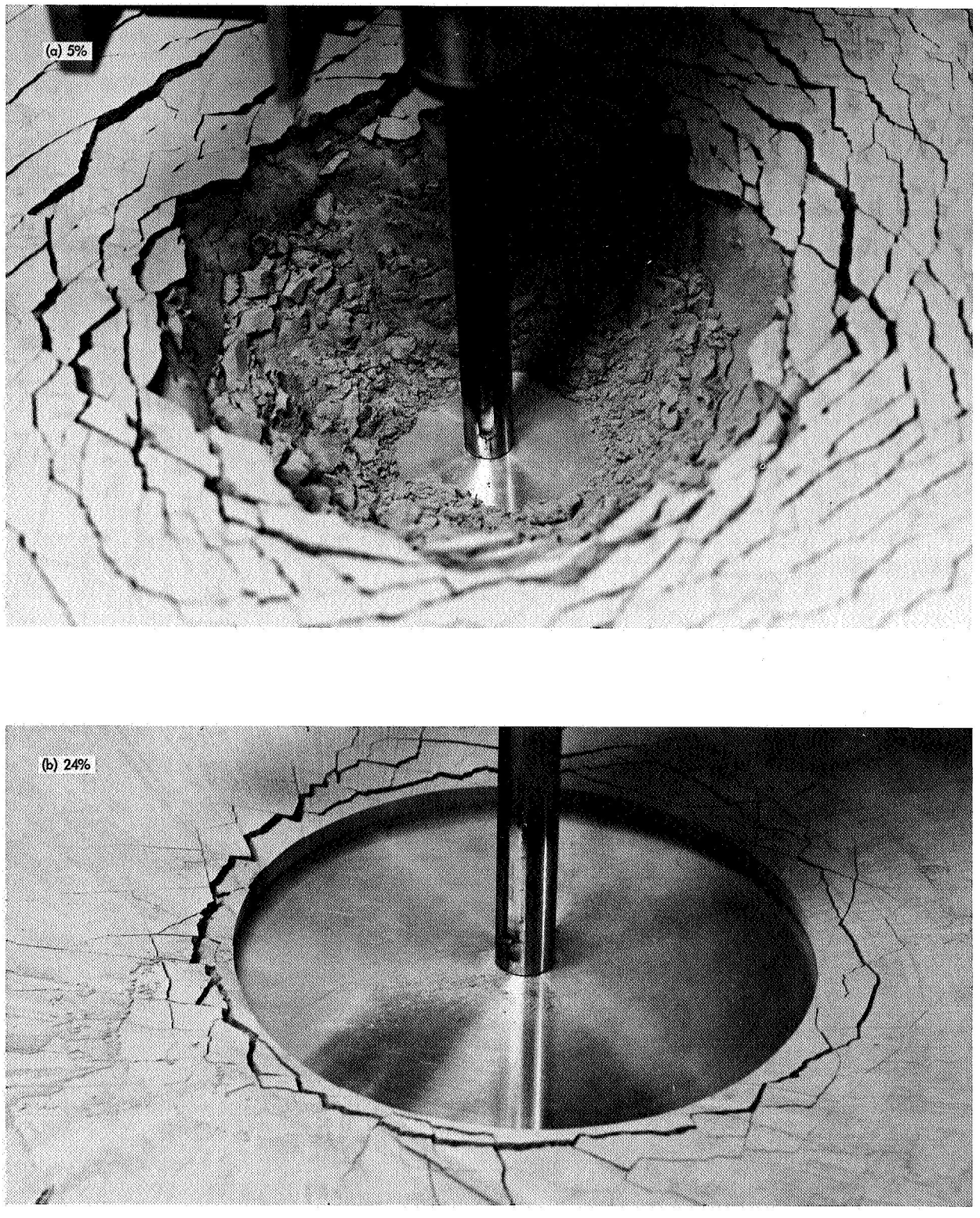

Fig. 13. Penetration test with 26-μ aluminum at various relative densities

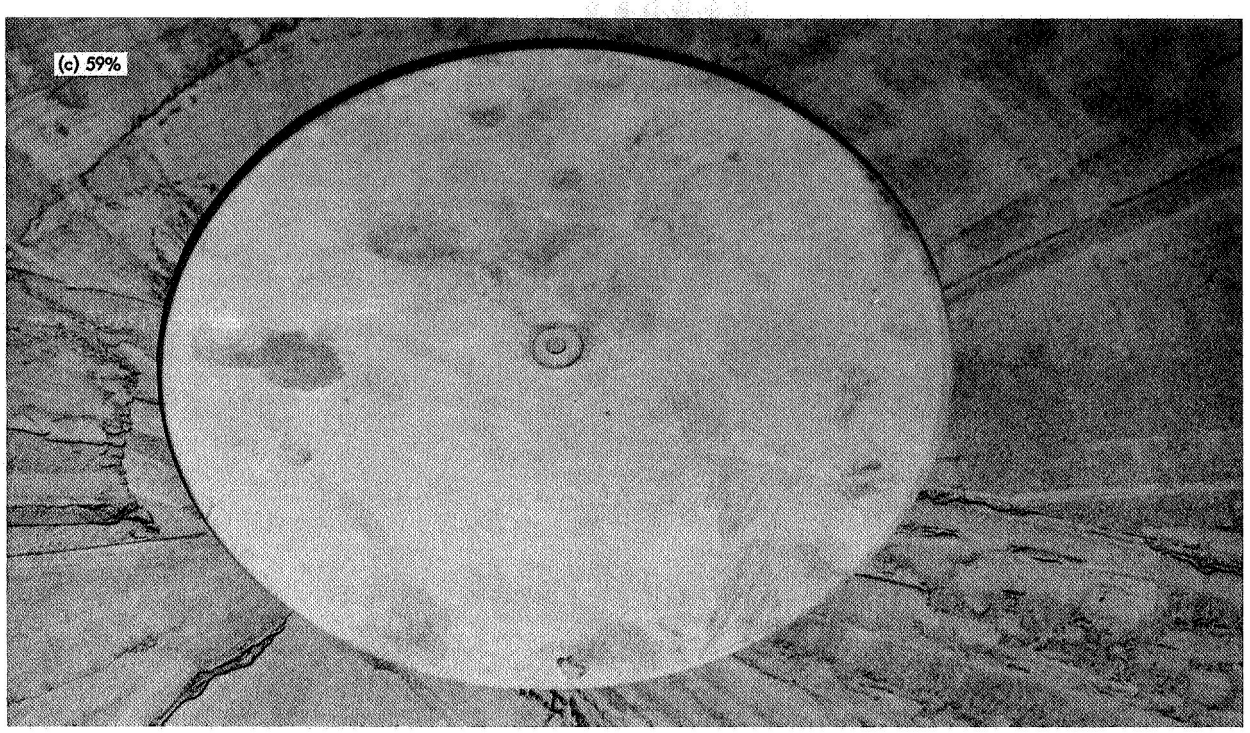

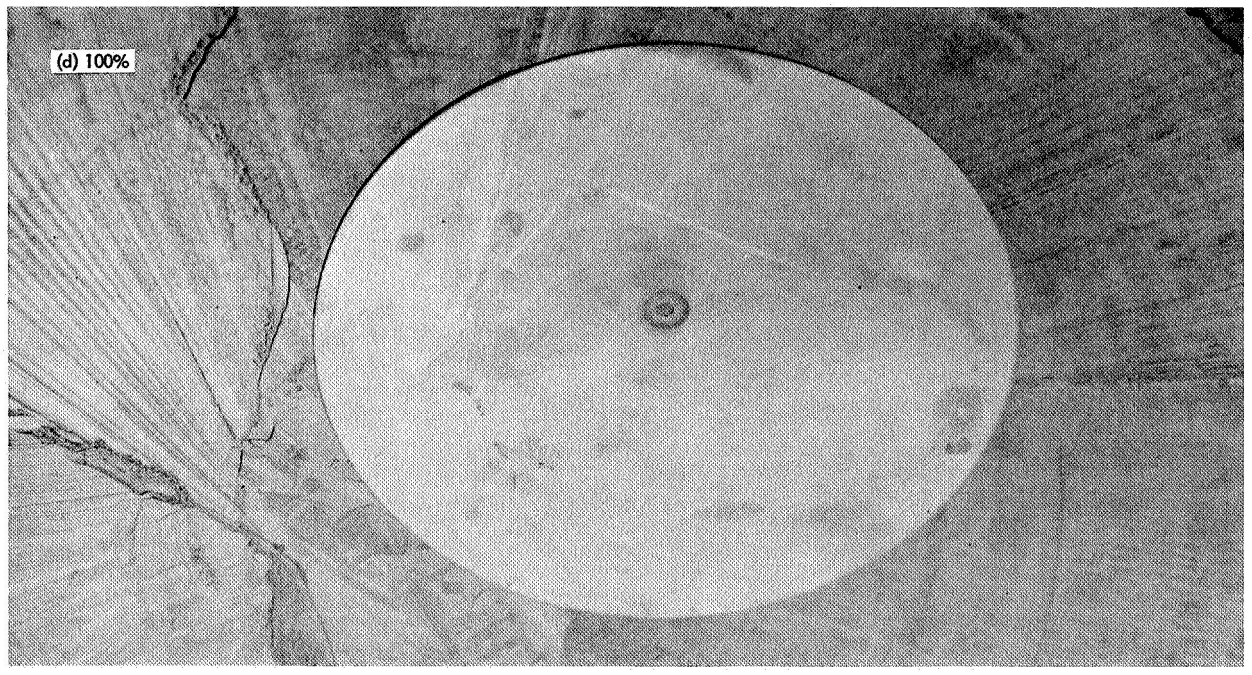

Fig. 13 (contd)

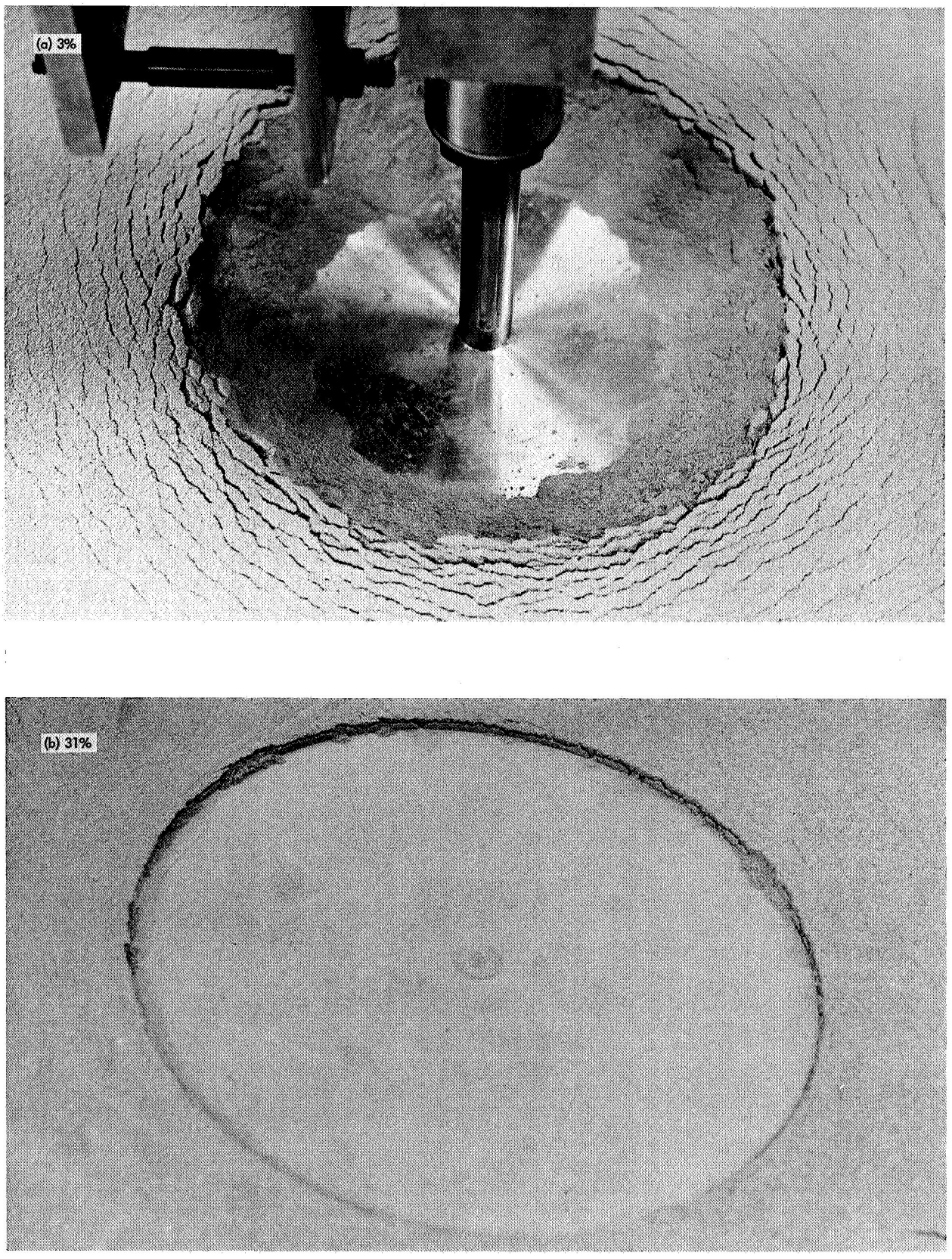

Fig. 14. Penetration test with 82-μ aluminum at various relative densities

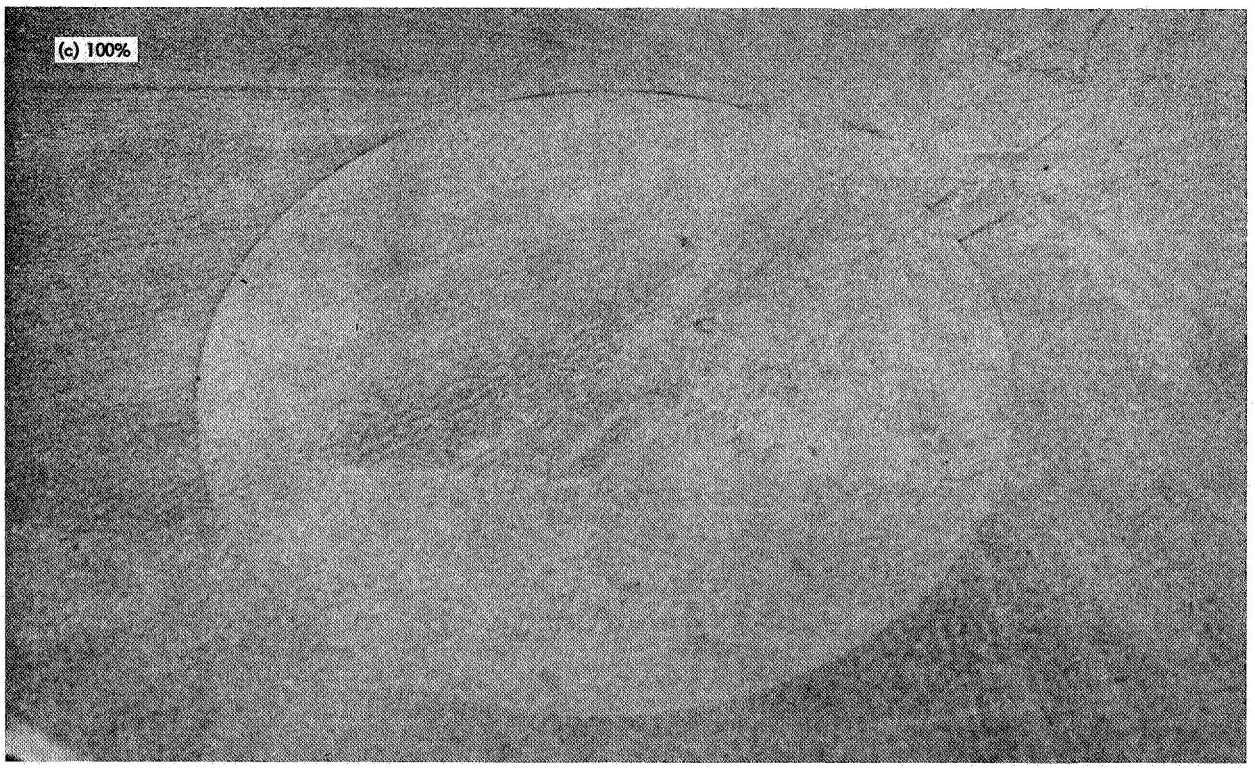

Fig. 14 (contd)

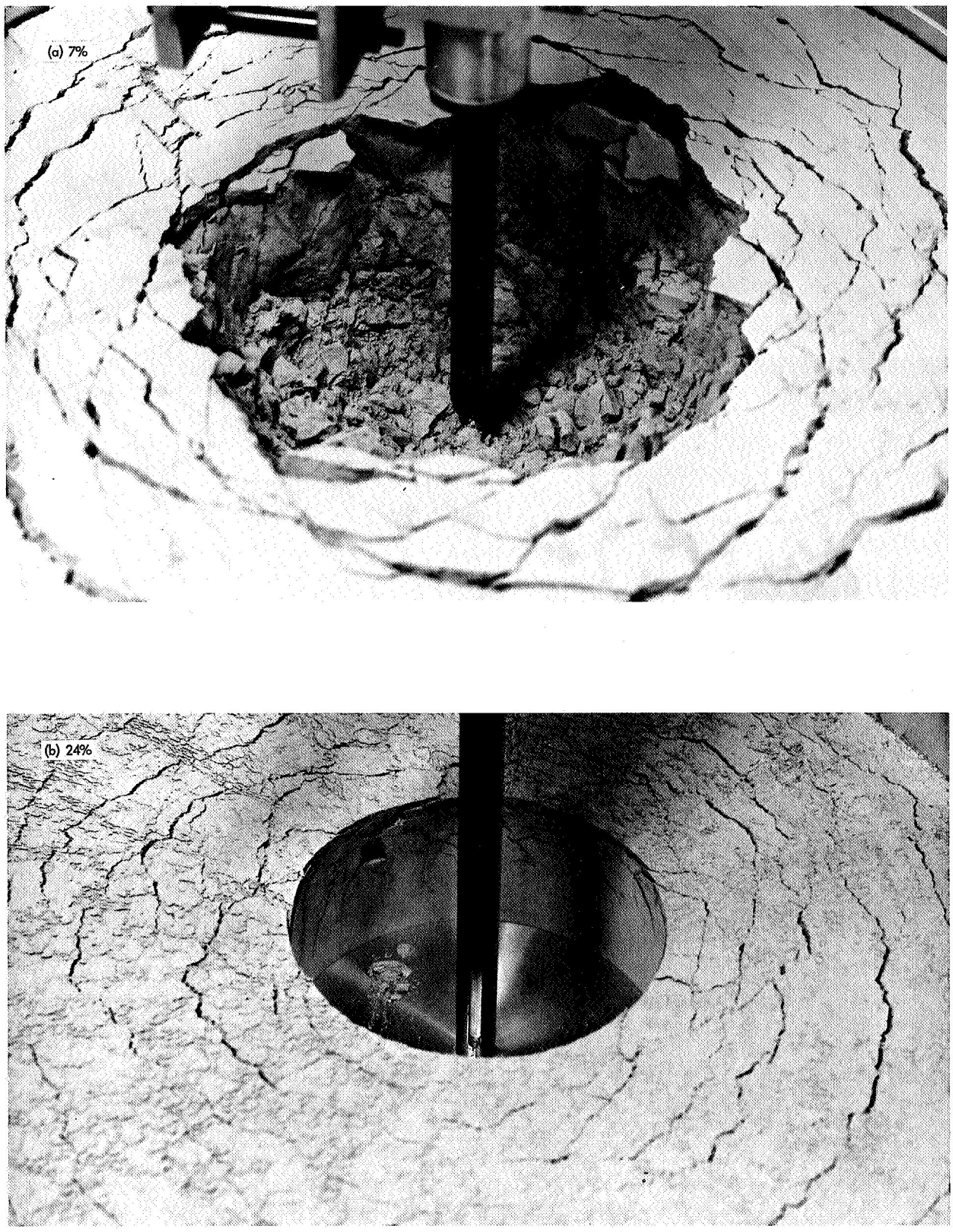

Fig. 15. Penetration test with 22-μ aluminum mixture at various relative densities

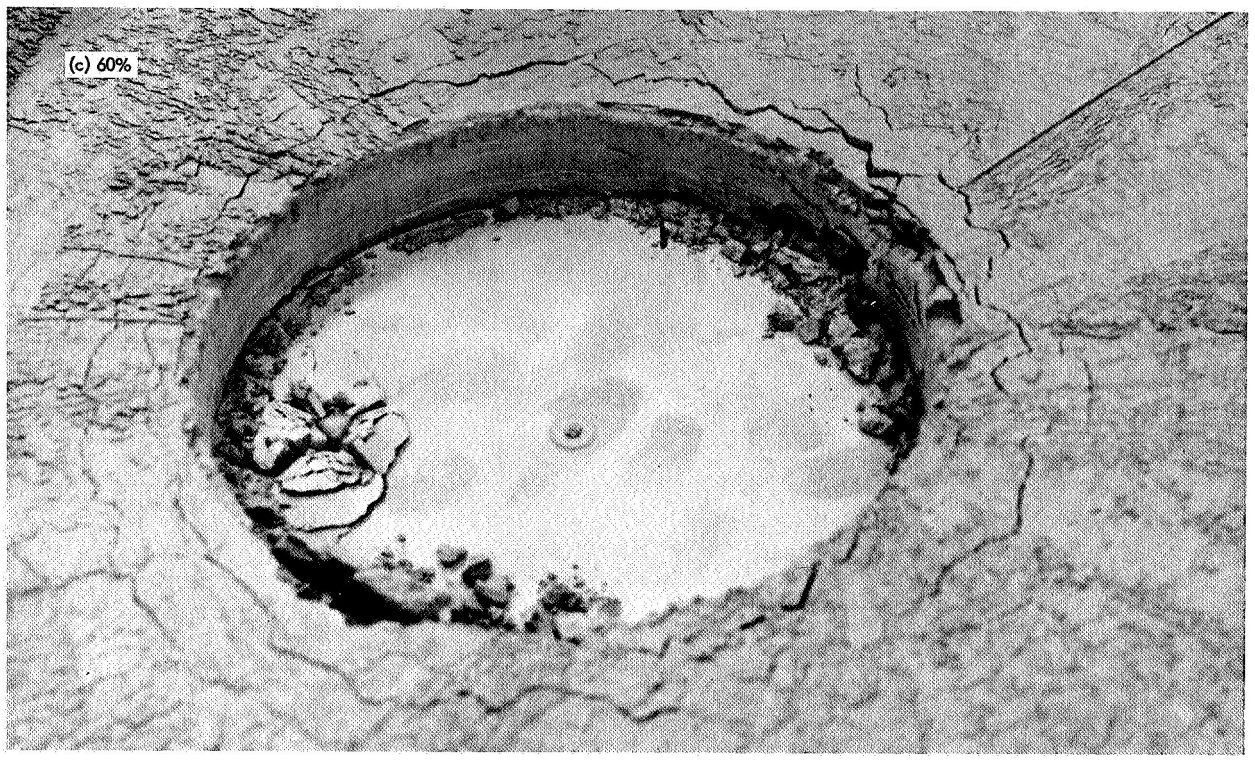

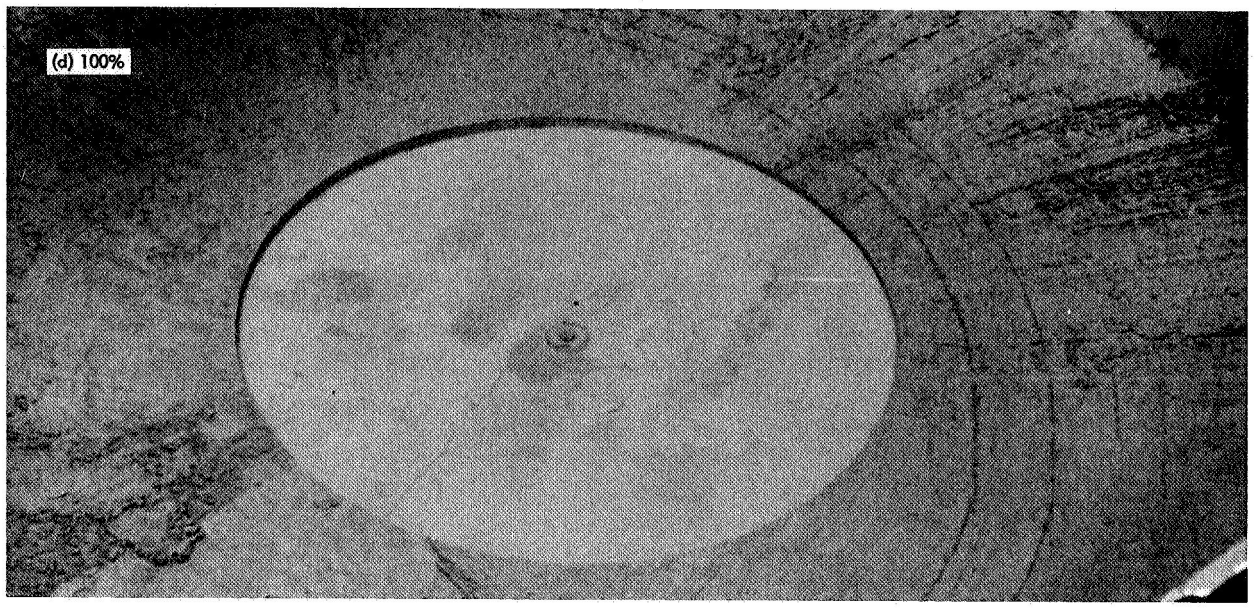

Fig. 15 (contd)

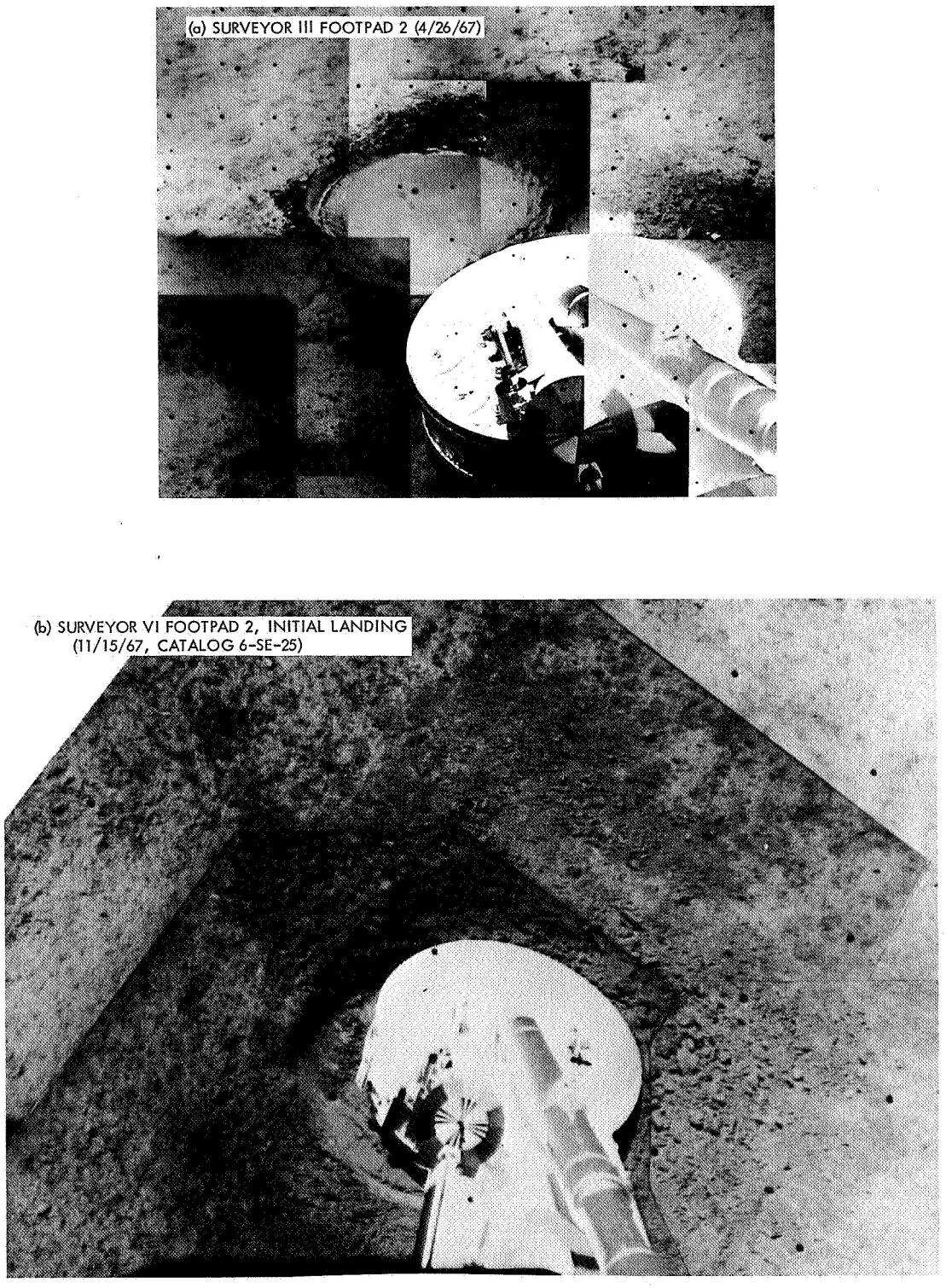

Fig. 16. *Surveyor* footpad imprints

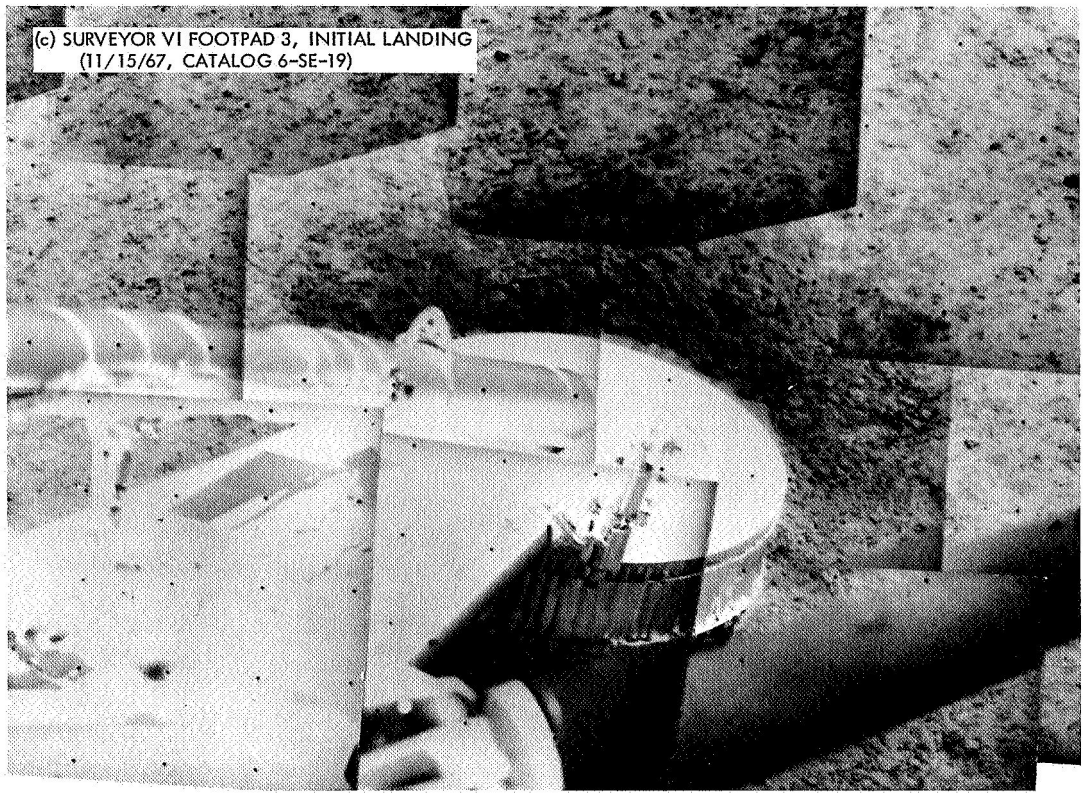
(c) SURVEYOR VI FOOTPAD 3, INITIAL LANDING
(11/15/67, CATALOG 6-SE-19)

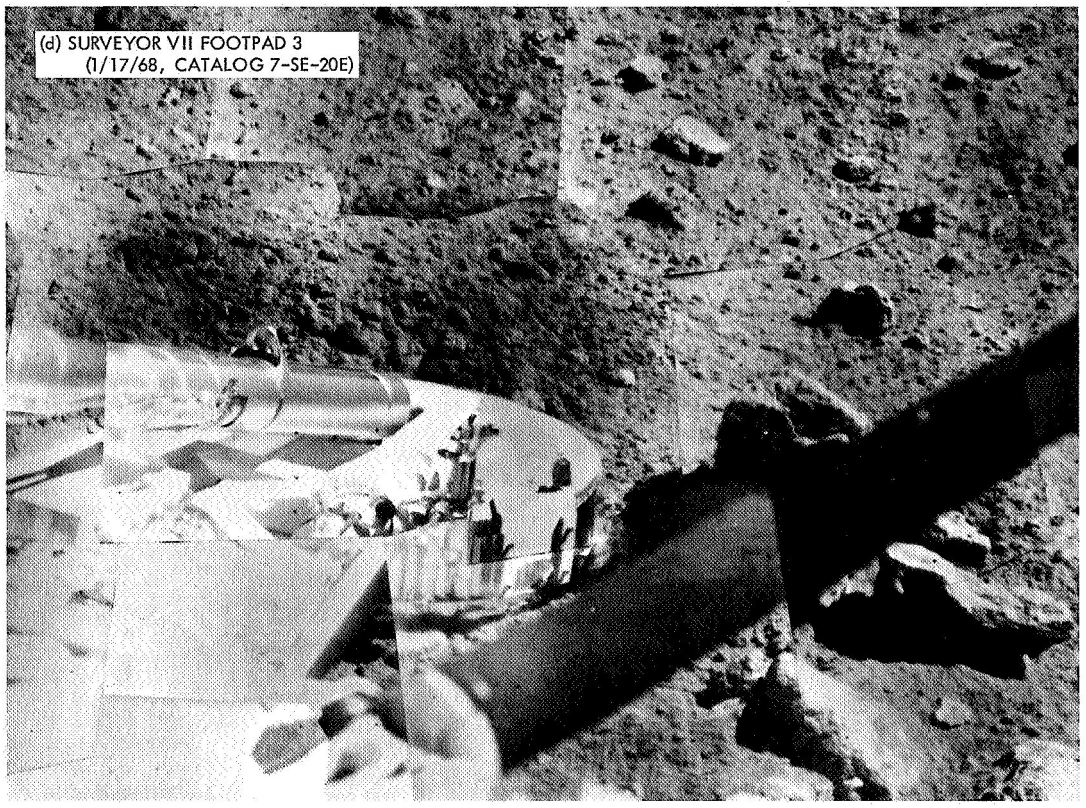
(d) SURVEYOR VII FOOTPAD 3
(1/17/68, CATALOG 7-SE-20E)

Fig. 16 (contd)

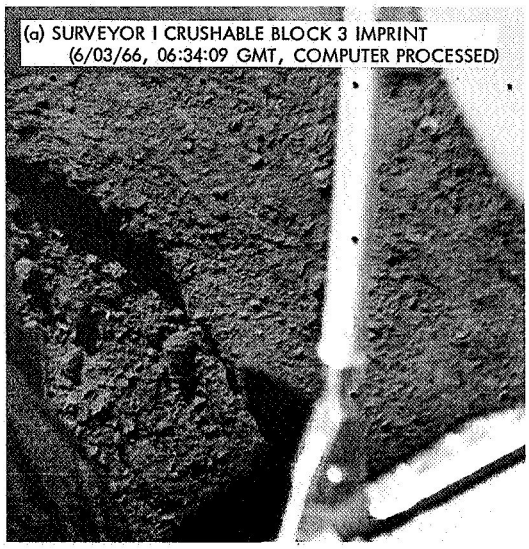

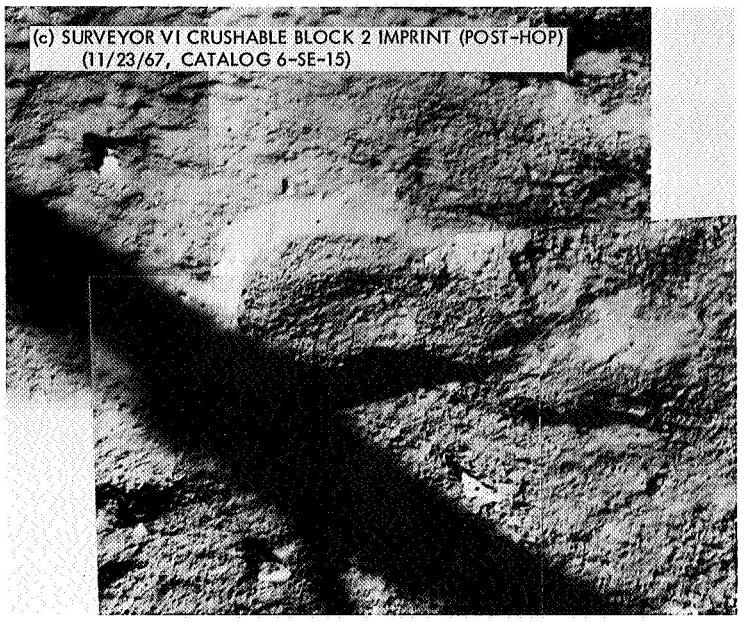

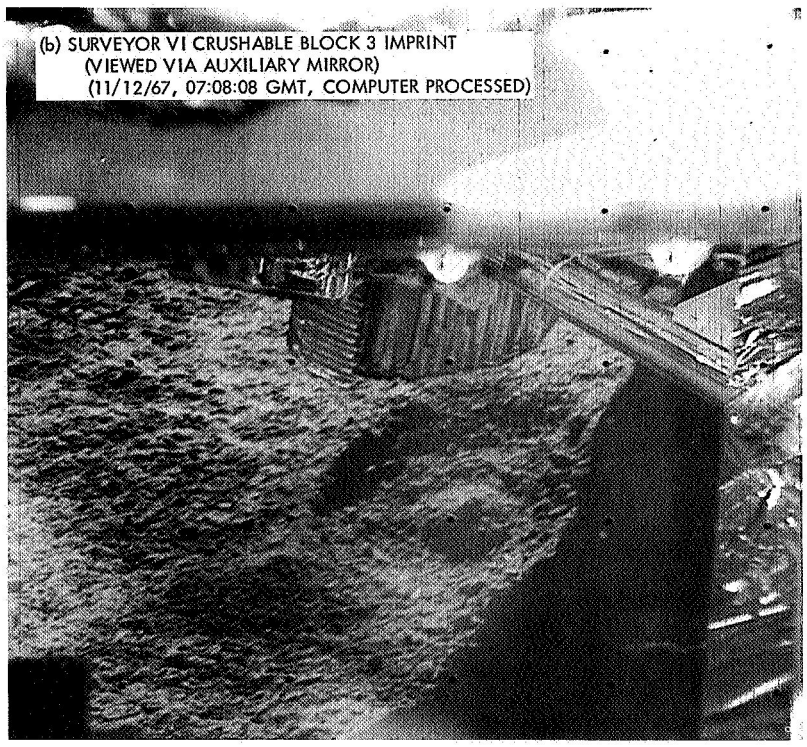

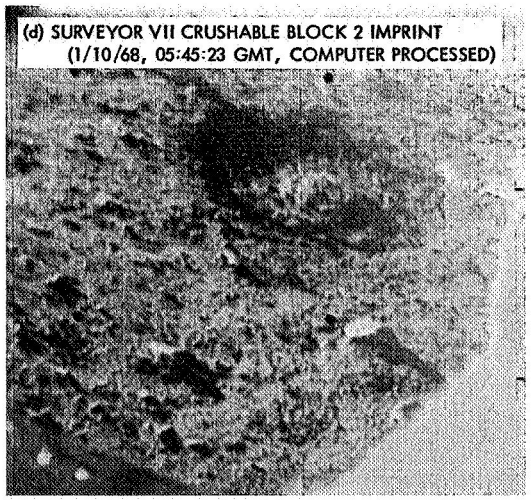

Fig. 17. *Surveyor* crushable block imprints

References

1. Christensen, E. M., et al., "Lunar Surface Mechanical Properties," *Surveyor I Mission Report: Part II. Scientific Data and Results,* Technical Report 32-1023, pp. 69–85. Jet Propulsion Laboratory, Pasadena, Calif., Sept. 10, 1966.

2. Christensen, E. M., et al., "Lunar Surface Mechanical Properties," *Surveyor III Mission Report: Part II. Scientific Results,* Technical Report 32-1177, pp. 111–153. Jet Propulsion Laboratory, Pasadena, Calif., June 1, 1967.

3. Christensen, E. M., et al., "Lunar Surface Mechanical Properties," *Surveyor V Mission Report: Part II. Science Results,* Technical Report 32-1246, pp. 43–88. Jet Propulsion Laboratory, Pasadena, Calif., Nov. 1, 1967.

4. Christensen, E. M., et al., "Lunar Surface Mechanical Properties," *Surveyor VI Mission Report: Part II. Science Results,* Technical Report 32-1262, pp. 47–108. Jet Propulsion Laboratory, Pasadena, Calif., Jan. 10, 1968.

5. Choate, R., et al., "Lunar Surface Mechanical Properties," *Surveyor VII Mission Report: Part II. Science Results,* Technical Report 32-1264, pp. 77–134. Jet Propulsion Laboratory, Pasadena, Calif., Mar. 15, 1968.

6. Choate, R., et al., "Lunar Surface Mechanical Properties," *Surveyor Project Final Report: Part II. Science Results,* Technical Report 32-1265, pp. 137–194. Jet Propulsion Laboratory, Pasadena, Calif., June 15, 1968.

7. Shoemaker, E. M., et al., "Television Observations from Surveyor," *Surveyor Project Final Report: Part II. Science Results,* Technical Report 32-1265, pp. 21–136. Jet Propulsion Laboratory, Pasadena, Calif., June 15, 1968.

8. Scott, R. F., and Roberson, F. I., "Soil Mechanics Surface Sampler: Surface Tests, Results, and Analyses," *Surveyor III Mission Report: Part II. Scientific Results,* Technical Report 32-1177, pp. 69–110. Jet Propulsion Laboratory, Pasadena, Calif., June 1, 1967.

9. Scott, R. F., and Roberson, F. I., "Soil Mechanics Surface Sampler," *Surveyor VII Mission Report: Part II. Science Results,* Technical Report 32-1264, pp. 135–185. Jet Propulsion Laboratory, Pasadena, Calif., Mar. 15, 1968.

10. Scott, R. F., and Roberson, F. I., "Soil Mechanics Surface Sampler," *Surveyor Project Final Report: Part II. Science Results,* Technical Report 32-1265, pp. 195–207. Jet Propulsion Laboratory, Pasadena, Calif., June 15, 1968.

11. Gault, D. E., et al., "Lunar Theory and Processes," *Surveyor VII Mission Report: Part II. Science Results,* Technical Report 32-1264, pp. 267–313. Jet Propulsion Laboratory, Pasadena, Calif., Mar. 15, 1968.

Lunar Soil Coefficient of Friction Determined From *Surveyor* Data and Laboratory Tests

R. Choate
Jet Propulsion Laboratory
Pasadena, California

I. Introduction

The *Surveyor* data showed that many of the physical properties of the lunar soil were similar at each of the five *Surveyor* landing sites (Refs. 1–6).

A series of laboratory tests on simulated soils was conducted to evaluate some of these physical properties. Using soils similar to lunar soil composition, particle size distribution, and cohesion as determined from the *Surveyor* mission, the coefficient of friction and bulk density were evaluated by reproducing soils with the same force vs penetration characteristics as demonstrated at the *Surveyor* landing sites. The determination of soil coefficient of friction is presented in this paper; the soil density is treated separately in the previous paper[1] of this report.

[1]Choate, R., "Lunar Soil Bulk Density as Determined From *Surveyor* Data and Laboratory Tests."

II. Equipment Description

The tests for coefficient of friction were performed in association with bearing strength vs penetration tests of simulated lunar soils with different bulk densities, compositions, size distributions, and values of cohesion.[1] To correlate test results, much of the same equipment and the basalt soils in the same physical states were used in both series of tests.

Soil container size (45.7-cm diameter by 35.6-cm depth[2]) was controlled by the need for a soil sample large enough to eliminate or minimize bottom and sidewall effects and by the need for a sample small enough

[2]Values are given in cm-g-s units; to convert to ft-lb-s units, the following factors apply: 1 cm = 0.394 in., 1N (newton) = 10^5 dyn = 0.225 lb, 1N/cm^2 = 1.45 lb/in.^{2}, and 1 μ (micron) = 1.0×10^{-4} cm = 3.94×10^{-5} in.

for two men to be able to handle and run several tests per day. Container volume was 0.0579 m^3.

Loading surfaces used for the friction tests were 15.2- and 7.6-cm diameter cylinders. These dimensions are one-half and one-fourth the scale of the maximum diameter of the *Surveyor* footpad. Effects of roughness of the sliding surface were evaluated by using three different surfaces: (1) a smooth surface of machined aluminum, (2) a fine rough surface of silicon carbide 360-A, and (3) a coarse rough surface of garnet 60.

Normal load was increased on the test cylinders by adding dead weights in multiples of 111 N through the range from 111 to 666 N for the 15.2-cm diameter cylinder and 27.8 N in the range from 27.8 to 167 N for the 7.6-cm diameter cylinder.

The horizontal pull load (force of friction) was applied by the mechanism shown in Fig. 1. This mechanism was originally designed as a penetrometer for performing bearing strength tests of the soil. Direction of force was changed by reversing the motor current to the drive mechanism and by adding a single pulley to the system below the lead-screw housing. Piano wire, attached to the lead-screw housing and guided around a 90-deg turn by the single pulley, was connected to the soil loading cylinder at a movable collar. Between the soil loading cylinder and the single pulley, the pull-wire passed through a narrow vertical slit in the container wall.

Continuous curves of force of friction vs displacement were recorded on an X–Y recorder. Displacement was measured by the potentiometer and load by the strain-gage bridge shown in Fig. 1. Forces on the entire lead-screw support system were restricted to the vertical direction by four thin-wall flexures (Fig. 1).

III. Test Results and Discussion

Seventy tests were performed in evaluating the effective coefficient of friction of basalt soils in three size distributions and various packing densities and values

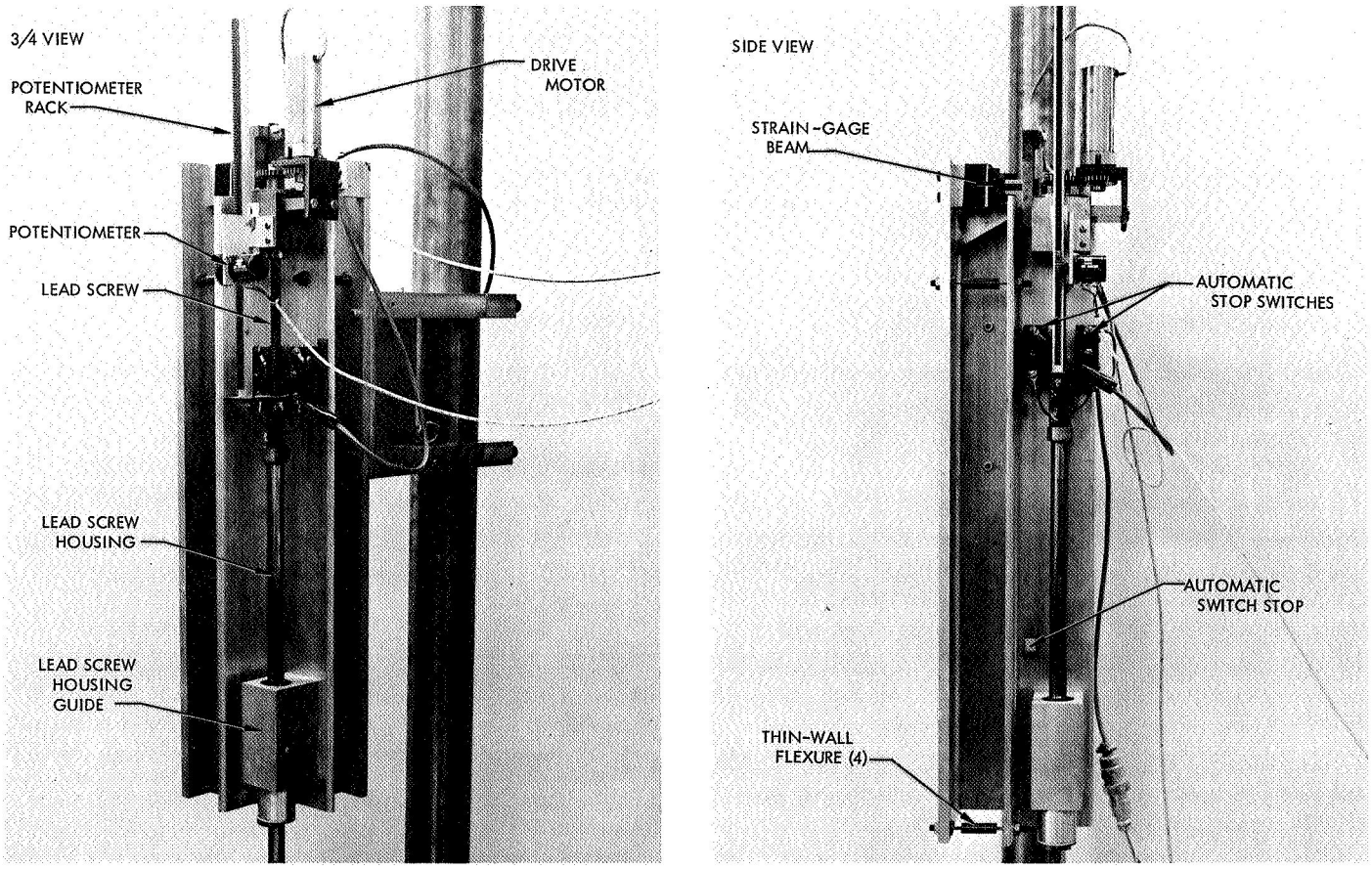

PENETROMETER

Fig. 1. Specially designed mechanism used for performing coefficient of friction tests

of cohesion. From these tests, the associated bearing strength tests, and the *Surveyor* penetration data, a probable curve was selected that showed lunar soil coefficient of friction vs distance of sliding. (The bearing strength, relative density, and cohesion data are shown for each test in Figs. 3a and 4a of the previous paper.[3])

Force of friction vs distance of sliding data for all tests are shown in Figs. 2–7. The values for effective coefficient of friction μ_e vs distance of sliding are shown in Figs. 8–13 (effective coefficient of friction includes the lateral resistance offered to an object "plowing" through the soil after sinkage as well as the frictional resistance offered at the interface of the soil and the sliding object).

A. Effects of Surface Roughness and Penetrometer Size

The first tests performed were to evaluate the effects of surface roughness and cylinder size on densely packed soils. Tests 1 through 14, with the 15.2-cm diameter cylinder, were to evaluate μ_e for a very smooth surface of machined aluminum, a finely roughened surface, and a very coarse surface. As shown in Fig. 11a, the μ_e values for these three surfaces after initial movement are 0.52, 0.58, and 0.62, respectively. For the machined aluminum surface, sliding occurred along the soil-aluminum interface; whereas, for both roughened surfaces, cavities in the surfaces filled with soil, and sliding occurred primarily along a soil-to-soil interface.

From these tests, it was decided to adopt the finely roughened silicon carbide 360-A surface as the primary standard for the rest of the tests. Results of the subsequent tests can be correlated to a machined aluminum surface by subtracting about 0.05 from the results obtained for silicon carbide 360-A surfaces. (Such a surface is probably a better standard for correlation to lunar tests than the smooth, machined aluminum surface. For example, *Surveyor* footpads, though made of aluminum, had roughened surfaces because of their honeycomb construction.)

Comparison of roughness effects were also performed using densely packed, 55-μ basalt with a 7.6-cm diameter cylinder. As shown in Fig. 8b, the μ_e values were 0.56 and 0.61 for machined aluminum and silicon carbide 360-A, respectively; difference in μ_e was 0.05.

In tests 20–29, the 7.6- and 15.2-cm diameter cylinders were used in densely packed 35-μ basalt. The values of μ_e for both cylinder sizes were identical, as shown in Fig. 8b. These results correlate with behavior of solid-on-solid sliding surfaces, where μ_e is known to be independent of surface area.

B. Bearing Strength vs Penetration Tests in Basalt

Tests with the same three size ranges of crushed basalt used in these coefficient of friction tests were also used in the series of bearing strength vs penetration tests to evaluate the state of packing, or bulk density, of lunar soil based on *Surveyor* penetration data. For the 12-, 55-, and 170-μ crushed basalt soils, the force vs penetration tests were performed with a 7.6- and 15.2-cm diameter plate in different states of packing, with relative densities of about 5, 30, 60, and 90–100%. Some intermediate packing densities also were selected to match more closely the penetration curves obtained during *Surveyor* footpad and surface sampler penetrations. The force vs penetration curves for these three soils, along with *Surveyor* penetration data, are shown in Fig. 6 of the previous paper by Choate. From these curves, the best matches with *Surveyor* penetration data, at approximately 4-cm depth, occur at bulk densities of 1.66 g/cm^3 (16% relative density) for 170-μ basalt, 1.49 g/cm^3 (18% relative density) for 55-μ basalt, and 1.34 g/cm^3 (52% relative density) for 12-μ basalt.

C. Coefficient of Friction

1. Laboratory tests. Relative densities used for μ_e measurements were 12, 30, and 100% for 170-μ basalt, 14, 30, 64, and 100% for 55-μ basalt, and 29, 48, 62, and 100% for 12-μ basalt.

Continuous recordings of the force of friction vs distance of sliding for each soil at each state of packing (relative density) are shown in Figs. 4–7. From these continuous curves, the values for the effective coefficient of friction μ_e vs distance of sliding were calculated at increments of 2.54 cm (see Table 1 and Figs. 8–11).

As shown in Figs. 8–11, there is little variation in the values of μ_e for any of the densely packed soils at the different normal pressures applied. However, for any of the loosely packed soils, the values of μ_e may vary by as much as 20% in the range of normal pressures applied.

[3]See footnote 1.

For each set of curves in Figs. 8–11, an average curve has been calculated and is shown in Fig. 12. In this figure, curves are also given for μ_e vs distance of sliding that would best fit the *Surveyor* penetration data, assuming that lunar soil had the particle size distribution of each of the test basalt soils.

As shown in Fig. 12, the three different size ranges of crushed basalt soils demonstrate marked similarities in the behavior of μ_e, as the state of packing ranges from dense to loose. For all three densely packed basalt soils, there is a very small range in μ_e for all values of normal pressure; the final μ_e is only slightly larger than the μ_e at initial displacement. However, in each subsequent series of test for each basalt soil, progressing from dense through loose packing, there occurs:

(1) A progressively wider range in values of μ_e for different normal pressures in any series of tests.

(2) Larger horizontal displacements before a constant μ_e is approached.

(3) A tendency for the most stable loadings (i.e., the lowest normal pressures, 0.64 and 1.22 N/cm^2) to approach constant μ_e more quickly and to have the lowest values of μ_e.

The greatest range in μ_e for any series of tests was with the 12-μ basalt with 29% relative density. In these tests, the most unstable conditions were encountered; the test cylinder tended to overturn and to dig continually deeper into the soil. A more stable test bed, say with a rigid three-legged structure (for example, a *Surveyor* spacecraft), should have a somewhat lower μ_e than indicated for this series of tests.

The three *Surveyor* best fit curves of Fig. 12 are shown in Fig. 13 for the 170-μ, 55-μ, and 12-μ basalt soils. With the μ_e curves for assumed lunar soils having these mean particle sizes, it is then possible to draw a curve for a soil with a mean particle size of 30–35 μ that best fits the *Surveyor* data based on soil reflectivity and cohesion characteristics.

A relatively narrow range of μ_e values exists for the three crushed basalt soils, which almost certainly brackets the size range of most lunar soils. At initial displacement, the μ_e values for the three soils range only from 0.31 to 0.36. After 15 cm of displacement, the μ_e values range from 0.81 for 170-μ basalt to 0.98 for 12-μ basalt. However, most of the *Surveyor* data indicates that the 55-μ basalt with a μ_e of 0.92 is probably a reasonable upper limit for the lunar soil size distribution.

The curve for a lunar soil with probable mean particle size of 30–35 μ of Fig. 13 thus provides μ_e with values of 0.35 at initial displacement, 0.72 at 2.5-cm displacement, 0.89 at 7.6-cm displacement, and 0.95 at 15.2-cm displacement. Tolerance for the above values is estimated to be ± 0.05.

2. Measurements from Surveyor data. During the *Surveyor V* mission, estimates of the lunar soil coefficient of friction were made by two different methods (Ref. 3). During landing on the inner slope of a small crater, the spacecraft slid downslope for 81 cm, digging a trench from 5- to 10-cm deep (Fig. 14). Effective coefficient of friction estimated from this slide was

$$\mu_e = \frac{\overline{F}_x}{F_n} = \frac{\overline{F}_x}{Mg} \cos\theta = 0.73$$

where

M = spacecraft mass

g = lunar gravity

θ = surface slope angle = 20 deg

$\overline{F}_x$ = constant stopping force

$$= M\left(g \sin\theta + \frac{2x_f}{t_f^2}\right) = 330 \text{ N}$$

with x as the spacecraft motion along the slope, and x_f and t_f as final distance and final time, respectively. A minimum value for $\mu_e = 0.36$ was obtained from $\mu_{\min} = \tan 20$ deg for the spacecraft at rest on a 20-deg slope.

The second method of estimating μ_e was from observations of the 11-cm downslope slide by the sensor head of the alpha scattering instrument when the vernier engines were fired for 0.55 s (Fig. 15). Upper and lower bounds for the coefficient of friction, as determined from the

sensor head, were 0.59 and 1.38, respectively. However, by assuming reasonable values for the duration of sliding to be 0.3–0.4 s, then the μ_e bounds became 1.10 and 0.84, respectively (Ref. 3).

D. Soil Failure Characteristics

Some information on the mean particle size of the lunar soil probably can be obtained from comparison of soil failure characteristics observed in the *Surveyor* pictures and in the laboratory coefficient of friction tests.

Figures 16 through 20 are pictures taken by the spacecraft television camera during the five *Surveyor* landings. Figure 16 shows footpad 3 and soil ejecta for *Surveyors I, V, VI,* and *VII*; Fig. 17 shows footpad 2 and ejecta for both the initial landing and the hop made by *Surveyor VI*; Fig. 18 shows the trench dug by the *Surveyor V* footpad 2 during landing on a 19–20-deg slope; and Fig. 19 shows the development of soil failure during the digging of a trench by the surface sampler on *Surveyor III*.

Soil ejected by the footpads in landing was displaced primarily in two ways:

(1) Soil was thrown out in a fairly uniform spray during the initial peak-force impact.

(2) Soil was displaced laterally at a much slower rate of movement into a ridge by sliding of the spacecraft and by outward extension of the footpads during compression of the leg shock absorbers (Fig. 20).

In all cases, much of the ejected soil is in clumps, demonstrating the cohesive nature of the soil.

Generally, the size of soil clumps is dependent on the cohesive properties of a soil. In turn, cohesiveness is dependent, in part, on the particle size of a soil; i.e., under similar conditions, fine soils form clumps more readily than coarse soils. Then, if the cohesion of the lunar soils tested by *Surveyor* is comparable to the basalt soils tested in the laboratory, reasonable conclusions can be made on lunar soil particle size. All lunar probe data thus far indicate that lunar soil cohesion is approximately 0.05–0.10 N/cm^2, and is probably no less than 0.035 and no greater than 0.17 N/cm^2 (Refs. 1–9).

A plot of the cohesion of the basalt soils tested in the laboratory is shown in Fig. 4 of the previous paper[4] in this report. As shown by the averaged curve, cohesion for the basalt soils ranges from 0.05 N/cm for relative densities of 15% to 0.15 N/cm for relative densities of 50%. These cohesion and relative density values for the laboratory tests almost exactly coincide with *Surveyor* data. Best fit for *Surveyor* data ranges from 0.06-N/cm^3 cohesion and 14% relative density for 170-μ basalt to 0.15-N/cm^3 cohesion and 52% relative density for 12-μ basalt.

Figures 21 through 23 show soil beds after those laboratory tests, which were conducted with normal pressures of 0.61 N/cm^2. The 0.61-N/cm^2 level is probably comparable to the pressure levels existing during *Surveyor* footpad extension and sliding processes. Principal interest in the pictures is the progressive increase in size of the soil clumps with decrease in particle size. The 170-μ basalt, as shown especially in Fig. 23c, does not form clumps of sizes comparable to any of the *Surveyor* pictures. The 55-μ basalt of Fig. 23b with relative density of 30% forms soil fragments quite comparable to *Surveyor* pictures; the 55-μ basalt with relative density of 64% (Fig. 22b) tends to form few fragments and the soil appears more granular than lunar soil. In contrast, the 12-μ basalt tends to deform more plastically and to form many fragments larger than those observed in *Surveyor* pictures.

Figure 24 shows failure characteristics with higher normal pressures. The higher pressures generally did not seem to have influenced the size of fragments formed in the three soil size ranges. In Fig. 24b, however, the 12-μ basalt in the densely packed state tends to form large crust-like fragments that compare with the fragments formed by the *Surveyor III* surface sampler during digging of the trench (Fig. 19). In general, the 12-μ basalt formed fragments more consistently than those formed by *Surveyor* operations. Figure 25 shows the three basalt soils with normal pressures of 0.61 N/cm^2 and with relative densities that most closely matched *Surveyor* bearing strength vs penetration data.

In general, sizes of fragments formed during the laboratory tests indicate that the lunar soil probably is not finer than the 12-μ basalt, probably not coarser than the 55-μ basalt, but falls between these two sizes.

[4]See footnote 1.

Table 1. Values derived from laboratory tests on basalt soils

Test	Basalt mean particle size, μ	Density		Cohesion, N/cm^2	Cylinder diam, cm	Cylinder surface	Normal pressure, N/cm^2	Coefficient of friction at distance of sliding, cm						
		Relative, %	Absolute, g/cm^3					0	2.5	5.1	7.6	10.2	12.7	15.2
1	170	100	2.09	0.7+	15.2	Al	0.61	0.472	0.524	0.520				
2							1.22	0.260	0.526	(0.526)[a]				
3							1.83	0.480	0.533	(0.533)				
4							2.44	0.464	0.518	(0.518)				
5							3.66	0.666	0.518	0.518				
							Av	0.468	0.524	0.523				
6	170	100	2.09	0.7+	15.2	360-A	0.61	0.52	0.59	0.59	0.60	0.58		
7							1.22	0.36	0.58	0.57	0.57	0.56	0.58	
8							1.83	0.50	0.58	0.57	0.56	0.56	0.57	
9							2.44	0.46	0.59					
10							3.66	0.44	0.58					
							Av	0.46	0.58	0.58	0.58	0.57	0.58	
11	170	100	2.09	0.7+	15.2	No. 60	0.61	0.524	0.632	0.636	0.640	0.652		
12							1.22	0.568	0.618	0.636	0.642	0.650		
13							1.83	0.453	0.624	0.617	0.622	0.622		
14							2.44	0.580	0.615	0.615	0.618	0.629		
							Av	0.531	0.623	0.626	0.631	0.638		
15	55	100	1.90	0.53	7.62	Al	0.64	0.505	0.538	0.528	0.513			
16							1.22	0.508	0.528	0.516	0.512			
17							1.83	0.523	0.528	0.522	0.528			
18							2.44	0.512	0.560	0.560	0.568			
19							3.05	0.523	0.661	0.646	0.646			
							Av	0.515	0.564	0.555	0.554			
20	55	100	1.90	0.53	7.62	360-A	0.64	0.585	0.631	0.615	0.600	0.600		
21							1.22	0.600	0.625	0.600	0.568	0.568		
22							1.83	0.598	0.602	0.602	0.576	0.576		
23							2.44	0.569	0.612	0.604	0.580	0.573		
24							3.05	0.616	0.616	0.608	0.602	(0.602)		
							Av	0.594	0.618	0.606	0.586	0.584		

[a]Values in parentheses are extrapolated.

Table 1 (contd)

Test	Basalt mean particle size, μ	Density		Cohesion, N/cm^2	Cylinder diam, cm	Cylinder surface	Normal pressure, N/cm^2	Coefficient of friction at distance of sliding, cm						
		Relative, %	Absolute, g/cm^3					0	2.5	5.1	7.6	10.2	12.7	15.2
25	55	100	1.90	0.53	15.2	360-A	0.61	0.640	0.627	0.612	0.607	0.592	0.624	0.608
26							1.22	0.608	0.610	0.600	0.608	0.590	0.606	0.598
27							1.83	0.605	0.611	0.618	0.606	0.611	0.604	0.614
28							2.44	0.601	0.602	0.616	0.598	0.602	0.594	0.602
29							3.05	0.585	0.594	0.592	0.592	0.587	0.592	0.585
							Av	0.607	0.610	0.606	0.602	0.597	0.604	0.601
30	170	30	1.74	0.09	15.2	360-A	0.61	0.432	0.688	0.680	0.680	0.672	0.688	0.652
31							1.22	0.282	0.634	0.734	0.766	0.776	0.780	0.780
32							1.83	0.257	0.544	0.671	0.723	0.731	0.761	0.781
33							2.44	0.213	0.555	0.747	0.760	0.791	0.816	(0.835)
							Av	0.296	0.605	0.708	0.732	0.743	0.756	0.762
34	170	12	1.65	0.06—	15.2	360-A	0.61	0.352	0.708	0.728	0.744	0.748	0.748	0.748
35							1.22	0.376	0.710	0.740	0.740	0.744	0.764	0.790
36							1.83	0.323	0.668	0.797	0.871	0.891	0.903	(0.955)
37							2.44	0.252	0.528	0.750	0.796	0.808	(0.825)	(0.850)
							Av	0.326	0.654	0.754	0.788	0.798	0.810	0.836
38	55	64	1.72	0.21	15.2	360-A	0.61	0.464	0.629	0.629	0.612	0.633	0.628	0.633
39							1.22	0.420	0.598	0.594	0.602	0.606	(0.605)	(0.605)
40							1.83	0.400	0.600	0.626	0.645	0.625	0.626	0.624
41							2.44	0.413	0.617	0.650	0.650	0.656	0.675	(0.670)
							Av	0.424	0.611	0.624	0.627	0.630	0.634	0.633
42	55	30	1.55	0.13	15.2	360-A	0.61	0.425	0.724	0.748	0.748	0.760	0.755	0.751
43							1.22	0.310	0.622	0.672	0.675	0.695	0.708	0.730
44							1.83	0.360	0.632	0.787	0.794	0.803	0.812	0.820
45							2.44	0.330	0.588	0.743	0.768	0.775	0.802	0.819
							Av	0.356	0.642	0.738	0.746	0.758	0.769	0.780
46	55	14	1.47	0.58	15.2	360-A	0.61	0.384	0.844	0.847	0.864	0.889	0.924	0.992
47							1.22	0.356	0.760	0.905	0.924	0.936	(0.950)	(0.960)
48							1.83	0.290	0.628	0.835	0.885	0.900	(0.910)	(0.920)
							Av	0.343	0.744	0.862	0.894	0.908	0.928	0.957

Table 1 (contd)

Test	Basalt mean particle size, μ	Density		Cohesion, N/cm^2	Cylinder diam, cm	Cylinder surface	Normal pressure, N/cm^2	Coefficient of friction at distance of sliding, cm						
		Relative, %	Absolute, g/cm^3					0	2.5	5.1	7.6	10.2	12.7	15.2
49	12	100	1.57	0.41	15.2	360-A	0.61	0.58	0.71	0.72	0.71	0.72		
50							1.22	0.53	0.69	0.72	0.75			
51							1.83	0.51	0.64	0.65	0.67			
52							2.44	0.45	0.62					
53							3.05	0.48						
54							3.66	0.49						
								Av 0.51	0.67	0.70	0.71	0.72		
55	12	62	1.39	0.25	15.2	360-A	0.61	0.42	0.86	0.91	0.93	0.98	1.00	1.01
56							1.22	0.32	0.70	0.81	0.82	0.84	0.89	(0.90)
57							1.83	0.30	0.65	0.75	0.78	0.82	(0.85)	(0.88)
								Av 0.35	0.74	0.82	0.85	0.88	0.91	0.93
58	12	48	1.32	0.10	15.2	360-A	0.61	0.328	0.824	0.862	0.876	0.888	0.908	0.920
59							1.22	0.269	0.752	0.910	0.972	1.00	1.06	1.09
60							1.83	0.267	0.598	0.757	0.860	1.00	1.05	1.08
								Av 0.295	0.725	0.842	0.902	0.962	1.01	1.03
61	12	29	1.23	0.62	15.2	360-A	0.61	0.433	0.800	0.938	1.12	1.20	1.44	
62							0.61	0.260	0.940	1.12	1.19	1.25	1.35	
63							0.61	0.474	0.967	1.14	1.28	1.35	1.35	
64							0.61	0.340	0.930	1.20	1.35	1.48	1.60	
								Av 0.38	0.91	1.11	1.23	1.32	1.44	
65	12	29	1.23	0.62	15.2	360-A	1.22	0.330	1.00	1.32	1.49	1.58	1.65	
66							1.22	0.330	0.96	1.15	1.27	1.37	1.51	
67							1.22	0.330	0.80	1.07	1.23	1.58	1.65	
								Av 0.33	0.92	1.18	1.33	1.44	1.55	
68	12	29	1.23	0.62	15.2	360-A	1.83	0.257	0.680	0.980	1.18			
69							1.83	0.374	0.773	0.975	1.17			
70							1.83	0.240	0.758	1.04	1.20			
								Av 0.29	0.74	1.00	1.18			

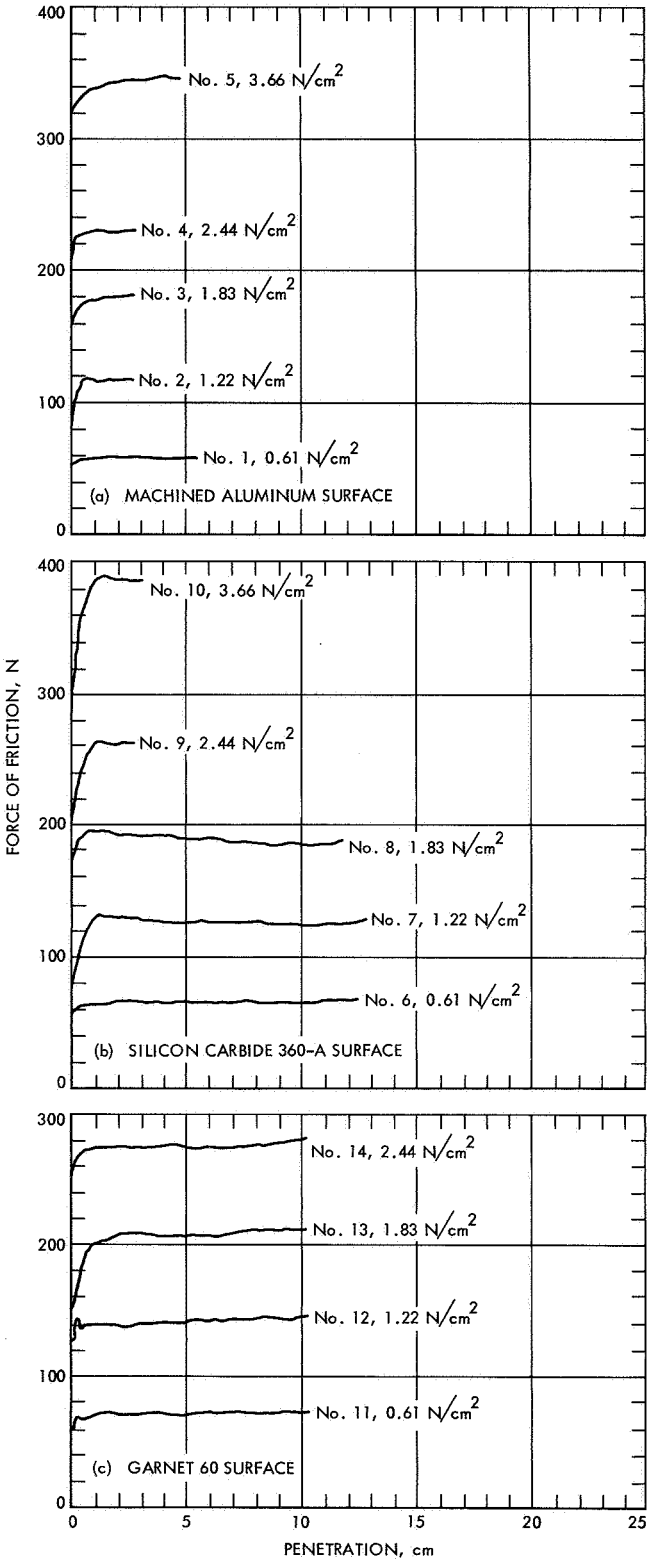

Fig. 2. Force of friction vs displacement curves for densely packed 170-μ basalt (15.2-cm diameter cylinder)

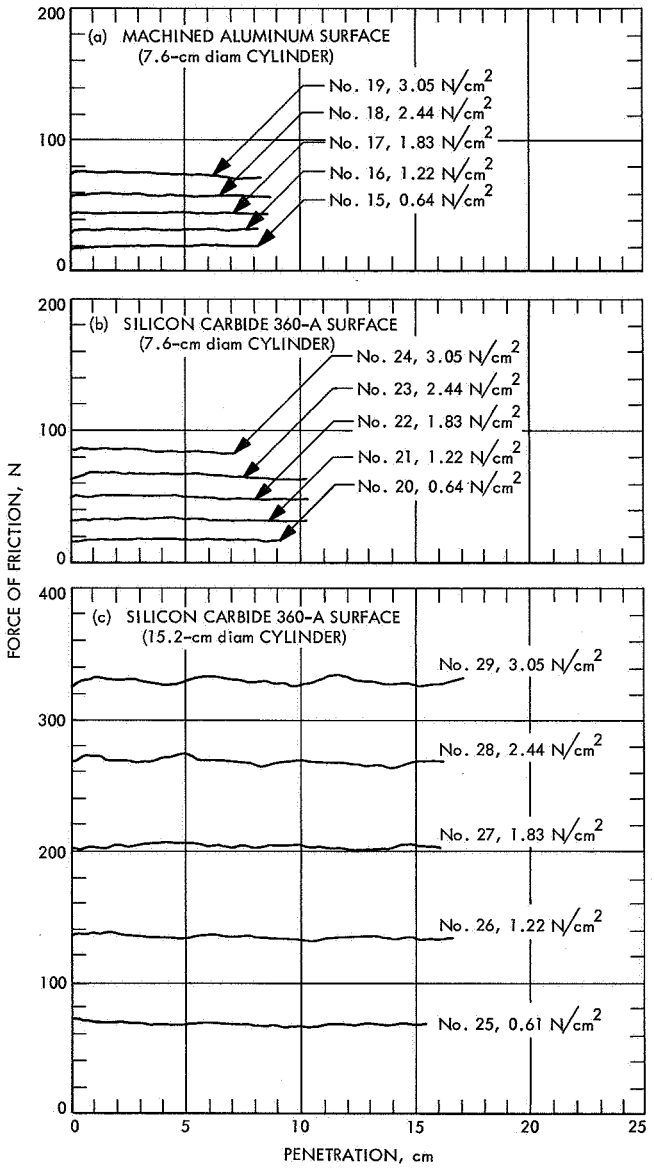

Fig. 3. Force of friction vs displacement curves for densely packed 55-μ basalt

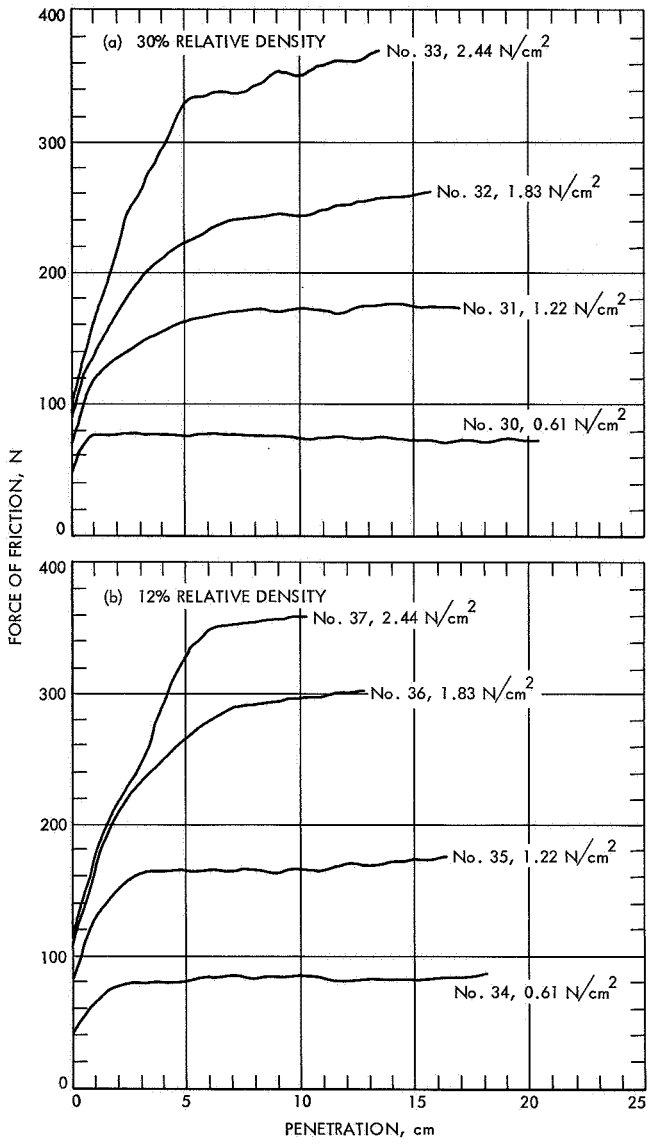

Fig. 4. Force of friction vs displacement curves for 170-μ basalt

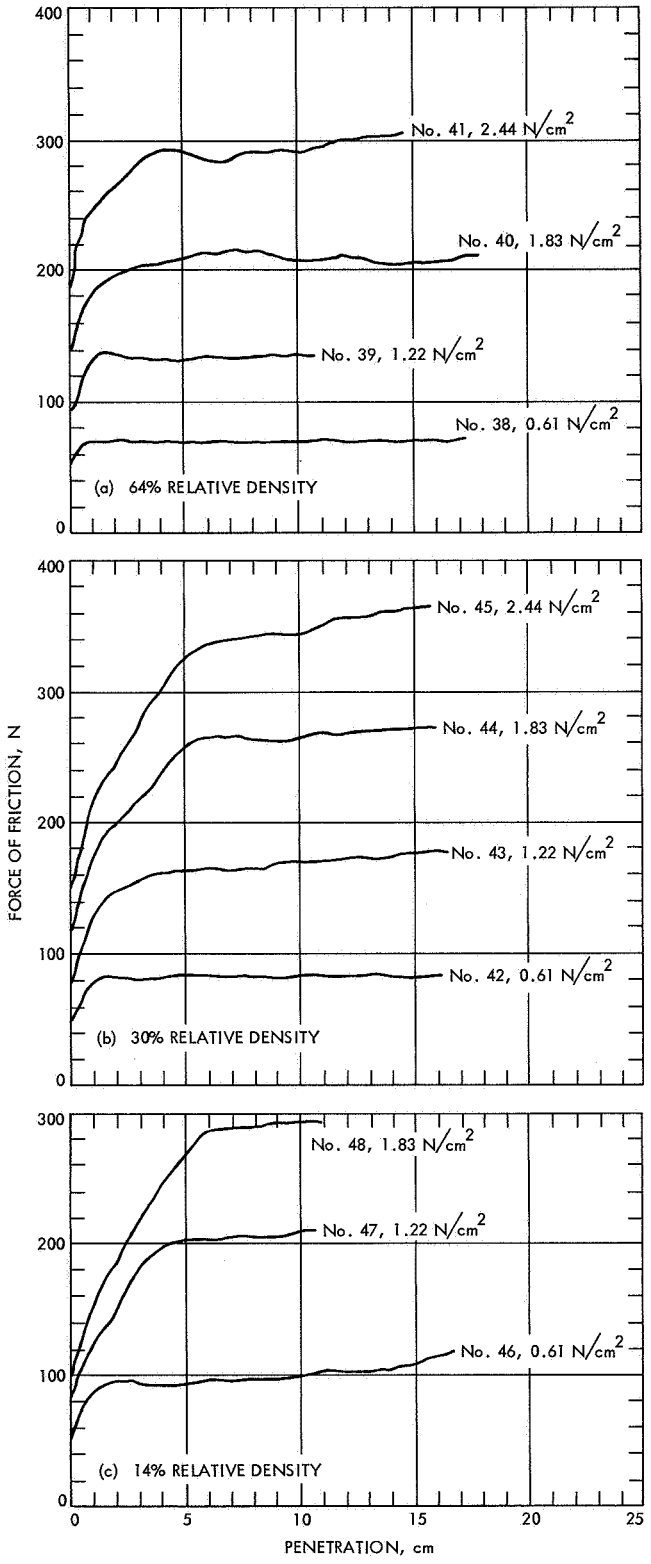

Fig. 5. Force of friction vs displacement curves for 55-μ basalt

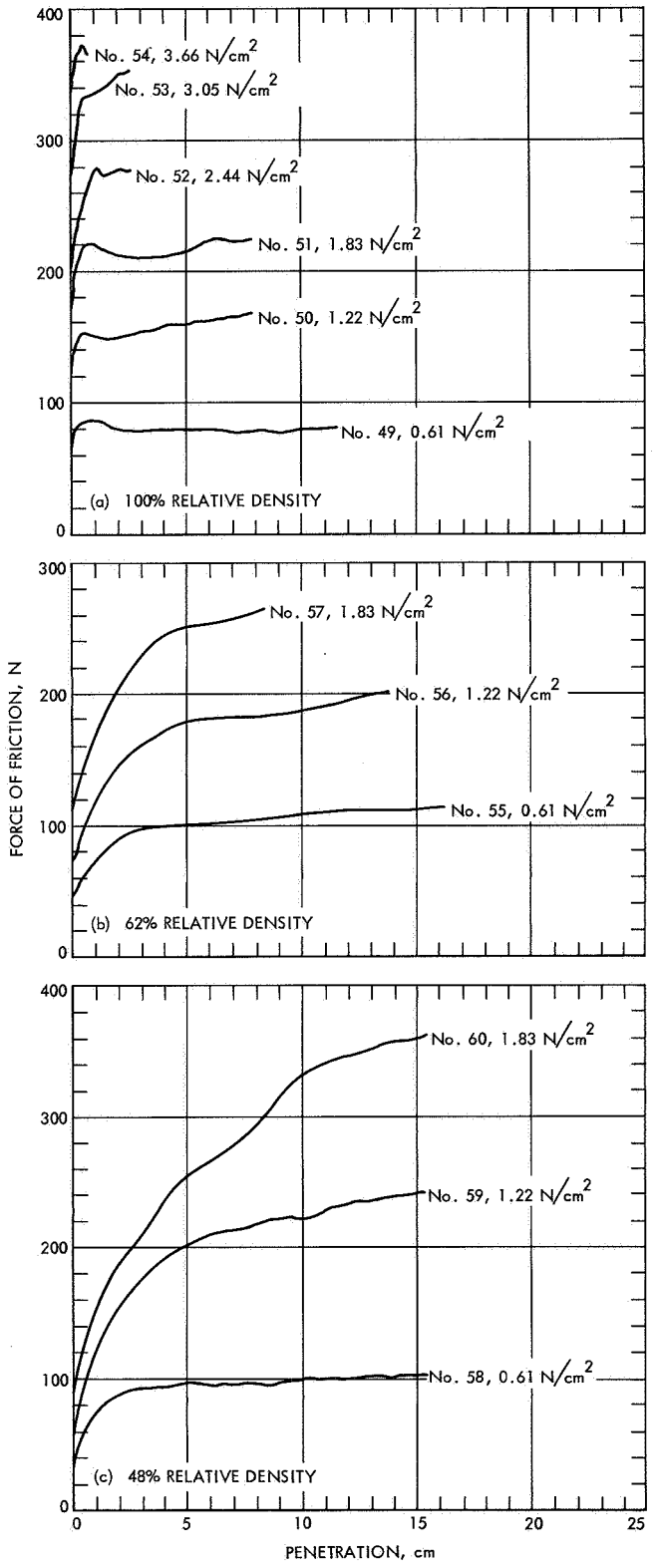

Fig. 6. Force of friction vs displacement curves for 12-μ basalt

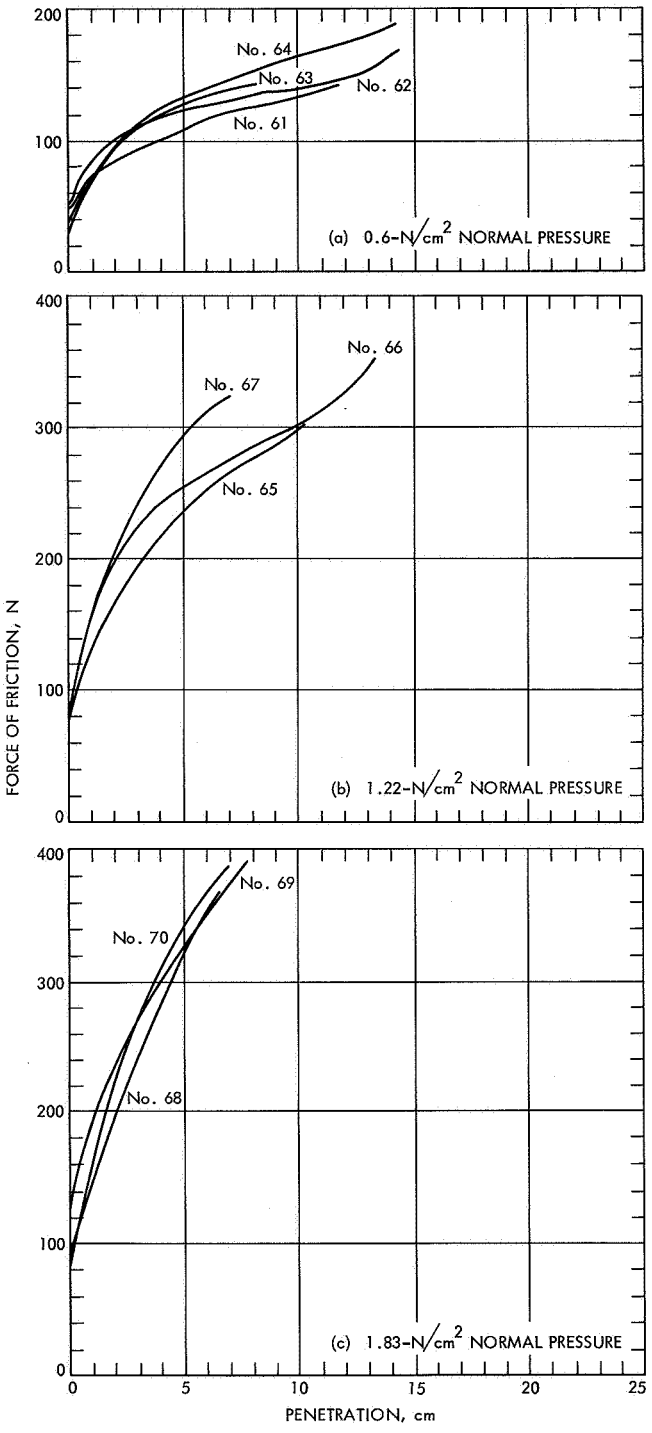

Fig. 7. Force of friction vs displacement curves for 12-μ basalt at 29% relative density

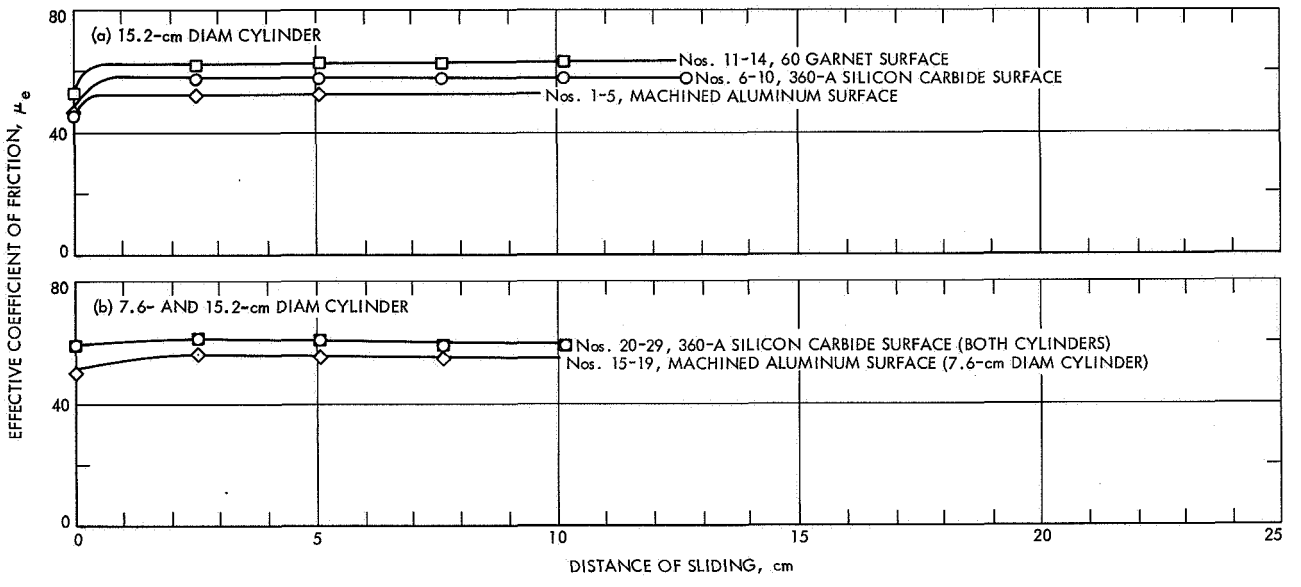

Fig. 8. Coefficient of friction vs displacement curves comparing composition of sliding surfaces

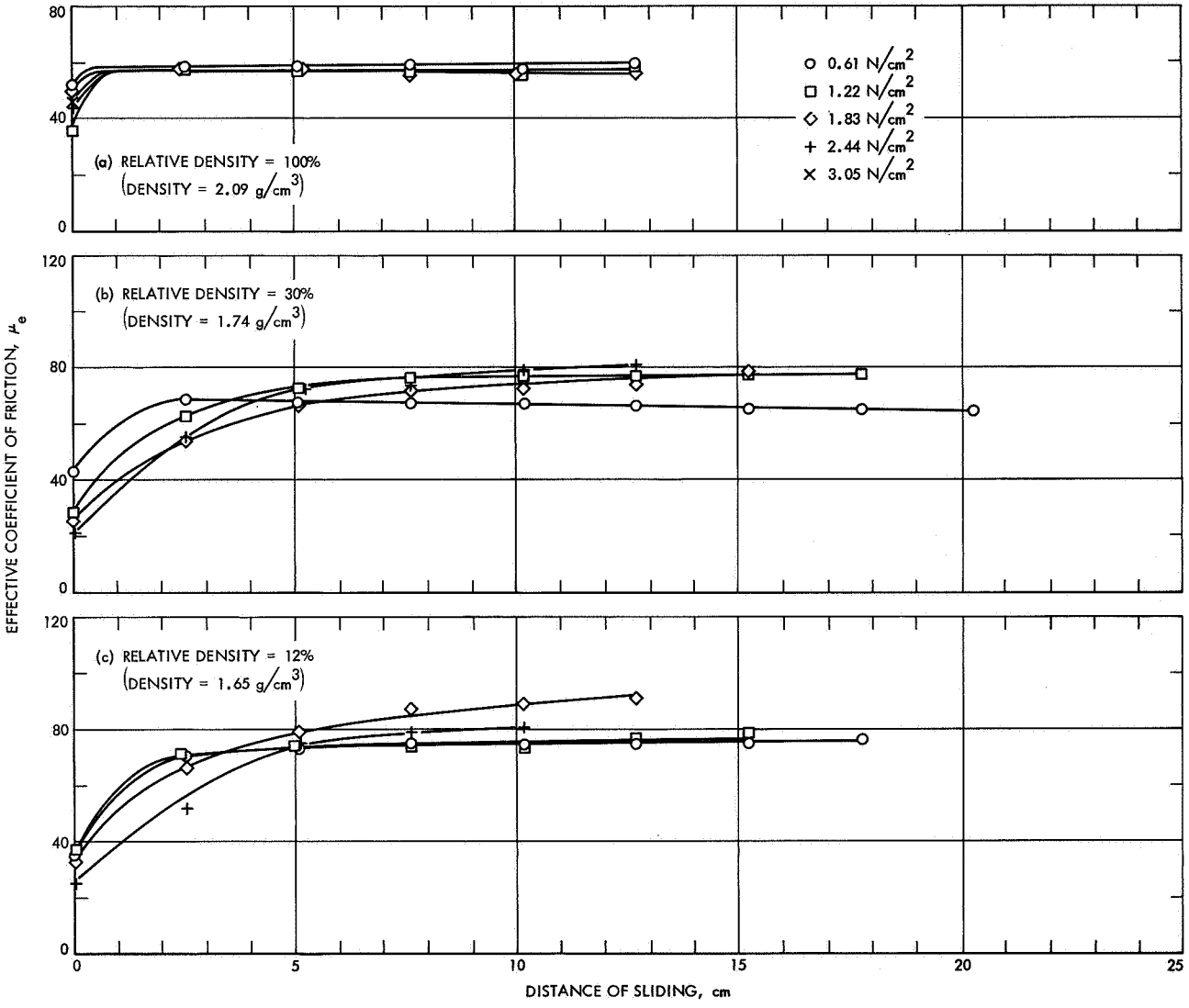

Fig. 9. Coefficient of friction vs displacement curves for 170-μ basalt

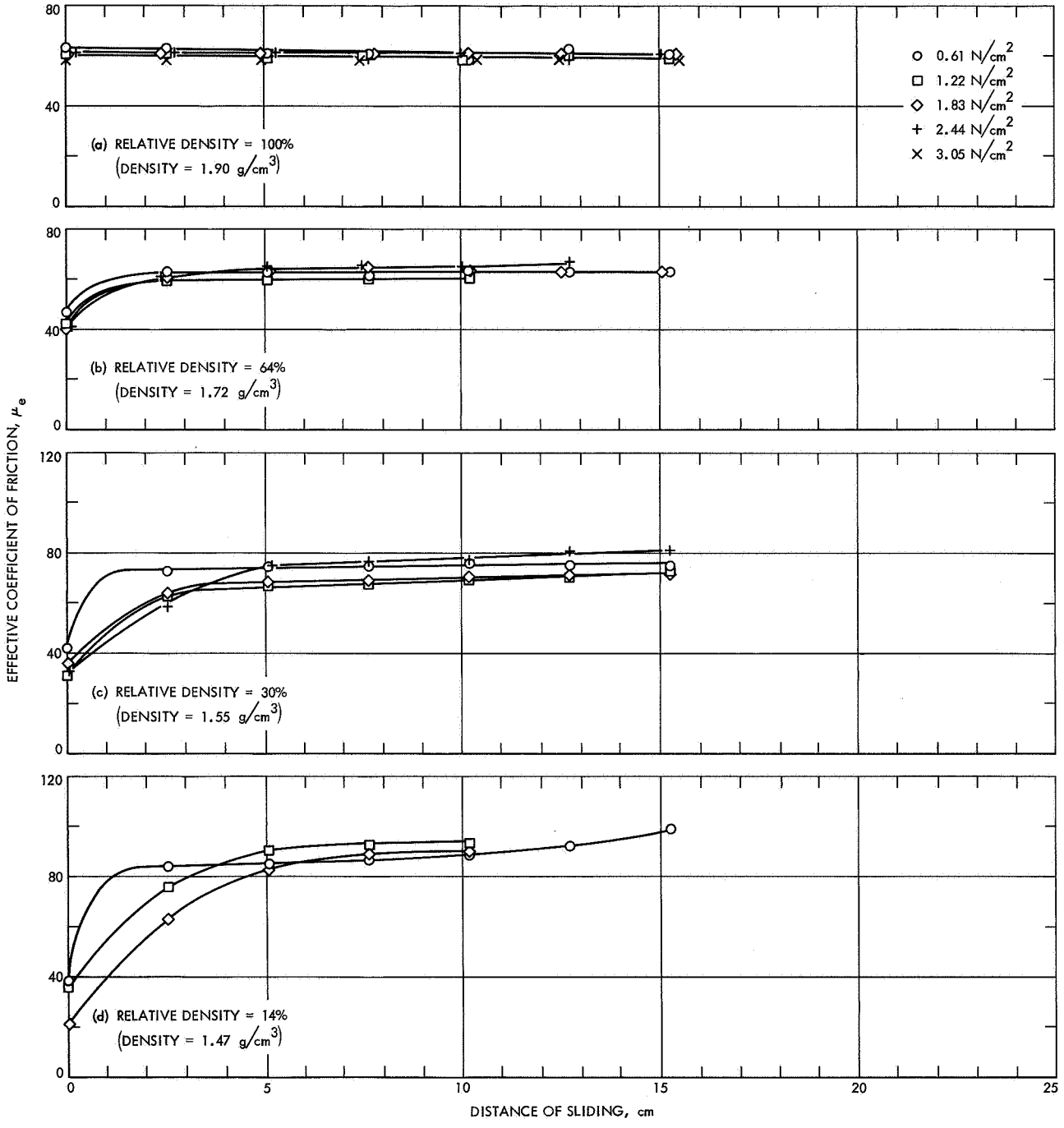

Fig. 10. Coefficient of friction vs displacement curves for 55-μ basalt

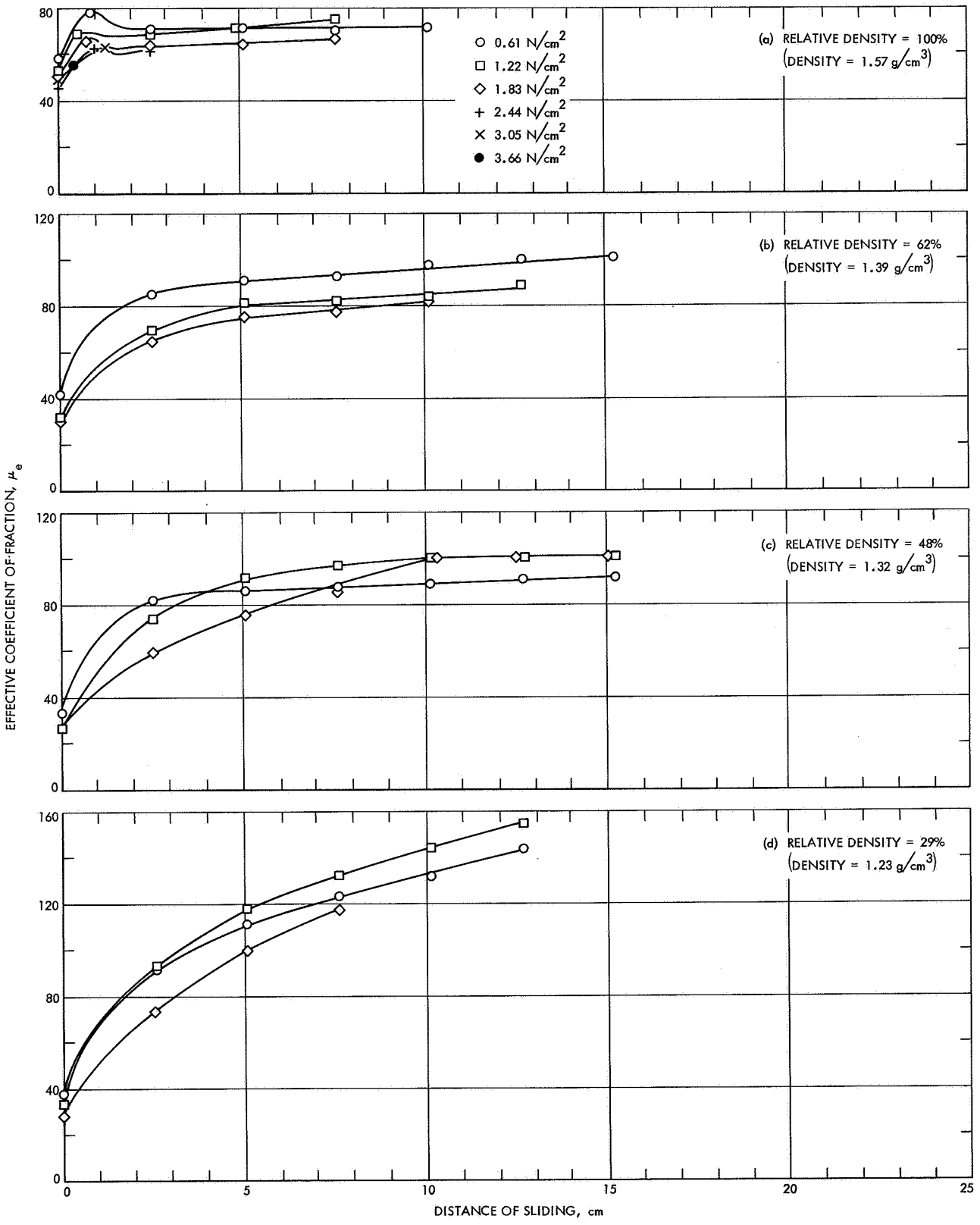

Fig. 11. Coefficient of friction vs displacement curves for 12-μ basalt

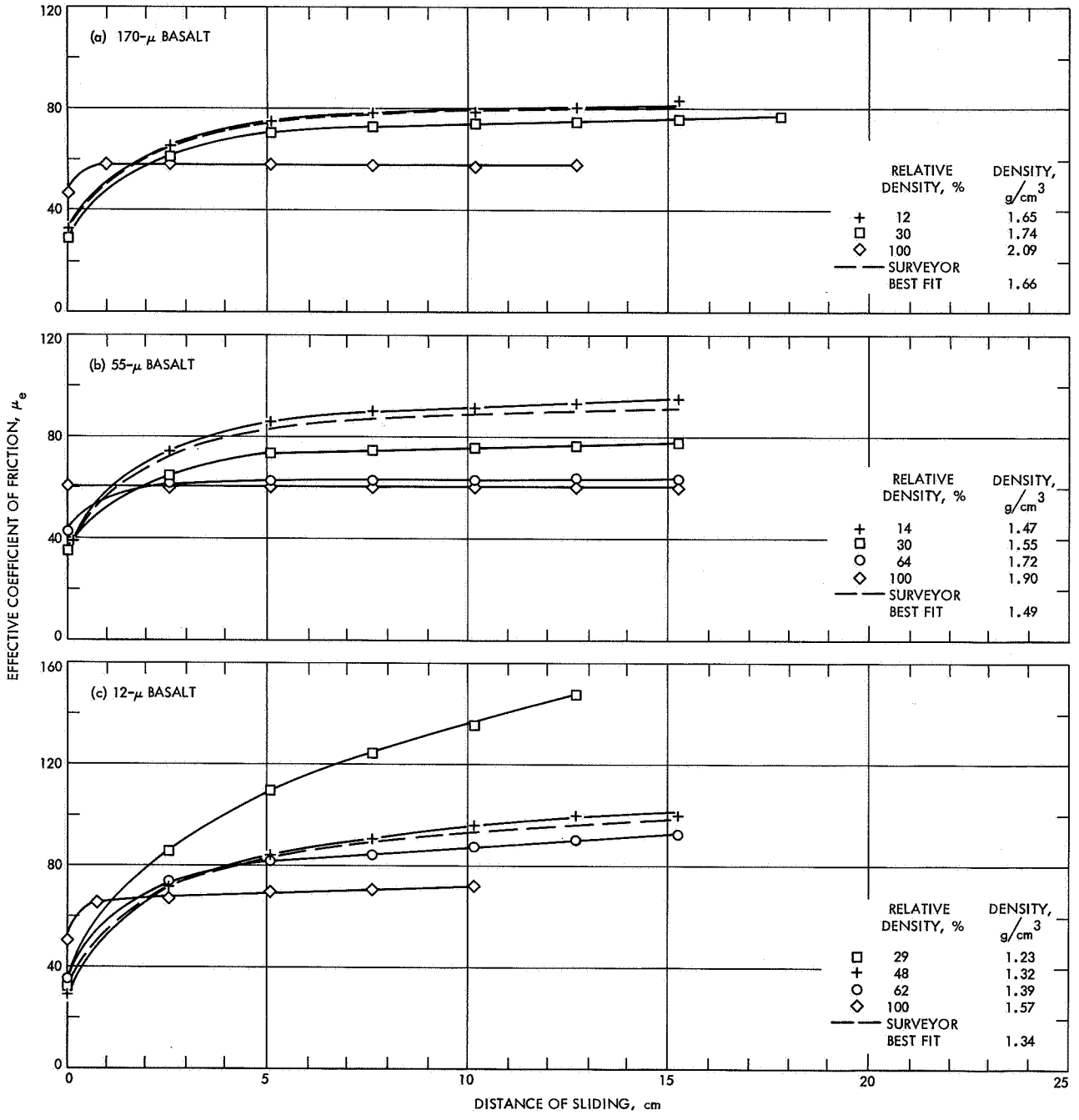

Fig. 12. Average coefficient of friction vs displacement curves

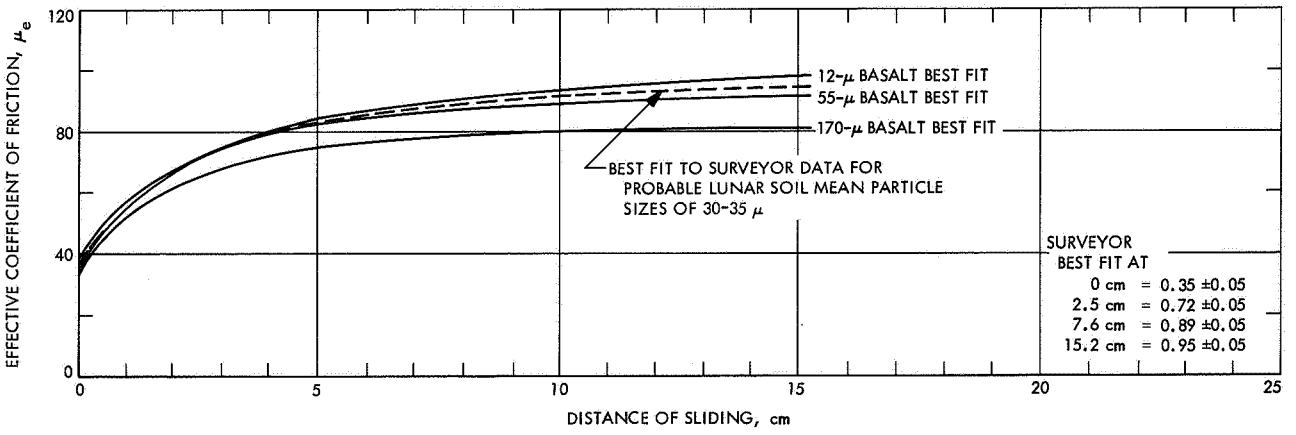

Fig. 13. Basalt soil coefficient of friction curves that best fit *Surveyor* bearing strength data

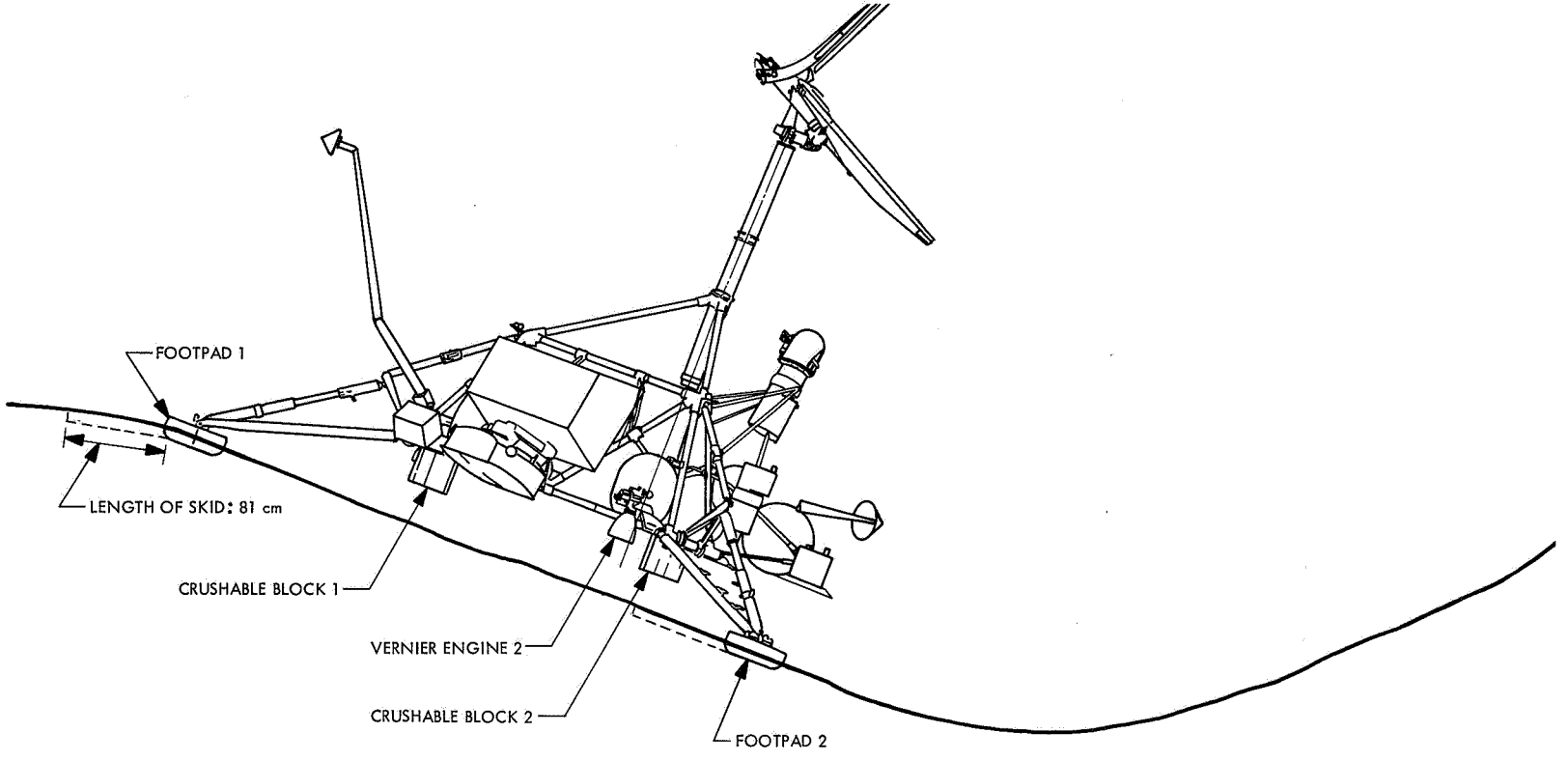

Fig. 14. Profile of *Surveyor V* and the small crater in which it landed

Fig. 15. Annotated mosaics of the *Surveyor VI* alpha scattering instrument area for vernier engine pre-firing and post-firing

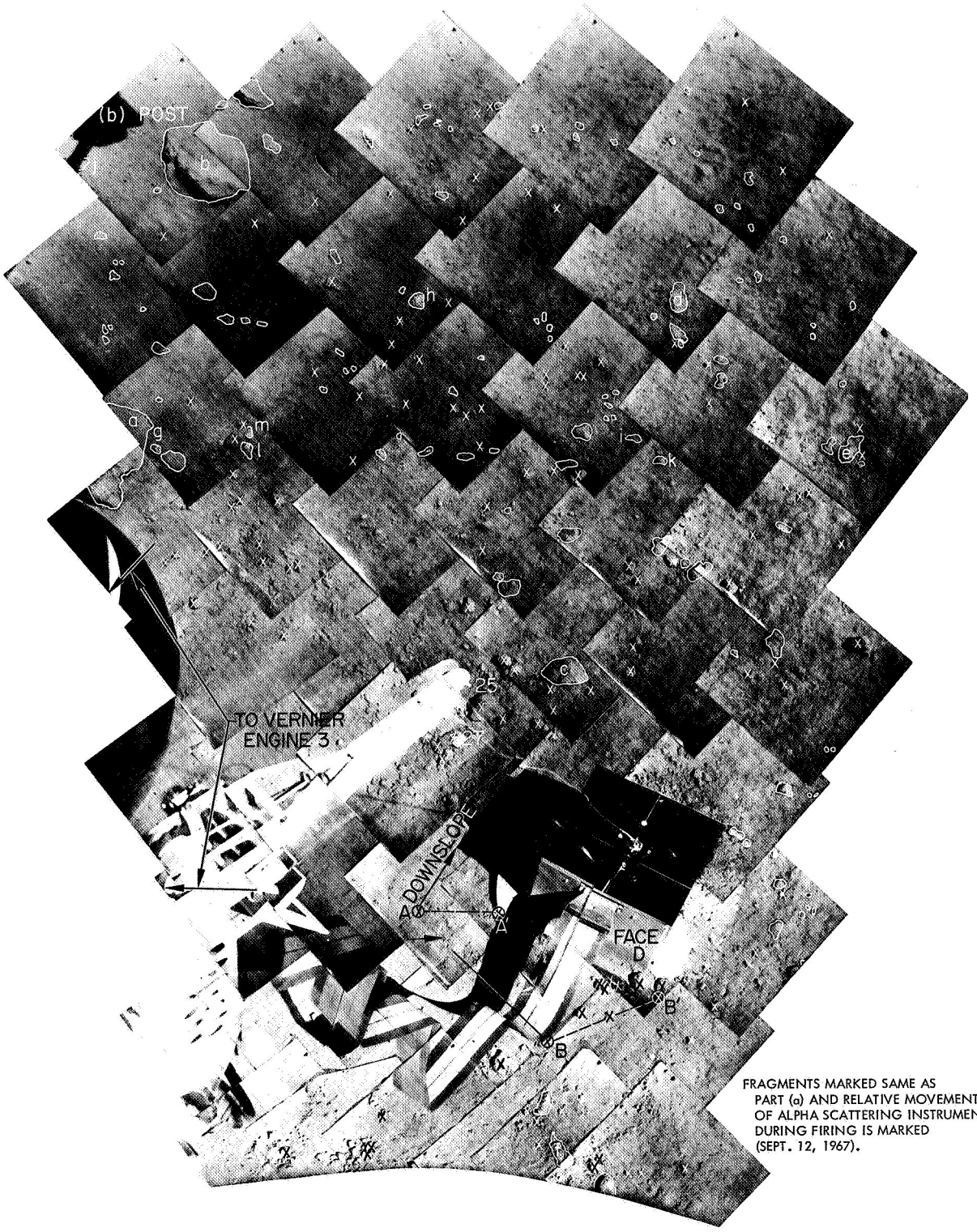

FRAGMENTS MARKED SAME AS PART (a) AND RELATIVE MOVEMENT OF ALPHA SCATTERING INSTRUMENT DURING FIRING IS MARKED (SEPT. 12, 1967).

Fig. 15 (contd)

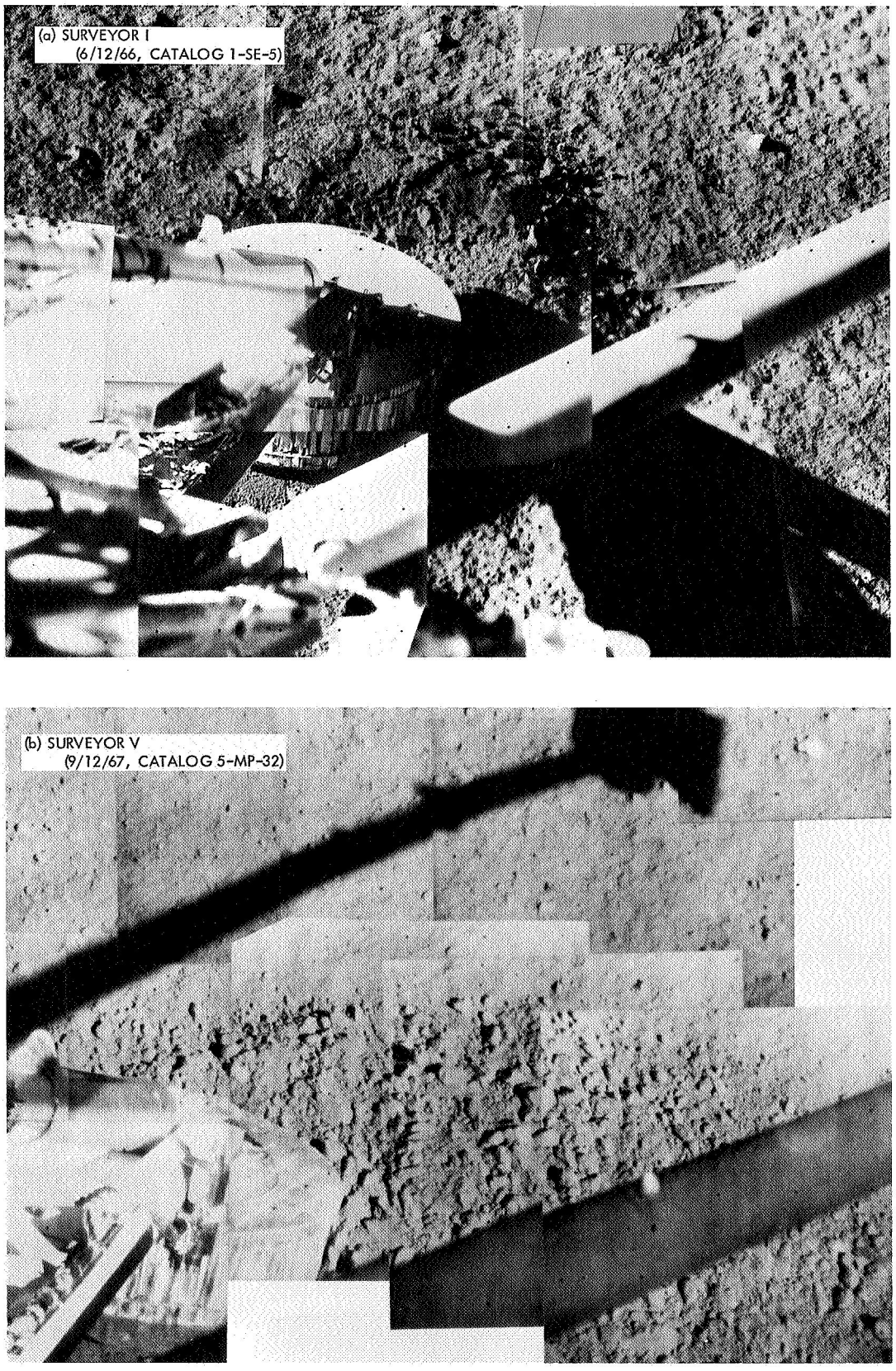

Fig. 16. Pictures of footpad 3 and ejecta for landings of *Surveyors I, V, VI,* and *VII*

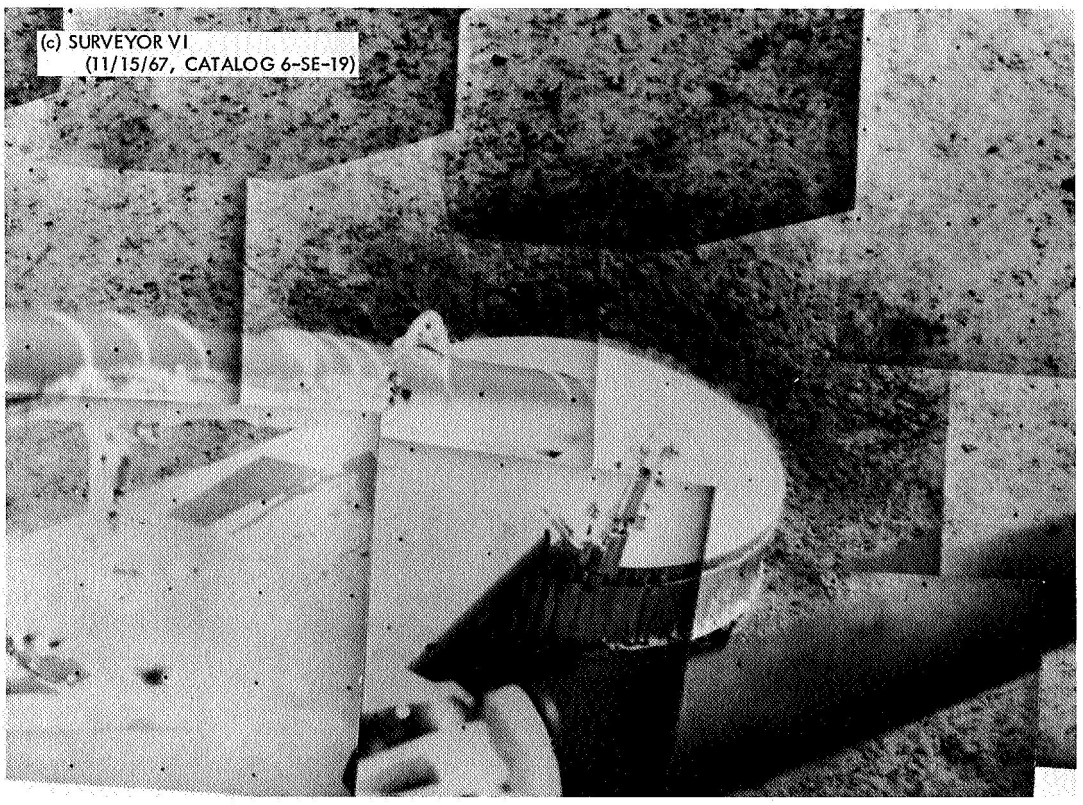
(c) SURVEYOR VI
(11/15/67, CATALOG 6-SE-19)

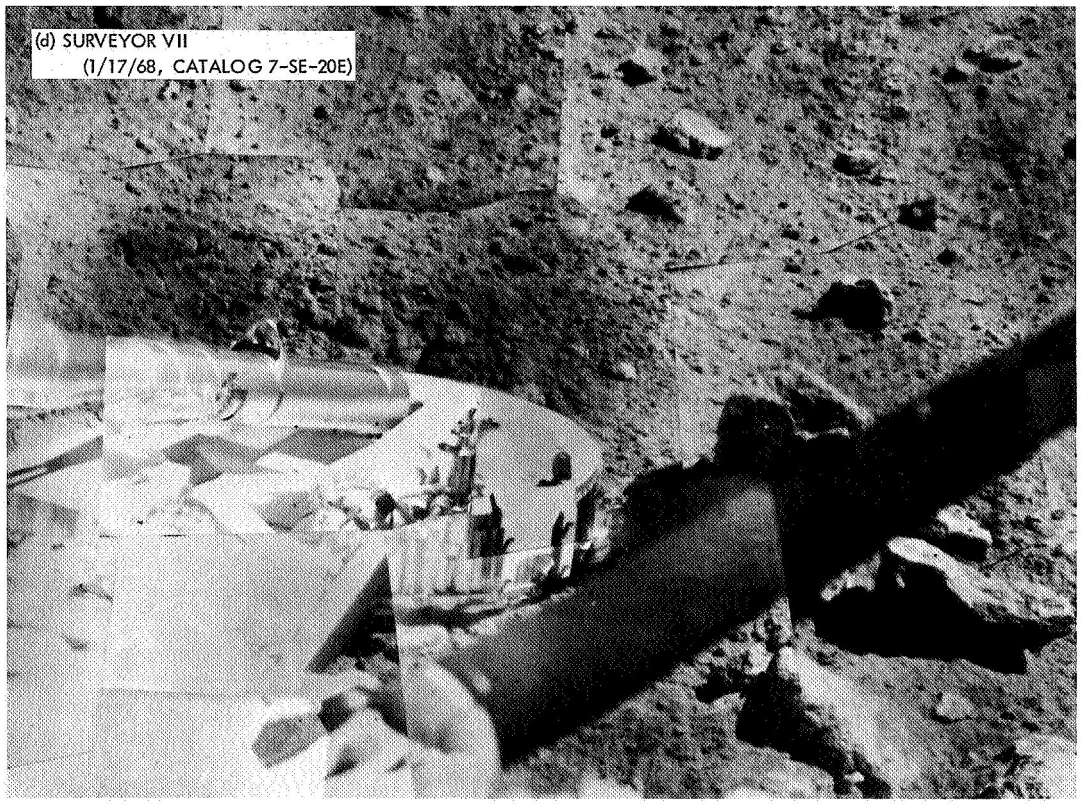
(d) SURVEYOR VII
(1/17/68, CATALOG 7-SE-20E)

Fig. 16 (contd)

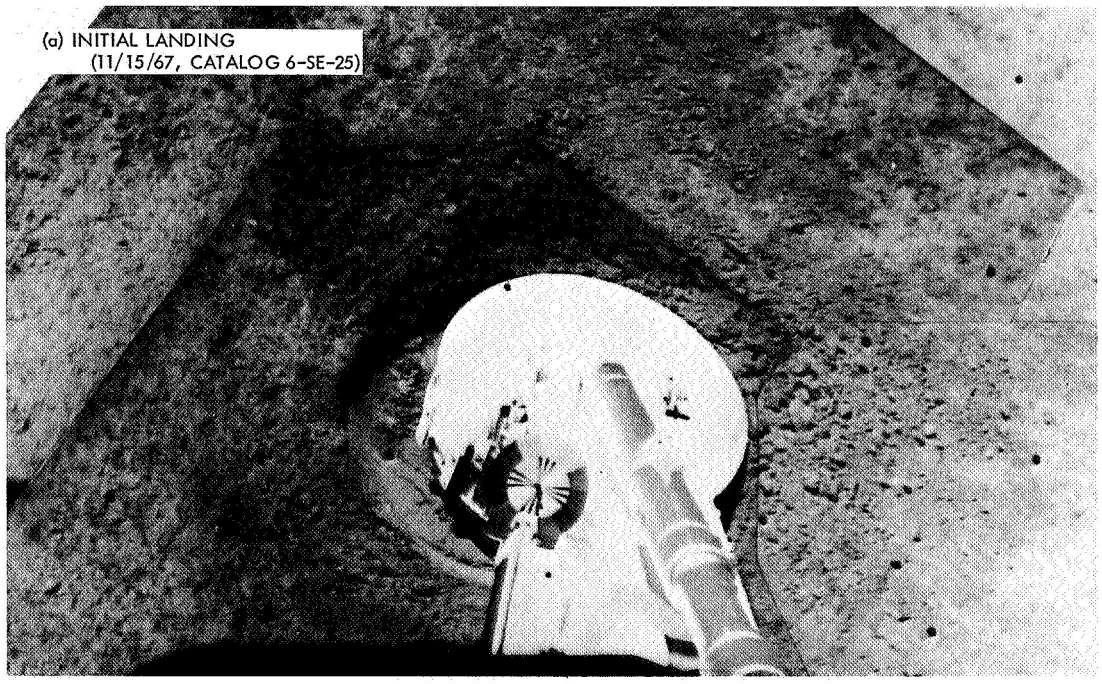

Fig. 17. *Surveyor VI* footpad 2 and ejecta


(b) HOP LANDING
(11/17/67, CATALOG 6-SE-9)

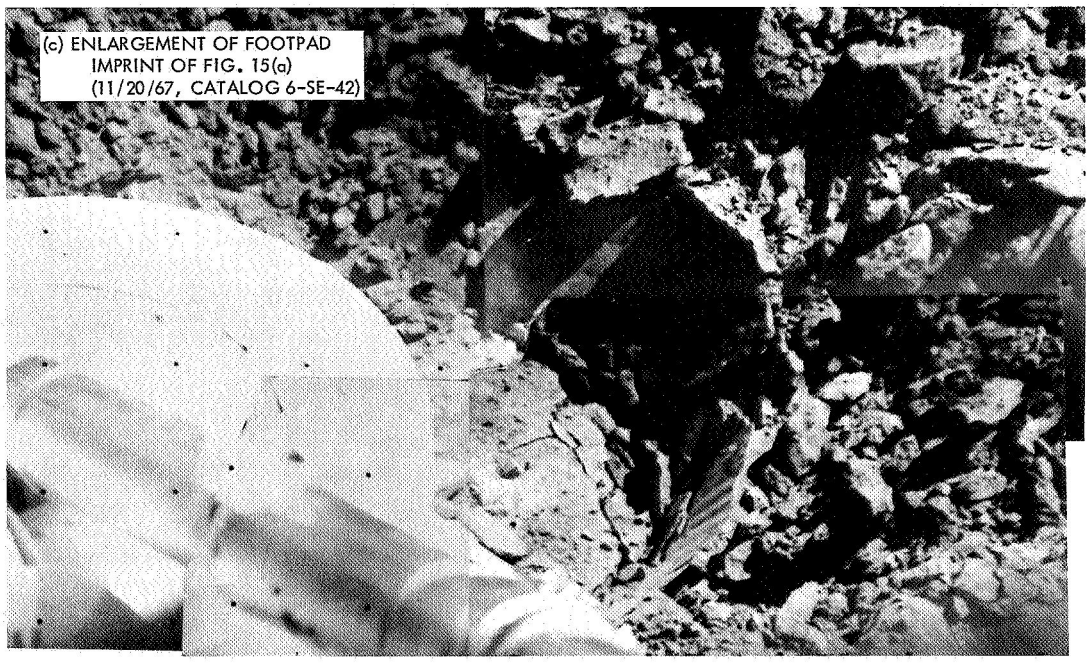
(c) ENLARGEMENT OF FOOTPAD
IMPRINT OF FIG. 15(a)
(11/20/67, CATALOG 6-SE-42)

Fig. 17 (contd)

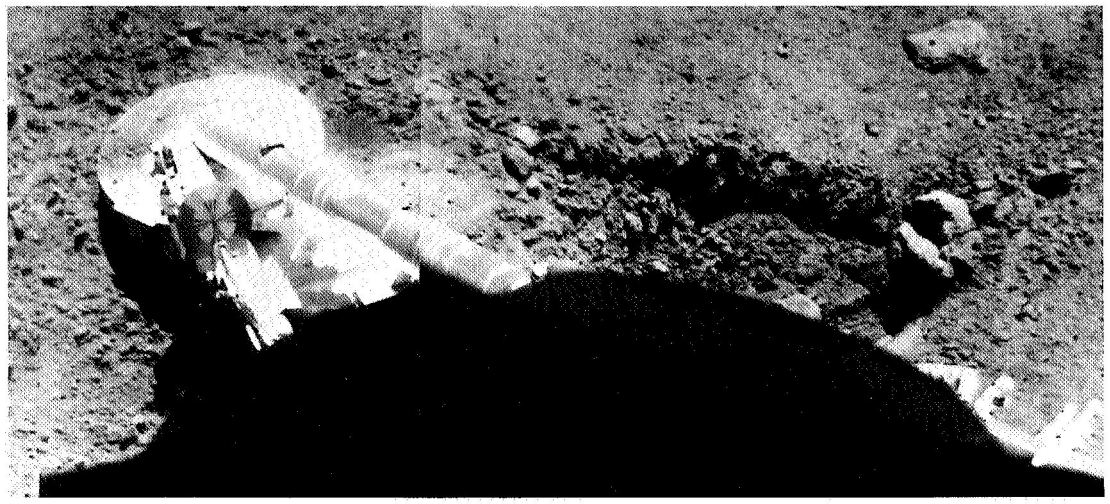

Fig. 18. Trench dug by *Surveyor V* footpad 2 (9/14/67, Catalog 5-MP-19)

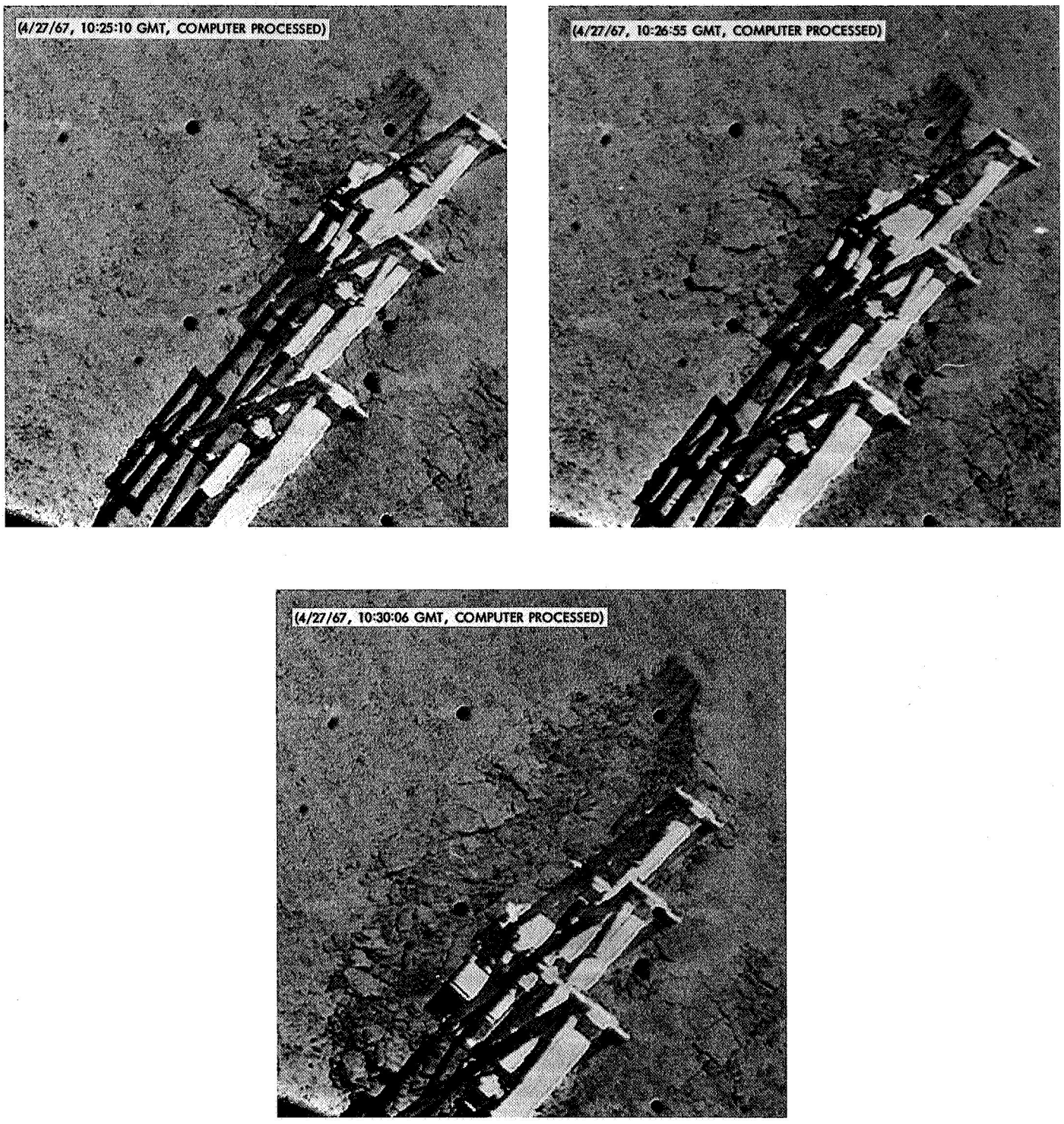

Fig. 19. Sequence of pictures showing progressive soil failure patterns during digging of trench by the surface sampler on *Surveyor III*

(a) SHOCK ABSORBER EXTENDS FULLY BEFORE TOUCHDOWN

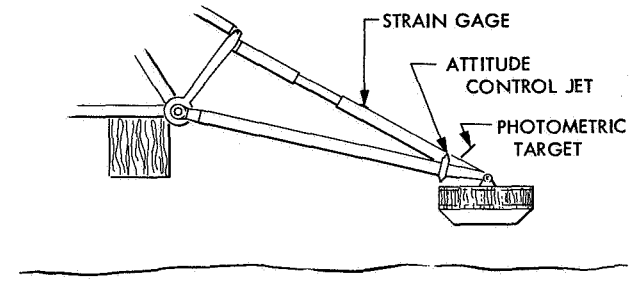

(b) DURING LANDING, THE SHOCK ABSORBER COMPRESSES, CAUSING FOOTPAD TO SLIDE OUTWARD PUSHING SOIL IN FRONT OF IT AS THE LEG ROTATES ABOUT ITS HINGE POINT

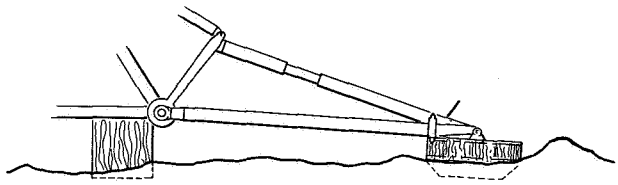

(c) SPACECRAFT COMES TO REST WITH SHOCK ABSORBER AGAIN FULLY EXTENDED

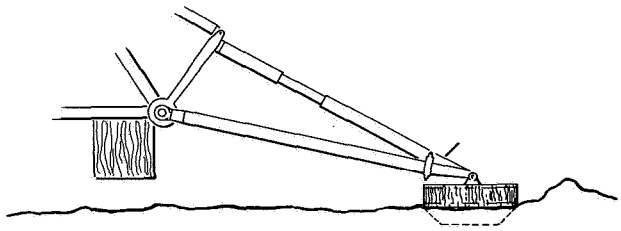

Fig. 20. Surveyor landing leg assembly touchdown sequence

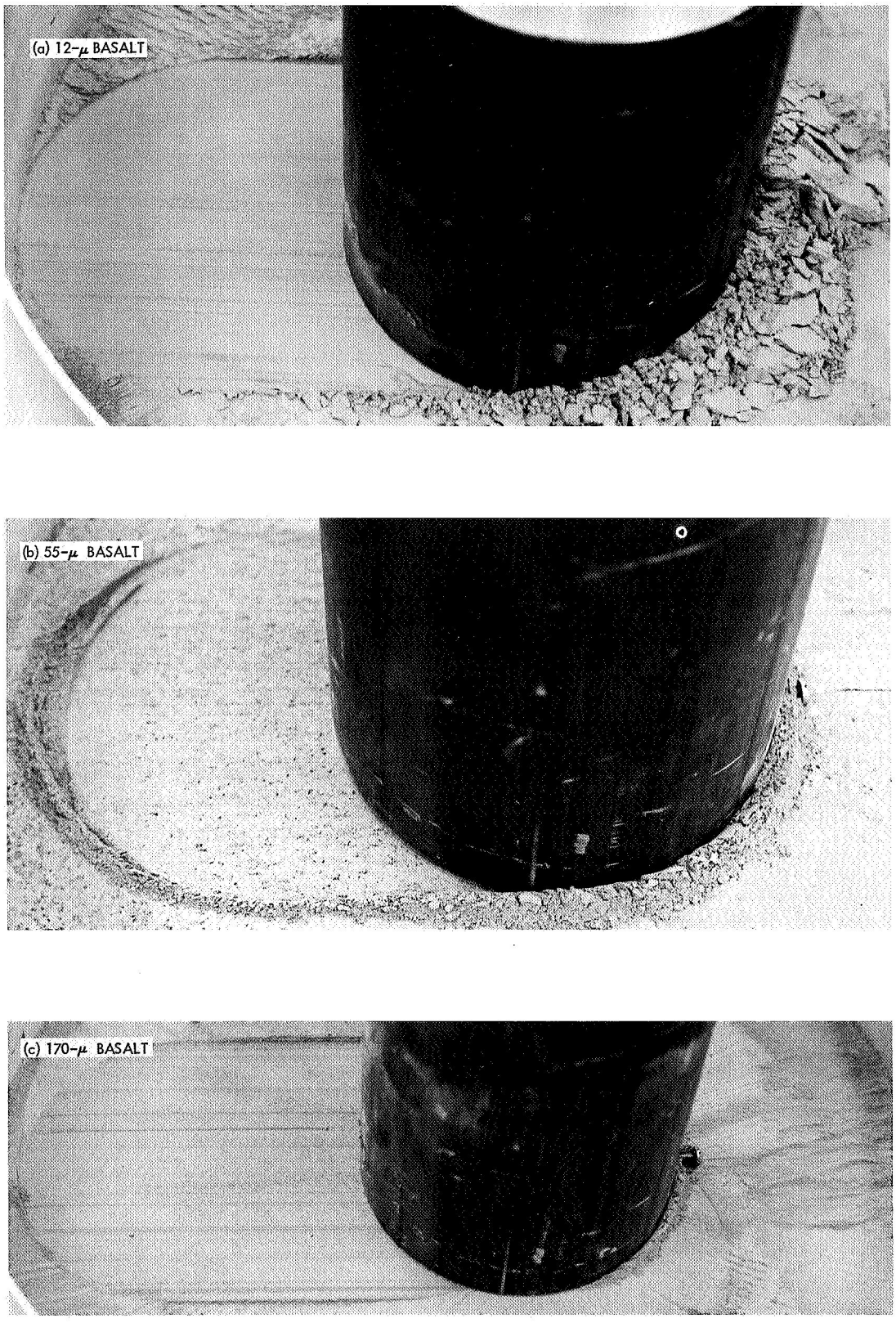

Fig. 21. Coefficient of friction tests at about 90–100% relative density and 0.61-N/cm² normal pressure

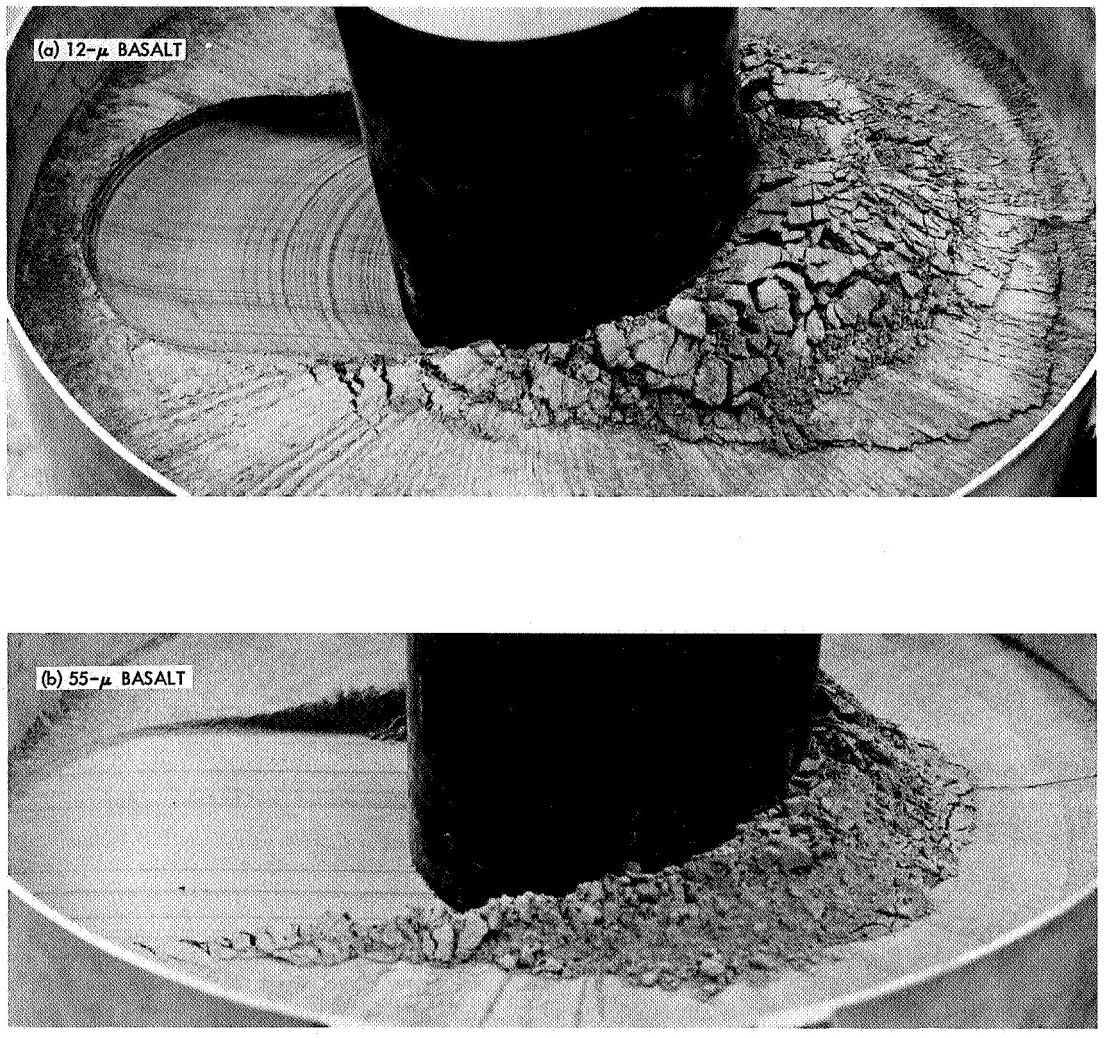

Fig. 22. Coefficient of friction tests at approximately 60% relative density and 0.61-N/cm² normal pressure

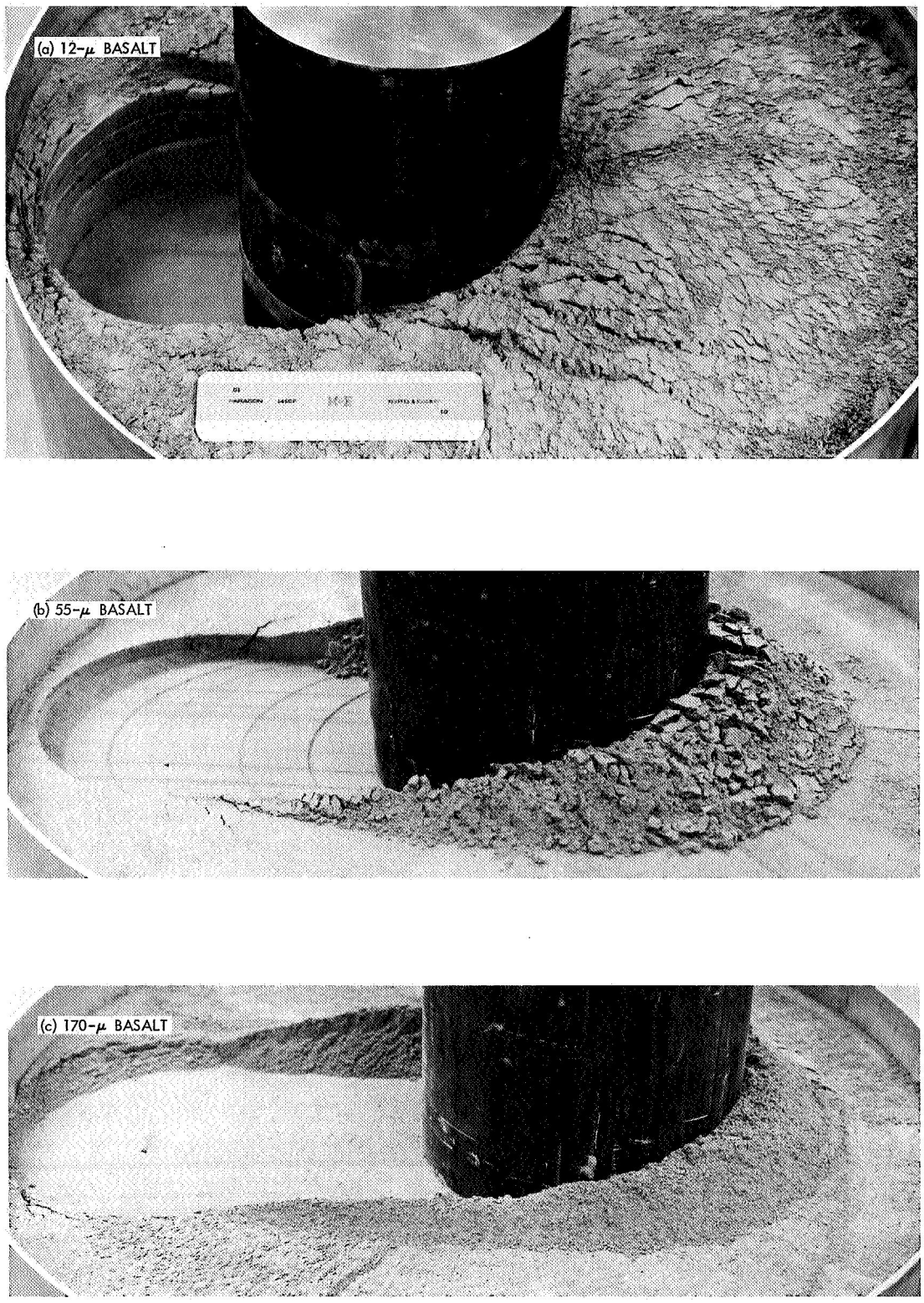

Fig. 23. Coefficient of friction tests at about 30% relative density and 0.61-N/cm² normal pressure

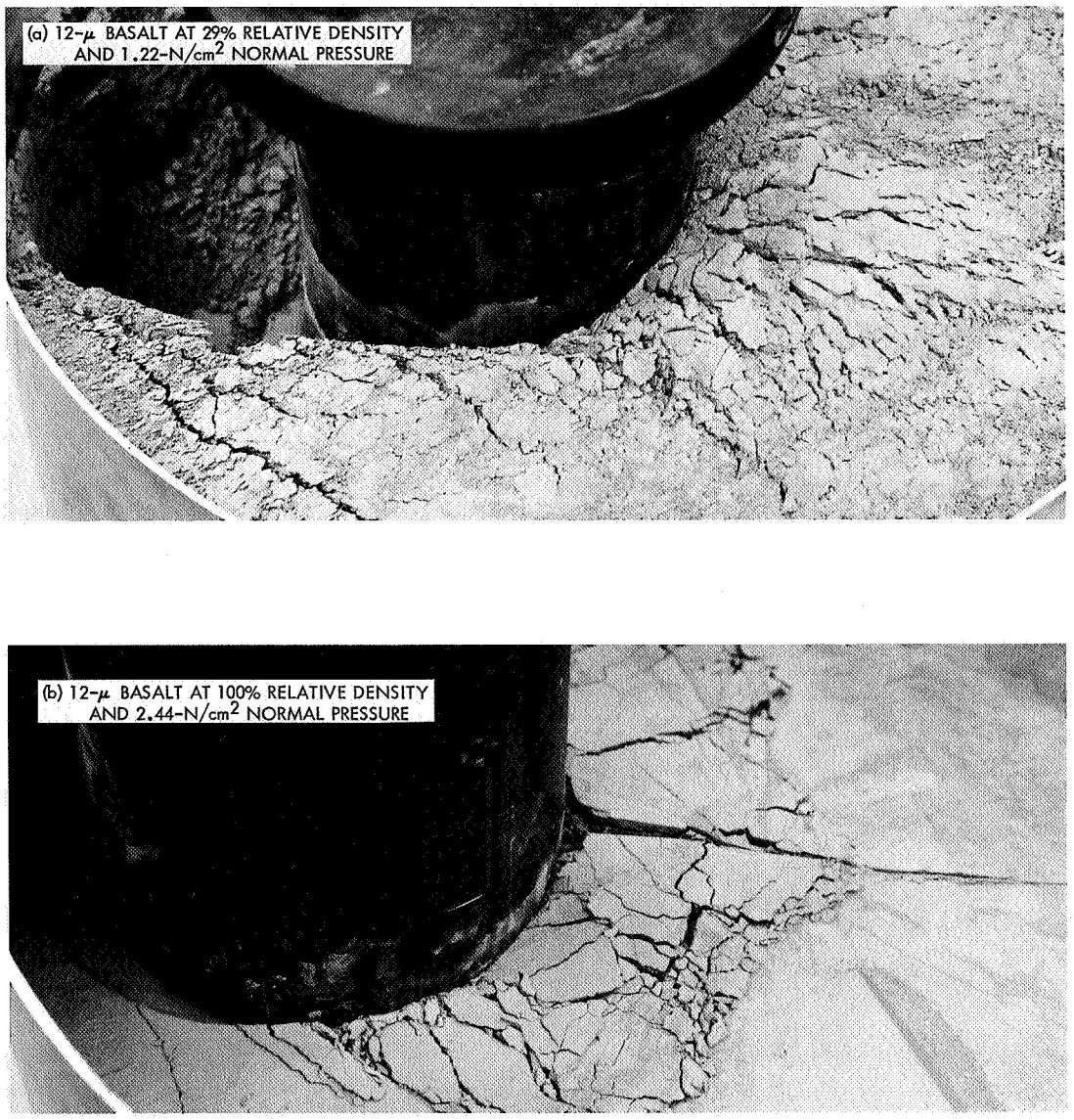

Fig. 24. Coefficient of friction tests at loads greater than 0.61-N/cm^2 normal pressure

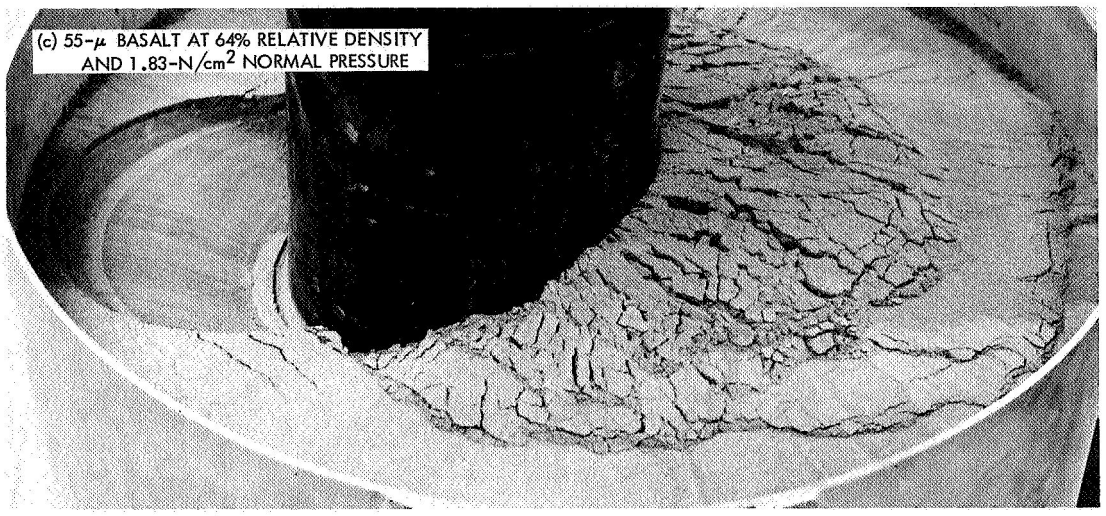
(c) 55-μ BASALT AT 64% RELATIVE DENSITY
AND 1.83-N/cm2 NORMAL PRESSURE

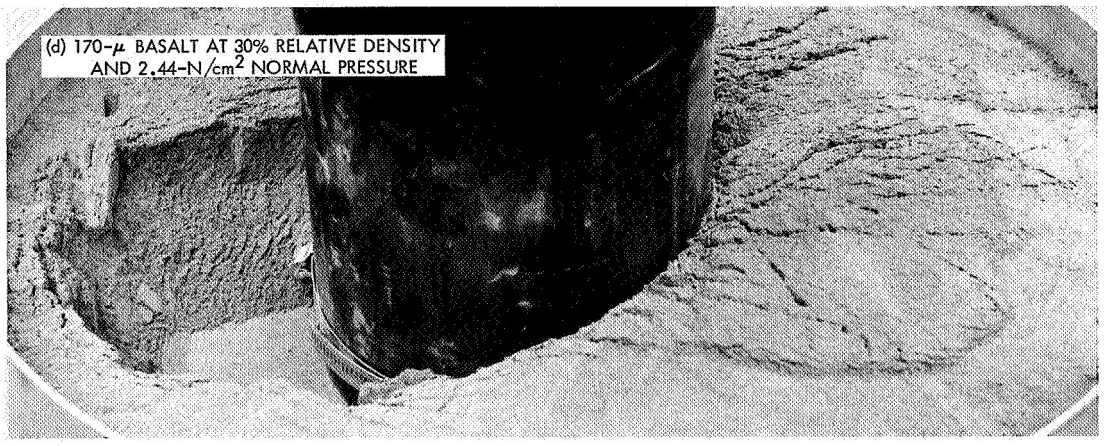
(d) 170-μ BASALT AT 30% RELATIVE DENSITY
AND 2.44-N/cm2 NORMAL PRESSURE

Fig. 24 (contd)

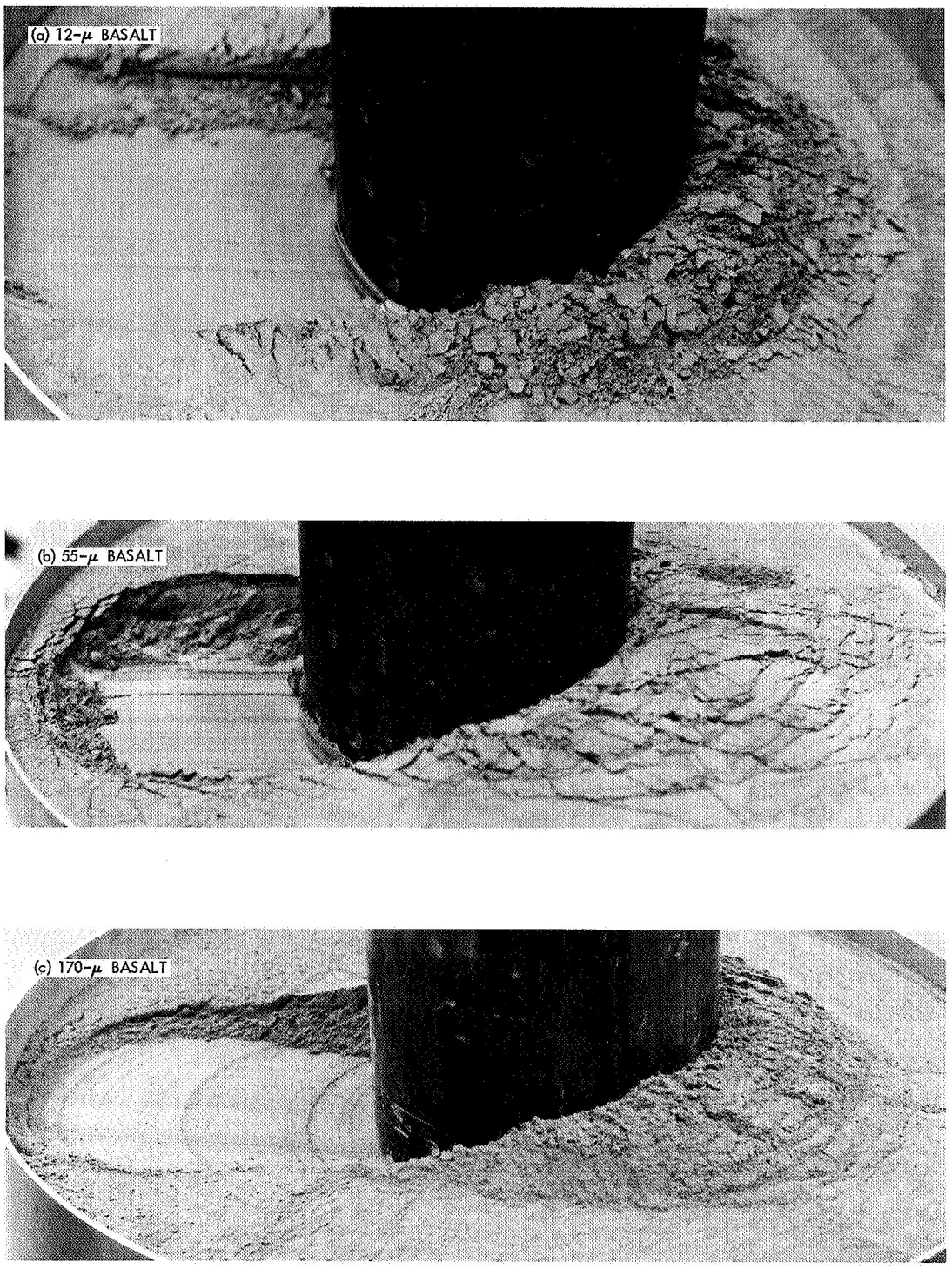

Fig. 25. Coefficient of friction tests at packing densities that best fit *Surveyor* bearing strength vs penetration data (normal pressures at 0.61 N/cm^2)

IV. Summary and Conclusions

The lunar soil coefficient of friction has been estimated, based on the 70 laboratory tests of three basalt soils at various densities ranging from dense to loose packing. Selection of coefficient of friction values that best represent lunar soil incorporates knowledge obtained on soil cohesion, particle-size distribution, and bearing strength measurements obtained at the five *Surveyor* landing sites. The best fit to *Surveyor* data provides a coefficient of friction for lunar soil of 0.35 at initial displacement, 0.72 at 2.5-cm displacement, 0.89 at 7.6-cm displacement, and 0.95 at 15.2-cm displacement. Tolerance for the above values is estimated to be 0.05.

These laboratory test values agree with the coefficient-of-friction estimates made directly from *Surveyor V* data, which were 0.73 for sliding of the spacecraft, and between 0.84 and 1.10 for sliding of the sensor head of the alpha scattering instrument when the vernier engines were fired.

Acknowledgment

The author wishes to acknowledge the assistance of William Peer, Jet Propulsion Laboratory, for his valuable help with the laboratory testing.

References

1. Christensen, E. M., et al., "Lunar Surface Mechanical Properties," *Surveyor I Mission Report: Part II. Scientific Data and Results,* Technical Report 32-1023, pp. 69–85. Jet Propulsion Laboratory, Pasadena, Calif., Sept. 10, 1966.
2. Christensen, E. M., et al., "Lunar Surface Mechanical Properties," *Surveyor III Mission Report: Part II. Scientific Results,* Technical Report 32-1177, pp. 111–153. Jet Propulsion Laboratory, Pasadena, Calif., June 1, 1967.
3. Christensen, E. M., et al., "Lunar Surface Mechanical Properties," *Surveyor V Mission Report: Part II. Science Results,* Technical Report 32-1246, pp. 43–88. Jet Propulsion Laboratory, Pasadena, Calif., Nov. 1, 1967.
4. Christensen, E. M., et al., "Lunar Surface Mechanical Properties," *Surveyor VI Mission Report: Part II. Science Results,* Technical Report 32-1262, pp. 47–108. Jet Propulsion Laboratory, Pasadena, Calif., Jan. 10, 1968.
5. Choate, R., et al., "Lunar Surface Mechanical Properties," *Surveyor VII Mission Report: Part II. Science Results,* Technical Report 32-1264, pp. 77–134. Jet Propulsion Laboratory, Pasadena, Calif., Mar. 15, 1968.
6. Choate, R., et al., "Lunar Surface Mechanical Properties," *Surveyor Project Final Report: Part II. Science Results,* Technical Report 32-1265, pp. 137–194. Jet Propulsion Laboratory, Pasadena, Calif., June 15, 1968.
7. Scott, R. F., and Roberson, F. I., "Soil Mechanics Surface Sampler: Surface Tests, Results, and Analyses," *Surveyor III Mission Report: Part II. Scientific Results,* Technical Report 32-1177, pp. 69–110. Jet Propulsion Laboratory, Pasadena, Calif., June 1, 1967.
8. Scott, R. F., and Roberson, F. I., "Soil Mechanics Surface Sampler," *Surveyor VII Mission Report: Part II. Science Results,* Technical Report 32-1264, pp. 135–185. Jet Propulsion Laboratory, Pasadena, Calif., Mar. 15, 1968.
9. Scott, R. F., and Roberson, F. I., "Soil Mechanics Surface Sampler," *Surveyor Project Final Report: Part II. Science Results,* Technical Report 32-1265, pp. 195–207. Jet Propulsion Laboratory, Pasadena, Calif., June 15, 1968.

Depths of *Surveyor* Footpad Penetrations at First Impact: Their Relation to the Bearing Strength of the Lunar Soil

R. Choate
Jet Propulsion Laboratory
Pasadena, California

I. Introduction

Knowledge of the bearing strength of the lunar surface is essential for economic design of spacecraft landing gear, design of roving vehicles, and planning of energy expenditure for manned or unmanned lunar surface traverses.

Determination of the lunar surface bearing strength requires accurate measurements of the force exerted by the penetrating object and of the depth of penetration. This paper is a review of, and presents improvements in, the depth of penetration measurements made by footpads and crushable blocks in seven touchdowns of five *Surveyor* spacecraft. The bearing strength values determined from these penetration measurements are included.

A. Bearing Strength Determinations and Analyses

Preliminary bearing strength estimates of the lunar soil, based on its penetration by various spacecraft components at touchdown and during postlanding operations, were made during each *Surveyor* mission. These estimates were derived by measuring penetrations made by the spacecraft footpads and crushable blocks, the alpha scattering instrument on *Surveyor V*, and the surface sampler instruments on *Surveyors III* and *VII*. Preliminary results of these measurements have been reported in each *Surveyor* Mission Report and in the *Surveyor* Project Final Report (Refs. 1–9).

Bearing strength determinations derived from the spacecraft footpads were based on the peak axial forces

at landing impact (measured by strain gages mounted on each leg shock absorber) and on the depth of penetration of each footpad. The measurements from the footpads at landing provided the primary source of bearing strength values. The penetration values used in the calculations given in Refs. 1–6 were based on: (1) preliminary estimates of first impact depths, and (2) depths of the footpads in their final positions. Data analyses conducted after the completion of the *Surveyor* Project provided refinements of these values.

The follow-on analyses were performed to review all available data concerning footpad and crushable block penetrations and, where possible, to improve all penetration depth measurements for use in recalculating the lunar surface bearing strength at the *Surveyor* landing sites. These recalculations have been performed, using different computer programs, by R. Jones of the Hughes Aircraft Company (Ref. 10) and F. Sperling of the Jet Propulsion Laboratory.

B. Description of Measurement Technique

Each *Surveyor* spacecraft landed with the peak force occurring at initial impact. The spacecraft then bounced and reimpacted with a force history that had a lower peak than that for the initial impact. Strain-gage force histories for all landings are shown in Fig. 1. Except for the *Surveyor I* landing, there was enough horizontal velocity at touchdown to move the footpads to a new location, thus enabling their original imprints to be seen by the television camera. The landing conditions for each spacecraft are given in Table 1.

Parts of the initial footpad imprints are visible in some of the television pictures received during the missions. Although the television camera was mounted between footpads 2 and 3, it was closest to footpad 2; therefore, the imprints of footpad 2 were clearest, and provided the primary data for subsequent bearing strength determinations. Because of the position of the *Surveyor* spacecraft frame relative to the television camera, views of footpad 1 could not be obtained.

1. Laboratory comparison method. After many tests conducted during and after *Surveyor* mission operations, it was determined that the most accurate way to measure footpad penetrations at first impact was to use a full-scale model spacecraft with an operational television

Table 1. Surveyor landing conditions

Parameter	Mission								Tolerance
	Surveyor I	*Surveyor III*			*Surveyor V*	*Surveyor VI*		*Surveyor VII*	
		Touchdown 1	Touchdown 2	Touchdown 3		Initial	Hop		
Vertical landing velocity, m/s	3.6	1.8	1.4	1.5	4.2	3.4	3.8	3.8	±0.4
Horizontal landing velocity, m/s	0.3	0.2	0.8	0.9	0.3	0.3	0.5	0.1	±0.2
Angle of surface slope, deg	1.0	11.5	14.0	9.2	19.5	0.9	~3	3.1	±0.5
Maximum axial shock-absorber load (leg 1), N	6190	2970	1420	3860	5620	7000	14900	7330	±5%
Maximum axial shock-absorber load (leg 2), N	7110	3060	2800	2440	7280	8000	7800	7800	±5%
Maximum axial shock-absorber load (leg 3), N	6220	3680	2350	4120	7300	7000	8600	6540	±5%
Mass of spacecraft at landing, kg	294.5	305.7	—	299.0	303.7	300.5	299.8	306.0	±0.5
Maximum travel distance of ejecta, cm	50	—	—	70	80	50	90	40	±5

system and to simulate each footpad imprint in the laboratory.

For each lunar imprint visible to the television camera, footpad imprints of different depths were made in a soil of crushed basalt. These laboratory imprints were placed in correct orientation to the full-scale model spacecraft and then photographed by the model television camera. These imprint pictures were then compared with those in the *Surveyor* lunar pictures. The depths of the lunar imprints were interpolated from the laboratory imprints whose depths most closely matched the corresponding lunar imprint.

The full-scale model spacecraft with the operational television system is shown in Fig. 2. A *Surveyor* footpad and a crushable body block are shown in Figs. 3 and 4, respectively. In Fig. 4, the thin sheet of aluminum covering the bottom of the crushable block has been stressed to rupture, exposing the hollow core of the block. This rupture causes the mound of soil observed in all lunar crushable block imprints.

2. Camera calibration. On each vidicon tube of the television camera are 25 reseau marks, or reference dots, in a rectangular pattern with 5 reseau marks on a side. The aspect ratio of the vidicon tube was not constant for each mission; i.e., the ratio of the picture horizontal vs vertical coverage was different. The aspect ratio of the laboratory television system was set to match the *Surveyor* pictures as closely as practical for each mission. In this paper, every attempt was made to have all pictures at correct scale relative to each other; however, if measurements are made from the pictures by the reader, scale for such measurements should be controlled by the position of the reseau marks.

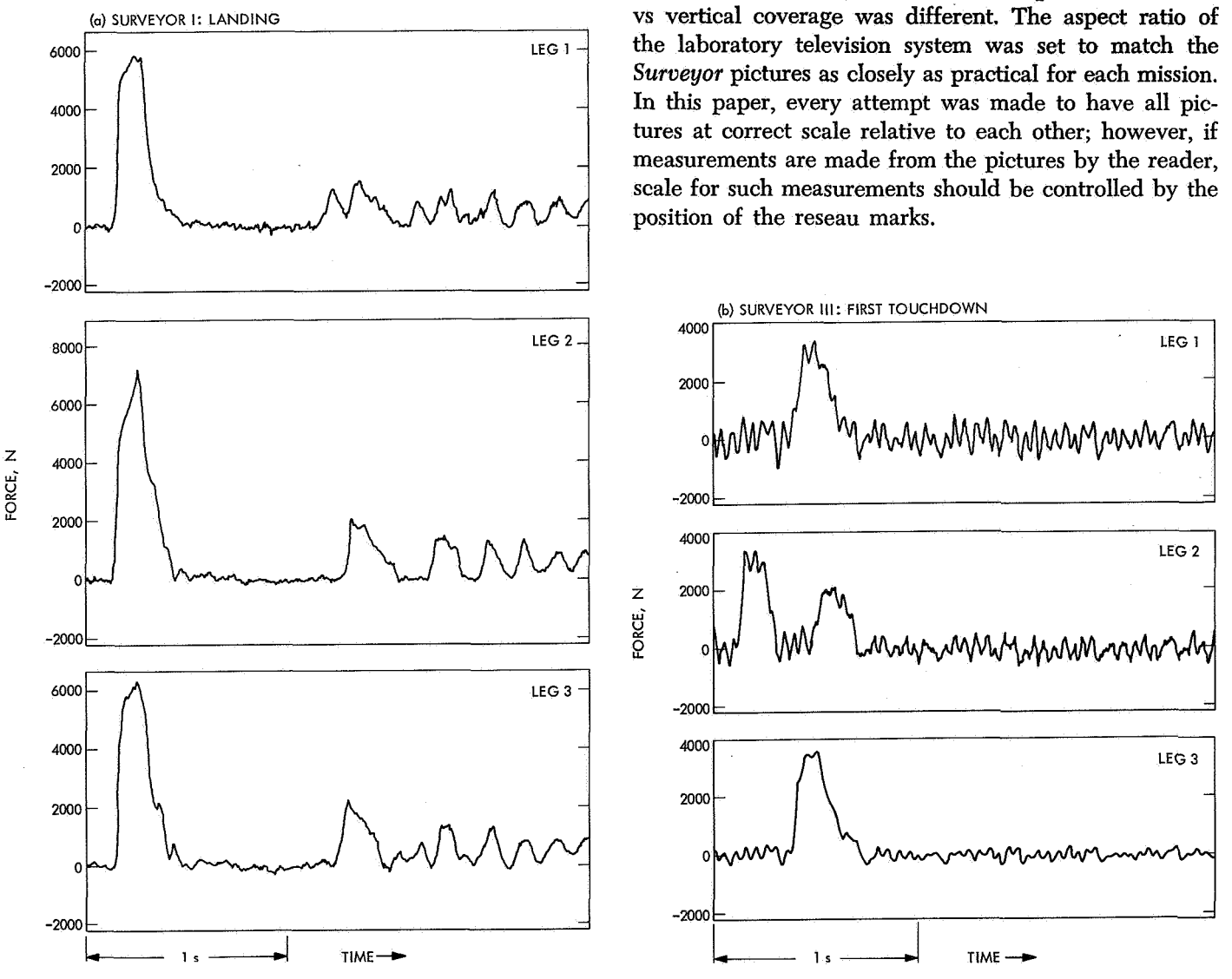

Fig. 1. Telemetry data showing initial shock-absorber axial load histories during *Surveyor* landings (in most cases, oscillations continue beyond the 2.5 s shown)

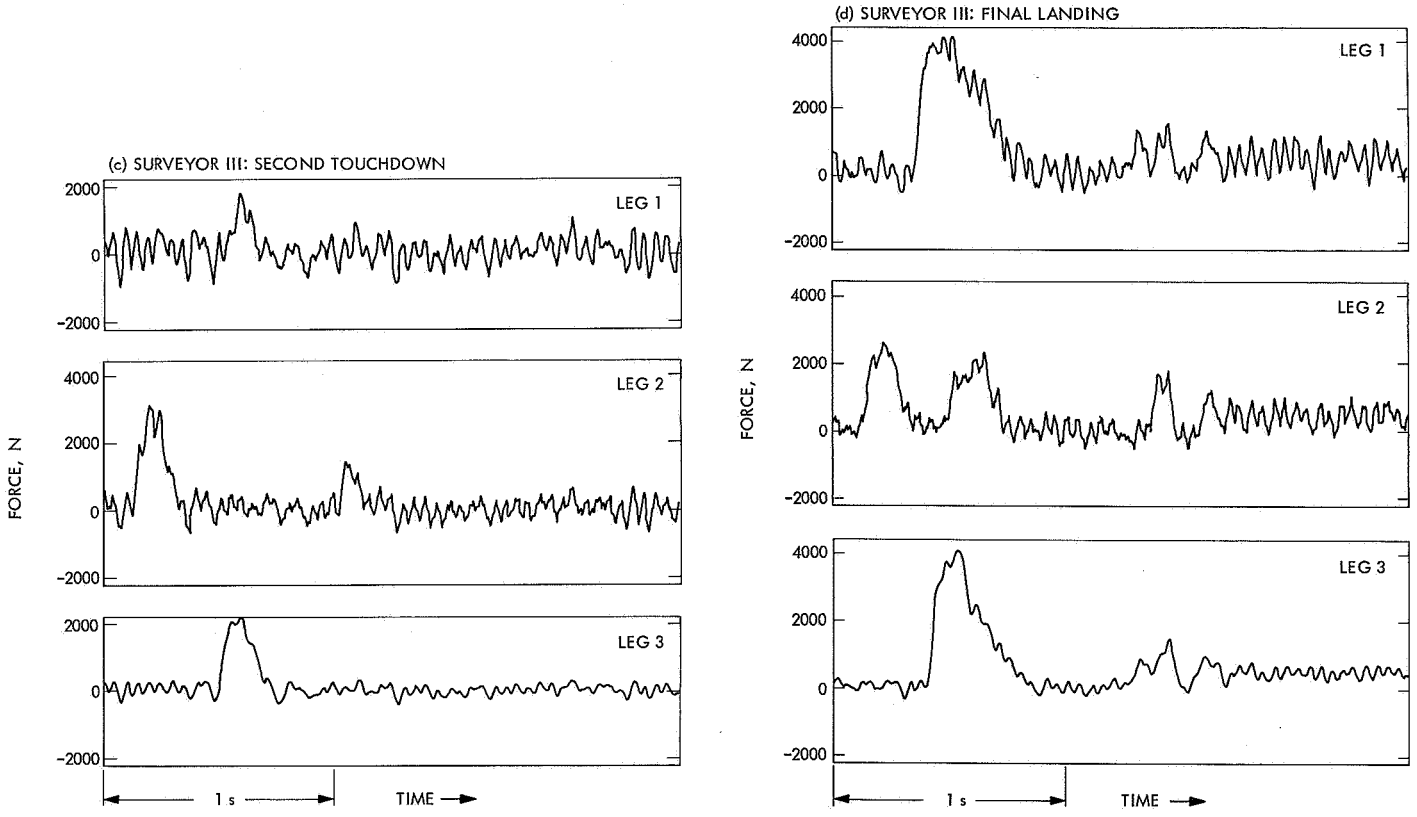
(c) SURVEYOR III: SECOND TOUCHDOWN
LEG 1
LEG 2
LEG 3
2000
0
-2000
4000
FORCE, N
1 s
TIME
(d) SURVEYOR III: FINAL LANDING
LEG 1
LEG 2
LEG 3
4000
2000
0
-2000
FORCE, N
1 s
TIME

Fig. 1 (contd)

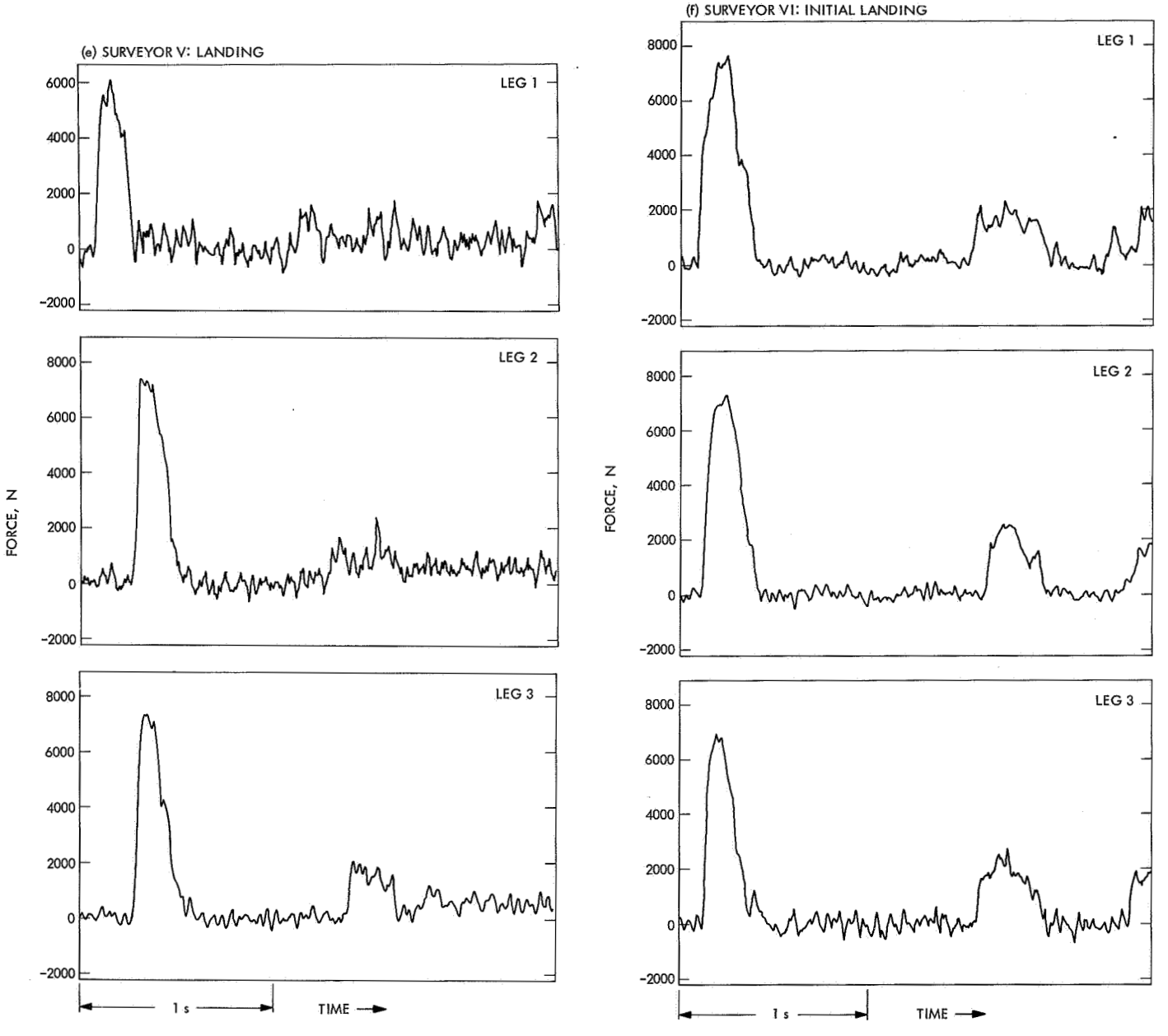
(e) SURVEYOR V: LANDING
LEG 1
LEG 2
LEG 3
6000
4000
2000
0
-2000
8000
FORCE, N
1 s
TIME
(f) SURVEYOR VI: INITIAL LANDING
LEG 1
LEG 2
LEG 3
8000
6000
4000
2000
0
-2000
FORCE, N
1 s
TIME

Fig. 1 (contd)

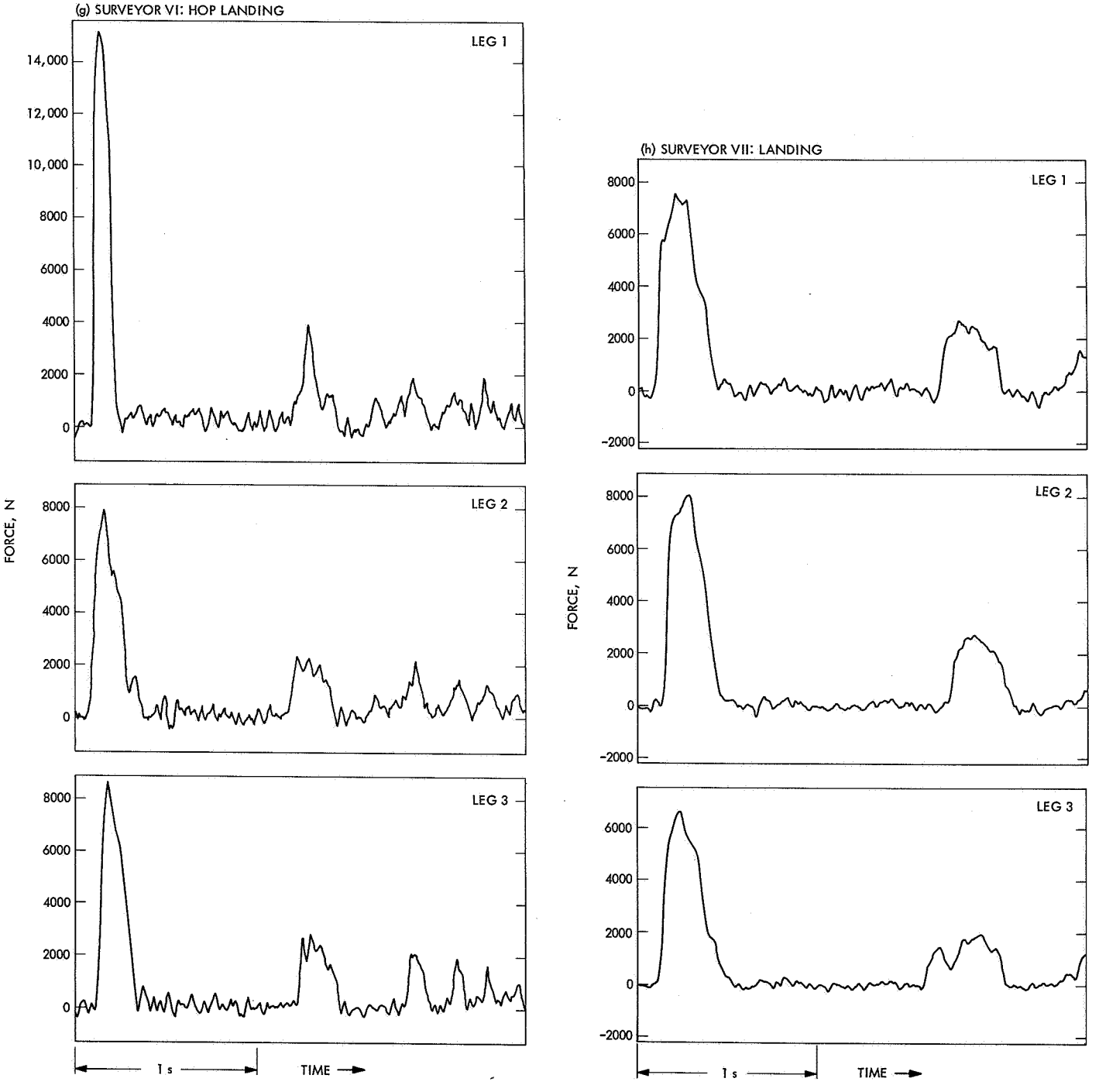
(g) SURVEYOR VI: HOP LANDING
LEG 1
LEG 2
LEG 3
14,000
12,000
10,000
8000
6000
4000
2000
0
FORCE, N
1 s
TIME
(h) SURVEYOR VII: LANDING
LEG 1
LEG 2
LEG 3
8000
6000
4000
2000
0
-2000
FORCE, N
1 s
TIME

Fig. 1 (contd)

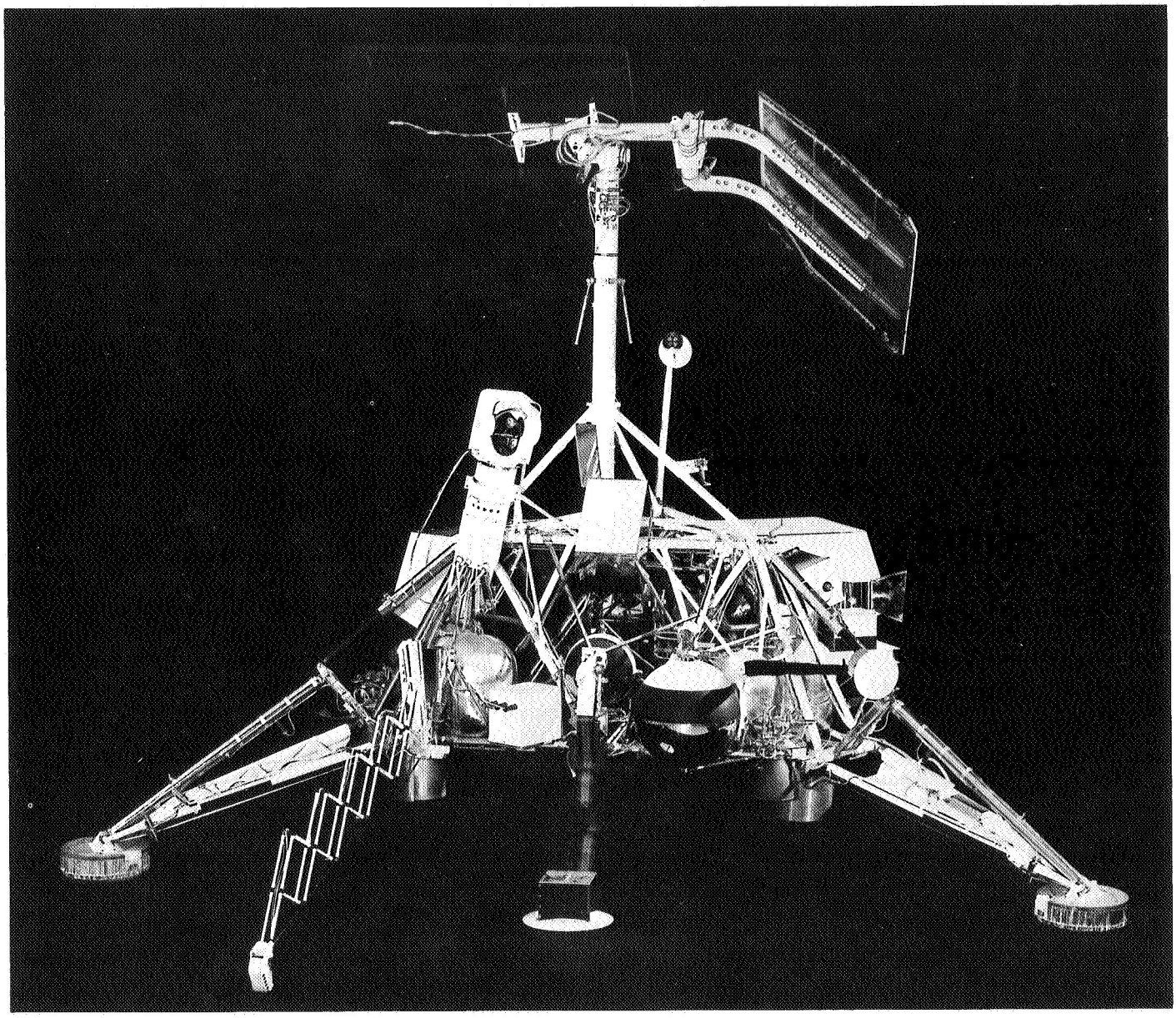

Fig. 2. Full-scale model spacecraft with operational television system used to determine the depth of *Surveyor* footpad and crushable block penetrations of the lunar surface

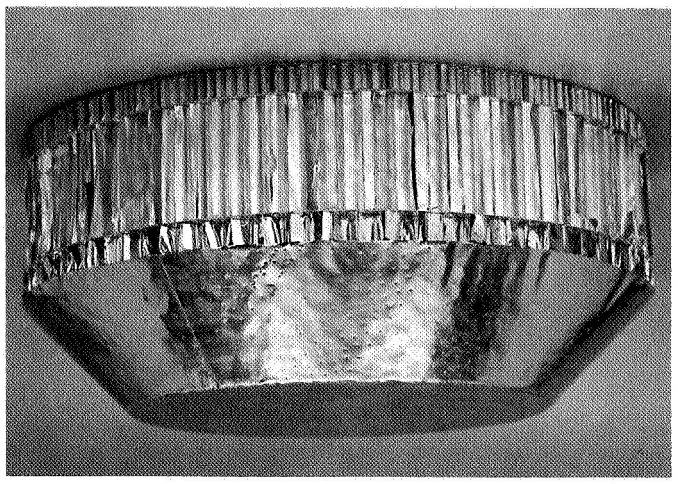

Fig. 3. *Surveyor* footpad showing honeycomb construction

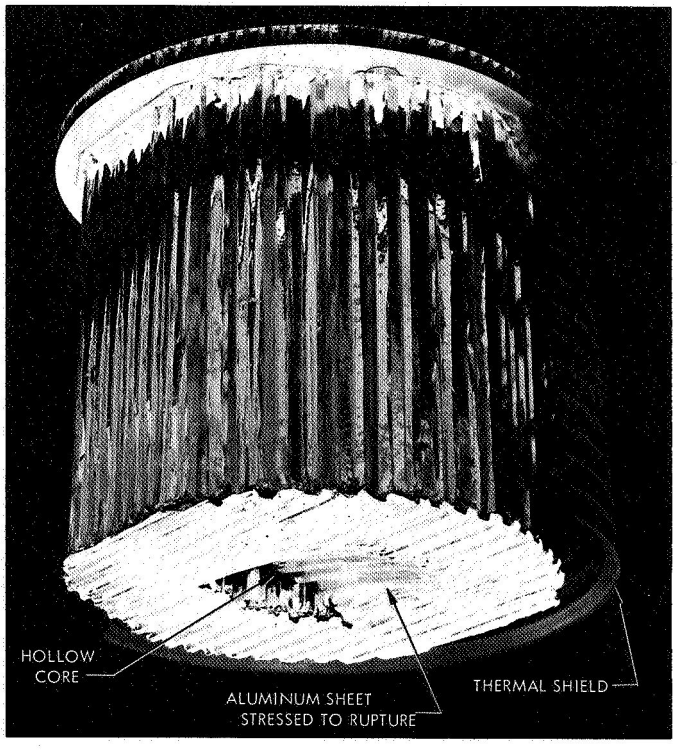

Fig. 4. *Surveyor* crushable block assembly showing partly encircling thermal shield

II. Description of Imprint Measurements

It was possible to calculate the forces acting on the footpads at initial impact from the shock-absorber axial force histories. However, because of the complex history of forces acting throughout the spacecraft frame, no such comparable force histories could be determined for the crushable blocks at the time of their contact with the lunar surface. Thus, footpad penetration depths were used quantitatively in force vs penetration measurements; measurements derived from the crushable blocks are useful only in qualitative comparisons.

A. Footpad Imprints

1. Surveyor I. Because *Surveyor I* landed, from an almost vertical descent, on a level surface with a slope of less than 1 deg, the spacecraft came to rest in its original imprints after the landing bounce. No improvement in footpad penetration values over those reported in Ref. 6 could be made. The values were derived from shadow relationships established by the spacecraft in its final landing position (Ref. 11).

Lunar pictures of footpads 2 and 3 are shown in Figs. 5 and 6, respectively. The penetration depth reported for footpad 2 is 3 cm; the penetration depth for footpad 3 is 2 cm.

2. Surveyor III: second landing event. The *Surveyor III* spacecraft, in its first two landing events, touched down with the vernier engines still firing. The second of these two touchdown sites can be seen from the third and final landed position. In Fig. 7, the bottoms of the imprints of footpads 1 and 2 can be seen, thus permitting an estimate of the imprint depths. The imprints are uphill from the final landed position, and almost level with the camera mirror. The distance to the footpad 1 imprint is about 11 m, and about 15 m to the footpad 2 imprint.

The imprint bottoms are about 20 cm in diameter (the diameter of the bottom of the footpad). The visible uphill part of the footpad 1 imprint ranges from 2.5 to 8 cm in depth and averages 5 cm; for footpad 2, the depth ranges from 4 to 6 cm and averages about 5 cm. After considering the height of the ejecta and the slope of the ground, the average penetration depths at first impact are estimated to be 3.0 $\pm$1.0 cm for footpad 1 and 3.5 $\pm$1.0 cm for footpad 2.

3. Surveyor III: final landing event. During the final landing event, footpad 2 touched down first with a

double impact, after which the spacecraft bounced, making a third and a fourth imprint (Fig. 1d). The first (double) imprint made during the final landing is seen in Fig. 8a, which shows the 2.1 ±1.0-cm depth of penetration, that was estimated to have occurred at first impact. This correlates with the first peak in the strain-gage history of Fig. 1d. Simulated footpad 2 imprints, with depths of 1.78 and 2.80 cm, are shown in parts b and c of Fig. 8, respectively.

During the *Surveyor III* landing, the spacecraft bounced such that the imprint made by footpad 3 was left partly exposed to the television camera. This was the only time during the *Surveyor* missions that the footpad 3 imprint was so exposed. The imprint depth and associated ejecta, and the depths of the two correlating laboratory imprints, are shown in Fig. 9. The total depth is 5.4 cm, of which about 20% is estimated to be formed by ejecta.

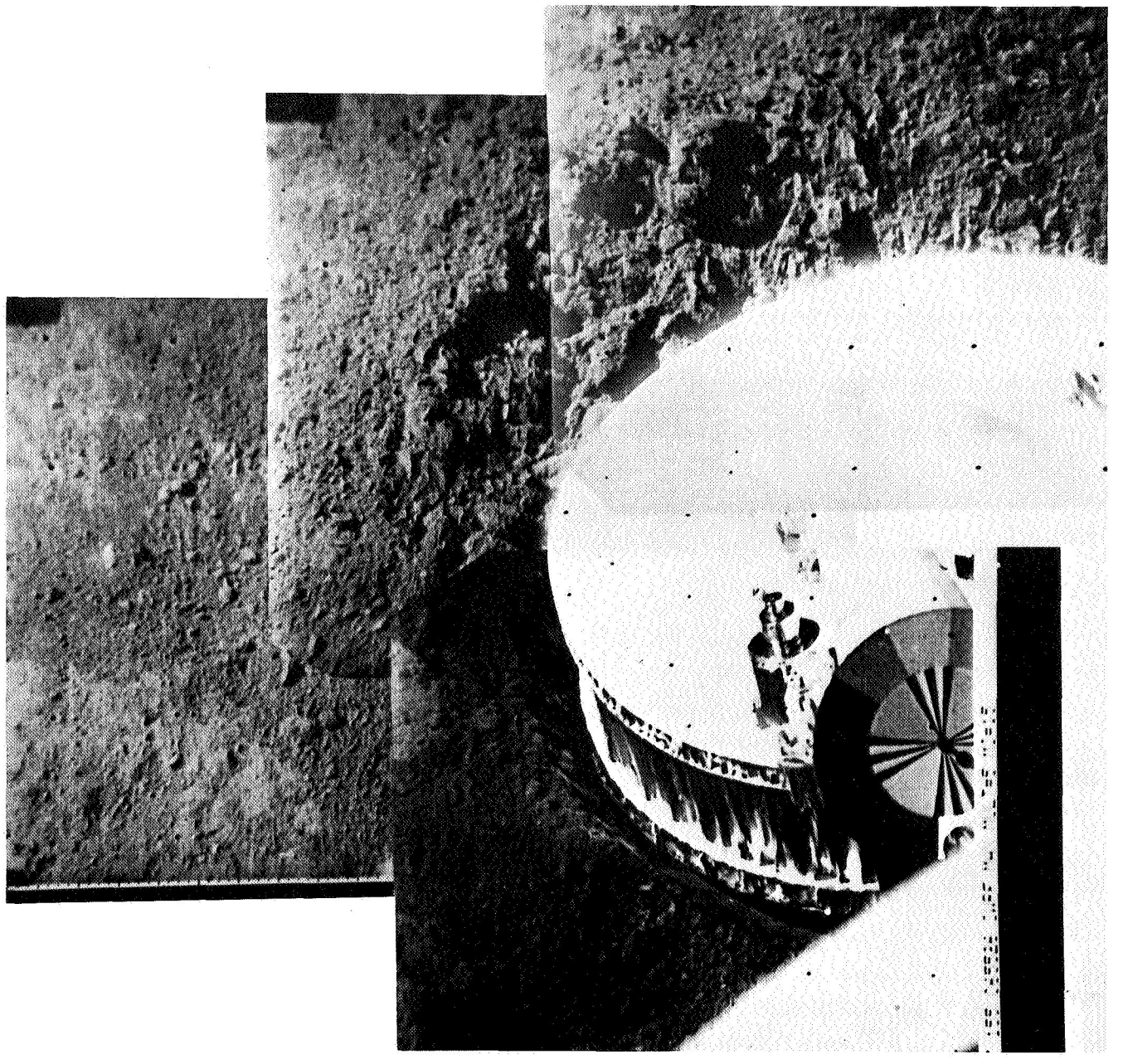

Fig. 5. Footpad 2 of *Surveyor I* (note the ejected soil; 6/4/66, computer processed)

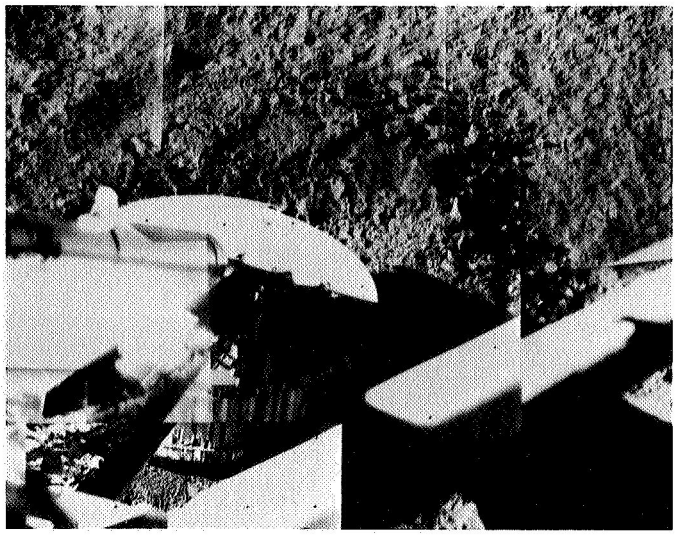

Fig. 6. Footpad 3 of *Surveyor I*
(6/12/66, Catalog 1-SE-5)

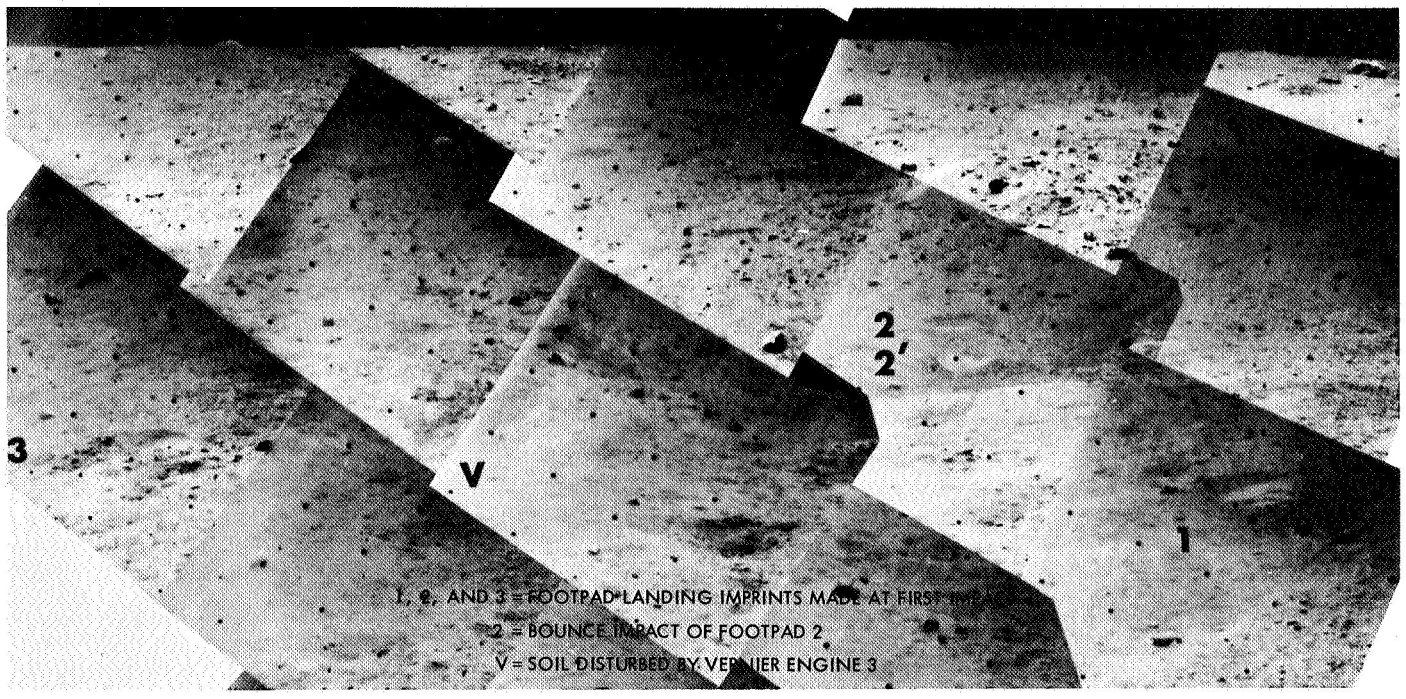

Fig. 7. *Surveyor III* touchdown site as seen from the final landed position, about 11 m away
(4/26/67, 08:00 GMT)

(a) LUNAR IMPRINT; INTERPOLATED DEPTH: 2.1 cm (4/26/67)

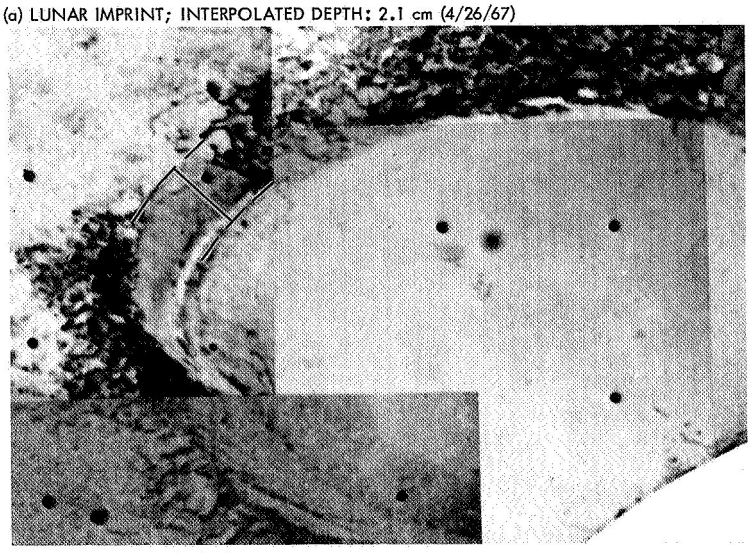

(b) LAB IMPRINT; DEPTH: 1.78 cm

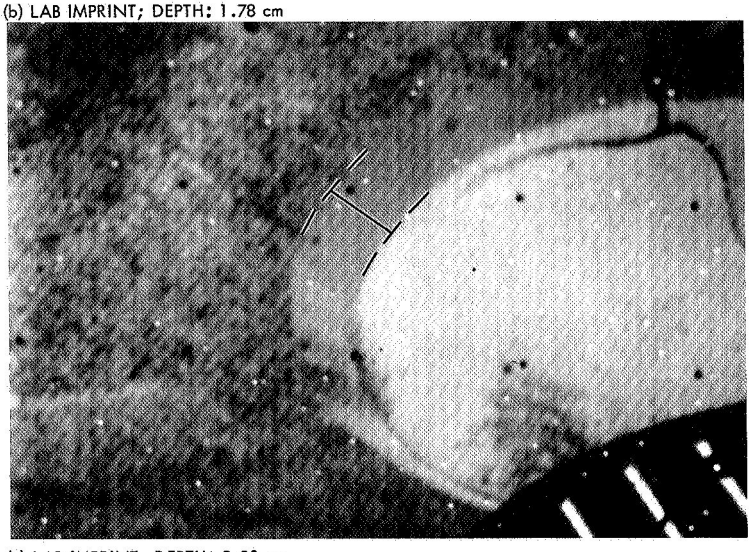

(c) LAB IMPRINT, DEPTH: 2.80 cm

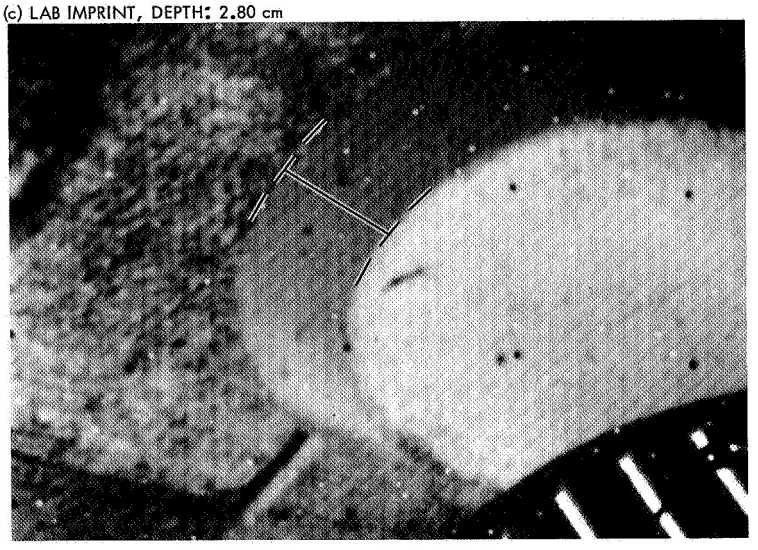

Fig. 8. Footpad 2 imprints, *Surveyor III* final landing event

(a) LUNAR IMPRINT, INTERPOLATED DEPTH, INCLUDING EJECTA: 5.35 cm (4/30/67, 14:56:04 GMT)

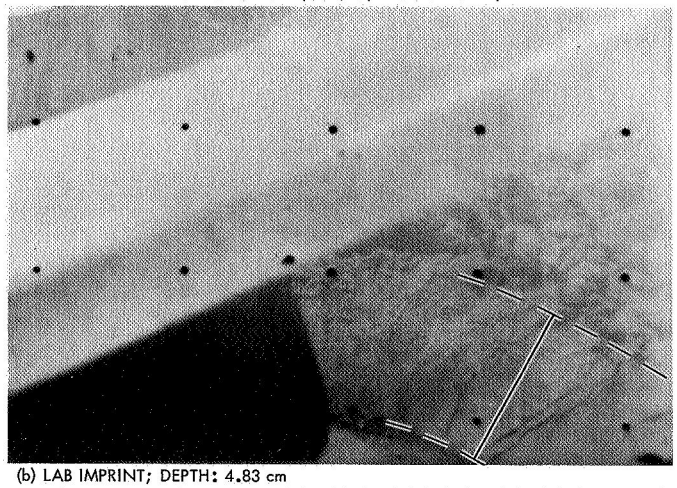

(b) LAB IMPRINT; DEPTH: 4.83 cm

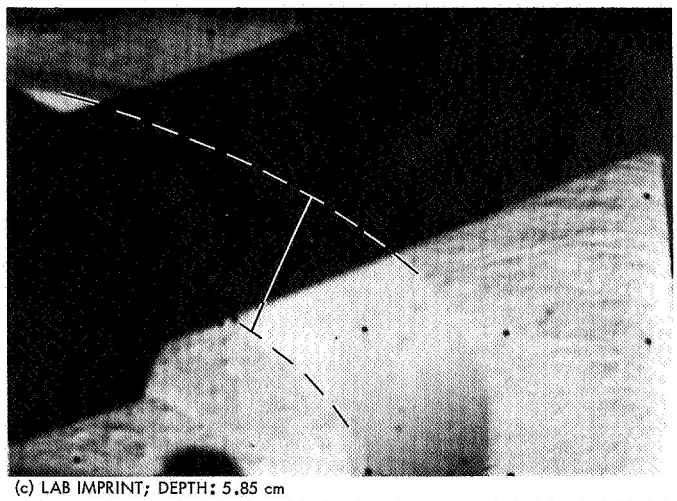

(c) LAB IMPRINT; DEPTH: 5.85 cm

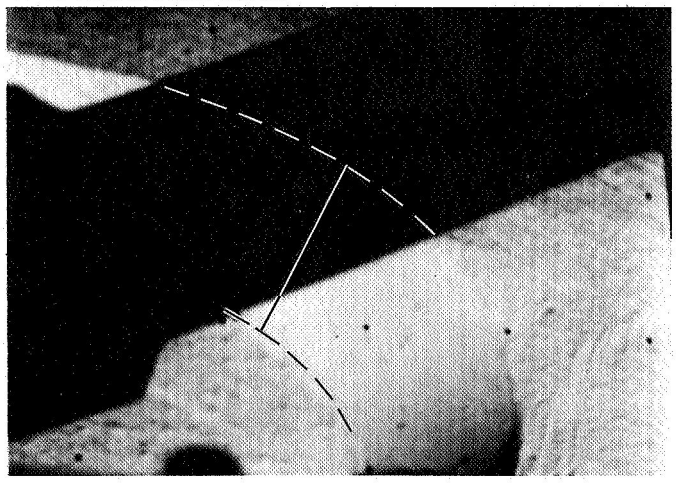

Fig. 9. Footpad 3 imprints, *Surveyor III* final landing event

The relative depths measured for footpad 2 and 3 impacts correlate with the peak axial forces of 2440 and 4120 N, measured at first impact (Table 1 and Fig. 1d).

4. Surveyor V. The *Surveyor* V spacecraft landed on the inner slope of a small crater and slid 81 cm downslope, thus forming the trench shown in the wide-angle mosaic of Fig. 10. A narrow-angle view of the uphill end of the trench is shown in Fig. 11a; the estimated depths of penetration at first impact are indicated. Correlating trench simulations are shown in Fig. 11b and c. The maximum depth at the point shown is 12.6 cm, and the minimum depth is 10.5 cm; the average is 11.5 cm. Because the footpad was tilted about its axis as it slid downslope, the center of the trench is estimated to be 1 cm shallower than the outboard point measured. The depth of penetration at first impact is estimated as 10.5 $\pm$2.0 cm.

5. Surveyor VI. The *Surveyor VI* spacecraft landed in Sinus Medii on November 10, 1967. On November 17, the spacecraft was commanded to fire its vernier engines, causing the spacecraft to hop 2.4 m horizontally. This hop, in addition to providing a second set of data on landing impacts, also exposed to the full view of the television camera the imprints made by the footpads and crushable blocks of legs 2 and 3.

Although footpad 2 left an imprint visible to the camera after its first landing, the only method available for measuring the rim height was to use shadows cast on the imprint bottom for a short period of time on November 10 (Fig. 12a). The direction of shadows is indicated by the markers in Fig. 12b and c. The depth of 1.6 cm measured at this point is too small to represent average penetration, because it is at the inboard portion of the imprint and the footpad is tilted down, outward about its hinge axis. A post-hop view of this imprint is shown in Fig. 13a.

The simulated imprint of Fig. 13b was made to match the lunar picture as closely as possible. The average depth of the simulated imprint at the hinge axis, including ejecta, is 5.6 cm. However, the height of the ejecta in the lunar picture could not be measured directly; it is greater than 1.0 cm, and probably less than 3.0 cm. The estimate of penetration at first impact, taken as the average of the pre- and post-hop measurements, is 3.5 $\pm$1.0 cm.

The footpad 2 imprint made during the hop is shown in Fig. 14. The rim (as marked in Fig. 14a), when compared with other *Surveyor* pictures (Ref. 4), appears to be part of the relatively undisturbed original surface. The depth is estimated as 6.5 $\pm$1.0 cm.

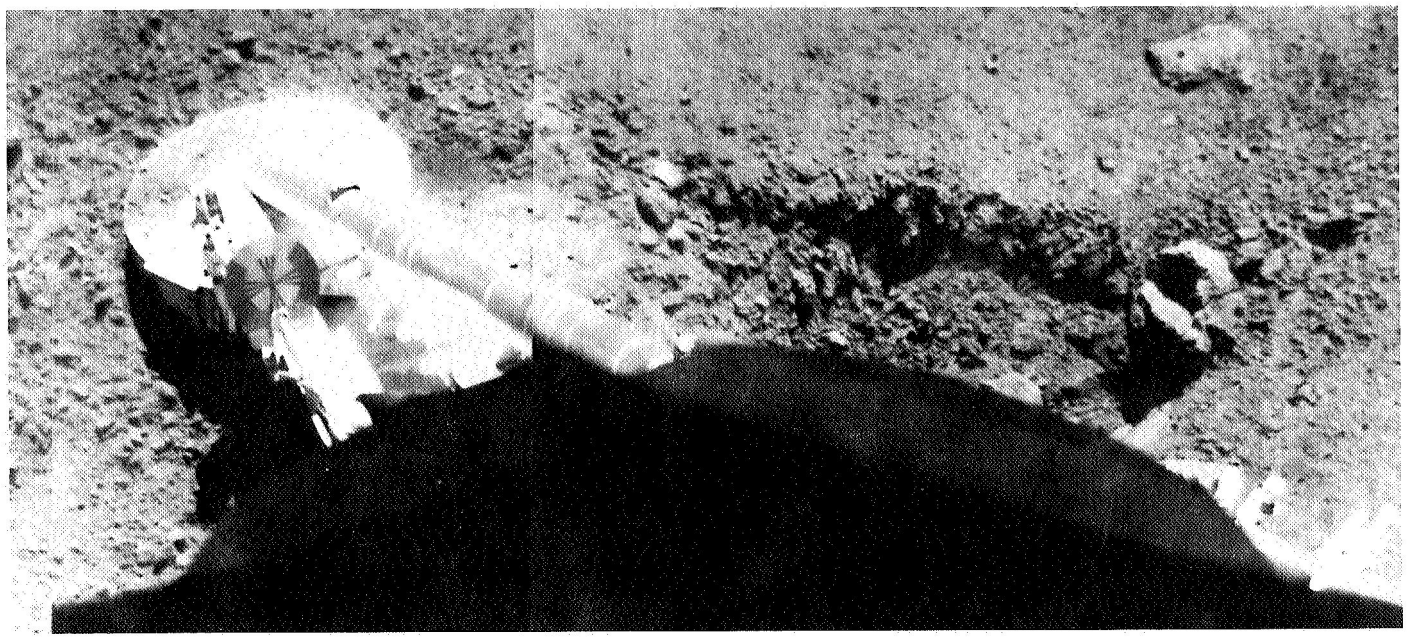

Fig. 10. Trench dug by footpad 2 on *Surveyor V* during landing on a 19–20-deg slope (9/17/67, Catalog 5-MP-9)

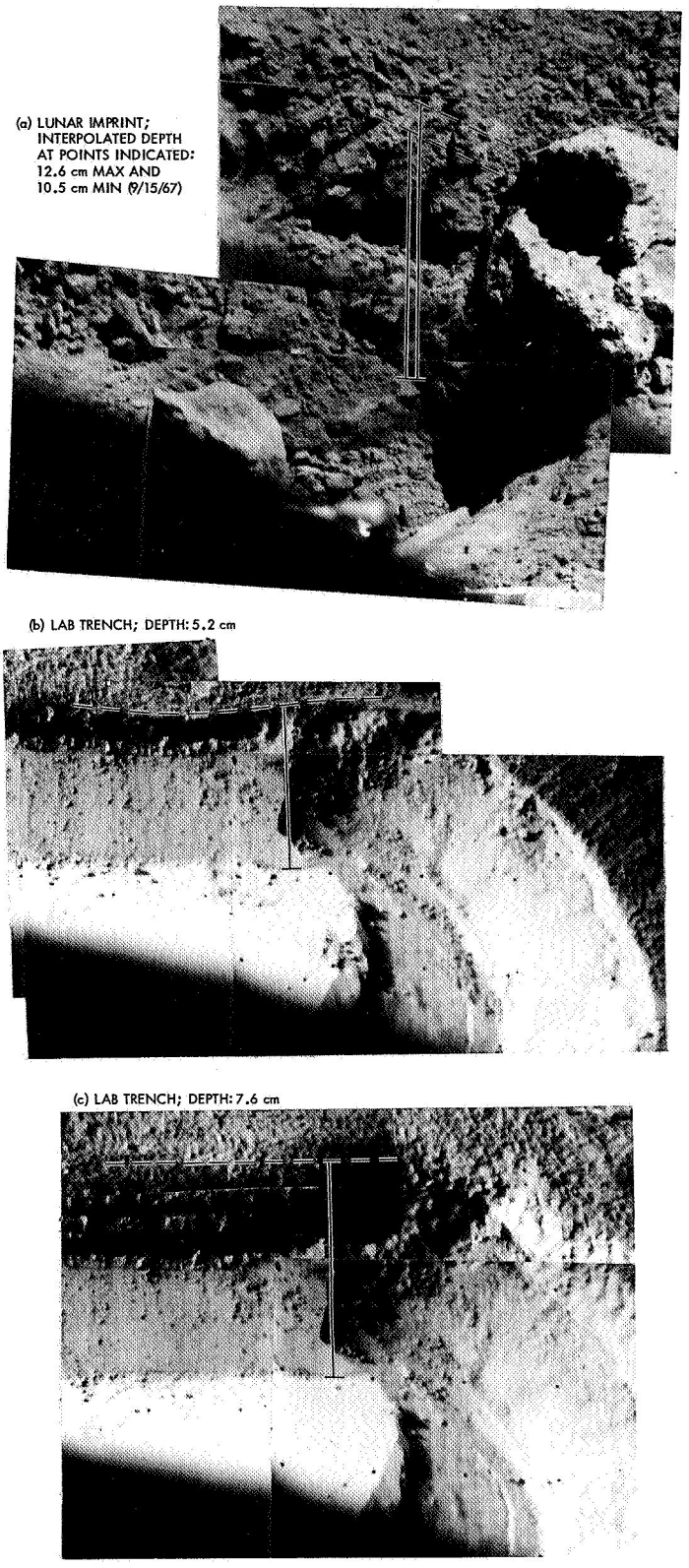

Fig. 11. Footpad 2 imprints, *Surveyor V* (imprints are at first impact at uphill end of trench)

(a) LUNAR IMPRINT; INTERPOLATED DEPTH: 1.6 cm

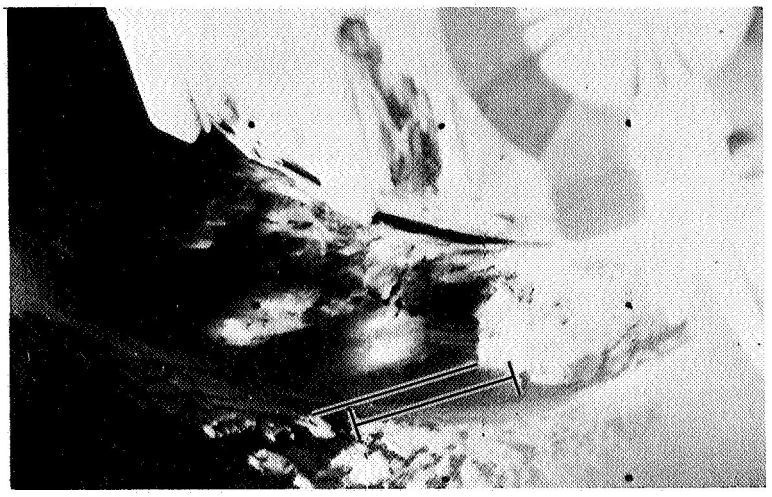

(b) LAB IMPRINT; DEPTH: 1.3 cm

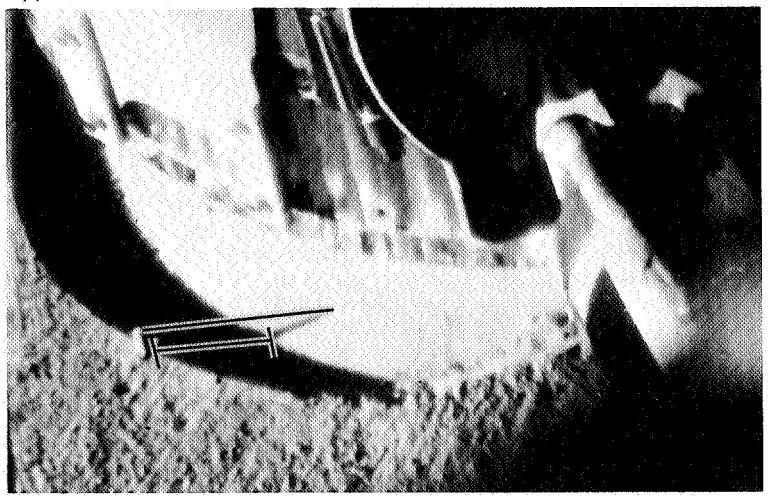

(c) LAB IMPRINT; DEPTH: 2.2 cm

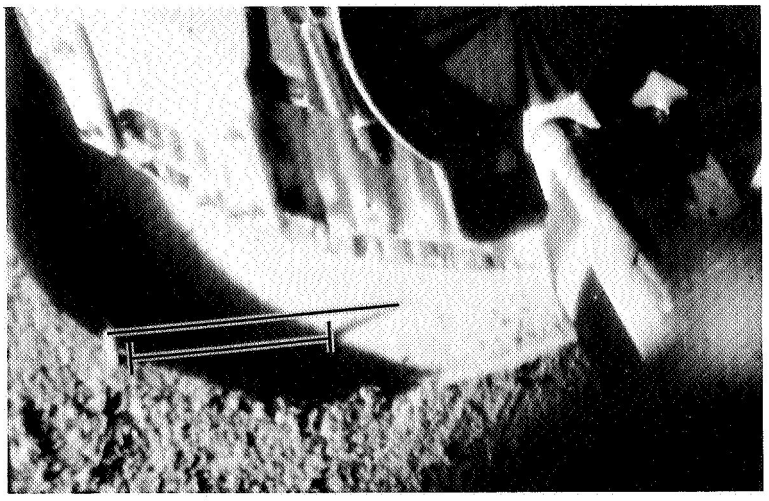

Fig. 12. Footpad 2 imprints, *Surveyor VI* initial landing (shadow is cast near the back of the imprint; the outboard edge of the footpad is tilted down; 9/10/67, 23:29:41 GMT)

(a) LUNAR IMPRINT; AS SEEN AFTER HOP (11/22/67, 16:55:25 GMT)

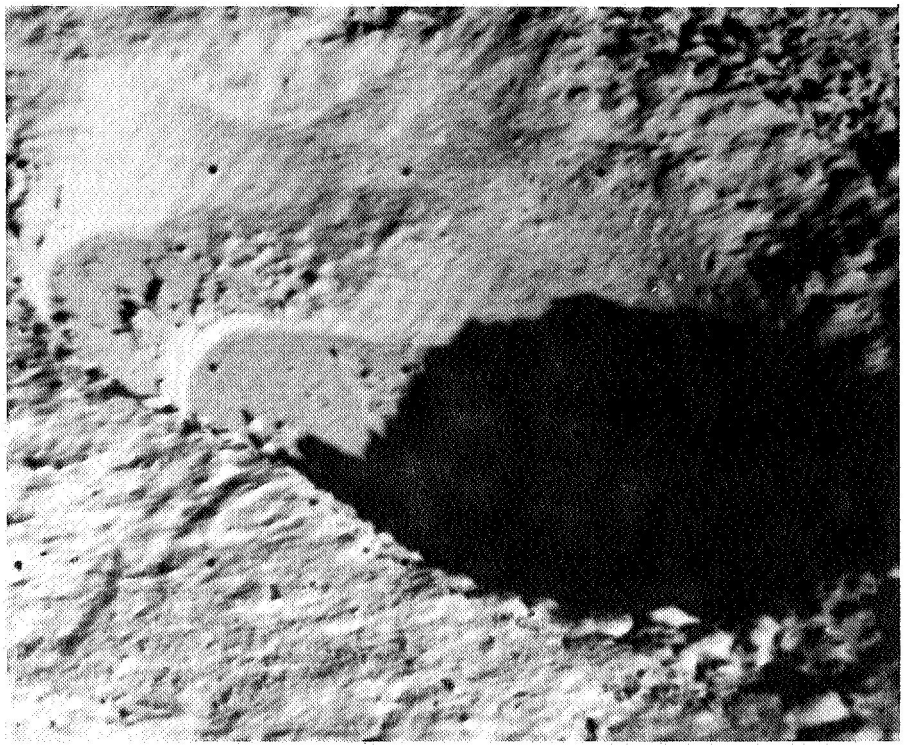

(b) LAB IMPRINT; DEPTH AT HINGE AXIS, INCLUDING 1–3 cm OF EJECTA: 5.6 cm

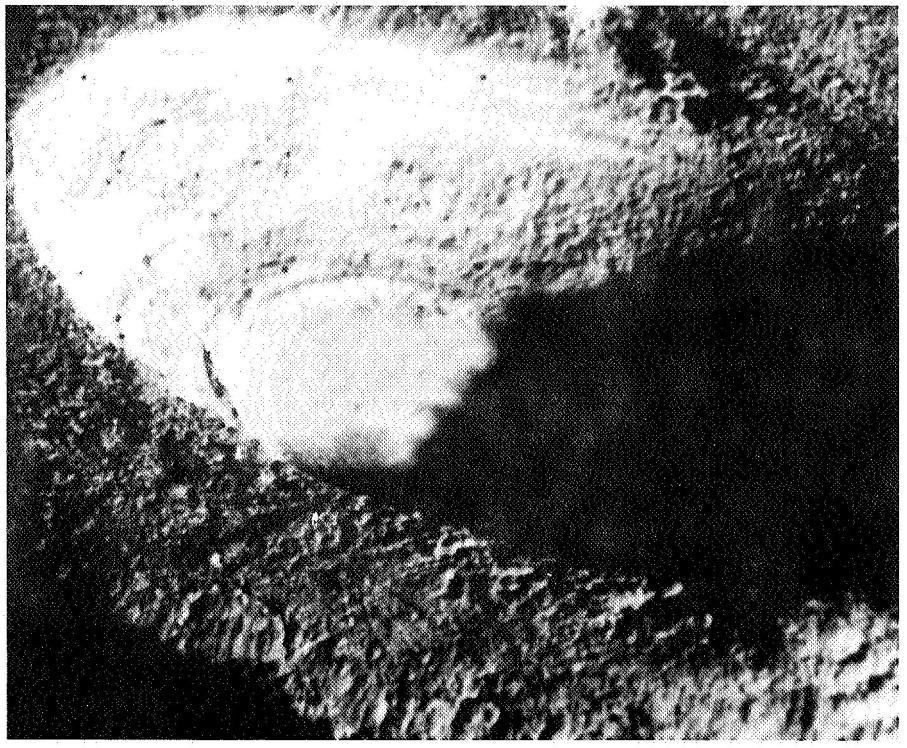

Fig. 13. Footpad 2 imprints, *Surveyor VI* initial landing

Footpad 3 initial imprint, though not visible before the hop, was visible after the hop (Fig. 15a). Depth of penetration at first impact, as measured at the hinge axis, is 2.6 ±0.5 cm. The footpad 3 imprint for the hop was not exposed to the camera. Depth of penetration, at the final rest position, was determined from shadow analysis to be 3.0 ±1.0 cm (Ref. 5).

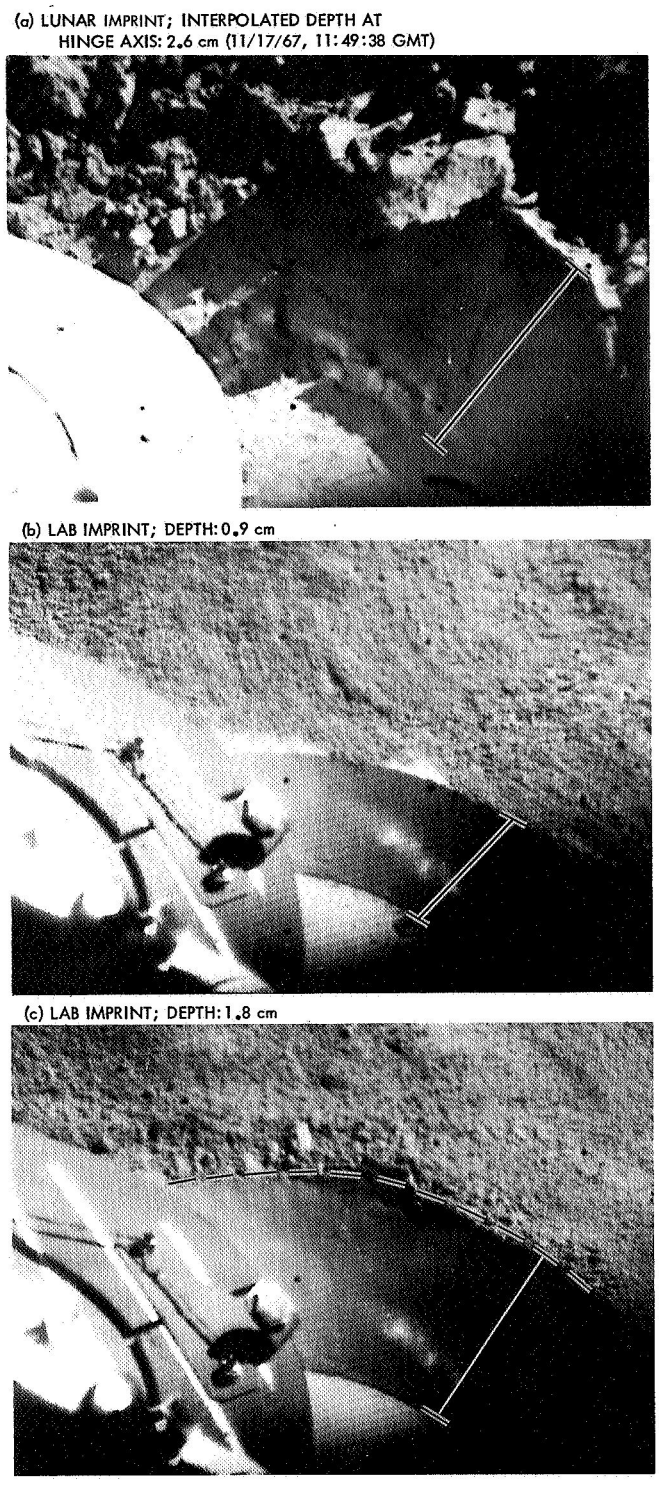

Fig. 14. Footpad 2 imprints, *Surveyor VI* hop landing

6. Surveyor VII. Depth of the footpad 2 imprint, as shown in Fig. 16, is 4.7 ±0.5 cm. However, shadow measurements made at low sun angle indicated that 1.0 ±0.5 cm of this rim consisted of soil ejected at first impact. Therefore, the depth of penetration at first impact is 3.7 ±1.0 cm.

The depth of footpad 3 at final rest position was calculated from shadow measurements to be 4.0 ±1.0 cm (Ref. 5).

B. Crushable Block Imprints

Part of the imprint made by the *Surveyor I* crushable block 3 can be seen in Fig. 17. Depth as determined by length of shadow comparisons was 2.9 ±0.5 cm.

Crushable block imprints made by *Surveyors III* and *V* were blocked from view by the spacecraft structure. The addition of an auxiliary mirror on *Surveyor VI* permitted block 3 to be viewed after the initial landing, as shown in Fig. 18. By comparing photographs taken just before launch at Cape Kennedy and after final camera adjustment and calibration, it was possible to make a detailed scale drawing of this imprint (Fig. 19); the depth is 3.0 ±0.5 cm. Because of the hop, the imprint made by crushable block 2 was visible to the camera (Fig. 20); the depth is 1.7 ±0.5 cm. The depth of the *Surveyor VII* crushable block 2 imprint (Fig. 21) is 2.5 ±0.5 cm.

III. Results: Relation of Footpad Penetration to Lunar Soil Bearing Strength

Detailed study of *Surveyor* landings (four in mare areas, one in a highland area) indicate that the lunar soil has remarkably uniform bearing strength properties. Data are available for seven touchdowns of the five *Surveyors*, including two of the three touchdowns of the *Surveyor III* landing and the two touchdowns of the *Surveyor VI* landing. Of these seven touchdowns, the *Surveyor I*, *Surveyor VI* initial touchdown, and *Surveyor VII* provided normal vertical final descents onto nearly horizontal surfaces.

(a) LUNAR IMPRINT; INTERPOLATED DEPTH AT POINT MARKED: 6.5 cm (11/21/67, 11:08:31 GMT)

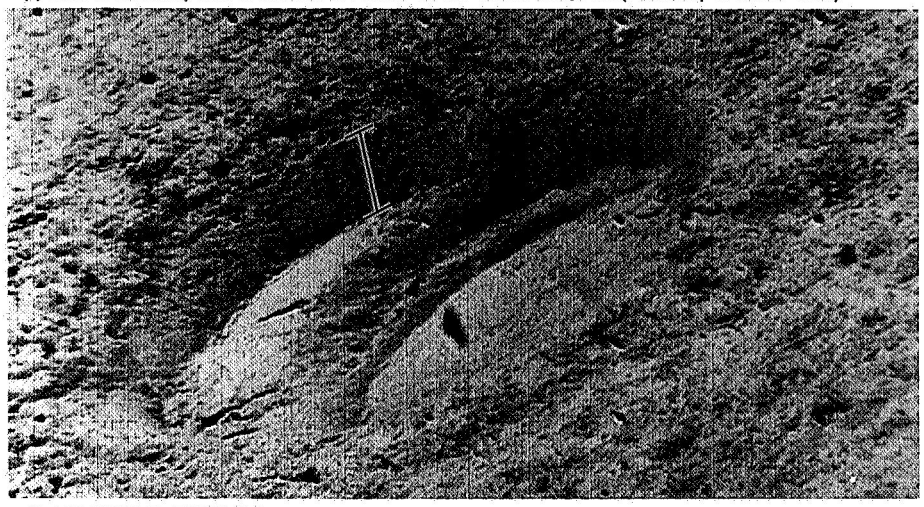

(b) LAB IMPRINT; DEPTH: 3.8 cm

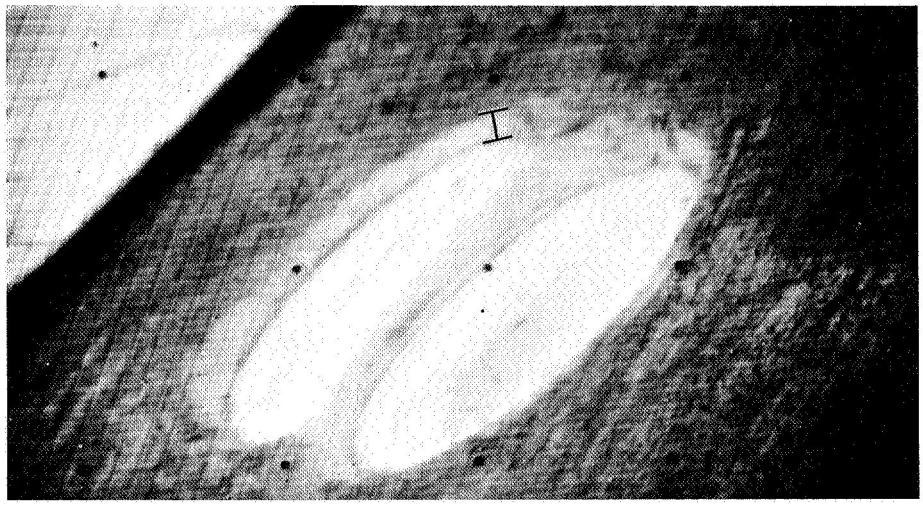

(c) LAB IMPRINT; DEPTH: 6.0 cm

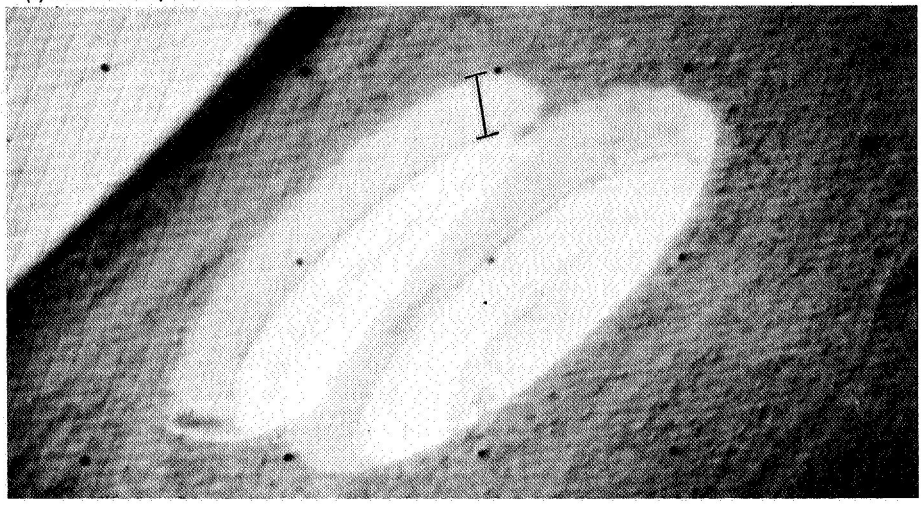

Fig. 15. Footpad 3 imprints, *Surveyor VI* initial landing

(a) LUNAR IMPRINT; INTERPOLATED DEPTH: 4.7 cm (1/14/68, 01:25:34 GMT)

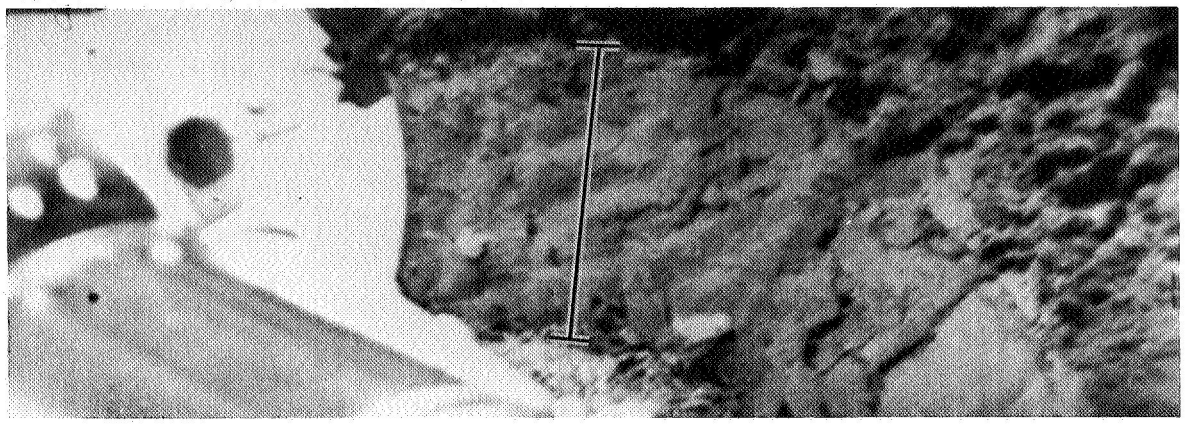

(b) LAB IMPRINT; DEPTH: 3.9 cm

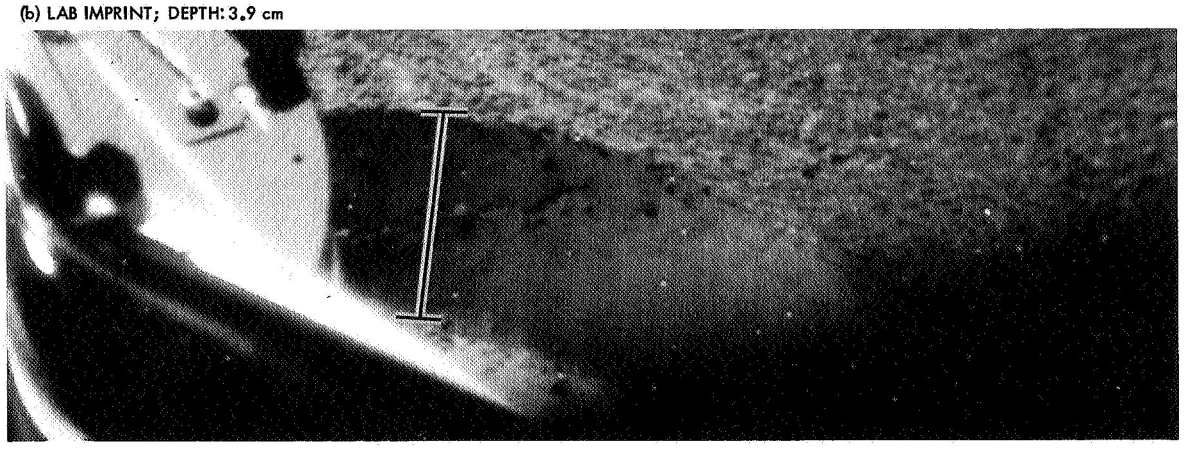

(c) LAB IMPRINT; DEPTH: 4.6 cm

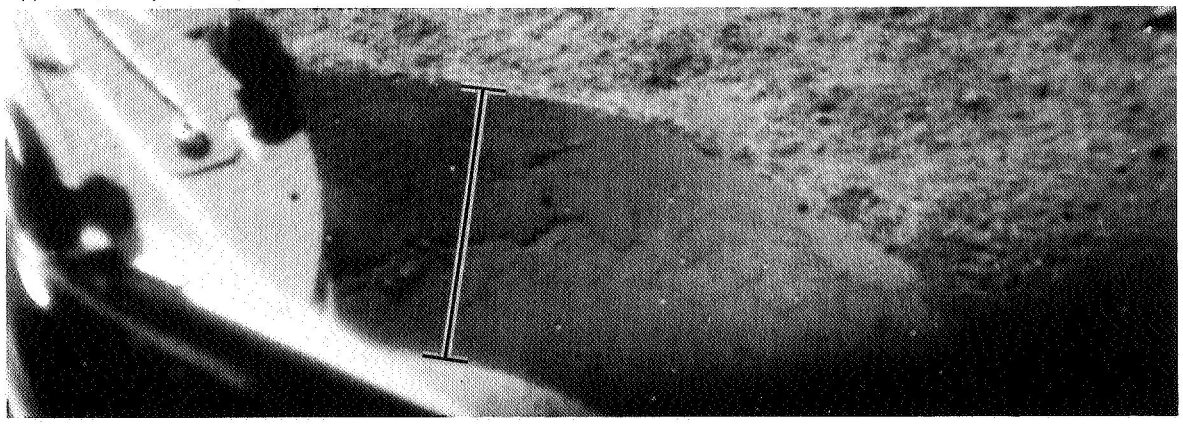

Fig. 16. Footpad 2 imprints, *Surveyor VII*

(a) LUNAR IMPRINT; INTERPOLATED DEPTH: 2.9 cm

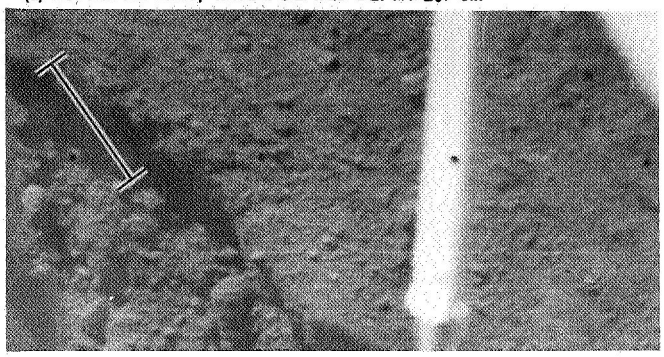

(b) LAB IMPRINT; DEPTH: 1.5 cm

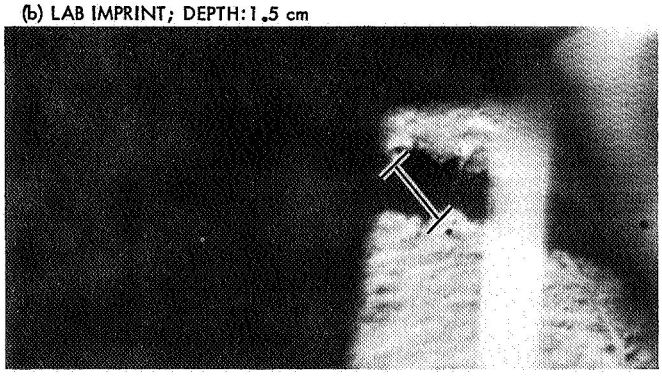

(c) LAB IMPRINT; DEPTH: 2.8 cm

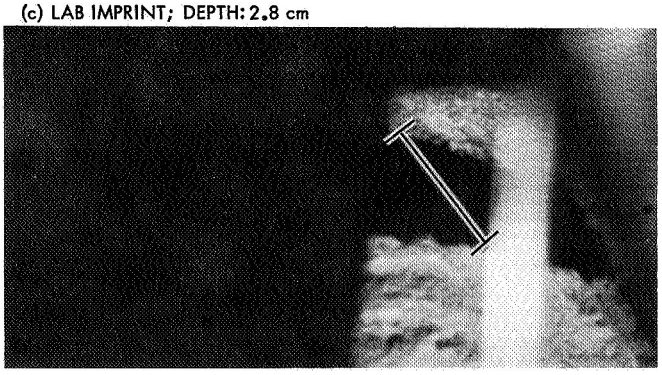

Fig. 17. Crushable block 3 imprints, *Surveyor I* (6/03/66, 06:34:09 GMT)

(a) LUNAR IMPRINT (11/11/67, 01:28:20 GMT)

(b) LAB IMPRINT; DEPTH: 1.9 cm

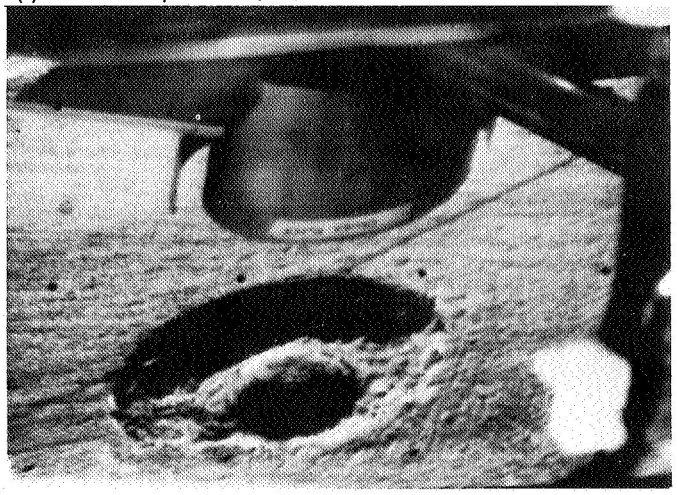

(c) LAB IMPRINT; DEPTH: 3.0 cm

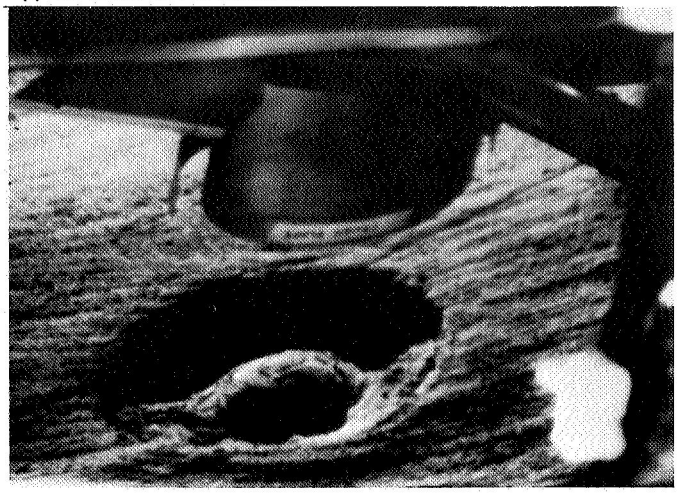

Fig. 18. Crushable block 3 imprints, *Surveyor VI*

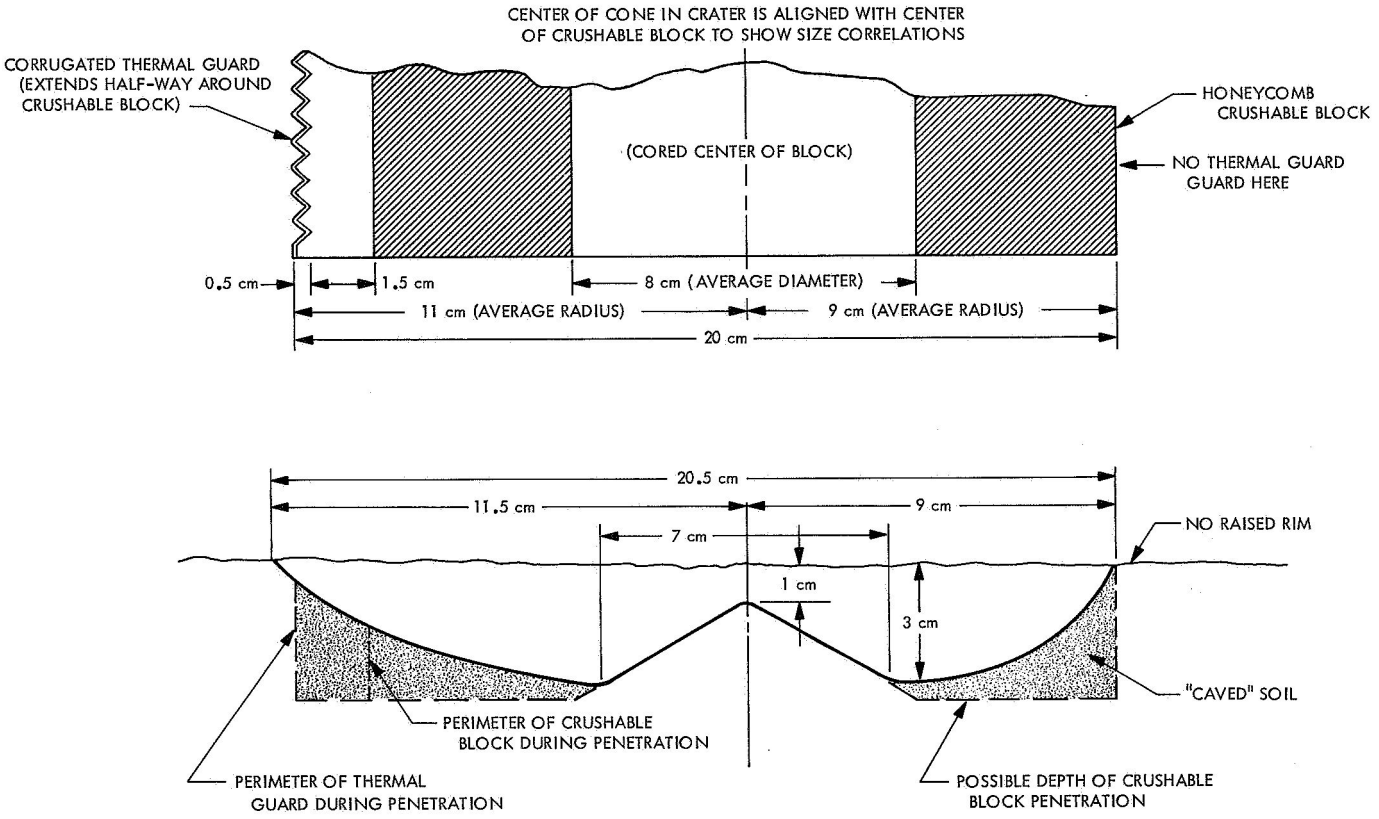

Fig. 19. Cross section of the 20-cm diameter imprint visible through the auxiliary mirror in the pre-hop picture (Fig. 18a)

(a) LUNAR IMPRINT; INTERPOLATED DEPTH: 1.7 cm (11/23/67, 10:53:19 GMT)

(b) LAB IMPRINT; DEPTH: 1.7 cm

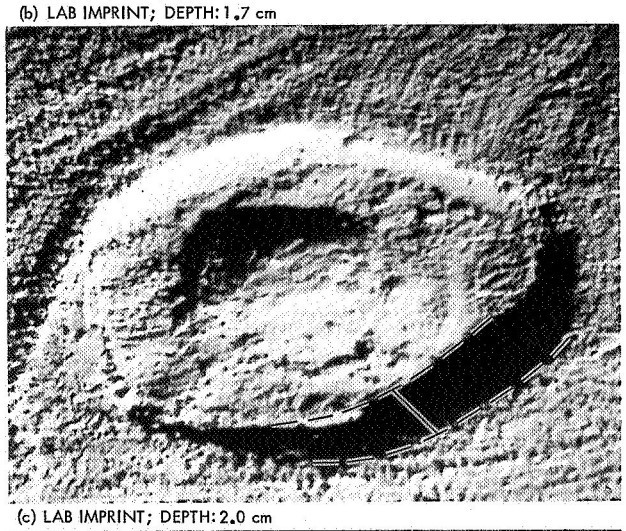

(c) LAB IMPRINT; DEPTH: 2.0 cm

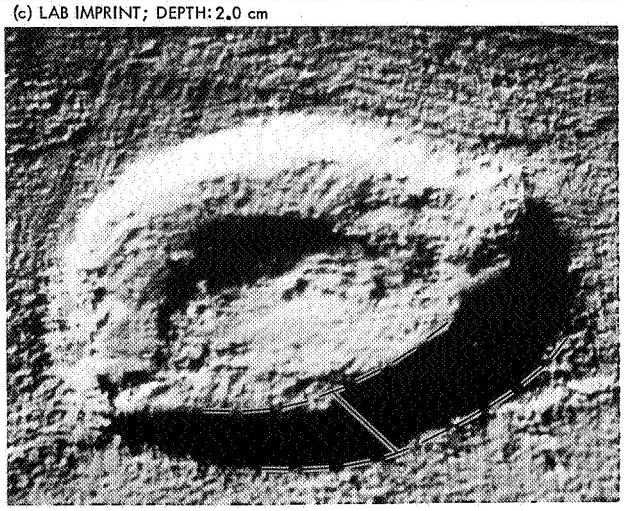

Fig. 20. Crushable block 2 imprints, *Surveyor VI* (as seen post-hop)

(a) LUNAR IMPRINT; INTERPOLATED DEPTH: 2.5 cm (1/10/68, 05:45:23 GMT)

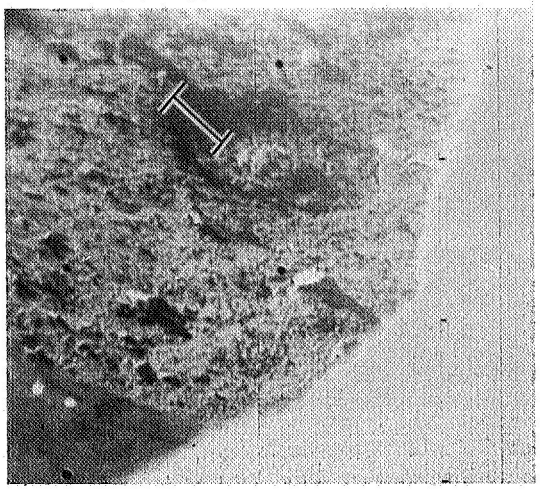

(b) LAB IMPRINT; DEPTH: 2.3 cm

(c) LAB IMPRINT; DEPTH: 3.5 cm

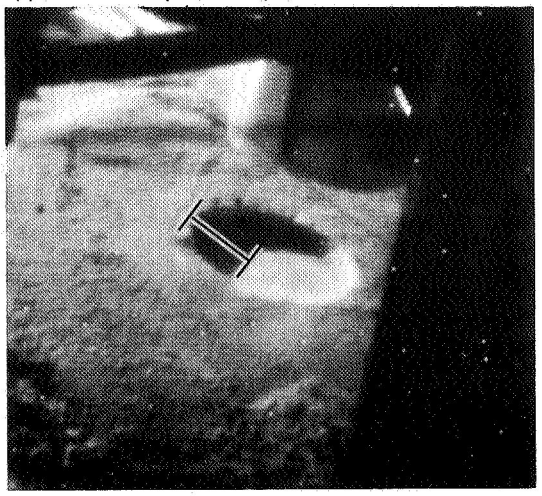

Fig. 21. Crushable block 2 imprints, *Surveyor VII*

Table 2. *Surveyor* penetration values

Spacecraft landing	Footpad penetration, cm					Crushable block penetration, cm	
	At first impact			At final position			
	Footpad 2	Footpad 3	Footpad 1	Footpad 2	Footpad 3	Block 2	Block 3
Surveyor I				3.0 ±1.0	2.0 ±1.0		2.9 ±0.5
Surveyor III second landing event	3.5 ±1.0		3.0 ±1.0				
Surveyor III final landing event	2.1 ±0.5	4.3 ±1.0					
Surveyor V	10.5 ±2.0						
Surveyor VI initial landing	3.5 ±1.0	2.6 ±0.5				1.7 ±0.5	3.0 ±0.5
Surveyor VI hop landing	6.5 ±1.0				3.0 ±1.0		
Surveyor VII	3.7 ±1.0				4.0 ±1.0	2.5 ±0.5	

The second and third touchdowns of *Surveyor III* were on the 10–13-deg inner slope of a large crater, *Surveyor V* on the 19–20-deg inner slope of a small crater, and the hop landing of *Surveyor VI* had a substantial horizontal component to the landing force. Because of these unique circumstances, these four landings had significant horizontal forces that caused the spacecraft footpads to skid, digging deeper into the soil and throwing more ejecta for greater distances than during the other three spacecraft landings. As listed in the bottom row of Table 1 for *Surveyor III*, *Surveyor V*, and *Surveyor VI* (hop landing), soil ejected by the footpads was thrown 70, 80, and 90 cm, respectively; for *Surveyor I*, the *Surveyor VI* initial landing, and *Surveyor VII*, soil was thrown only 40–50 cm.

The three deepest footpad penetrations (Table 2) are:

(1) 10.5 cm for *Surveyor V*.

(2) 6.5 cm for the hop landing made by *Surveyor VI*.

(3) 4.3 cm for *Surveyor III*.

Footpad penetrations for all other landings range from only 2.1 to 3.7 cm.

In studies of *Surveyor* landing forces versus depth of penetration, direct comparisons of peak axial shock-absorber forces for the different spacecraft cannot be made because major redesign of the shock absorbers during the missions, as well as different spacecraft orientations for the landings, caused substantial changes in shock-absorber responses. However, R. Jones (Ref. 10), by using computer stress analyses, has derived the landing forces at the footpads for each *Surveyor* mission. Using the footpad 2 measurements reported here as the prime penetration data for each mission, his calculations of the average bearing strength for *Surveyor I*, *Surveyor VI* initial landing, and *Surveyor VII* were 5.10, 5.77, and 5.85 N/cm², respectively (Table 3). As previously explained, these three *Surveyors* are considered the prime examples of normal landings; i.e., for near vertical descents onto almost horizontal surfaces.

The maximum and minimum values for bearing strength per centimeter of penetration are also given in Table 3; averages of bearing strength per centimeter of penetration for *Surveyors I*, *VI*, and *VII* are 1.70, 1.65, and 1.58 N/cm²/cm, respectively. These values show remarkable similarity in bearing strength for such widely separated lunar landing sites.

Table 3. Bearing strengths derived from footpad 2 penetration

Surveyor	Footpad 2 penetration, cm	Av bearing strength, N/cm²	Bearing strength/cm of penetration, N/cm²/cm		
			Min	Max	Av
I	3.0 ±1.0	5.10	1.00	2.40	1.70
VI[a]	3.5 ±1.0	5.77	1.00	2.30	1.65
VII	3.7 ±1.0	5.85	1.00	2.25	1.58

[a]Initial landing.

Acknowledgment

The assistance of William Peer, Jet Propulsion Laboratory, who helped to perform the laboratory simulations, is gratefully acknowledged.

References

1. Christensen, E. M., et al., "Lunar Surface Mechanical Properties," *Surveyor I Mission Report: Part II. Scientific Data and Results,* Technical Report 32-1023, pp. 69–85. Jet Propulsion Laboratory, Pasadena, Calif., Sept. 10, 1966.
2. Christensen, E. M., et al., "Lunar Surface Mechanical Properties," *Surveyor III Mission Report: Part II. Scientific Results,* Technical Report 32-1177, pp. 111–153. Jet Propulsion Laboratory, Pasadena, Calif., June 1, 1967.
3. Christensen, E. M., et al., "Lunar Surface Mechanical Properties," *Surveyor V Mission Report: Part II. Science Results,* Technical Report 32-1246, pp. 43–88. Jet Propulsion Laboratory, Pasadena, Calif., Nov. 1, 1967.
4. Christensen, E. M., et al., "Lunar Surface Mechanical Properties," *Surveyor VI Mission Report: Part II. Science Results,* Technical Report 32-1262, pp. 47–108. Jet Propulsion Laboratory, Pasadena, Calif., Jan. 10, 1968.
5. Choate, R., et al., "Lunar Surface Mechanical Properties," *Surveyor VII Mission Report: Part II. Science Results,* Technical Report 32-1264, pp. 77–134. Jet Propulsion Laboratory, Pasadena, Calif., Mar. 15, 1968.
6. Choate, R., et al., "Lunar Surface Mechanical Properties," *Surveyor Project Final Report: Part II. Science Results,* Technical Report 32-1265, pp. 137–194. Jet Propulsion Laboratory, Pasadena, Calif., June 15, 1968.
7. Scott, R. F., and Roberson, F. I., "Soil Mechanics Surface Sampler: Surface Tests, Results, and Analyses," *Surveyor III Mission Report: Part II. Scientific Results,* Technical Report 32-1177, pp. 69–110. Jet Propulsion Laboratory, Pasadena, Calif., June 1, 1967.
8. Scott, R. F., and Roberson, F. I., "Soil Mechanics Surface Sampler," *Surveyor VII Mission Report: Part II. Science Results,* Technical Report 32-1264, pp. 135–185. Jet Propulsion Laboratory, Pasadena, Calif., Mar. 15, 1968.
9. Scott, R. F., and Roberson, F. I., "Soil Mechanics Surface Sampler," *Surveyor Project Final Report: Part II. Science Results,* Technical Report 32-1265, pp. 195–207. Jet Propulsion Laboratory, Pasadena, Calif., June 15, 1968.
10. Jones, R. H., "Lunar Surface Bearing Strength Characteristics from *Surveyor* Touchdown Data," *J. Geophys. Res.* (to be published).
11. Spencer, R. L., *Determination of Footpad Penetration Depth From Surveyor Spacecraft Shadows,* Technical Report 32-1180. Jet Propulsion Laboratory, Pasadena, Calif., Oct. 15, 1967.

Optical Systems and Station Procedures for the *Surveyor VII* Laser Pointing Test

Compiled
by
M. S. Shumate
Jet Propulsion Laboratory
Pasadena, California
for the
*Surveyor Working Group on Laser Tests**

I. Introduction

The *Surveyor VII* Laser Pointing Test, conducted during the active portion of the *Surveyor VII* mission, served to verify procedures for aiming lasers at a specific point on the lunar surface. This paper presents a description of the optical systems and alignment procedures used by each of the six earth-based stations participating in the test.

During one phase of the *Surveyor VII* mission on the lunar surface, the television camera was used to take pictures of the earth while several earth-based stations were aiming argon-ion laser beams at the *Surveyor VII* position. A description of the Laser Pointing Test and its scientific results has been presented by C. O. Alley and D. G. Currie in Refs. 1 and 2. The material presented in these references did not discuss the optical system details of each of the six individual stations.

All six stations used argon-ion lasers as the light source, and reduced the laser output beam divergence to acceptably small angles by the use of beam expanding telescopes. The expanded beams were then aimed at the *Surveyor VII* position on the lunar surface.

The following sections of this paper contain enough information to permit the interested reader to make an objective comparison of the methods used by each station. The source of the material used by the author for this paper was the individual station reports that were submitted to the Laser Working Group after the

*C. O. Alley, Chairman, University of Maryland; L. H. Allen, Jet Propulsion Laboratory; H. Bostick, Lincoln Laboratories; J. Brault, Kitt Peak National Observatory; D. G. Currie, University of Maryland; J. E. Faller, Wesleyan University; H. Plotkin, Goddard Space Flight Center; S. Poultney, University of Maryland; M. Shumate, Jet Propulsion Laboratory.

Surveyor VII mission was completed. The author has attempted to organize each station's contribution into a common format, with enough detail so that the reader can understand the basic optical system used by each station. Emphasis has been placed upon each station's method of collimating the laser beam expanding optics, and boresighting the expanded beam to the guide optics.

II. Lexington Station

A. Site Data

1. Station operator: Massachusetts Institute of Technology, Lincoln Laboratories.

2. Station location: Lexington, Massachusetts.

3. Basic tracking mount: Azimuth-elevation type heliostat carrying a 16-in. mirror. Tracking motion was provided in azimuth only, with elevation corrections inserted by hand.

4. Laser: Nominal 3.5-W multiline, loaned by Spacerays, Inc.

B. Optical System Description

The output beam from the laser was directed, through a 10:1 Galilean beam expanding telescope, toward an almost totally reflecting beam splitter, and into the tracking mount (Fig. 1). Visual tracking was accomplished by direct viewing through a guide telescope that was boresighted to the laser beam. The beam spread angle was adjusted to 20 arc-s.

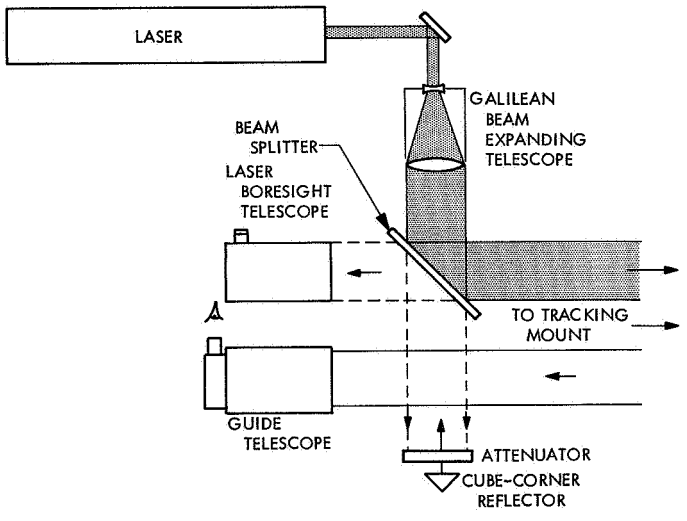

Fig. 1. Lincoln Laboratories station optical system

C. Boresighting Procedure

As shown in Fig. 1, the beam out of the Galilean beam expander was directed to a beam splitter. The transmitted beam was retroreflected by a cube corner reflector back off the beam splitter and into an alignment telescope. The crosshair reticle in the alignment telescope provided an accurate reference, which was then used to properly align the 3-in. guide telescope to an appropriately chosen celestial reference point.

An attenuator was placed in the beam to facilitate viewer safety and alignment accuracy. The alignment accuracy was thought to be ~5 arc-s.

D. Moon Pointing Procedure

With the laser beam and the guide telescope properly boresighted, as indicated by the alignment telescope, the tracking mount was driven in azimuth at a rate matching the rate of the moon, with elevation corrections being inserted by the operator to keep the system aimed at the *Surveyor VII* landing site.

III. Waltham Station

A. Site Data

1. Station operator: Raytheon/Wesleyan University.

2. Station location: Raytheon Research Laboratory, Waltham, Massachusetts.

3. Basic tracking mount: A 6-in. 2-mirror portable coelostat.

4. Laser: Research model developed by Raytheon, located inside a Raytheon building, nominally 50 W, but with power output changing over the period of the tests.

B. Optical System Description

The beam from the laser was directed outside the building by several mirrors through a hole in the wall and into a fixed 4-in. f/15 beam expanding telescope (Fig. 2), and thence to the coelostat.

The condensing lens was followed by a focal plane diaphragm with a No. 80 hole (0.0135-in. diameter), a clear pellicle beam splitter, and the 4-in. f/15 primary objective lens. Guiding was accomplished by providing an appropriate eyepiece at the side arm focus, with the operator's eye protected by a yellow filter.

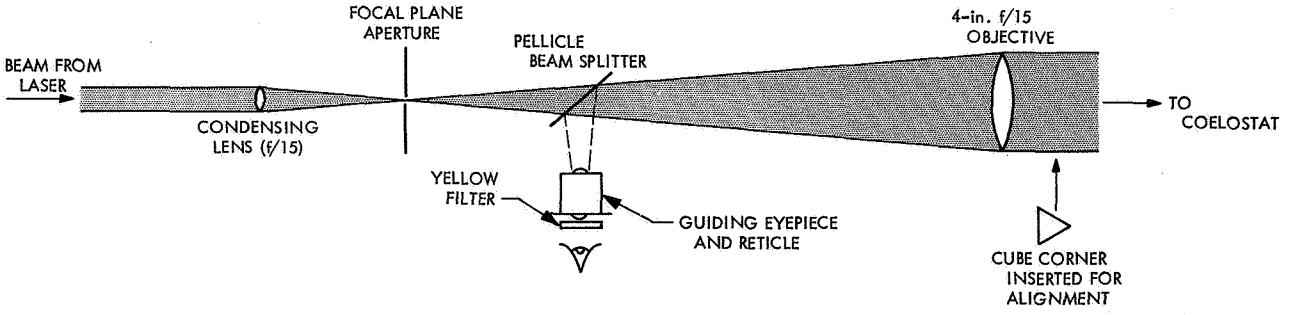

Fig. 2. Raytheon/Wesleyan station optical system

The expanded beam was directed into the coelostat, which was adjusted to track the moon by using an appropriate drive frequency for the synchronous drive motor.

C. Alignment and Boresighting Procedure

Alignment of the optical system consisted of assuring that the laser beam passed through the condensing lens, the focal plane pinhole, and the primary lens.

Boresighting was accomplished by adjusting a crosshair reticle located in the viewing eyepiece to coincide with the image of the focal plane pinhole, attained by placing a cube-corner reflector in front of the primary.

Some problems were encountered with the high-power laser beam causing thermal distortions in some of the optical mirrors used to direct the laser beam out of the laboratory toward the optical apparatus.

D. Moon Pointing Procedure

Guiding on the moon was accomplished by an observer looking through the viewing eyepiece, and aiming at the appropriate moon features. During the latter series of runs, the coelostat was guided in a manner to sweep the laser beam back and forth across the *Surveyor* spacecraft location.

IV. Norwalk Station

A. Site Data

1. Station operator: Perkin-Elmer Corporation, Norwalk, Connecticut.

2. Station location: New Canaan, Connecticut.

3. Basic tracking mount: A 24-in. astronomical-type cassegrain telescope, designed by Boller and Chivens, on an equatorial mount with quartz optics for both primary and secondary. The telescope is equipped with 6- and 4-in. finder scopes.

4. Laser: Nominal 2-W multiline, single mode, developed by Perkin-Elmer. Power for the laser was supplied by a 10-kW portable generator at the observatory. The laser was cooled by a closed-cycle water cooling system.

B. Optical System Description

The optical system used for the experiment is shown in Fig. 3. The laser itself was mounted on the sidewall of the 24-in. telescope tube. The 6-in. finder scope was equipped with a special dark-field reticle for moon feature tracking.

The collimated argon beam was folded down to two microscope objectives (L_1 and L_2), which are used to provide a known amount of beam divergence by moving L_1 along the optic axis. These lenses were mounted on adjustable slides to aid in the alignment of the system. A dichroic mirror, with angular adjustments, reflected 99% of the argon laser beam to a "matching" microscope objective L_3, and the output of this lens provided an f/16 beam to the telescope.

This design permitted the divergence of the outgoing beam to be varied by an adjustment of a movable stage that had a readout attached to it. Thus, the transmitted beam divergence could be changed from atmospheric limited conditions to beam spreads up to 10 arc-s. This divergence change could be accomplished during the course of the experiment.

C. Alignment and Boresighting Procedure

The 24- and 6-in. telescopes were boresighted by observing one of the moons of Jupiter. The image was centered on the crosshairs of the 6-in. telescope and the

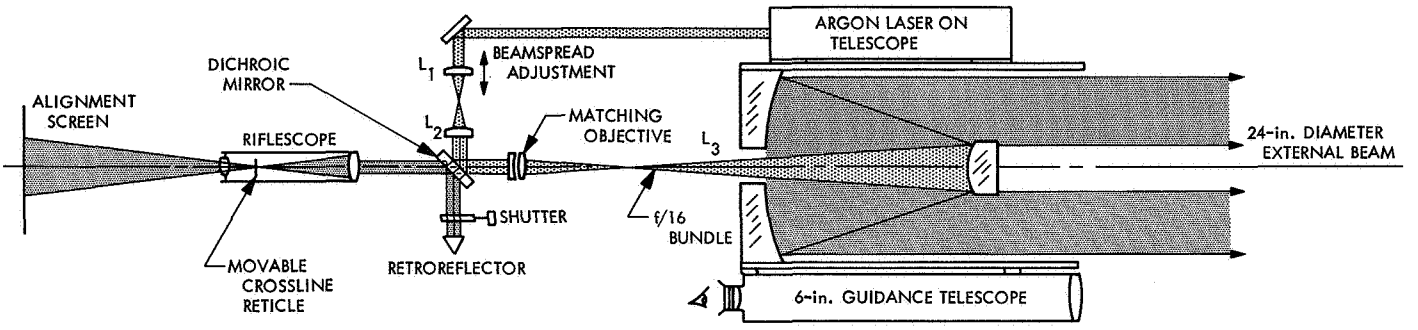

Fig. 3. Perkin-Elmer station optical system

movable crosshairs on the riflescope were then centered over the image as seen through the 24-in. telescope.

To align the laser to the 24-in. telescope, use is made of the 1% of collimated light that leaks through the dichroic mirror. This light is reflected by a cube-corner reflector back into the riflescope, and is too intense to be viewed by an observer. Therefore, adjustments are made by placing a white screen behind the riflescope and observing the image of the crosshairs and the focused laser beam on the screen. Boresighting of the laser and telescope is then achieved by adjusting the lens L_1 and the dichroic mirror.

A final check on vignetting in the outgoing system was made by observing the exit beam distribution when projected onto the inside of the observatory dome. If vignetting was present, its effect could be removed by a combined adjustment of L_1 and the dichroic mirror such that the return beam from the retroflector remained centered in the crosshairs of the riflescope.

D. Moon Pointing Procedure

The normal equatorial drive on the telescope was modified so that the polar axis was exactly tracking the crater Tycho. The rate was adjusted until the drift of the dark reticle was less than 1 Tycho pinnacle movement in 5 min. The drive was calibrated to provide a fast sweep and a slow sweep in the polar axis so that the telescope moved, respectively, 1 Tycho crater radius in 1 min east and a corresponding speed west. The drive was recalibrated each night of the observation.

The declination drive was under control of the observer, who used a very fine offset control button to keep the north-south reticle on the *Surveyor VII* landing site. The button was depressed approximately once every 10 s of actual observation time. The optical design of the equipment permitted alignment of the laser beam with the main 24-in. telescope optical axis as well as to the 6-in. boresight telescope.

The rms aiming error depended, for all practical purposes, on the illumination of the landing site (contrast of Tycho, Tycho A, and Tycho U, F, and T) and both turbulence and transparency of the local atmosphere. Quantitatively, the equipment aiming error in the east-west direction was probably under 0.5 arc-s, while north-south was under 1 arc-s. Systematic errors in pointing were minimized by boresighting on the lunar features to within 5 min of time before the experiment at the appropriate equipment inclinations. A point-ahead offset of 1.2 mi in the easterly direction on the moon was used. Following the 10 min of operation, the boresight and alignment were checked and no driftoff was observed.

V. Greenbelt Station

A. Site Data

1. Station operator: Goddard Space Flight Center (GSFC).

2. Station location: Goddard Optical Research Facility, 2 mi NE of GSFC, Greenbelt, Maryland.

3. Basic tracking mount: Modified Nike-Ajax radar pedestal, in an azimuth-elevation configuration. There are three optical systems on the mount: (1) an alignment telescope for direct viewing, (2) a 16-in. f/15.4 telescope with an image orthicon television camera for remote viewing, and (3) a 5.5-in. objective lens used to collimate the laser beam that is brought up through the pedestal by a series of mirrors (Fig. 4).

4. Laser: Nominal 10-W multiline, developed by Radio Corporation of America for GSFC for another project.

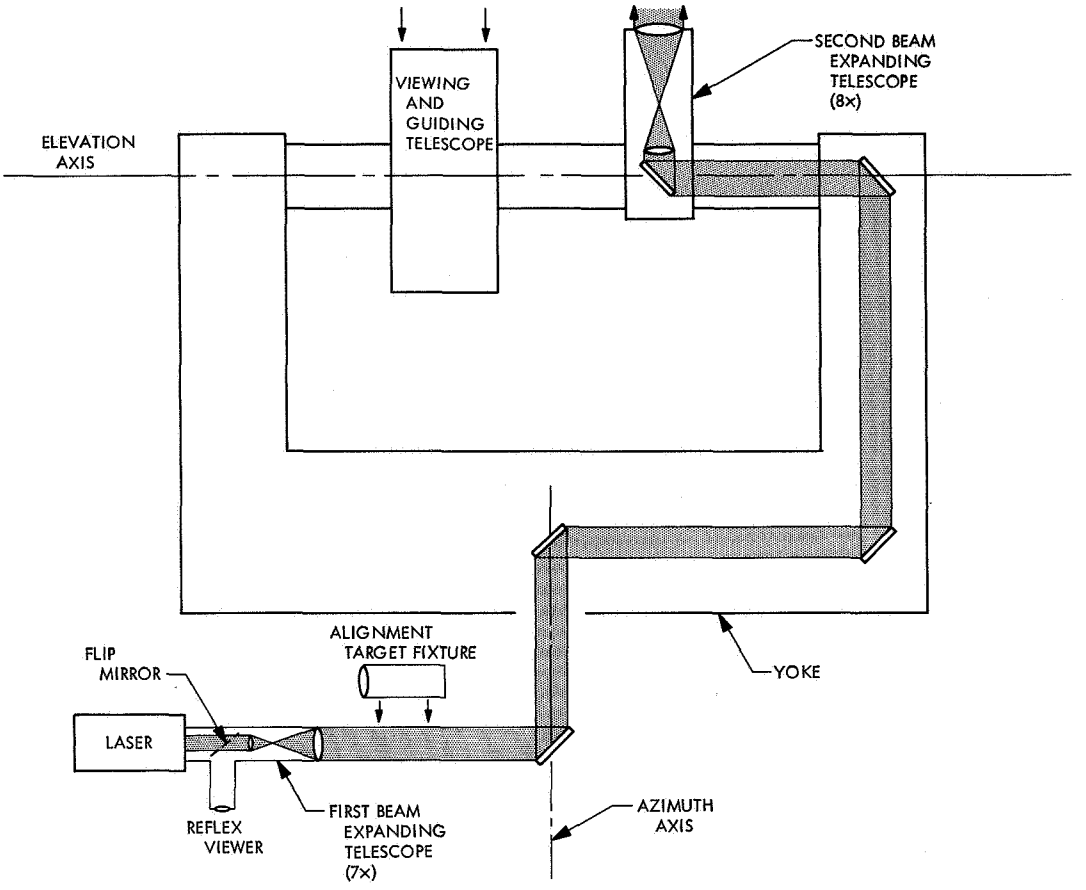

Fig. 4. Goddard Space Flight Center station optical system

Output beam diameter is 2.5 mm and output beam angle is 7 arc-min.

B. Optical System Description

Attached to the output end of the laser was a 7-power telescope combined with a reflex viewer. By inserting a flip-mirror, the operator could look through the transmitter optical system in the direction that the beam would travel. After passing through the 7-power telescope, which consisted of two positive lenses, the beam had a diameter of 1.75 cm and a divergence of approximately 58 arc-s.

At this point, the laser beam was sent up into the rotation axes (see Fig. 4). A fixed, flat 45-deg mirror brought the beam vertically up the azimuth axis into the moving yoke, where a diagonal mirror rotating with the platform reflected it horizontally to one of the yoke arms. A third mirror brought it up to the elevation axis, a fourth reflected it along the elevation axis, and a fifth finally brought the beam out parallel to the optical axis.

Each of the flat mirrors was adjustable with micrometer screws in two degrees of freedom. They were aluminum coated mirrors, with a standard SiO overcoating. Reflectivity at each mirror was estimated (but not measured) to be about 85%.

The second telescope had 8-power magnification, with an output lens 5½ in. in diameter. At the exit aperture, the laser beam was 14 cm in diameter and had a divergence angle of about 7 arc-s. These figures are based upon measured divergence of the raw laser beam and measured power of the telescopes, which were adjusted using a laboratory collimator. No independent measurement of output beam divergence was possible.

C. Alignment and Boresighting Procedure

Referring once more to Fig. 4, considerable care was taken to insure that the transmitted laser beam was directed along the rotation axes, and parallel with the viewing axis of the 16-in. telescope. It should be recalled that the Nike-Ajax mount was not built to the standards

of astronomical precision. Its overall accuracy, in terms of bearing eccentricity, orthogonality of axes, and deflections is probably about 10 arc-s, which is sufficient for the intended satellite tracking purposes. Therefore, to get higher accuracy for this experiment, in each case, the final adjustments were made by sighting on stars in the vicinity of the expected position of the moon, before each *Surveyor* test. Over limited regions of the sky, the estimated lineup precision was within several arc-s.

With the mirrors aligned using the autocollimation techniques, the laser beam was then aligned to the optical system by using the following method. To determine the direction of the laser beam, a "target fixture" was placed in front of the 7-power telescope. The fixture consisted of a lens that collected the entire laser beam and focused it onto a thin paper or aluminum foil target. With the flip-mirror of the reflex viewer withdrawn from the beam, the laser shutter was opened for a short time so that a small hole (0.002-in. diameter) was pierced in the target. When the flip-mirror is re-inserted, the target hole can be seen in the reflex viewer. A crosshair in the reflex eyepiece was adjusted so that it bisected the target hole. This provided a reference direction that coincided with the direction of the beam.

With the target fixture removed, the reflex viewer could be used to sight through the entire transmitter optical system. The crosshair indicated the point at which the laser beam would be aimed if the flip-mirror were removed and the laser beam turned on. This procedure was checked repeatedly by directing the beam onto a target board 1000 ft away. The beam was always centered at the target point to within a small fraction of its diameter, after the telescope was turned so that the reflex crosshairs fell on the target.

The 16-in. telescope and television system were then boresighted with the laser, as represented by the crosshair in the reflex viewer. The telescope could be set reliably onto a fixed distinct target to within an uncertainty corresponding to one encoder resolution element of ± 3.6 arc-s, using either the television system or the reflex viewer.

The tracking system was programmed to a star in the area of the sky where the actual experiment was to be conducted. Both the television fiducial point and the crosshairs were centered simultaneously on the star. In moving from one part of the sky to another, it was found that only a small adjustment was required to remove small errors that were apparently caused by deflection of the telescope tube or misalignment in the transmitter optical system. Just prior to conducting the experiment, the system was programmed to the very visible peak at the center of Tycho, and the relative alignment of the reflex viewer and the television system was checked again.

While the system was tracking, it was observed that the servo jitter was generally limited to the encoder resolution. The actual position display usually differed from the command position at most by ± 3.6 arc-s, and deviations of the target on the screen from the television fiducial point also corresponded to the same angular distance. During intervals in the experiment when the laser was off, the alignment was checked quickly through the reflex viewer; adjustments were never necessary.

The maximum power radiated from the laser was 11 W. Although the final transmitted power was not measured, we can estimate it as follows. There were 4 lenses in the two collimating telescopes, or 8 surfaces. If 5% of the power were lost at each surface, this would lead to a transmission of 66.4%, due to the lenses alone. There are, in addition, 5 mirror reflections, with an estimated loss of 15% per surface, leading to a transmission of 44.3%. Estimated power radiated is thus, $29.5\% \times 11\ \text{W} = 3.25\ \text{W}$. An additional factor should be inserted for transmission through the atmosphere, probably about 70%. The estimated beam power directed toward the moon is thus 2.28 W.

D. Moon Pointing Procedure

The basic operation is controlled from a trailer located near the mount. The equipment in the control trailer is dominated by a Raytheon 520 digital computer, which is used as an integral part of the telescope pointing servo system. Only the coefficients of the lunar orbit and time signals are inserted into the computer. It is then programmed to compute the necessary look angles to the *Surveyor VII* from the station in azimuth-elevation coordinates. These are compared 50 times per second with the output of digital encoders on the azimuth and elevation shafts, and the necessary control signals are developed to drive the telescope along the predicted path.

The shaft-angle encoders were Wayne-George BD-19-100 19 bit binary, with a resulting resolution of 2.47 arc-s. However, although this was the resolution actually utilized in the servo loop, the display presented to the

operator at the control console was expressed in thousandths of a degree, with a 0.001 deg or 3.6 arc-s as least significant figure.

The operator could also look at a television screen displaying the scene from the image orthicon camera on the 16-in. telescope. This was a special system that was built by General Electric. The scan raster consisted of 1000 horizontal lines per frame, at a rate of 10,000 horizontal lines per second and 10 vertical scans or frames per second. Horizontal resolution was about 500 lines. The television display represented a field of about 450 by 600 arc-s, or a scale of about 50 arc-s/in. on the monitor screen. This resulted in a convenient scale by which the moon could be observed, with the crater Tycho about 1 in. in diameter.

Under good viewing conditions, the surrounding craters and features were clearly identified in relation to the *Lunar Orbiters IV* and *V* pictures and Lunar Atlas charts. After locating the *Surveyor VII* coordinates on these reference charts, the corresponding location on the television display was usually pinpointed with an estimated uncertainty of 3 arc-s.

A bright square on the television raster, subtending 50 scan lines, served as a reticle and was used to mark the optical axis and pointing direction. In the ultimate application of the system, this square represented the limits of an acceptance gate for autotracking on illuminated point targets. For our present purposes, however, it was sufficient that the square could be positioned so that the upper right corner was centered in the field. It was then used as reference for all other optical alignment and boresighting procedures.

VI. Tucson Station

A. Site Data

1. Station operator: University of Maryland and Kitt Peak National Observatory.

2. Station location: Kitt Peak, near Tucson, Arizona.

3. Basic tracking mount: The McMath Solar Telescope (60-in.).

4. Laser: Nominal 2-W multiline, single mode, built by Spectra-Physics Corp., and loaned by Aerospace Corp.

B. Optical System Description

The output beam from the laser (Fig. 5) was directed through the condensing lens, and an Amici prism then directed the beam upward through a narrow split in a front surface (split) mirror. The diverging beam above the split mirror was directed into the McMath Solar Telescope.

Guiding was accomplished by using the side path directed by the split mirror. An appropriate field lens was placed close to the split mirror, with an exit pupil and a yellow safety filter arranged to aid the operator in positioning his eye in the proper location. A specially constructed reticle was placed in front of the field lens to provide appropriate reference marks as aids in locating the *Surveyor VII* landing site.

C. Alignment and Boresighting Procedure

The condensing lens and Amici prism were adjusted so that the upward going laser beam was directed along the optic axis of the telescope, and so that no vignetting of the laser beam occurred. The split mirror was positioned so that the laser beam passed through the slit, with the focal point occurring somewhat below the front surface of the mirror. The telescope focal plane was positioned so that it coincided with the plane of the guide reticle. The extreme focal length of the McMath telescope minimized errors caused by not having the

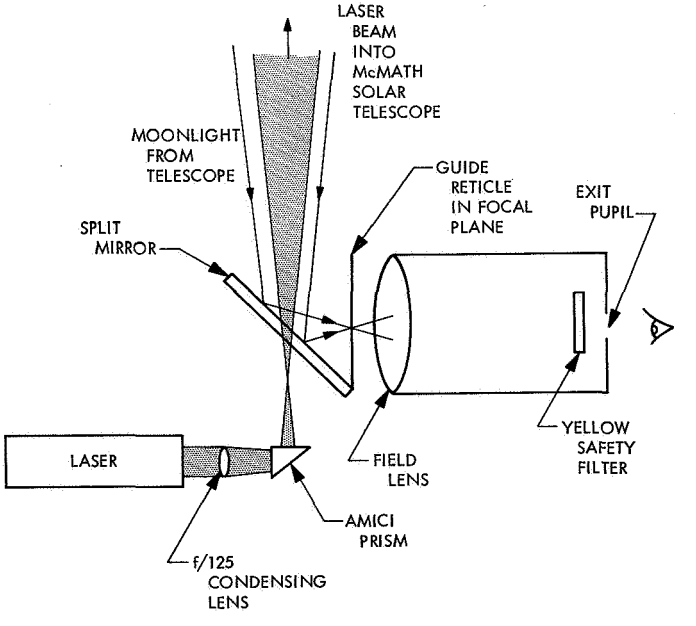

Fig. 5. University of Maryland and Kitt Peak National Observatory station optical system

guide reticle and the condensing lens focal point parfocal, although they were, in fact, quite close. This alignment procedure assures that the laser beam will be collimated when it leaves the telescope.

Boresighting was accomplished by adjusting the position of the reference spot on the guide reticle so that it coincided with the position of the laser spot when viewed in the slit of the split mirror from the exit pupil. Since the viewing optics were positioned so as to minimize parallax errors, the fact that the laser spot mentioned above was not in the focal plane produced no boresighting errors. Proper boresight was verified by direct observation of a nearby mountain peak.

D. Moon Pointing Procedure

The drive of the McMath telescope was adjusted to track the moon, with the guide operator providing small corrections to keep the moon image properly positioned on the guide reticle.

The guide reticle had many additional marks corresponding to the positions of several clearly defined craters and other lunar features near the *Surveyor VII* landing site. The reticles were constructed by using appropriate coordinates for each feature, computing the effects of libration and observatory locating, and scaling for the particular telescope used. During the Laser Pointing Test, the telescope remained adjusted so that the laser beam divergence was atmospheric-seeing limited, usually about 3 arc-s.

VII. Wrightwood Station

A. Site Data

1. Station operator: California Institute of Technology, Jet Propulsion Laboratory, Pasadena, California.

2. Station location: Table Mountain Observatory, Wrightwood, California.

3. Basic tracking mount: A 24-in. astronomical telescope, configured for an f/36 coudé focus, on an equatorial mount.

4. Laser: Nominal 2-W multiline, multimode, research laser loaned by Hughes Research Laboratories.

B. Optical System Description

The laser was mounted so that its output beam was directed along the optic axis of the telescope, through the position of the coudé focus. A condensing lens, whose focal length provided an f/36 converging beam, directed the laser beam through a 200-μ diameter pinhole in an aluminized mirror and into the telescope (Fig. 6). The light coming from the telescope was directed out at a 90-deg angle by the aluminized mirror, through a Schott OG-1 filter, and into a low-power microscope used as a long relief viewing eyepiece.

C. Alignment and Boresight Procedure

After the laser beam was aligned with the telescope optic axis, the condensing lens was inserted into the beam and positioned so that no vignetting of the outgoing beam occurred. The aluminized mirror was positioned so that the laser beam passed through the pinhole, with the waist of the converging beam lying in the front plane of the mirror. The low-power viewing microscope was adjusted so that it was focused on the pinhole, and so that no vignetting of the light coming out of the telescope occurred. The telescope was then adjusted so that a star image was in focus, as seen through the viewing microscope. Since the focal point of the laser beam, the telescope's focal plane, and the focal plane of the viewing optics were all coincident, the reciprocity of the ray paths through the telescope assured that the outgoing laser beam was collimated and aimed at the point in the viewing image that was obscured by the pinhole. The plate scale at the coudé focus was such that the diameter of the spot obscured by the pinhole was approximately 2 arc-s.

The collimation and boresight accuracies were checked by aiming the telescope at personnel stationed on a mountain ridge 2.7 km to the south of the observatory.

D. Moon Pointing Procedure

The telescope drive was adjusted to track the moon, with small guide corrections being supplied by the telescope operator looking through the low-power microscope. The telescope was positioned so that the pinhole obscured the lunar features that were around the *Surveyor VII* landing site. Guiding was aided by a crosshair reticle in the microscope eyepiece. During one of the Laser Pointing Tests, the telescope was guided so as to dither the laser beam around the *Surveyor* spacecraft position.

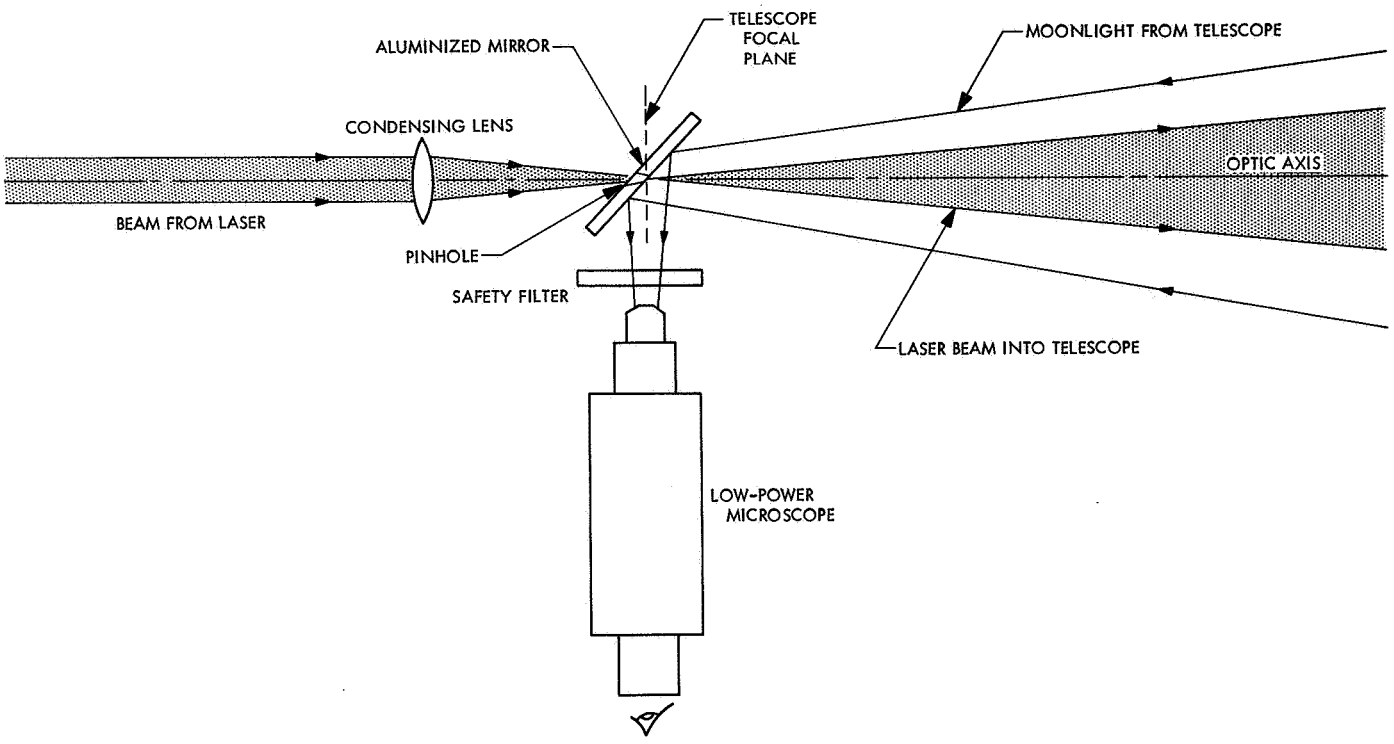

Fig. 6. Jet Propulsion Laboratory station optical system

Acknowledgment

The material presented in this paper has been contributed mainly by those associated directly with the operation of each of the six laser stations. The compiler has extensively abridged their contributions into a common format, and has tried to objectively eliminate unnecessary details in the interest of brevity.

The specific contribution of the following people is gratefully acknowledged:

(1) Massachusetts Institute of Technology, Lincoln Laboratories	Hoyt A. Bostick R. H. Kingston
(2) Raytheon Research Laboratories and Wesleyan University	James E. Faller
(3) Perkin-Elmer Corporation	Herbert F. Wischnia Morley Lipsett
(4) Goddard Space Flight Center	Henry H. Plotkin Herbert Richard
(5) University of Maryland and Kitt Peak National Observatory	Sherman Poultney C. O. Alley D. G. Currie James Brault
(6) California Institute of Technology, Jet Propulsion Laboratory	L. Harold Allen James W. Young

The compiler wishes to extend his apologies to these individuals for any misconceptions that may arise from his liberal editing procedures.

References

1. Alley, C. O., and Currie, D. G., "Laser Beam Pointing Tests," *Surveyor VII: A Preliminary Report*, NASA SP-173, pp. 289–294. National Aeronautics and Space Administration, Washington, D.C., 1968.

2. Alley, C. O., and Currie, D. G., "Laser Beam Pointing Tests," *Surveyor Project Final Report: Part II. Science Results*, Technical Report 32-1265, pp. 441–448. Jet Propulsion Laboratory, Pasadena, Calif., June 15, 1968.

Photometry and Polarimetry of the Earth

J. J. Rennilson
California Institute of Technology
Pasadena, California

H. H. Holt
U. S. Geological Survey
Flagstaff, Arizona

I. Introduction

During the *Surveyor VII* mission, the earth was easily visible in the narrow-angle mode of the television camera. The objectives of observing the earth were twofold: to measure the average luminance of the earth over as great a range of phase angles as possible, and to measure the degree and orientation of the polarization of light reflected from the earth. Each of these objectives was new, as the only complete previously existent data on the photometric and polarimetric properties of the earth were derived by indirect astronomical measurements of the moon.

This paper summarizes the results, thus far, of these measurements and does not attempt to explain or correlate the data with other factors, such as geographic location, weather conditions, etc.

II. Observing Conditions

The landed site of *Surveyor VII* at 11.47 deg W and 40.86 deg S positioned the earth at camera elevations ranging from 45 to 55 deg during the lunar day. Figure 1 shows the variation of phase angle of the earth with the terrestrial date during the mission. The circles on the figure indicate the times when camera exposures were made of the earth. The last two days of the mission were devoted to observations made on the average of once every two hours.

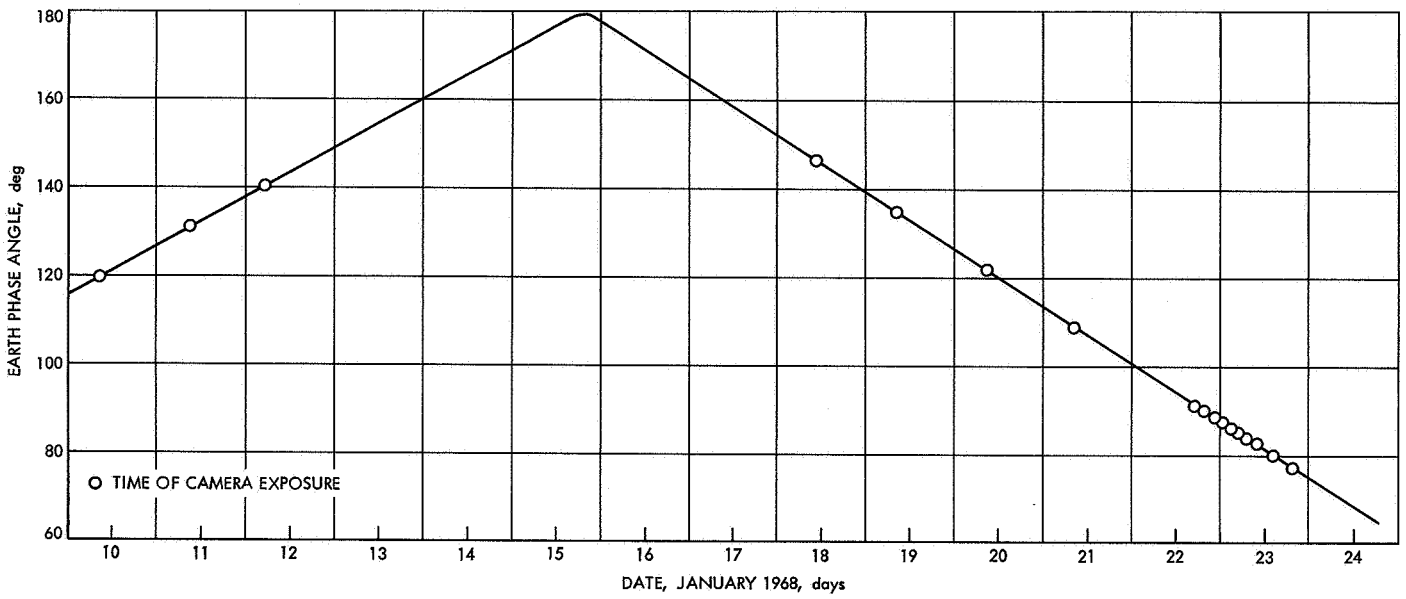

Fig. 1. Plot of phase angle of earth as seen from the *Surveyor VII* site

The general procedure in making these measurements was to expose the camera to the earth luminance such that the brightest portions would register a video signal just below the saturation level. A series of two frames each was then taken through each of the four filter positions. The camera was then opened one full iris setting; the above procedure was repeated. By using this technique, the entire range of earth luminances was measured by a camera response of more limited exposure latitude.

Close to the actual times of earth observation, a measurement was made of one of the three illuminated photometric targets on the spacecraft. The preflight calibration values for absolute luminance could be thus verified.

A total of 823 frames were taken of the earth during the lunar day. Not all of these frames were taken for photometric and polarimetric purposes. From the total number only 135 frames were selected for computer processing. The results given in this paper are the first reduction of these observations (Ref. 1).

III. Camera Parameters

A. Polarizing Filters

The *Surveyor VII* camera was equipped with an accurate position filter wheel so that the measurement with polarizing filters would be precise. The polarizing filters on this camera were formed of glass laminated, linearly polarizing dichroic (KN-36) material, 3 mm thick. The filters were cut such that their transmission axes were oriented at angles of 0, 45, and 90 deg when they were rotated into the light path. The 0-deg orientation was parallel to the mirror surface and perpendicular to the plane containing the mirror normal and the camera optical axis. The filter wheel, and thus the polarizing filters, are an integral part of the mirror housing and rotate with it. The fourth position on the wheel was a piece of clear glass with a coating of inconel of sufficient density so that the transmission of the glass was equal to that of the polarizing filters.

The exact position of the transmission axes of the filters with respect to the mirror assembly was determined in preflight calibration. A polarizing filter of the same type was mounted in a graduated rotating cell before the light source. The light source was positioned along the tilt axis of the camera. Thus, the mirror elevation axis and an exact 0-deg transmission axis of the first polarizing filter would be horizontal. The polarizing filter was then rotated until extinction, which was marked by a minimum camera signal, occurred. The angle was then read and the corresponding orientation of the polarizing filter in the filter wheel was then determined. This method was repeated for each filter position.

The measurement of the polarization of earth light was further complicated in the *Surveyor VII* camera by

the viewing mirror. The polarized earth light undergoes an alteration of type and orientation after reflection by the metallic mirror. In general, linearly polarized light incident on an overcoated aluminized mirror will be transformed into elliptical polarization. Measurement of this polarization by three linear analyzers will result in erroneous values dependent on the amount of elliptical polarization.

Figure 2 shows the effect of a metallic mirror on linear polarization at varying angles of incidence. For observation of the lunar surface especially close to the spacecraft at $i = 25$ deg (camera elevation -40 deg), the effect is not too serious. For the earth observation, however, incidence angles of 65–70 deg are the rule, and mirror effect is very important.

One method of eliminating this source of error is to measure the property of the mirror to alter the linear polarized light. Known amounts and orientations of linear polarized light are made incident on the mirror at various incident angles. The resultant elliptical polarization is then measured.

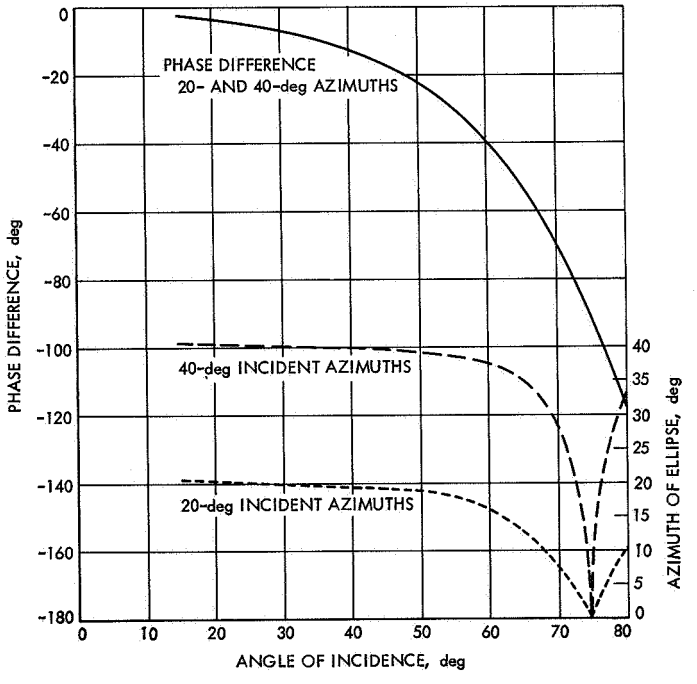

Fig. 2. Plot of elliptical polarization resulting from incident linear polarized light incident on a *Surveyor* mirror (phase difference is plotted against angle of incidence for azimuths of incident linear polarization of 20 and 40 deg; azimuth of incident light is measured from plane of mirror counter-clockwise; and azimuth angle of ellipse is also shown for 20 and 40 deg)

The capability of a metallic mirror to alter the polarization form of incident light may be described mathematically by a 4×4 matrix of coefficients, known as the Mueller matrix. A four-component vector, called the Stokes vector, completely describes any form of polarization. Thus, the resultant polarization form of reflected light specified by a Stokes vector can be calculated by premultiplying the incident polarized light (Stokes vector) by the Mueller matrix of the mirror. Thus,

$$\mathbf{S}' = M\mathbf{S}$$

The incident Stokes vector is then given by the equation $\mathbf{S} = M^{-1}\mathbf{S}'$.

In measuring partially polarized light using only three linear polarizing filters, the complete Stokes vector (which includes phase information) cannot be determined. Thus, an assumption must be made concerning the type of incident polarized light; e.g., that it is linear. In the case of the lunar surface, this is probably a reasonable assumption; however, it may be somewhat in doubt when applied to the earth. In this paper, however, only linear polarization is assumed.

B. Photometry

Photometric measurements of the earth were taken through the clear filter position, thus using the entire camera spectral response. Hence, the measurements would not be correct unless the spectral distribution of the scene closely corresponded with that used during calibration. Fortunately, the spectral power distribution of sunlight reflected from clouds was very similar to that of sunlight above the atmosphere. The light sources used to calibrate the television camera before flight possessed spectral power distributions very similar to the sun. Exact correction factors for even the slight deviation between the sunlight and these sources were determined for *Surveyor VII*.

For the clear position, the luminances have a correction factor of 1.17 and have been corrected for this paper. The parts of the earth, such as the oceans and continents, having different distributions must of necessity have larger correction factors. However, for this

paper, they were not estimated because of the large dominance of the cloud cover.

IV. Data Reduction

The computer processing of the selected earth frames follows the flow diagram outlined in Fig. 3. After selection of the most important frames (flight pictures), processing begins with analog to digital conversion.

The composite video signal is recorded during the mission on magnetic tape simultaneously with the photographic image. This composite signal consists of all associated data, such as horizontal and vertical synchronization pulses, camera parameters given in a pulse code, and video frame. The signal is recorded in the frequency domain.

The analog tape then is replayed at a reduced speed (from 60 to 7½ ips) and passed through a 30-kHz filter to a demodulator. The demodulator converts the composite video to voltages. The voltages are converted to digital values scaled at 8 bits. The most significant 6 bits are then recorded on digital magnetic tape. Digitized black is given the value of 63, and white of 00. The digital values are then rearranged in the computer, line by line, until a picture frame of 600 lines is complete. Each line is broken into 684 elements rather than the normal 600 elements in order to utilize more of the densely packed information (frequency) along a line. Thus, a digitized frame consists of 600 × 684 picture elements (or pixels as they are called).

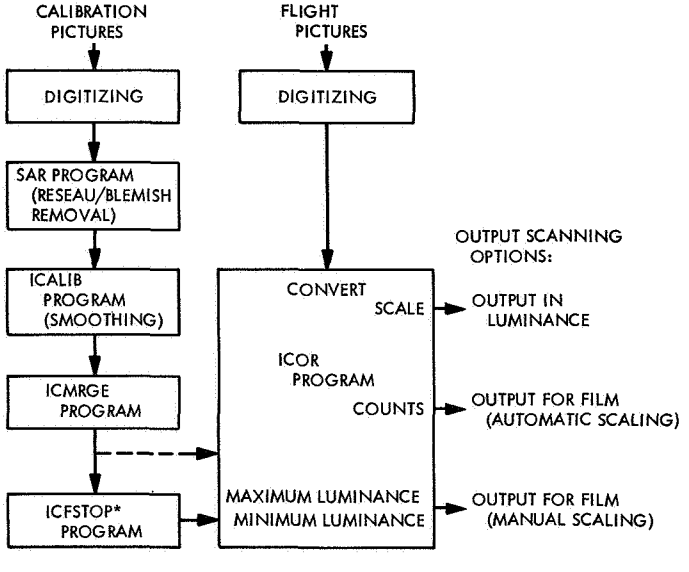

*NOT REQUIRED IF CALIBRATION AND FLIGHT PICTURES ARE AT SAME f-STOP.

Fig. 3. Computer processing flow diagram

Referring to the flow diagram, the processing continues with the digitization of the calibration pictures. These frames, taken at increasing luminance levels, are chosen to allow close interpolation of the light-transfer characteristics. Removal of reseau and blemishes is then applied. The ICALIB program smoothes the data by an averaging routine and eliminates effects of periodic noise. The resulting smoothed frames are then combined into calibration data set, using the ICMRGE program. For a given digital value, the scaled luminance is calculated from this data set.

The *Surveyor* cameras have shown a variation of transfer characteristics that is dependent on the iris and requires the actual monitoring by a potentiometer.

The frame position, as well as the signal amplitude, requires that an interpolated data set be made between calibration data sets used at the same iris setting as the flight frame. The large number of frames taken on the lunar surface were not taken at the iris positions that the preflight pictures were. The program that generates the interpolated data set is ICFSTOP.

The final processing uses a program called ICOR to compute the scaled luminances from the digitized flight picture, using the ICFSTOP data set at the same iris position. Scaled luminances are obtained by adjusting the output so that the maximum luminance is less than the product of the scaling factor and 255 (8 bits). All frames included in this reduction have been processed in this manner.

To check the absolute luminances, a measurement of the photometric targets was made during the mission. These frames were processed in the same manner as the earth pictures, and the resultant luminances were plotted against assumed values determined from preflight goniophotometric calibration of the targets. Correction to these assumed values was made for spacecraft reflection. Luminances determined by this technique are believed to be within an accuracy of ±10%.

V. Photometric Results

The average earth luminance was obtained by summing the pixel luminances and dividing by the number

of elements. Certain judgment was required as to the geometrical limit of the image, especially along the terminator; however, the results are believed well within the measurement error.

The plot of the average earth luminance as a function of phase angle is given in Fig. 4. The black dots represent the values before conjunction. The spread of the luminances is due to meteorological conditions. For comparison, the curves obtained previously by astronomical observation (Ref. 2) of earthshine on the moon are also included in the figure. The ρ symbol is the Bond albedo or the reflectance in the new photometric terminology defined by the CIE (Commission Internationale d'Eclairage) standard. The specular peak appears to start earlier than previously measured, and all the values are higher than that observed.

The value of earthshine at the lunar surface was calculated from these average luminances. For this purpose, the solid angle was calculated using the equation:

$$E = \pi L_\tau \sin^2 \theta$$

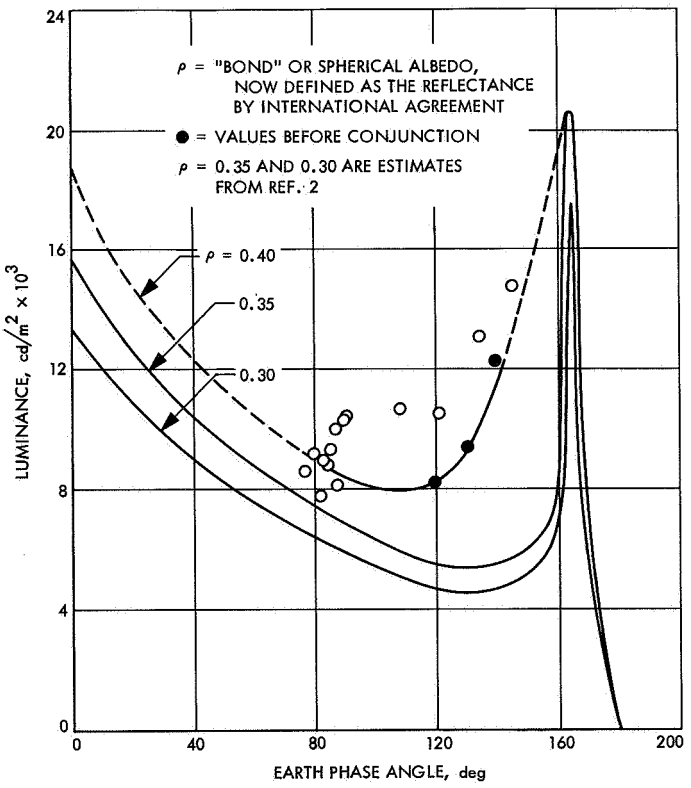

Fig. 4. Plot of average earth luminance as a function of phase angle

where L is the average earth luminance, τ is the fraction of the disk illuminated by sunlight, and θ is the angular semidiameter of the earth on the date of observation. The average earth illuminance normal to the surface is given in Fig. 5.

VI. Polarimetric Results

The images of the earth (Figs. III-95 and III-96 of Ref. 1) show a prominent patch of light on the spheroid that is directly associated with specular reflection of sunlight from the oceans. This reflection, as is the sun glint off the surface of a lake or pond, is heavily polarized. The polarization of this patch of light amounts to 32% as measured on one image of the earth.

Polarization measurements of similar areas on the remaining earth frames are in progress. It is expected that the specularly reflected sunlight will be the predominant factor in the integrated polarimetric function of the earth.

The orientation of polarization is perpendicular to the phase plane. The phase plane is being defined as the plane formed by the vectors from the earth center to the center of the moon and sun, respectively.

It is interesting to note that the degree of polarization (i.e., its magnitude) should be associated with the roughness of the ocean surface. In oceanography, this condition is called sea state. Exact identification of the ocean areas where maximum polarization exists is currently in progress, and inquiry as to the sea state condition at the time of earth observation has begun. Future use of polarization analysis from earth resources satellites provides possibilities of monitoring the sea state of ocean areas not normally covered by other means.

VII. Summary

The first results of the photometry and polarimetry of the earth are given in this paper. The earth reflectance is slightly higher than expected from some astronomical data, although some authors (Ref. 3) have predicted such values. Specular reflection of sunlight from the ocean areas show large amounts of polarization. A possible correlation exists between the degree of polarization and the sea state of the ocean.

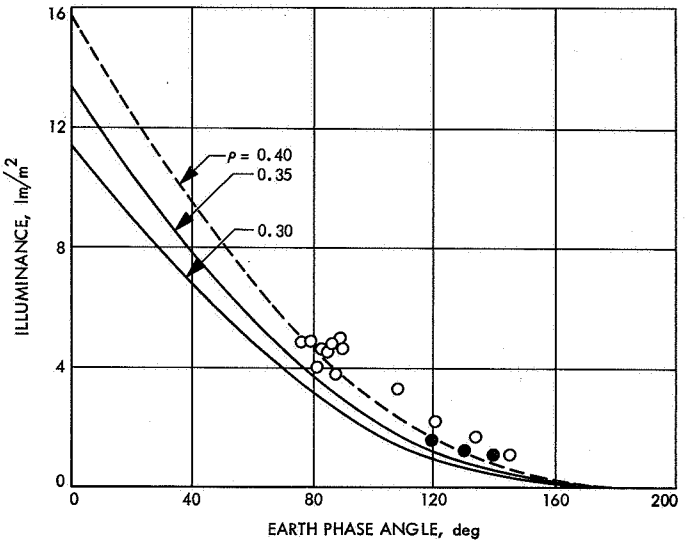

Fig. 5. Calculated average earth luminance obtained from the data presented in Fig. 5 and known angular size of earth

References

1. *Surveyor Project Final Report: Part II. Science Results,* Technical Report 32-1265. Jet Propulsion Laboratory, Pasadena, Calif., June 15, 1968.

2. De Vancouleurs, G., *Phase Curves and Albedos of Terrestrial Planets,* DDC AD-261165, June 1961 (also available as R-TR-61-26-A, Geophysics Corporation of America).

3. Danjon, A., "Albedo, Color, and Polarization of the Earth," *The Moon, Meteorites, and Comets—The Solar System,* Chapter 15. University of Chicago Press, 1962.

Lunar Soil Erosion — *Surveyor* Attitude Control Jets

H. Y. Ko
University of Colorado
Boulder, Colorado

E. M. Christensen
Jet Propulsion Laboratory
Pasadena, California

I. Introduction

Throughout the five successful *Surveyor* missions, consideration was given to the operation of the attitude control jets and vernier rocket engines mounted on the spacecraft for studying the effects of exhaust gas impingement on the lunar surface. Such experiments on the moon would potentially provide information on the mechanical properties of the lunar surface, such as cohesion, angle of internal friction, permeability, and grain size distribution. The information would also be valuable to an *Apollo* mission, since the landing of an *Apollo* lunar module on the moon requires the continuous firing of the retro-rocket engine to a distance of a few feet above the lunar surface.

The effects of firing rocket engines and cold gas jets onto soil materials have been discussed by Scott and Ko (Ref. 1). It was suggested that, as a result of the interaction of the jet gases and the soil medium, the following three processes can take place:

(1) Erosion by entrainment of soil particles in the gas flow (Ref. 2).

(2) Rapid cratering as a result of jet-caused normal surface gas pressures exceeding the bearing capacity of the soil (Ref. 3).

(3) Soil movement as a result of the upward flow of gases through pores of the soil during and at the end of firing (Ref. 1).

Lunar soil erosion experiments with the attitude control jet and the vernier engines should be able to identify which of these, or other phenomena, would take place on the moon.

After *Surveyor I* landed successfully on the moon in June 1966, one of the experiments performed during the first lunar day was the firing of one of the attitude control jets onto the lunar surface. The jets, employing cold nitrogen gas, can exert a nominal thrust of 0.07 lb; the jet on leg 2 of the spacecraft was situated about 6 in. above the lunar soil surface. However, the results were considered to be inconclusive (Ref. 4), because of inadequate photographic coverage of the impingement area of the lunar surface.

Experiments in which a *Surveyor* vernier rocket engine was fired onto a soil surface in June and September 1966 at the JPL Edwards Testing Station were described in Refs. 1, 5, and 6. The possibility of firing the three vernier engines of *Surveyor I* was also considered during the first lunar day, but the results of the Edwards tests showed that firing such engines could potentially cover the thermal compartments with thrown-out soil particles. It was decided, therefore, not to fire the vernier engines. An attempt was made to fire the *Surveyor I* vernier engines in the second lunar day, but the spacecraft did not respond to these commands.

Prior to the launch of *Surveyor III* in April 1967, the suggestion was again made to fire the attitude control jets to obtain information on the lunar soil properties. Laboratory experiments were planned and carried out at the Jet Propulsion Laboratory in early April 1967 for an attitude control jet firing from different heights onto different soils. Although these experiments had produced interesting results, the attitude control jet was not operated on *Surveyor III*. The results did suggest that further studies were desirable to obtain a better understanding of the jet-erosion phenomenon in preparation for vernier engine firing and/or attitude control jet experiments in later *Surveyor* missions. These two groups of experiments were performed in the same facility during July 1967 and will be collectively referred to as the Series A experiments. The results of these experiments will be given later.

In November 1967, the attitude control jet on leg 2 of the *Surveyor VI* spacecraft was operated after the lunar landing for a 4-s and then a 60-s duration. Comparison of the pre- and post-firing television pictures showed that some erosion of the lunar soil-like surface did occur (Ref. 7). It was then believed that further experiments involving the jet firing on different simulated soil surfaces might be worthwhile for defining lunar soil properties. As a result, in July 1968, Series B of soil erosion experiments were carried out, this time in a vacuum facility of much larger volume and at a lower pressure that was far superior to what was used before.

Meanwhile, the vernier engines on the spacecraft in *Surveyors V* and *VI* were operated after the spacecraft landings, with interesting and significant erosion of lunar surface observed (Refs. 7 and 8). Simulation experiments involving the vernier engine were planned and carried out, the results of which are to be reported elsewhere (Ref. 9). In this paper, only the attitude control jet experiments are reported.

II. Experimental Procedures

A. Soil Erosion Tests, Series A

The attitude control jet used in this study was a flight quality equipment as used on the *Surveyor* spacecraft shown in Fig. 1. The conical nozzle of the jet has an 0.1-cm diameter throat and 0.35-cm diameter exit plane. Nominally, the jet operates at a chamber pressure of 40 psi and produces a thrust of 0.07 lb. The gas flow rate is nominally 0.024 cm^3/min.

A total of 17 Series A experiments were performed in April and another 9 in July and August 1967, using such a jet. In these experiments, among the variables considered were the pressure in the jet, the height of the nozzle above the soil surface, the duration of firing, the soil type, and the cohesion of the soil. Most soil samples were

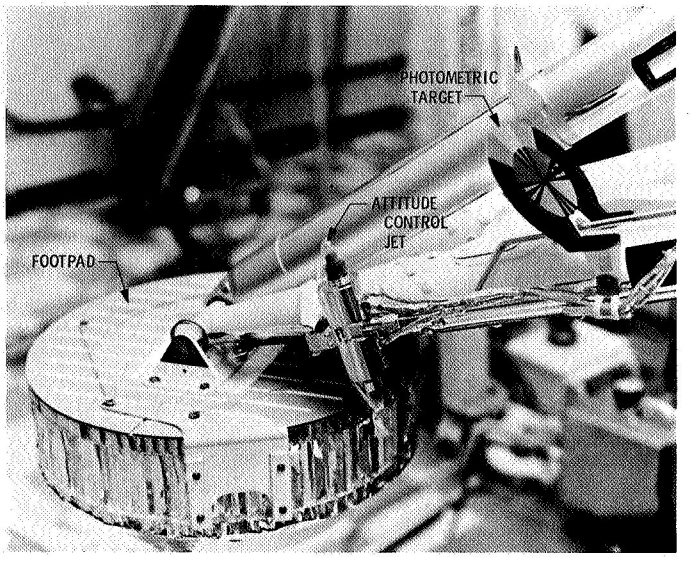

Fig. 1. A typical *Surveyor* leg 2 assembly

contained in 6-in. diameter, 3-in. deep metal cans. The experiments were set up in a vacuum chamber about 5 ft long and 2 ft in diameter; this setup is shown in Fig. 2. High-speed movies (500 frames/s) were taken (through a window in the chamber) of the soil surface during each test, and still pictures were taken before and after each test. The ambient pressure in the chamber could not be lowered to less than 10×10^{-3} torr; thus 50×10^{-3} torr was the nominal initial pressure used in these experiments. The jet was controlled to operate for a duration of one-half second, one second, or longer.

One of the more important soil parameters in the study of soil erosion by jet impingement is the cohesion of the soil. Scott and Ko (Ref. 1) pointed out that a small amount of cohesion in the soil would considerably affect the depth of erosion due to diffusion. Alexander, et al. (Ref. 3), found, from the study on soil erosion by landing rockets in atmospheric conditions, that cohesion made a big difference in the shape of the crater. Since the *Surveyor* results (Ref. 7) show that the lunar soil probably has a cohesion of the order of 0.05–0.17 psi, any attempt to simulate lunar soil conditions in jet erosion studies must take the cohesion into consideration.

To prepare cohesive soil samples for the Series A experiments, the desired cohesion was obtained by controlling the water content of the wet soil and the degree of compaction. The soil was thoroughly mixed with a measured amount of water, placed into a container, and in some cases slightly compacted by tamping as uniformly as possible. By varying the water content of the wet soil and the degree of compaction, the soil was given a cohesion that was measured by an *in situ* vane-shear test consisting of pushing a vane into the soil and measuring the torque required to shear the soil by turning the vane. The water content of the soil when prepared varied between 10 and 25% (water content being defined as the weight of water divided by the weight of solids in the sample), and the bulk density of the dried sample varied between 0.8 and 1.2 g/cm^3. Since it was believed that cohesion is much more important than density with regard to soil erosion, it was decided to emphasize the effects of cohesion.

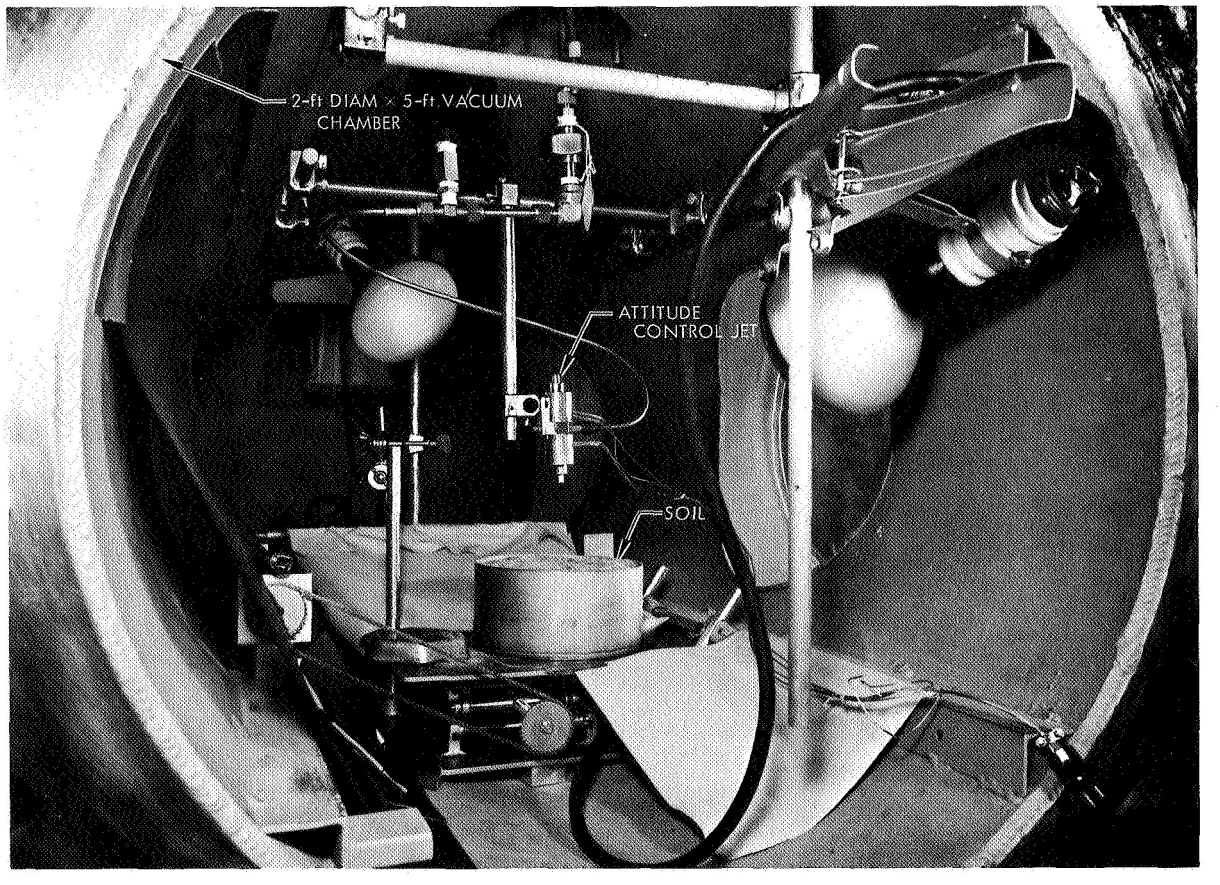

Fig. 2. Series A test setup

For those tests that were to be conducted in vacuum, the soils were dried prior to placement in the vacuum chamber. The drying took place in an oven for a period of 24 h at 220°F, and the cohesion was again measured by turning a shear vane that had been placed into the soil before drying. In most cases, the readings of the soil cohesion before and after drying were quite close to one another. The types of soils used in the Series A tests are shown in Table 1, and their grain size distributions are shown in Fig. 3.

The shear vane used to measure the cohesion was similar in principle to the type described by Gibbs, et al. (Ref. 10), for the measurement of *in situ* shear strength of cohesive soils, and was one of two sizes (Fig. 4). They were both made of brass sheet metal of about 0.02 in. thickness. In using the vane, its stem was attached to a torque wrench as shown in Fig. 4, and the vane was pushed gently without rotation into the soil. The torque wrench was slowly turned until its reading registered a maximum value. It is assumed that the resisting torque to the turning of the vane in the soil was due solely to the overcoming of the shearing resistance (cohesion) of the soil along the cylindrical surface and the bottom surface of the disturbed soil formed by the turning vane. Then, it is possible to relate the maximum measured torque to the cohesion of the soil tested.

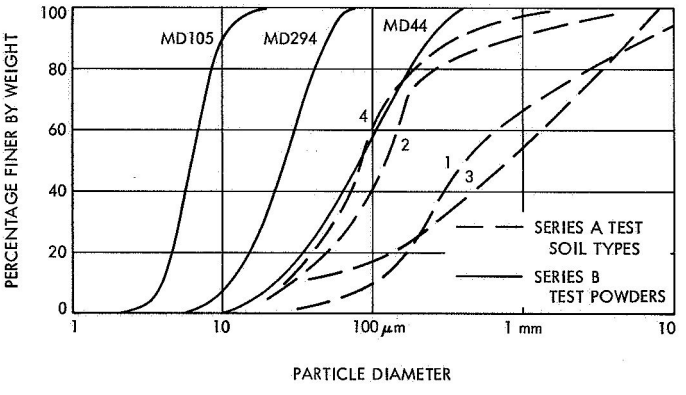

Fig. 3. Particle size distribution curves for the soils used

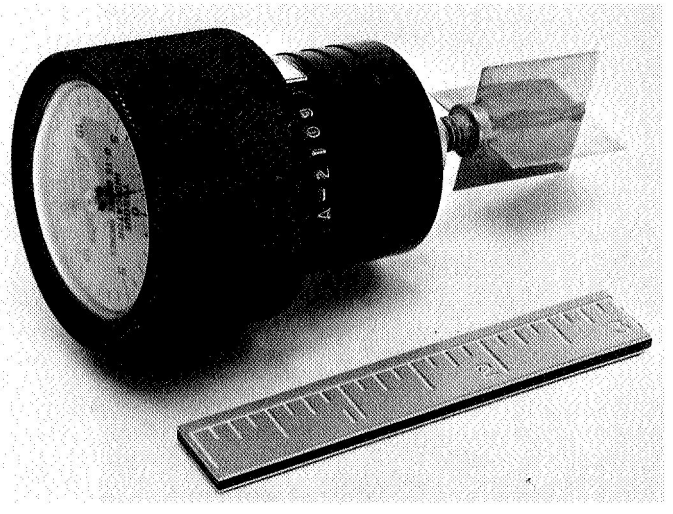

Fig. 4. Shear vane shown mounted on a torque wrench

This method works best for soils with a zero or small angle of internal friction, and for soils with a relatively low bulk density. For soils with a high angle of internal friction, the assumption that shearing of the soil takes place on the cylindrical surface formed by the turning vane will be in error. However, the cohesion of the soils tested in this study could be reasonably estimated by this simple vane method, since, for the soils tested, the observed rupture surface (when the torque wrench was operated) in the soil was very close to the cylindrical surface assumed in the calculations.

B. Study of Jet Plume Characteristics

After the first few Series A tests in which large amounts of erosion were observed, there arose the question as to whether the jet was exerting a thrust comparable to its nominal value. A calibration test was performed to determine approximately the thrust exerted by the jet firing in air. The test consisted of firing the jet in air continuously onto one side of a sensitive beam balance from a height of about 5 in., while weights were added to the other side of the balance until the beam was restored to its horizontal position. Although the thrust at nominal operational conditions was lower than rated (0.07 lb), perhaps due to the fact that not all of the jet thrust was exerted on the balance pan, it is believed that the jet was performing satisfactorily for the purpose of the present experiments.

In a high vacuum such as that existing on the moon, the exhaust plume from the jet would be fully expanded; whereas when operating in atmosphere, the jet action would be very concentrated. During the Series A erosion experiments, it was fully realized that the vacuum level attainable with the facilities used might not be high enough for the jet plume to correspond to its conditions in the lunar vacuum. The tests were nevertheless carried out, because of the unavailability of better facilities at the time when testing was needed, and because they would be valuable for studying the effects of various soil parameters.

Table 1. Soil types and test conditions of Series A soil erosion experiments

Test	Initial facility pressure[a]	Soil type[b]	Soil cohesion, psi	Firing conditions		
				Duration, s	Jet chamber pressure, psig	Nozzle height above soil, in.
A1	A	1	0	1	40	3
A2a	V	1	0	1	45	3
b	V	1	0	Misfire	45	3
A3	V	1	0	1	50	6
A4	V	2	0	1	40	6
A5a	V	2	0	1	40	3
b	V	2	0	1	40	3
c	V	2	0	1	40	3
d	V	2	0	1	40	3
e	V	2	0	1	40	3
A6a	A	2	0	1	25	3
b	A	2	0	1	40	3
c	A	2	0	1	40	3
d	A	2	0	1	40	3
A7a	A	2	0.05	1	25	3
b	A	2	0.05	1	40	3
c	A	2	0.05	1	40	1.5
d	A	2	0.05	1	40	1.5
e	A	2	0.05	1	40	1.5
A8a	A	1	0.05	1	25	3
b	A	1	0.05	1	40	3
c	A	1	0.05	1	40	1.5
d	A	1	0.05	1	40	1.5
A9a	V	2	0	1	20	3
b	V	2	0	1	20	3
c	V	2	0	1	20	3
A10	V	1-2[c]	0	1	25	3
A11a	V	1	0.4	1	40	3.5
b	V	1	0.4	1	40	2.5
c	V	1	0.4	1	40	1.5
d	V	1	0.4	1	40	0.5
A12a	V	2	0.3	1	40	2
b	V	2	0.3	1	40	1
c	V	2	0.3	1	40	0.5

[a]V = vacuum condition was about 50 × 10^{-3} torr and A = test conducted under atmospheric pressure.

[b]Soil 1 is the coarse soil used in September 1966 Edwards vernier engine tests; soil 2 is the fine soil used in Edwards tests; and soil 3 is ground rubble.

[c]Soil used in test A10 is the fine portions of soils 1 and 2 mixed together; no detailed grain size analysis of this soil is available.

Table 1 (contd)

Test	Initial facility pressure	Soil type	Soil cohesion, psi	Firing conditions		
				Duration, s	Jet chamber pressure, psig	Nozzle height above soil, in.
A13a	V	1	0.1	1	40	3
b	V	1	0.1	1	40	3
c	V	1	0.1	4	40	3
A14a	V	2	0.07	1	40	3
b	V	2	0.07	7	40	3
A15a	V	2	0.25	1	40	3
b	V	2	0.25	1	40	3
c	V	2	0.25	1	40	3
d	V	2	0.25	1	40	3
e	V	2	0.25	3–4	40	3
f	V	2	0.25	3–4	40	3
g	V	2	0.25	30	40	3
A16a	V	2	0.25	4	40	2.5
b	V	2	0.25	4	40	2.5
c	V	2	0.25	8	40	2.5
d	V	2	0.25	1	40	1
e	V	2	0.25	4	40	1
f	V	2	0.25	37	40	1
A17a	V	3	0.05	1	40	3
b	V	3	0.05	1	40	3
c	V	3	0.05	1	40	3
d	V	3	0.05	2	40	3
e	V	3	0.05	4	40	3
f	V	3	0.05	6	40	3
A18a	V	4	0.05	1	40	3
b	V	4	0.05	1	40	3
A19a	V	4	0.06	Misfire	40	3
b	V	4	0.06	1	40	3
c	V	4	0.06	1	40	3
A20a	V	4	—	Misfire	40	3
b	V	4	—	After many misfires	40	3
A21a	V	4	0.07	1	40	6
b	V	4	0.07	1	40	6
c	V	4	0.07	1	40	6
d	V	4	0.07	4	40	6
A22a	V	4	0.09	1	40	6
b	V	4	0.09	1	40	6
c	V	4	0.09	1	40	6

Table 1 (contd)

Test	Initial facility pressure	Soil type	Soil cohesion, psi	Firing conditions		
				Duration, s	Jet chamber pressure, psig	Nozzle height above soil, in.
A23	V	4	0.07	4	40	6
A24a	V	4	0.05	1	40	6
b	V	4	0.05	1	40	6
c	V	4	0.05	1	40	6
d	V	4	0.05	5	40	6
A25a	V	4	0.10	1	40	6
b	V	4	0.10	1	40	6
c	V	4	0.10	1	40	6
d	V	4	0.10	4	40	6
A26a	V	4	0.11	1	40	6
b	V	4	0.11	1	40	6
c	V	4	0.11	1	40	6

However, at the end of the Series A soil experiments, a calibration test was performed to measure the jet plume characteristics. A pressure transducer, which was a Statham gage of the unbonded strain-gage type with a ½-in. diameter diaphragm, was mounted flush at the center of a 12 × 12-in. flat plate that could be remotely translated horizontally or moved vertically. With the transducer placed at different locations underneath the jet, it measured the pressure history at various points on the plate; another Statham pressure transducer, mounted 2 ft away, recorded the ambient pressure in the chamber. The signals from both transducers were recorded on an Autograf strip chart recorder. The recorder response was relatively slow; however, the results did show that the position of the maximum pressure on the plate did move toward the center of the impingement area with an increase in the facility ambient pressure. The recorder response was limited by a pen speed of approximately 20 in./s for the full scale reading of 0–5 psi (8-in. pen travel).

The pressure profile exerted by the jet at initial ambient pressure of 15×10^{-3} torr on the plate 6 in. below the jet nozzle is shown for various times up to 1 s in Fig. 5a, and the pressure profile at the same ambient pressure for a 3-in. jet plate separation is shown in Fig. 5b. Typically, the ambient pressure rose from 15×10^{-3} to 500×10^{-3} torr during the 1-s firing. For firings at 50×10^{-3} torr ambient pressure, the pressure also rose to about 500×10^{-3} torr in 1 s.

The strip chart recorder has a rather slow response time of about 0.5 s. It is realized that the transducer under the jet did not indicate the true values of the pressure (the measurement is smaller than the true value when the record shows an increasing pressure), but the lack of better instrumentation precluded a more accurate measurement.

The record does, however, indicate how the pressure profile was affected by the increasing ambient pressure. At the 6-in. separation between the jet and the impinged surface (Fig. 5a), maximum pressure on the plate occurred at a radial distance of 1 in. between 0.2 and 0.3 s into the firing. However, the point where the peak pressure occurred moved towards the axis of the jet as time went on, and after ½ s into the firing, the jet action was concentrated over a central circular region with a radius of about ½ in. Since the pressure transducer had a ½-in. diameter diaphragm and did not measure pressure at a point, the profiles mentioned here are not accurate; but they still demonstrated that, when the jet was fired at an ambient pressure of 15×10^{-3} torr in the present setup, the plume quickly collapsed. At a nozzle height of 3 in., the pressure on the plate directly below the jet axis was lower than that at a radius of ½ in. The pressures at both these points were rising with time for the 1-s operation. However, the pressure at a radius of 1 in. showed a peak value at 0.3 s and decreased as time went on, indicating once again the collapse of the jet plume.

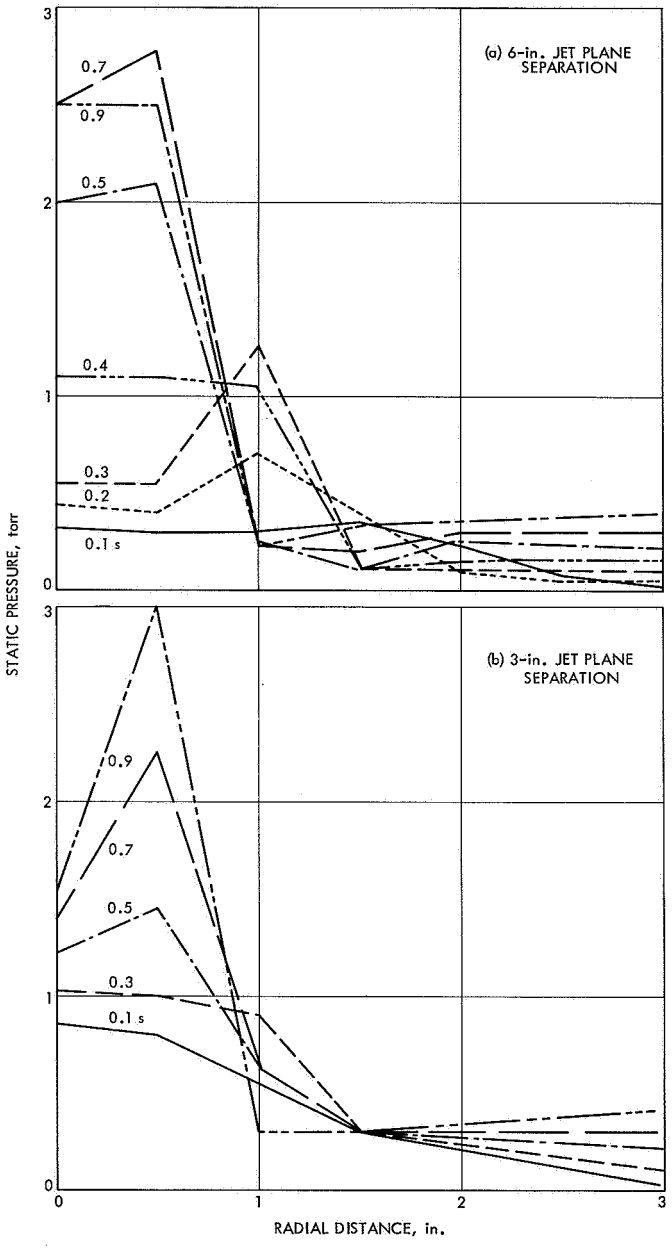

Fig. 5. Static pressure profiles on a flat plate, initial ambient pressure at 15 × 10^{-3} torr

Since the lunar environment remained essentially unchanged while the jet was operated on *Surveyor VI* and, hence, had no effect on the jet plume, it appeared to be highly desirable to carry out simulation experiments in a higher vacuum environment.

In August 1967, the JPL 7-ft diameter by 14-ft vacuum chamber became available and a second series of pressure measurements was carried out in this facility. This chamber was capable of being pumped down to a pressure of about 1 × 10^{-5} torr. The same arrangement was used as previously employed in the smaller chamber with the Statham unbonded strain-gage pressure transducer mounted flush with a flat plate, and the jet was fired for 1 s onto the plate. The output of the pressure transducer (range 0–5 psi) was recorded on a galvanometer-type recorder, which had a very fast response time. The plate/transducer assembly was placed about 3 ft from one end of the chamber. The ambient pressure in the chamber was measured by a thermal-couple vacuum gage mounted on the chamber at about 4 ft above the jet.

The transducer was placed at several radial positions from the vertical jet axis (0, ½, 1, 1½, 2, 2½, and 3 in.) and at two different separation heights between the jet nozzle exit plane and the plate (3 and 6 in.). Firings at ambient pressures of 3 × 10^{-5}, 3 × 10^{-4}, and 3 × 10^{-3} torr were performed and recorded. At the 3 and 6-in. jet nozzle heights, the pressure profiles on the plate did not vary with respect to the three ambient pressure levels, and are as shown in Fig. 6. This figure shows that, at the 6-in. separation, the pressure profile on the plate was spread out; whereas, at the 3-in. separation, the pressure profile had a more noticeable bell shape. All the records show that there is very little delay in the signal rise time. At the end of each 1-s firing at any of these ambient pressures, the pressure shown by the reference thermal-couple gage was only about 10 × 10^{-3} torr.

The magnitude of pressure profile measured in the 7 × 14-ft chamber was quite comparable to those obtained previously in the smaller chamber when the jet plate separation was 6 in. But at the 3-in. separation, the present measurements are considerably higher than the previous measurements in the 2 × 5-ft chamber. This is probably due to the slow recorder in the previous measurement being unable to respond to the rapid increase in pressure during the firing.

Based on these two series of pressure measurements, it was suspected that, for the jet to perform as it should on the moon, it might have to be fired in a vacuum chamber with at least an initial vacuum of 10^{-3} torr and the pressure should remain below 10 × 10^{-3} torr throughout the jet operation. Hence, the jet in the Series A tests might not have performed in a manner simulating lunar conditions.

In July 1968, the 25-ft space simulator at JPL became available and a second series of jet-soil erosion experiments, Series B, was performed in this facility. As will

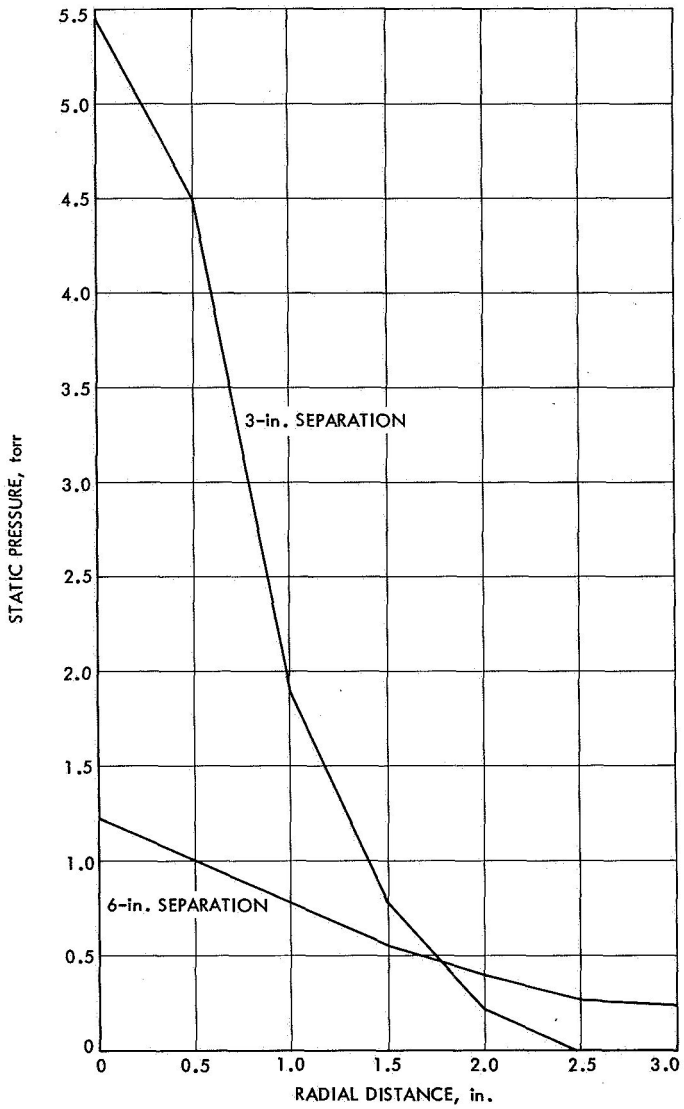

Fig. 6. Static pressure profiles on a flat plate, initial ambient pressure at 3×10^{-5} torr

be described, the Series A and B experiments produced quite different soil erosion results that clearly demonstrated the effect of ambient pressure on the performance of the jet.

C. Soil Erosion Tests, Series B

The Series B tests, carried out in the 25-ft space simulator, used aluminum powders as the simulated soils as well as a sand and a silt. By mixing the aluminum powders with different-sized grains of roughly spherical shape, it was possible to prepare with the aid of vibration the simulated soils of the desired bulk density and cohesion. The basic ingredients used were three aluminum powders: MD44, MD105, and MD294 (manufactured by Alcan Company). The particle size distribution curves of these powders are shown in Fig. 3. Table 2 shows the mixtures of these powders and some of their properties. Originally, it was anticipated that the same aluminum powders would be used as simulated soils in the *Surveyor* vernier engine experiments (Ref. 9), but because of safety measures, they were not used.

The soil used in test B16 (Table 2) was a medium, fairly uniformly graded Ottawa sand, and the silt in tests B17 and B18 was the fine silt used in the *Surveyor* spacecraft resonant frequency tests (Ref. 11). The shear vane method was again used in estimating the cohesions of the simulated soil samples in the Series B experiments.

Figure 7 shows the setup inside the JPL 25-ft space simulator in which the attitude control jet was mounted at the end of a horizontal boom that could swing horizontally and position the jet above each of three soil containers. The elevation of the jet could also be controlled from outside of the space simulator. Lights for photographic purposes were installed on the floor, and the entire assembly was surrounded by a tent built of mylar sheets to trap any loose powder that might be blown out from the soil containers. The tent was open

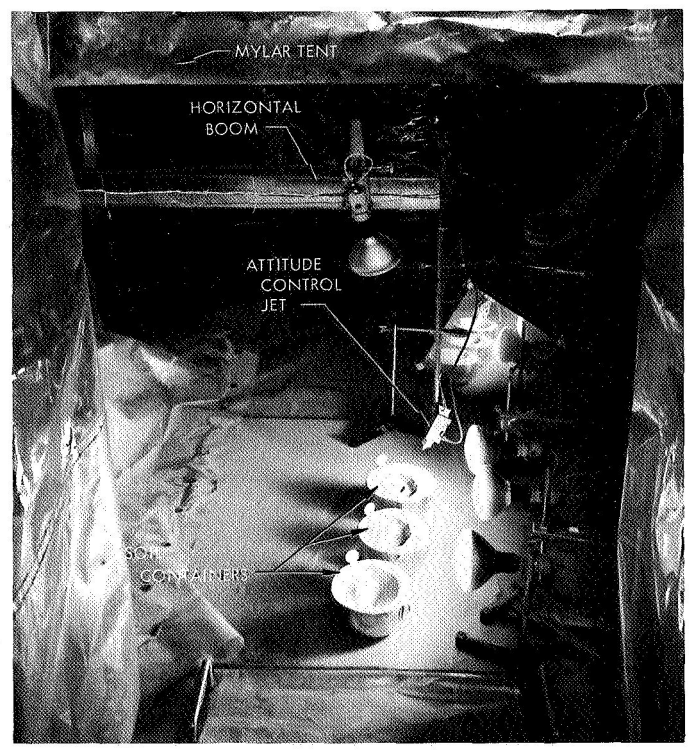

Fig. 7. Series B test setup inside 25-ft space simulator

enough to allow gases to escape. The jet was mounted with its axis at an angle of 12 deg from the vertical to simulate the mounting of a jet on leg 2 of the spacecraft. The same control mechanism as in Series A experiments was used to operate the jet. High-speed movies (500 frames/s) were taken of the soil erosion during jet operation through a porthole in the door of the simulator. Still pictures were taken of the disturbed surfaces of the three soils only after the space simulator door was open at the completion of each testing sequence of the three soils. (Further details of the setup for Series B experiments are contained in "*Surveyor* Soil Erosion Test 25-108" by K. W. Dyckman, JPL, 1968.) Table 3 shows the test conditions for the Series B experiments.

Table 2. Soil types of Series B soil erosion experiments

Test	Soil	Bulk density, g/cm³	Porosity[a]	Average apparent cohesion,[b] psi	Remarks
B1	MD105	1.06	0.61	0.17	
B2	MD294	1.38	0.49	0.20	
B3	MD44	1.59	0.41	—	Soil essentially granular and has no cohesion
B4	MD105	0.78	0.71	0.034	
B5	MD44	1.28	0.53	—	Soil essentially granular and has no cohesion
B6	MD294	1.07	0.60	0.024	
B7	MD105	1.00	0.63	0.029	
B8	MD105	0.93	0.66	0.041	
B9	MD105	0.90	0.67	0.038	
B10	MD105, MD44(2:1)[c]	0.94	0.65	0.041	
B11	MD105, MD44(1:1)	1.16	0.57	0.11	
B12	MD44, MD294(2:1)	1.31	0.51	0.059	
B13	MD44, MD294(1:2)	1.28	0.53	0.041	
B14	MD105, MD294(1:1)	0.97	0.64	0.059	
B15	MD109, MD294(2:1)	1.00	0.63	0.076	
B16	Ottawa sand	1.63	0.40	—	Soil essentially granular and has no cohesion
B17	Silt	1.09	0.60	0.031	
B18	Silt	1.39	0.49	0.250	

[a]Assuming a grain density of 2.7 g/cm³. [b]Obtained by shear vane method. [c]Proportion by weight.

Table 3. Test conditions of Series B soil erosion experiments

Test	Initial facility pressure, × 10⁻³ torr	Nozzle height above soil, in.	Firing duration, s	Test	Initial facility pressure, × 10⁻³ torr	Nozzle height above soil, in.	Firing duration, s
B1a	0.03	6	4	B3a	10	6	1
b	10	6	1	b	10	4	4
c	10	6	4	B4a	0.14	4	1
d	10	4	1	b	0.38	4	4
e	10	4	4	c	50	4	1
B2a	10	6	1	d	50	4	4
b	10	4	1	B5a	0.13	6	1
c	10	4	4	b	0.13	4	1

Table 3 (contd)

Test	Initial facility pressure, $\times 10^{-3}$ torr	Nozzle height above soil, in.	Firing duration, s
B5c	0.13	4	4
d	50	6	1
e	50	4	1
f	50	4	4
B6a	0.13	6	1
b	0.13	4	1
c	0.13	4	4
d	50	4	1
e	50	4	4
B7a	0.07	4	1
b	0.07	4	4
c	1	4	1
d	1	4	4
e	10	4	1
f	50	4	1
g	50	4	4
B8a	0.07	4	4
b	50	4	1
c	50	4	4
B9a	0.07	4	4
b	50	4	1
c	50	4	4
d	63	4	10
B10a	0.14	6	1
b	0.14	4	1
c	0.39	4	4
d	50	6	1
e	50	4	1
f	51	4	4
B11a	0.14	4	1
b	0.39	4	4
c	51	6	1
d	52	4	1
e	54	4	4
B12a	0.14	4	1
b	0.39	4	4
c	0.4	4	4
d	56	6	1
e	56	4	1
B12f	58	4	4
B13a	0.14	6	1
b	0.14	4	1
c	0.35	4	4
d	50	6	1
e	50	4	1
f	53	4	4
B14a	0.14	6	1
b	0.12	4	1
c	0.37	4	4
d	54	6	1
e	55	4	1
f	55	4	4
B15a	0.12	6	1
b	0.12	4	1
c	0.44	4	6
d	55	6	1
e	55	6	1
f	55	4	1
g	56	4	4
B16a	9	6	1
b	9	4	1
c	9	4	4
d	50	6	1
e	50	4	1
f	50	4	4
B17a	9	6	1
b	9	4	1
c	9	4	4
d	53	6	1
e	56	4	1
f	56	4	4
B18a	9	6	1
b	9	4	1
c	9	4	8
d	56	6	1
e	58	4	1
f	62	4	6

III. Results and Interpretation of Soil Erosion by Jet Impingement

A. Series A Tests

In general, disturbance caused by the jet on cohesionless soils resulted in craters that had circular symmetric outlines on the surface and in slopes that were not too steep (30–40 deg). The dimensions of the crater would depend on the pressure in the jet chamber, on the height of the nozzle above the soil surface, and on the length of the firing. Firing of the jets in the atmosphere, at a nozzle height of 3 in. and at a chamber pressure of 40 psig, created craters about 3 in. in diameter and from ½ to 1 in. deep on both soil types 1 and 2 as tested in the cohesionless state (tests A1 and A6, see Table 1); the craters are shown in Figs. 8 and 9.

The high-speed movies of the firings at atmospheric pressure showed that the erosion in the cohesionless soils was a continuous process with a maximum rate of erosion occurring initially at a radius about ½ in. from the center line of the jet axis. The central region under the jet axis was only slightly eroded. After a few tenths of a second into the firing, the flow conditions of the jet exhaust plume appeared to have changed. The previously stagnant central region now began to be eroded and eventually a bowl-shaped profile was formed on the surface. This bowl-shaped crater increased in both depth and diameter until shutoff of the jet. At shutoff, no noticeable diffused gas blowoff was observed.

Movies taken of the firings at a facility pressure of 5×10^{-3} torr on cohesionless soils, show the same general pattern of erosion as in atmospheric firings. One difference was that during the vacuum tests, as in test A2, the initial maximum rate of erosion took place further away from the jet axis (1 to 1½ in.), Fig. 10a. After the firing had proceeded for a few tenths of a second, the position of maximum erosion occurred closer to the center of impingement, Fig. 10b. For soils 1 and 2 tested in the cohesionless state, the size of the crater did not seem to differ very much with respect to the ambient pressure condition (i.e., in air or at 50×10^{-3} torr vacuum).

The flat plate measurements in this small vacuum chamber later demonstrated that a vacuum of 50×10^{-3} torr was rapidly destroyed by the jet exhaust plume and

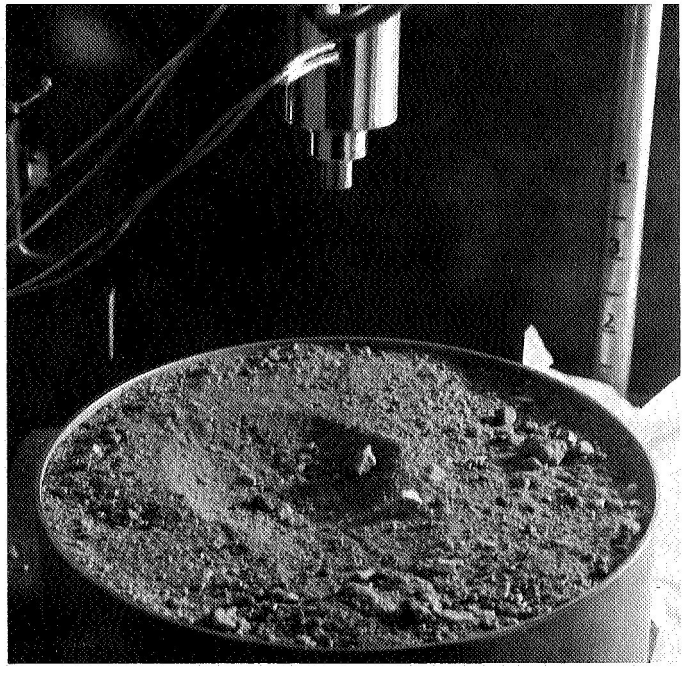

Fig. 8. Soil surface after test A1

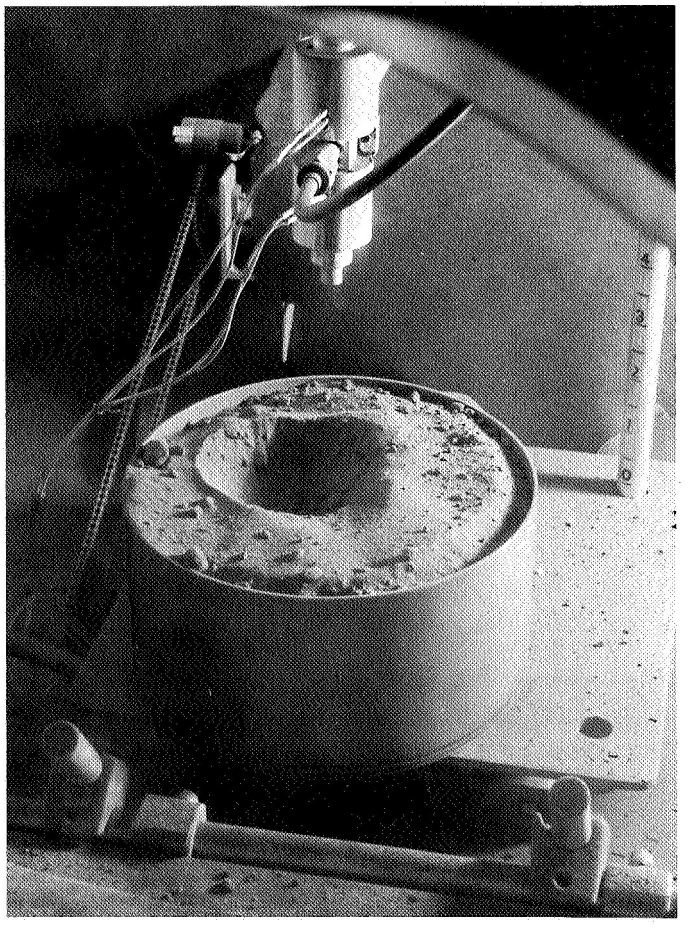

Fig. 9. Soil surface after test A6

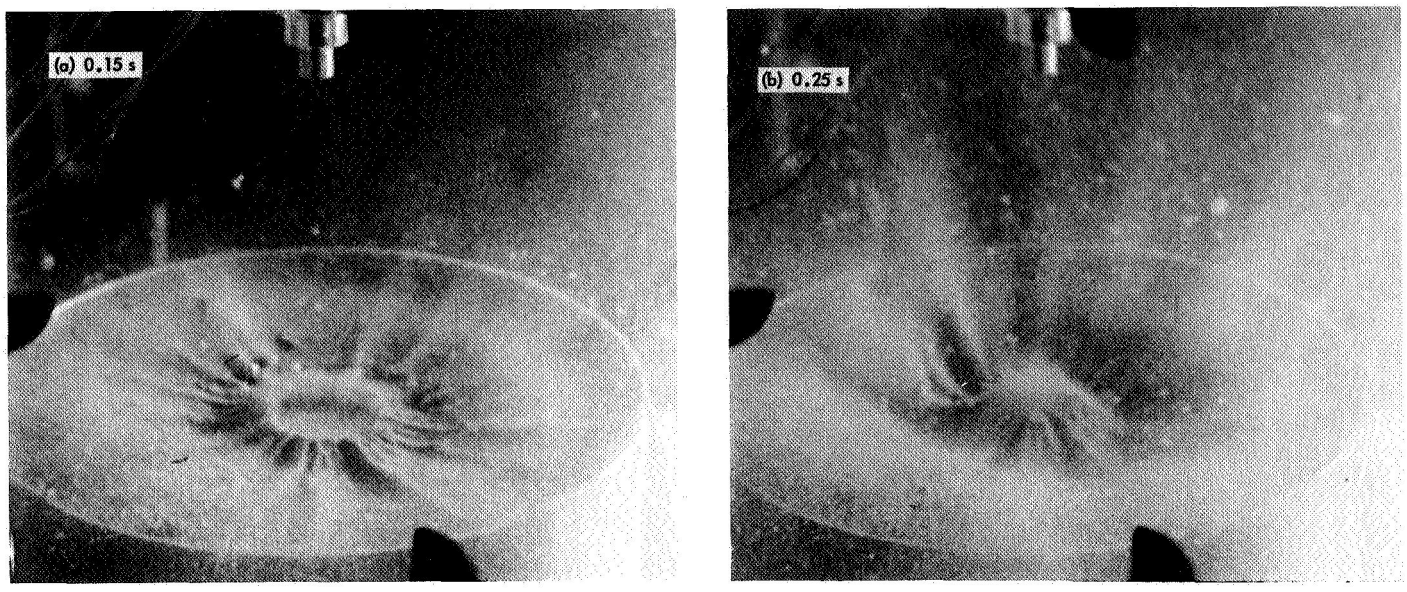

Fig. 10. Movie frames of jet firing in test A2a

resulted in a very concentrated jet, probably similar to the one obtained under atmospheric conditions. Later soil erosion tests in the 25-ft space simulator showed that a drastic change in the jet plume took place between 10×10^{-3} and 50×10^{-3} torr ambient pressure. It is then not surprising that soil erosion tests with a duration over a few tenths of a second in air and in 50×10^{-3} torr pressure produced similar results.

Firings on wet cohesive soils in air and dried-out cohesive soils in vacuum showed a drastic difference in the erosion pattern from that obtained on cohesionless soils. The resulting craters in the cohesive soils were usually not symmetrical and were irregular in shape with nearly vertical walls. The depths of these craters were dependent on the soil cohesion. In these experiments, the cohesion of the soil samples ranged from 0.05 to 0.4 psi. On the most cohesive soils (tests A11 and A12), no erosion was observed even at a nozzle height of ½ in. above the soil surface; while on a soil with a cohesion of 0.05 psi, a 1-s firing at a 3-in. nozzle height and 40-psi nozzle chamber pressure produced a crater 1½ in. in diameter and 1 in. deep (test A18). Examples of the eroded surface of cohesive soils are shown in Fig. 11.

In cohesive soils, erosion by the jet impingement took place in a less continuous fashion than in cohesionless soils. During these jet firings, clods of soils were loosened and blown away from the surface, and if the cohesion of the soil was large enough ($\geq$0.25 psi), there might be only a few clods eroded in this way. As observed in these tests, the time required by the jet to loosen the first clod and blow it off seemed to depend on the cohesion of the soil. However, during this time, the jet plume was collapsing and it might have been a local concentration of pressure that helped loosen the cohesive soil. (Notice in Fig. 5 how the maximum pressure location varied with time.) It is not clear whether this delayed erosion is due to the changing jet behavior under increasing ambient pressure or is a genuine effect from the soil cohesion.

B. Series B Tests

Typically, the gas jet operating for 1 s at an initial ambient cell pressure of 1.4×10^{-4} torr caused the cell pressure to rise to 3.8×10^{-4} torr. When the jet was operated at 50×10^{-3} torr ambient pressure for 4 s, no noticeable change in the ambient pressure could be observed. Thus, it appears that the plume characteristics of the jet remained stable for firings at each pressure level and were not affected by the small increases in the ambient pressure caused by the gas jet.

When the jet was operated at an ambient pressure in the sub-micron range, no noticeable gross erosion of the simulated soil surface was observable, regardless of the soil properties and the nozzle height (4 or 6 in.). After tests B1–B9 (the soils had leveled, smooth surfaces), it was thought that an uneven soil surface might erode more under the action of the jet. In tests B10–B15,

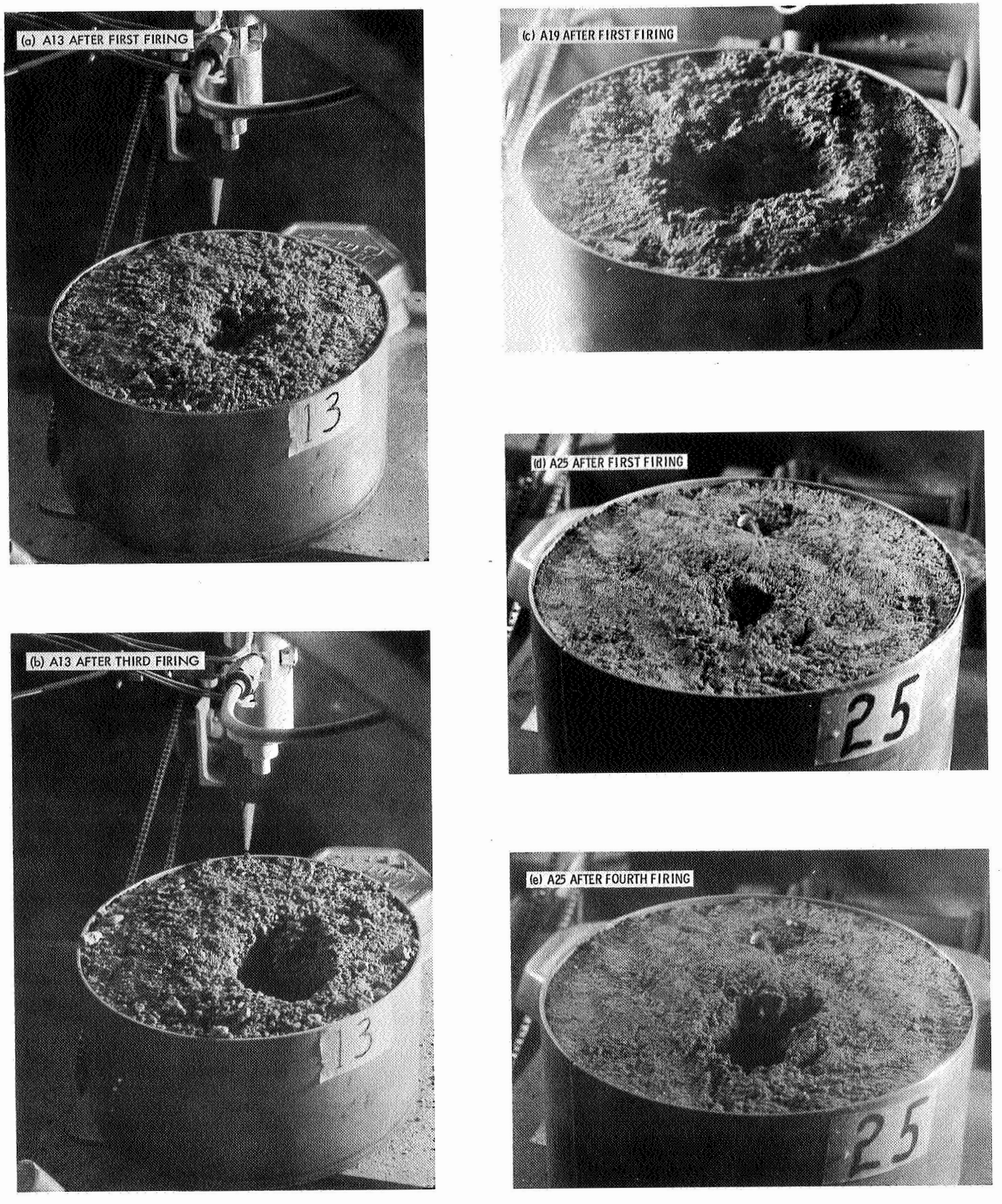

Fig. 11. Surfaces of cohesive soil samples after jet firing tests in 2- × 5-ft chamber

after deposition of the soil in the container, no attempt was made to get rid of the surface roughness. The samples thus prepared were tested, and no significant erosion (except the removal of a few loose particles on the surface) was observed when the jet was operated in the ambient pressure levels less than 10^{-3} torr.

No erosion could be detected by observing the movies or still pictures of the soil samples used in tests B1 and B2 with the jet firing for as long as 4 s, for nozzle heights as close as 4 in. to the soil surface, and at ambient pressure levels of 3×10^{-5} and 10×10^{-3} torr. These two samples were cohesive, with the cohesion estimated from the shear vane readings to be 0.17 and 0.20 psi, respectively.

For test B3 sample, which was essentially cohesionless and had a mean particle size of 82 μm, a 1-s firing of the jet (under an ambient pressure of 10×10^{-3} torr and at a height of 6 in.) eroded the surface slightly. A faintly noticeable annulus region was formed on the surface with an internal diameter of about 1½ in. and an outer diameter of about 3 in. No measurable depth ($<1/32$ in.) of erosion was obtained; however, the texture of the surface on the annulus region was different from the rest of the surface. The area inside of the annulus ring was apparently undisturbed. When the jet was lowered to a height of 4 in. above the soil surface and fired for 4 s at 10×10^{-3} torr ambient pressure, the resulting disturbance of the surface (shown in Fig. 12a) completely masked the first annulus and it consisted of a radial streak pattern.

The annulus type of erosion and the faint streak pattern were also visible after the soil sample of test B5 was blown on by the jet at elevations of 6 and 4 in. at an ambient pressure of 1.3×10^{-4} torr, as shown in Fig. 12b. The sample of test B5 was the same aluminum powder as the sample of test B3, but was less dense and was also cohesionless, as shown in Table 2.

The other cohesionless soil (an Ottawa sand) that was tested in this series, test B16, showed some erosion of the surface during the jet firings at an ambient pressure of 9×10^{-3} torr. Because of the different texture of the sand surface as compared to the greyishly dull surface of the aluminum powder sample, it was difficult to observe in the movies any annulus or streak pattern that might have been caused on the sand surface.

After soil samples of tests B4–B6 were tested at ambient pressures ranging from 3×10^{-5} to 10×10^{-3} torr

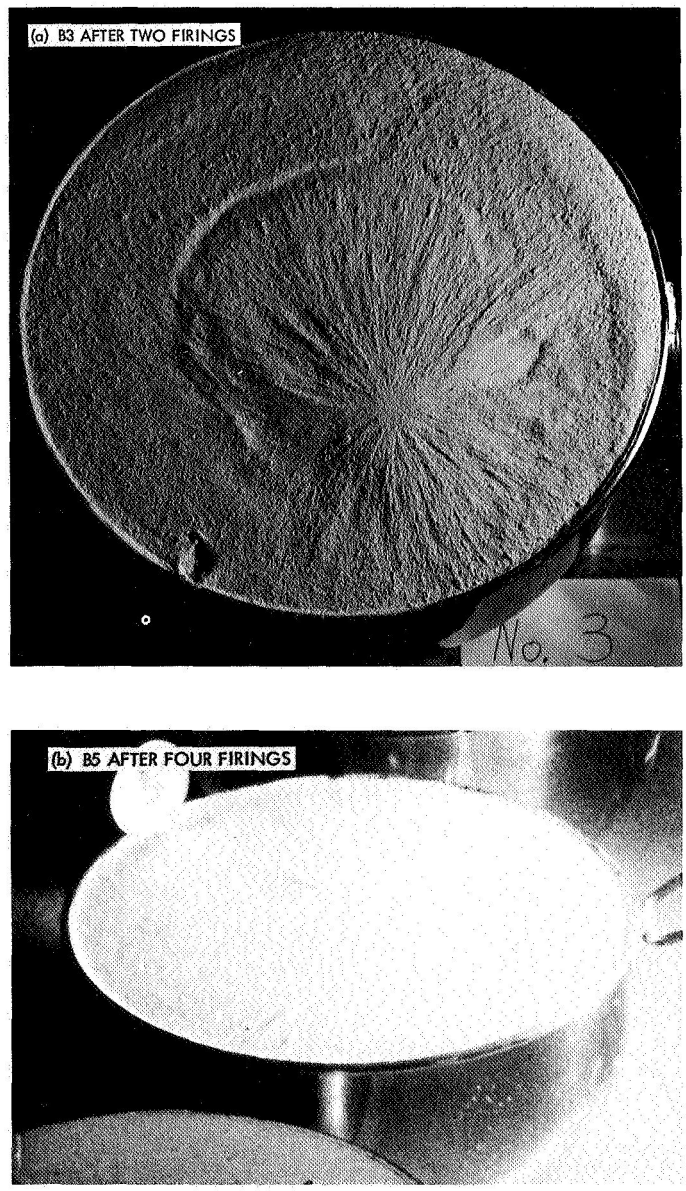

Fig. 12. Surfaces of cohesionless soil samples after jet firing tests in 25-ft space simulator

(no major surface erosion was observed), the ambient pressure was raised to 50×10^{-3} torr and the jet was operated above the soil surfaces in tests B4, B5, and B6. At a height of 6 in. above the horizontal surface in tests B4 and B5, the jet, whose axis was at an angle of 12 deg to the vertical, eroded the surface in a crescent-shaped depression with the open end of the crescent facing the same direction as the jet nozzle. The pattern of erosion during the jet operation was as shown in Figs. 13a and 13b for soils of tests B4 and B5, respectively. The particles were eroded away along trajectories

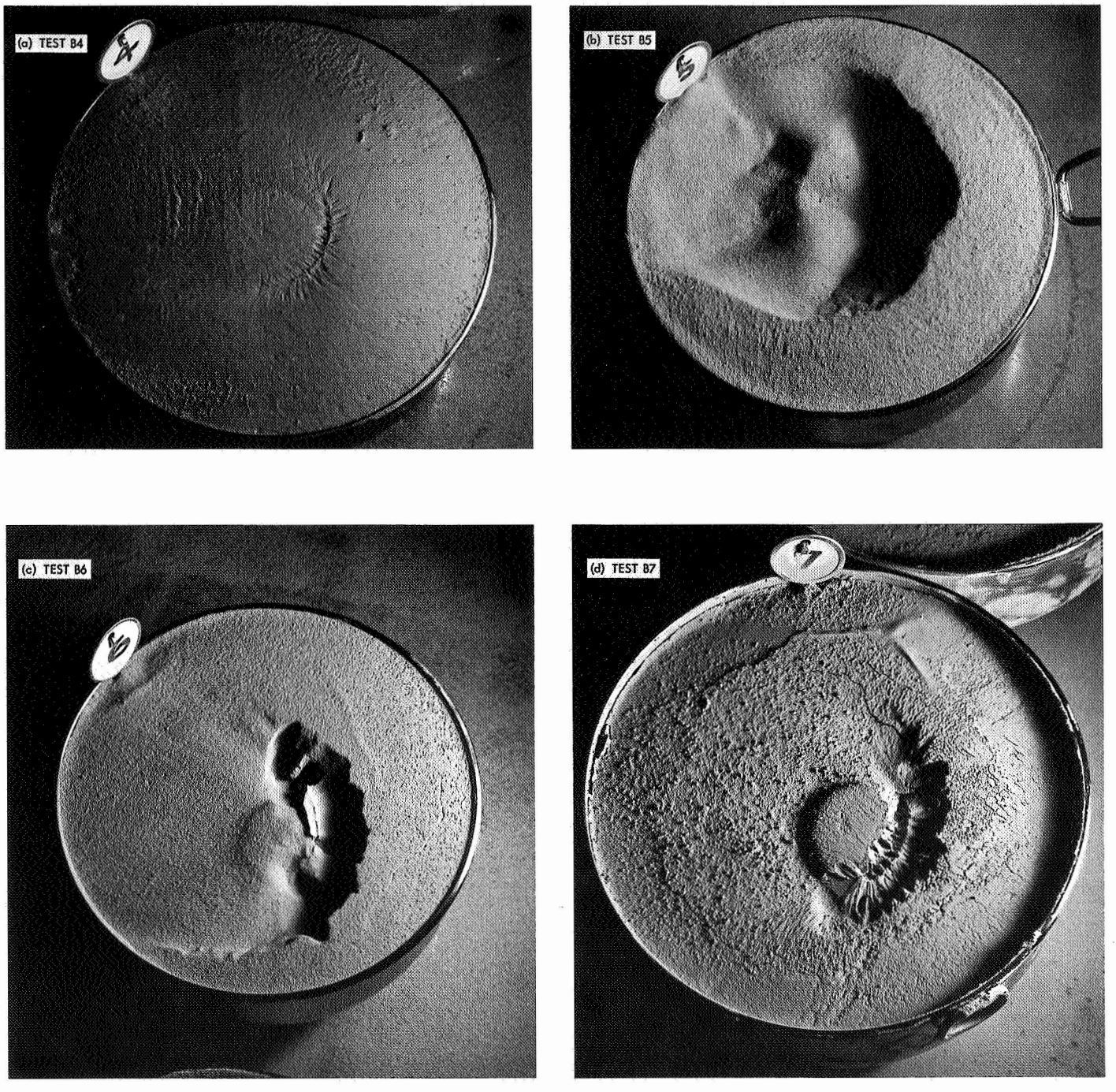

Fig. 13. Surfaces of soil samples after tests at 50 × 10^{-3} torr in 25-ft space simulator

that originated along the inclined walls of the crescent-shaped eroded crater. The size of the crescent varied from one soil to another and ranged from 3 to 4 in. in diameter, ½ to 1 in. wide, and up to 1 in. deep (these figures were estimated from the movies). After the jet was fired at a separation of 4 in., the surface of the sample in test B6 was as shown in Fig. 13c.

The considerable erosion caused by the jet on the samples of tests B5 and B6 in an ambient pressure of 50 × 10^{-3} torr, while no appreciable erosion occurred at a sub-micron pressure, showed that there was a significant change in the jet characteristic within the pressure range between 0.1 × 10^{-3} and 50 × 10^{-3} torr. From the comparison of the results of tests B1, B2, and B3 where

the pressure was 10×10^{-3} torr and tests B4, B5, and B6 where the pressure was 50×10^{-3} torr, it appears that the change in the jet characteristics occurred between these two pressure levels.

Hence, in the next group of tests, after no appreciable erosion had occurred when the samples of tests B7, B8, and B9 were tested by the jet at 7×10^{-5} torr pressure at a height of 4 in., the jet was positioned at 4 in. height above sample of test B7 (cohesion 0.029 psi) and was operated at increasing ambient pressure levels of 1×10^{-3}, 10×10^{-3}, and 50×10^{-3} torr. No noticeable erosion of the sample surface resulted until the ambient pressure level was raised to 50×10^{-3} torr. The resulting soil surface of test B7 sample was as shown in Fig. 13d. This sequence of tests clearly demonstrated the effect of ambient pressure on soil erosion.

The size of the crescent-shaped eroded crater on the test B7 sample at the end of this series of firings is apparent from Fig. 13d. Although the jet was positioned at an angle of 12 deg to the vertical as compared to the vertical jet in the pressure measurement tests, the annulus region where the maximum pressure gradient occurred (see Fig. 5) coincided with the position where maximum soil erosion occurred in the test B7 sample. Therefore, soil erosion can be a good indication of jet characteristics, as previously discussed in connection with test A2 in Fig. 10.

From the results of test B7, it appears that the attitude control jet is unlikely to cause any appreciable erosion of the lunar surface, under the conditions that existed at the *Surveyor VI* landing site. However, close examination of the pre- and post-firing pictures of the *Surveyor VI* attitude control jet experiment did show some disturbance of the lunar surface. For example, the lunar surface directly under the impingement of the jet mounted on leg 2 of the spacecraft was as shown in Fig. 14a. After the 4-s jet firing, the same surface area was as shown in Figs. 14b and 14c, and further jet operation for another 60 s produced a surface as shown in Fig. 14d. Although no major erosion such as the formation of a crater was obtained because of the jet firings on the lunar surface, there were particles and clods of soils that were disturbed by the firings. Most noticeably, the protrusions A and B, shown in Fig. 14, were blown off by the jet. These protrusions did not seem to be loose clods sitting on the surface; hence, some cohesive forces must have existed between them and the surface. The jet firings for 4 and 60 s were sufficient to produce a force that overcame this cohesion and dislodged these particles. These particles were estimated to be at a distance of about 5 to 6 in. from the center of the jet impingement area, although their height above the surrounding lunar surface could not be estimated from the pictures. Also, the largest soil fragment on the lunar surface that was moved by the jet was estimated to be 0.6 in. long and 0.4 in. in diameter; the distance from the jet impingement center to the farthest point of observed soil disturbance was 10 in. Further details of this attitude control jet experiment on the lunar surface are contained in Ref. 7.

The six samples of tests B10–B15 were prepared with uneven surfaces, a cohesion ranging from 0.04 to 0.11 psi, and a density ranging from 0.94 to 1.31 g/cm^3. These soil surfaces did not show any noticeable erosion when the ambient pressure was in the sub-micron level. Occasionally, a few particles on the surface might be blown away. Therefore, it seems that any erosion of the lunar surface that might have been caused by the firing of an attitude control jet on a *Surveyor* spacecraft was a random phenomenon. It is certainly difficult to analyze the *Surveyor VI* jet erosion and to define from the analysis any lunar soil parameter. However, by comparing the erosion caused on the samples of tests B10–B15 with that caused on the moon by the jet on *Surveyor VI*, the cohesion of these simulated soils (0.04–0.11 psi) seemed to be reasonable estimates for the lunar soil.

Firings of the jet on the uneven surfaces of the samples of tests B10–B15 under an ambient pressure of about 50×10^{-3} torr again eroded the surface in a much more significant manner than under a lower ambient pressure. However, since the surface was not a smooth one, a tendency to have the erosion occur in an irregular manner existed and no crescent-shaped depression was formed in these tests. For example, the erosion that occurred in test B13 sample can be observed from Fig. 15.

In the last group of tests in Series B, the Ottawa sand was cohesionless with a bulk density of 1.63 g/cm^3, the loose silt had a cohesion of 0.031 psi with a density of 1.09 g/cm^3, and the compacted silt had a cohesion of 0.25 psi with a density of 1.39 g/cm^3. These real soils prepared with a smooth surface for tests B16, B17, and B18 behaved like the aluminum powders under the impingement of the jet; that is, only slight erosion occurred until the ambient pressure was raised to 50×10^{-3} torr.

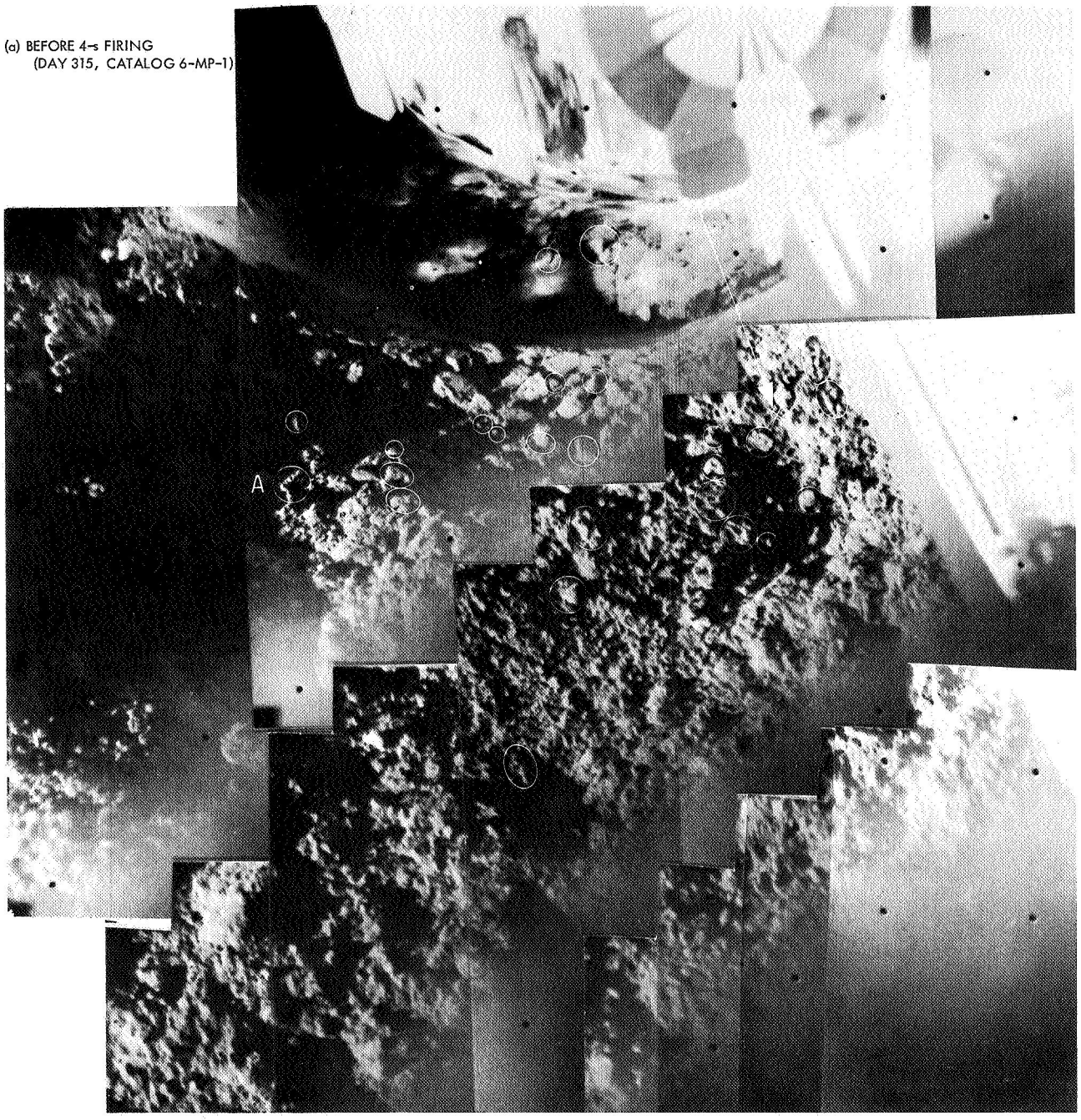

REPRESENTATIVE FRAGMENTS ARE CIRCLED, THE ARROW INDICATES THE LINE EXTENDING THROUGH CENTER OF ATTITUDE CONTROL JET TO LUNAR SURFACE (X)

Fig. 14. Mosaic of narrow-angle pictures of attitude control jet experiment at *Surveyor VI* landing site

(b) AFTER 4-s FIRING
(DAY 315, CATALOG 6-MP-2)

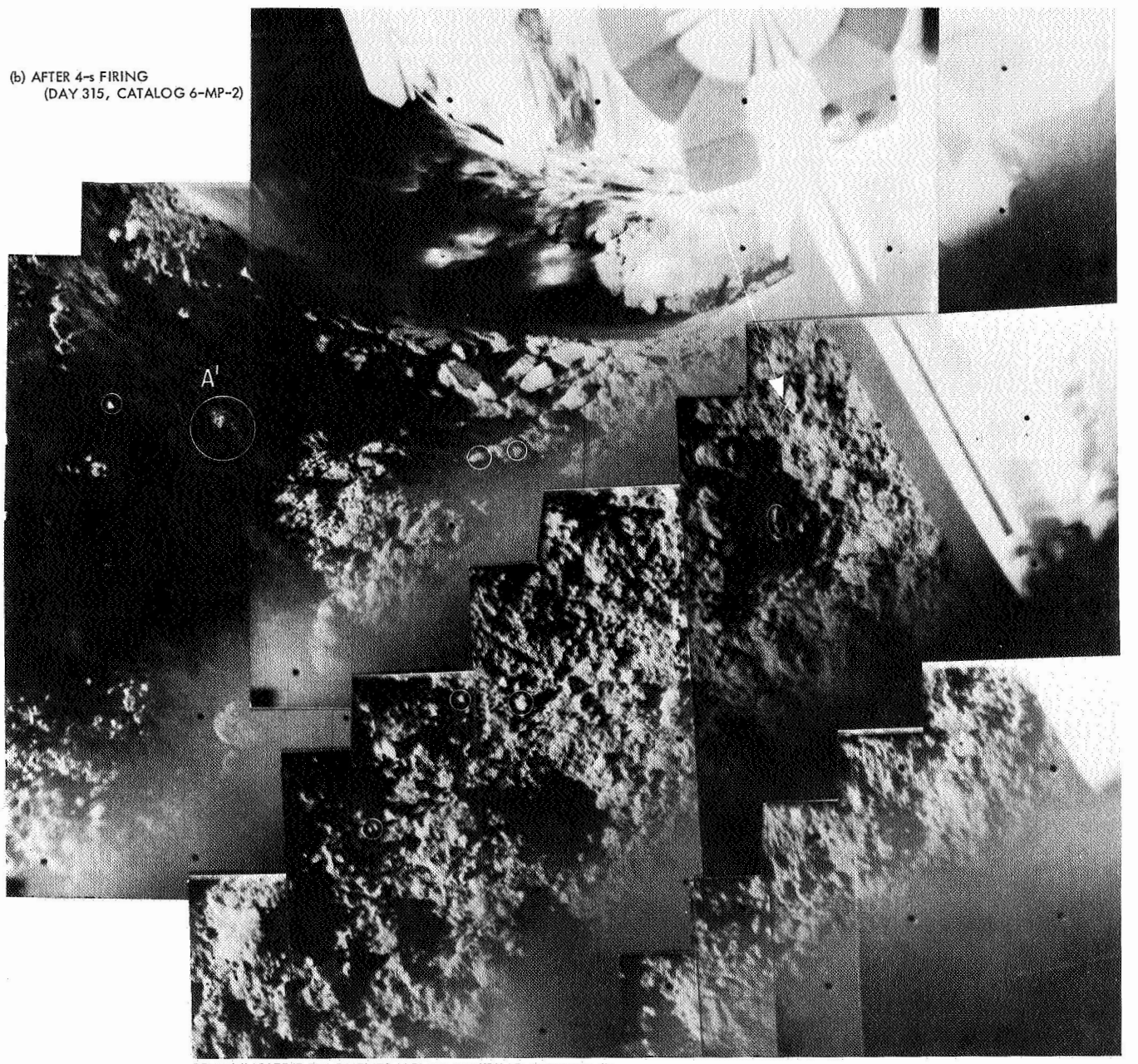

REPRESENTATIVE FRAGMENTS MOVED BY FIRING ARE CIRCLED

Fig. 14 (contd)

(c) BEFORE 60-s FIRING
(DAY 315, CATALOG 6-MP-2)

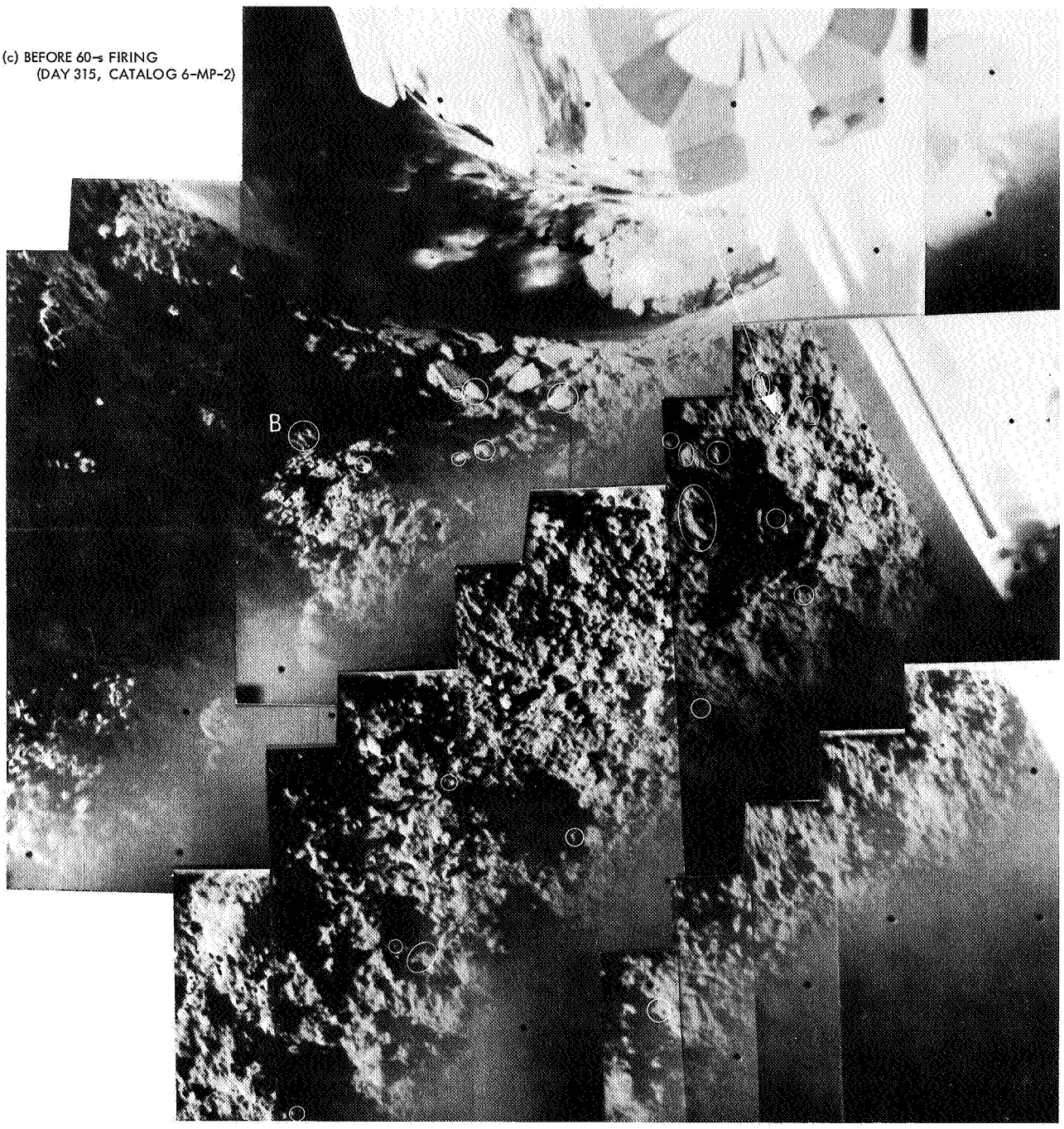

REPRESENTATIVE FRAGMENTS ARE CIRCLED

Fig. 14 (contd)

(d) AFTER 60-s FIRING
(DAY 315, CATALOG 6-MP-3)

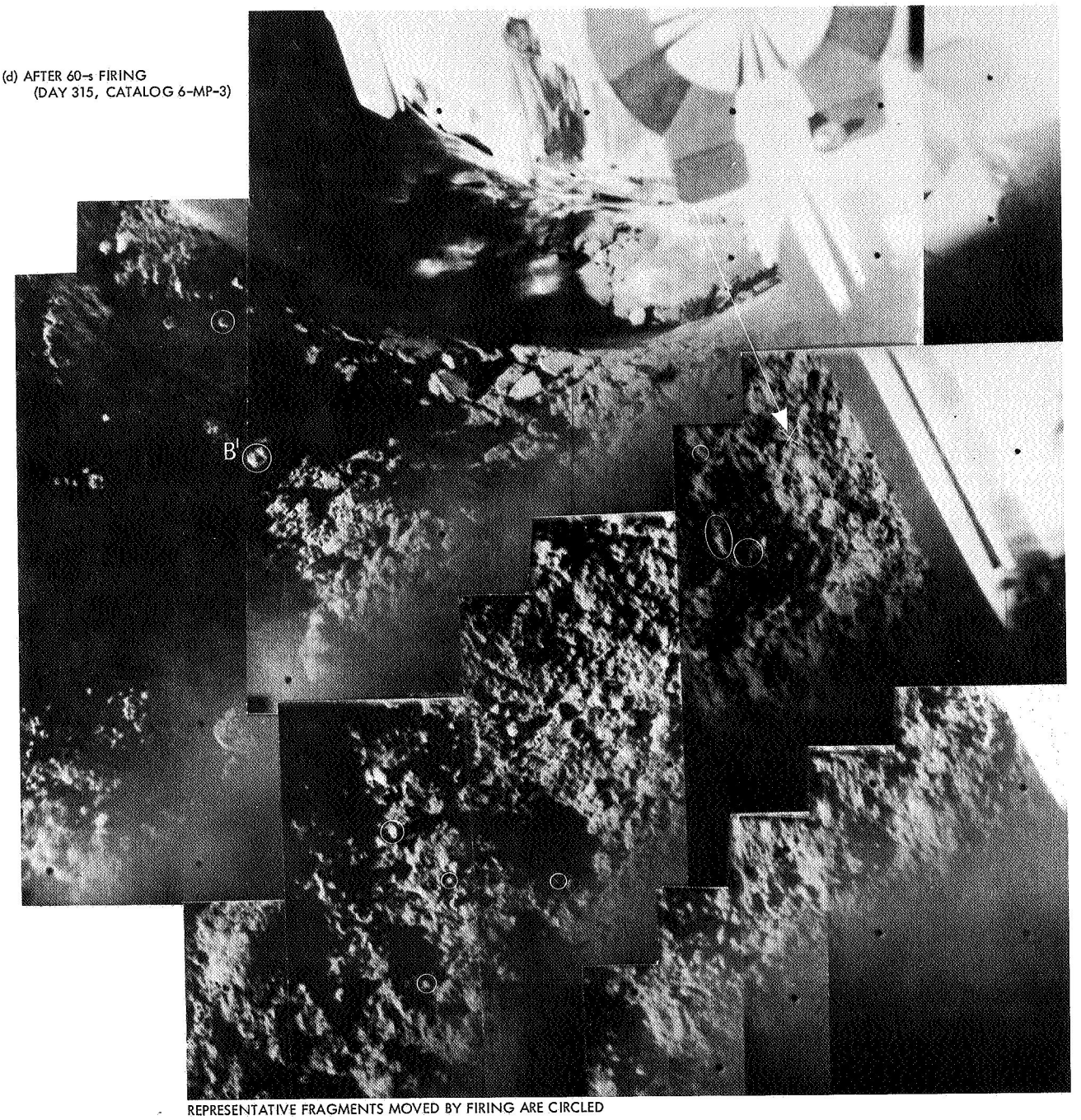

REPRESENTATIVE FRAGMENTS MOVED BY FIRING ARE CIRCLED

Fig. 14 (contd)

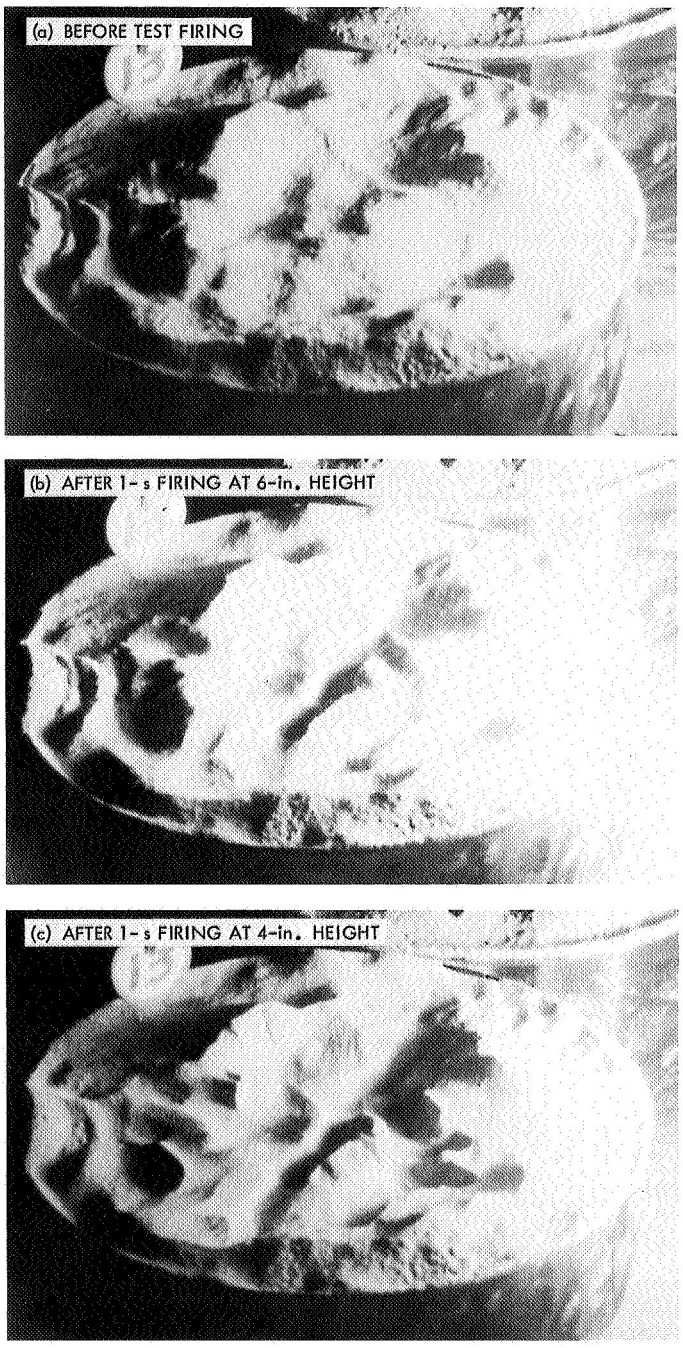

Fig. 15. Erosion of uneven soil surface, test B13

At that pressure, the same type of erosion as described for the previous samples occurred on these soils, which had the appearances shown in Fig. 16 after the tests were performed.

In the experiments described in this study, no major soil eruption occurred at shutdown of the jet, although there was evidence of diffused gases coming out of the

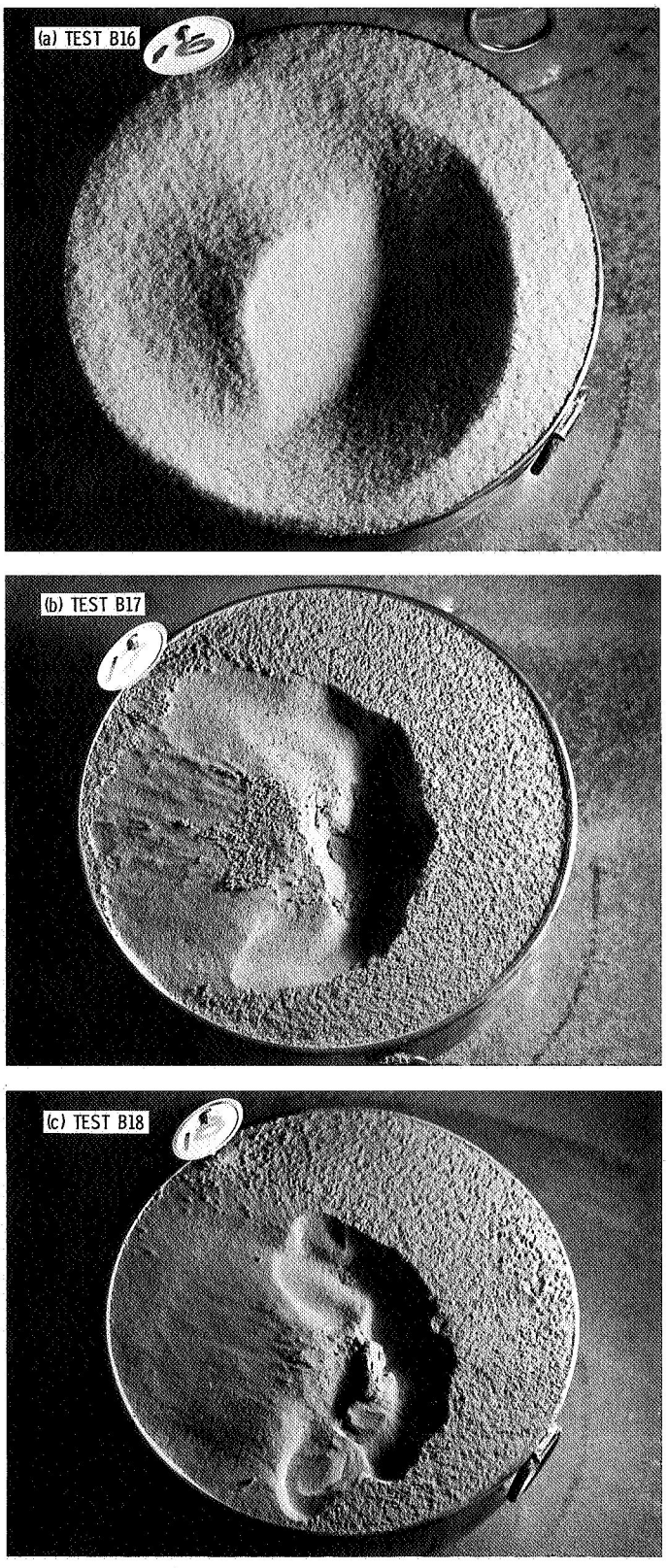

Fig. 16. Surfaces of soil samples after tests at 50×10^{-3} torr in 25-ft space simulator

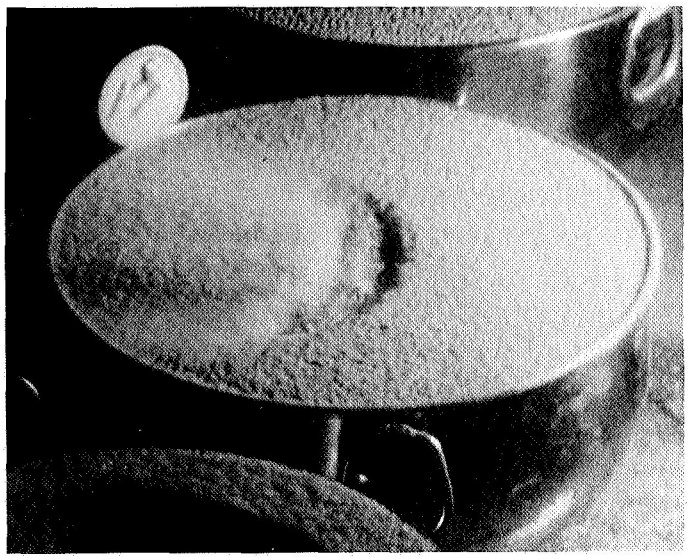

Fig. 17. Surface disturbance due to gas diffusion after shutoff of jet, test B17

soil surface when the jet was turned off. For example, in Fig. 17, the right wall of the eroded crater was shown crumpling down when the jet was turned off after firing at 56×10^{-3} torr. This effect is probably due to the removal of the pressure of the jet on the surface of the wall and/or to the diffusion of the gases out of the soil. This type of diffused soil erosion was analyzed by Scott and Ko (Ref. 1), but because of the small magnitude of gas pressure involved with the jet, the diffusion of gases did not account for a major proportion of the erosion caused by the jet. In addition, there did not seem to be any bearing capacity failure of the soils tested.

IV. Summary and Conclusions

The pressure characteristics of the exhaust plume of a *Surveyor* attitude control jet impinging on an instrumented surface and the effects of the plume impinging on soil surfaces were studied under different laboratory vacuum environments. The jet operating in an ambient pressure of 50×10^{-3} torr or higher created a collapsed, concentrated plume that can produce a large amount of soil erosion; whereas at an ambient pressure of 10×10^{-3} torr or less, only slight soil erosion occurred unless the jet nozzle was much closer to the soil surface than the jets were during the *Surveyor VI* jet firing against the moon surface (approximately 6 in. above the surface). Laboratory experiments under high-vacuum conditions on soils with cohesion between 0.04 and 0.11 psi showed that a rough soil surface was disturbed in a manner similar to the lunar surface disturbances caused by firing the *Surveyor VI* attitude control jets. These values of cohesion fall within the estimated range for lunar soil cohesion obtained by using other sources of *Surveyor* data such as the soil mechanics surface sampler and vernier engine soil erosion. However, since the erosion caused by the attitude control jet appeared to be a random phenomenon under conditions simulating the lunar environment, it is difficult to make more definitive statements on the lunar soil properties.

The estimates of cohesion given in Ref. 7 (as a result of the *Surveyor VI* attitude control jet experiment on the lunar surface) were based on the Series A experiments described in this report. As demonstrated in this report, the basis for these estimates (i.e., the Series A experiments) were not good simulations of the lunar experiment; therefore, the estimates of cohesion as reported in the *Surveyor VI* report are not as definitive as reported. However, they nonetheless agreed with the estimates based on other sources of information.

At an ambient pressure of 50×10^{-3} torr or higher, the soil erosion caused by the jet at an elevation of 3 to 6 in. distinctly depended on the soil properties, most noticeably the cohesion. For example, in a completely cohesionless soil, a bowl-shaped crater of about 3-in. diameter and ½-in. depth was formed during a 1-s firing of the jet at 3-in. height. On the other extreme, a soil with a cohesion of 0.4 psi did not erode at all with the jet as close as ½ in. to the soil surface.

It thus appears attractive to consider using a jet as an experiment on the surface of the planet Mars where the environmental pressure is currently estimated as several torr. The possibility of eroding the Martian surface by the jet exhaust plume, thereby leading to a determination of certain properties of the surface, merits consideration.

References

1. Scott, R. F., and Ko, H. Y., "Transient Rocket-Engine Gas Flow in Soil," *AIAA J.*, Vol. 6, No. 2, pp. 258–264, Feb. 1968.

2. Roberts, L., "The Action of a Hypersonic Jet on a Dusty Surface," paper presented at 31st Annual Meeting of the Institute of Aerospace Science, Jan. 1963.

3. Alexander, J. D., Roberds, W. M., and Scott, R. F., *Soil Erosion by Landing Rockets*, Final Report 1301. Hayes International Corporation, July 1966.

4. Christensen, E. M., et al., "Lunar Surface Mechanical Properties," *Surveyor I Mission Report: Part II. Scientific Data and Results*, Technical Report 32-1023, pp. 69–85. Jet Propulsion Laboratory, Pasadena, Calif., Sept. 10, 1966.

5. Stocky, J. F., and Breshears, R. R., "*Surveyor* Vernier Engine/Surface Interaction Experiments," *Flight Projects*, Space Programs Summary 37-47, Vol. I. Jet Propulsion Laboratory, Pasadena, Calif., Sept. 30, 1967.

6. Dodge, C. H., *The Lunar Program*, Space Programs Summary 37-43, Vol. I, pp. 7–11. Jet Propulsion Laboratory, Pasadena, Calif., Jan. 31, 1967 (Confidential).

7. Christensen, E. M., et al., "Lunar Surface Mechanical Properties," *Surveyor VI Mission Report: Part II. Science Results*, Technical Report 32-1262, pp. 47–108. Jet Propulsion Laboratory, Pasadena, Calif., Jan. 10, 1968.

8. Christensen, E. M., et al., "Lunar Surface Mechanical Properties," *Surveyor V Mission Report: Part II. Science Results*, Technical Report 32-1246, pp. 43–88. Jet Propulsion Laboratory, Pasadena, Calif., Nov. 1, 1967.

9. Christensen, E. M., and Ko, H. Y., "Lunar Soil Erosion: *Surveyor* Vernier Engine," to be submitted to *AIAA J.*

10. Gibbs, H. J., et al., "Shear Strength of Cohesive Soils," in *Proceedings of the ASCE Research Conference on Shear Strength of Cohesive Soils, Boulder, Colo., 1960*, pp. 33–162.

11. Sutton, G. H., "Lunar Seismic Characteristics," to be submitted to *J. Geophys. Res.*

Colorimetric Measurements of the Solar Eclipse and Earth From *Surveyor III*

J. J. Rennilson
California Institute of Technology
Pasadena, California

I. Introduction

Of the five successful *Surveyor* missions, *Surveyor III* was perhaps the most fortuitous of all because it was treated to an event never before seen by man, that of an eclipse of the sun by his own planet. Originally such observation was not planned for; indeed the physical limitations of the television camera were such as to prevent observation of this event. Fortunately, the spacecraft landed in a crater and in the exact orientation that enabled the camera to look well above its own horizon.

The television camera on the *Surveyor* spacecraft possessed a 16-deg tilt to a horizontally landed vehicle. Thus, when *Surveyor III* landed on a slope of 14 deg, the resultant camera tilt was 23 deg with respect to the local lunar vertical. Because the camera tilt plane was oriented toward the northwest, the earth could be observed only in the wide-angle mode.

The solar eclipse began at 09:48 GMT on April 24, 1967. Shortly after the start of the eclipse, the camera was commanded to its highest elevation step, to the wide-angle mode, and to photograph two sets of pictures. Later in the *Surveyor III* mission, the camera was pointed to its upper elevation limit and was commanded to photograph the earth in its crescent phase. On each of these series, the filter wheel containing color filters (blue, green, and red) was cycled. This paper describes the colorimetric results of these observations.

II. Conditions of Exposure

The solar eclipse as seen from the moon is, of course, a lunar eclipse viewed from the earth. The earth subtends an angle of about 1.9 deg at the lunar surface, thus the inner corona is only visible shortly after the beginning of totality and shortly before its end. The motion of the moon causes an apparent motion of the sun

relative to the earth, and its path has been calculated by E. Whitaker and presented in the *Surveyor III* mission report (Ref. 1). Figures 1 and 2 are repetitions of these figures in the report and are used here for convenience.

Because the television camera did not photograph the beginning or end of totality, the only light reaching *Surveyor III* was from sunlight refracted by the earth atmosphere. Present in this light path were aerosols that acted as scattering media and thus effectively filtered out the major contribution of blue light. In the case of the earth picture series, the predominately high reflectance of the clouds with respect to the oceans greatly exceeded the dynamic exposure range of the camera; hence, an exposure was chosen so that the oceans and land areas were underexposed.

III. Camera Parameters

Two complete series of frames were taken of the solar eclipse on April 24, 1967. The first series was taken at 11:24 GMT or about 42 minutes after the start of totality and a second series at 12:01 GMT. During each series, the filter wheel was rotated and two frames through each color filter were exposed. The first series was exposed using an iris of f/4 for the blue, for the green, and for the red filter. The second series was exposed at f/5.6. The earth series was taken at 10:37 GMT on April 30, 1967, and exposed at f/5.6 in the blue, the green, and the red.

A. Color Measurement

The color filters used on *Surveyor III* were the first *Surveyor* set designed to fit the CIE (Internation Commission on Illumination) color matching functions. These functions are derived from a system of color measurements using experimental laws of color matching by human observers. Such laws state that most real colors may be visually matched by an additive combination of not more than three fixed primary colors in suitable amounts.

The remaining spectral colors not matched by the above technique require the addition of either one or two of the primary colors to the spectral color before a match to the remaining primaries is possible. The choice of the three primaries is made on the basis of independence; i.e., no primary can be matched by the addition of the two remaining primaries.

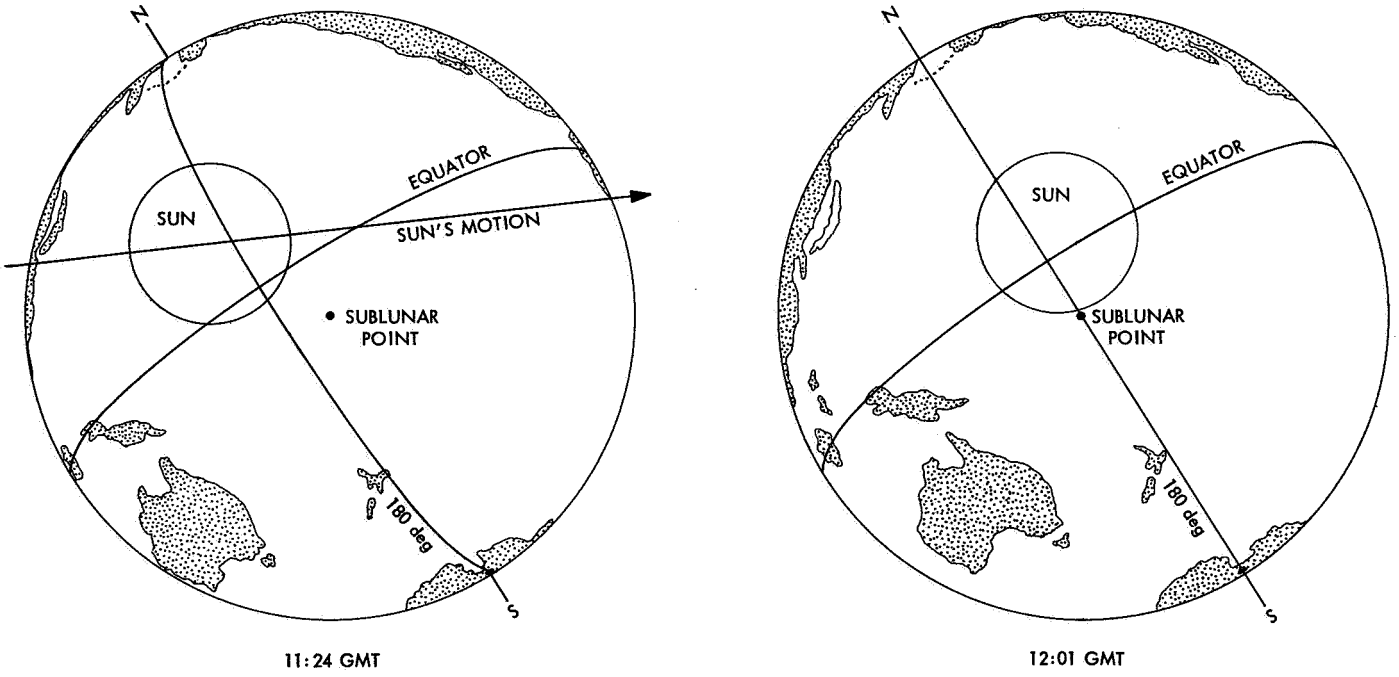

Fig. 1. Diagrams showing orientation of earth and position of sun, as seen from the moon on April 26, 1967, at 11:24 and 12:01 GMT

A color space is therefore tridimensional and may be represented by vector nomenclature. In Fig. 3, the real primaries formed from spectrum colors are base vectors **R**, **G**, and **B**. Each arbitrary color **Q** is then represented as a vector whose scalar magnitude is proportional to its luminance. The components of **Q** on the base vectors **R**, **G**, and **B** are *R*, *G*, and *B*; they are called tristimulus values. If a plane now cuts these base vectors at some angle, the vectors of all visual spectrum colors will trace an intersectional locus shown by the horseshoe-shaped curve in Fig. 3. Examination of a real color vector in a portion of the intersectional curve will show that the components are not all positive quantities, since the coordinates of these spectrum colors lie outside the triangle formed by the three primaries.

Since color space is a mathematical concept, it may be treated by the rules of vector transformation. Three new base vectors **X**, **Y**, and **Z** may then be formed by appropriate transformation from the original three **R**, **G**, and **B** vectors. Although such a transformation may take any mathematical form, one particular transformation was agreed upon in 1931 by an international body. It in this system of color measurement that is used in the *Surveyor III* data reduction.

The two main objectives used in establishing this specific transformation were:

(1) That the components (tristimulus values) of any real color vector on its base vectors **X**, **Y**, and **Z** always be positive quantities.

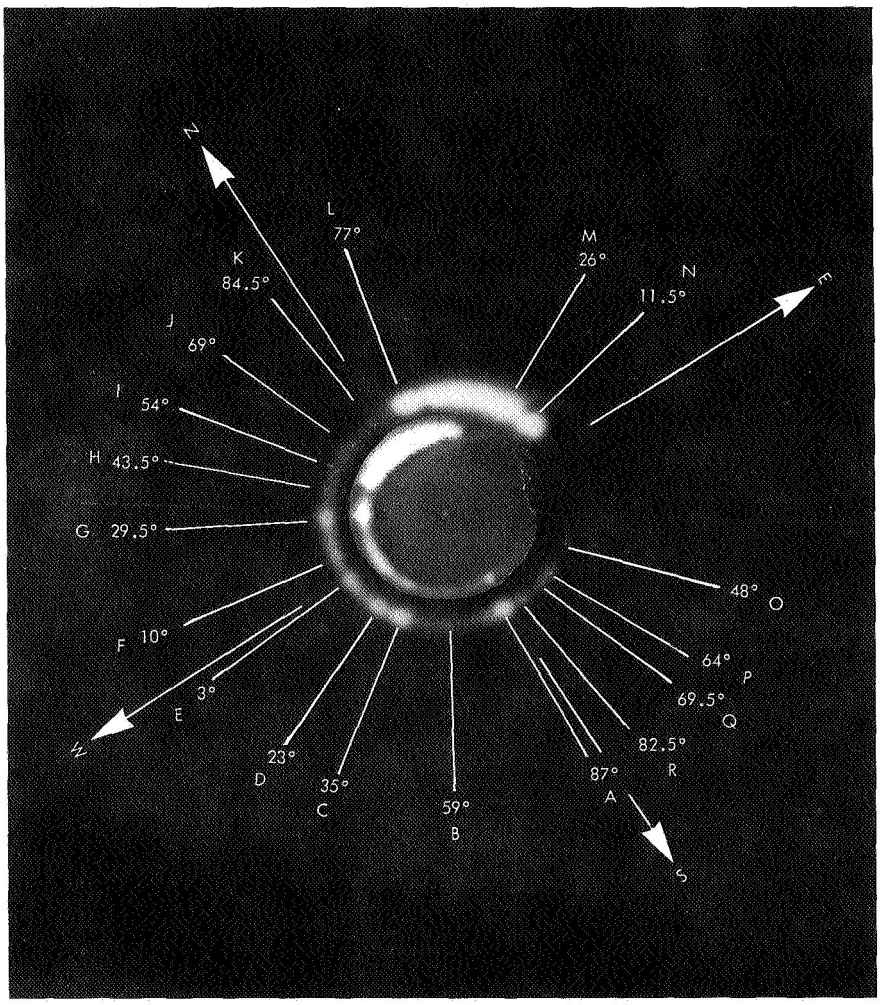

Fig. 2. Superimposed *Surveyor III* pictures (first and second series) showing distribution of light in refraction halo of earth (eighteen beads are identified by letters)

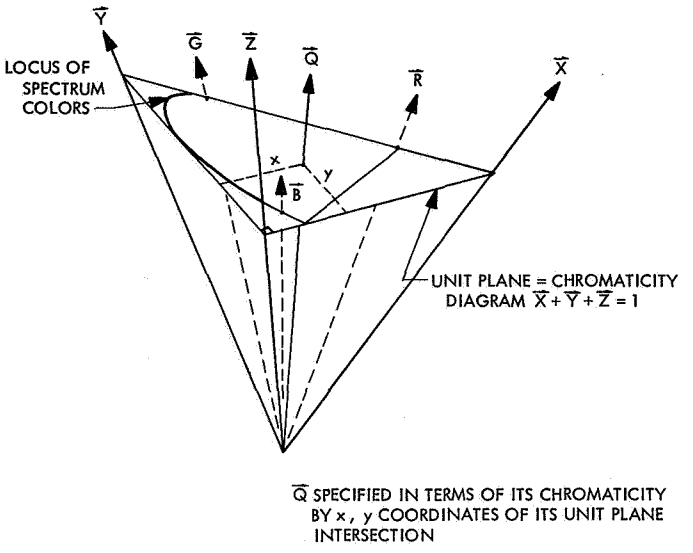

Fig. 3. Color space in vector notation

(2) That the Y component only be proportional to the luminance or reflectance of the color.

Thus, the determination of the tristimulus values X, Y, and Z of a given color specifies not only its color or chromaticity, but its luminance or reflectance as well.

When the components (tristimulus values) of each of the spectrum colors from an equal-energy spectrum (all wavelengths possessing equal radiant energy) are plotted at their corresponding wavelengths, the spectral response curves shown in Fig. 4 result. In the limiting case, the three components comprise three functions labeled $\bar{x}$, $\bar{y}$, and $\bar{z}$. These are often called color matching functions as they represent the quantities of the X, Y, and Z primaries required to match a constant radiant energy at each spectral wavelength. If a detector possesses the spectral responses corresponding to these color matching functions $\bar{x}$, $\bar{y}$, and $\bar{z}$, then its signal will be proportional to the tristimulus values X, Y, and Z of the measured color.

The *Surveyor III* camera was fitted with color filters to approximate the color matching functions $\bar{x}$, $\bar{y}$, and $\bar{z}$. The filter selection consisted of choosing glasses matching the spectral response of the vidicon, lens, and mirror combination (Fig. 5) for the best fit to the color matching functions. The two physical limitations imposed on this fit were: (1) that the total glass thicknesses be limited to 3 mm and (2) that the minimum thickness of any element of the filter be 1 mm.

A computer program using the method of Davies and Wyszecki (Ref. 2) is used to choose the glasses and then

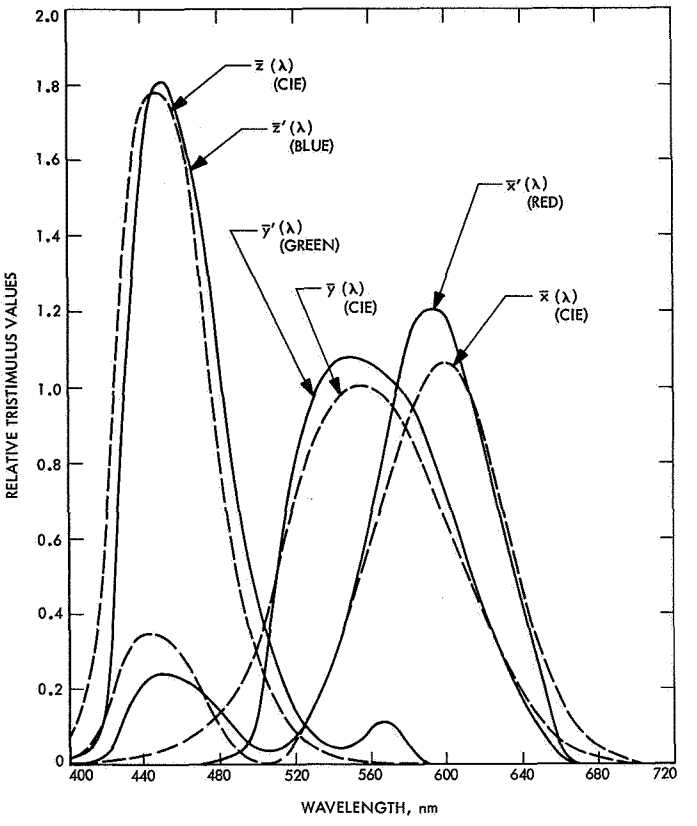

Fig. 4. Camera-filter spectral response functions of the *Surveyor III* camera, compared with CIE color-matching functions

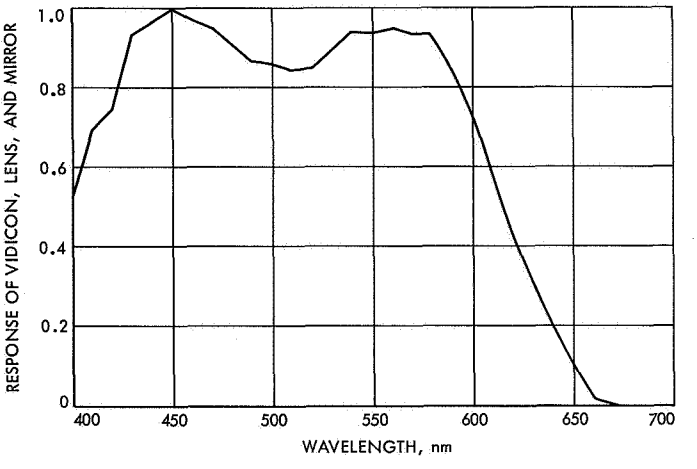

Fig. 5. Spectral response curve of the *Surveyor III* television camera at clear position

obtain the best fit to the CIE functions. The first maxima of the $\bar{x}$ function is simulated by using a reduced value of the $\bar{z}$ function added to the remaining $\bar{x}$ function. This simulation is standard practice in colorimetry since double-peaked filters are difficult to obtain. The resultant

best fit to the CIE function of the camera-filter combinations are shown by the dotted curves in Fig. 4. In addition, a light deposit of Inconel is applied to two of the three filters in order to equate the camera signals when measuring a neutral gray under sunlight.

B. Camera Measurement

The three camera signals as recorded on the ground do not automatically yield the tristimulus values. The degree of fit to the color matching functions, as well as the differences in the camera signals, accounts for this disparity. The tristimulus values are related to the camera signals by the following equations:

$$X = k_{x1}R_x + k_{x2}R_x \tag{1a}$$

$$Y = k_yR_y \tag{1b}$$

$$Z = k_zR_z \tag{1c}$$

where R_x, R_y, and R_z are the camera signals corrected for nonlinear response, and k_{x1}, k_{x2}, k_y, and k_z are proportionality factors. These factors are determined experimentally by measuring camera signals derived from known color stimuli. The proportionality factors are then calculated to minimize the sum of the squares of the differences between the true and measured tristimulus values.

The *Surveyor III* camera observed a nine filter and light source combination stimulus during preflight calibration. The proportionality factors thus determined were $k_{x1} = 3.820$, $k_{x2} = 15.412$, $k_y = 19.590$, and $k_z = 12.34$. A more complete explanation of proportionality factors and camera measurement is found in Ref. 3.

C. Colorimetric Accuracy

Color measurements are often described by coordinates of the intersectional point in the unit plane of the color vector. This unit plane, called the chromaticity diagram because it includes only the color and not the luminance values, is shown in Fig. 3. The coordinates are related to the tristimulus values by the equations

$$x = \frac{X}{X + Y + Z} \tag{2a}$$

$$y = \frac{Y}{X + Y + Z} \tag{2b}$$

Around the chromaticity of extraterrestrial sunlight ($x = 0.318$ and $y = 0.330$), the eye can detect color differences of about ± 0.001 in x and y under good observing conditions. The *Surveyor III* camera yielded proportionality factors that enabled chromaticities near the illuminant color to be measured with an accuracy of ± 0.006 in x and y.

The accuracy given above depends on three main factors:

(1) The degree of fit to the CIE color matching functions.

(2) The linearity of the camera to different luminance levels through each filter.

(3) The temperature and signal stability of the overall camera system.

Of these three effects, the latter two are the most important.

During preflight calibration, the camera observes a uniform light source of spectral radiance approximating the sun outside our atmosphere. This source completely fills the camera field-of-view in the narrow-angle mode. The luminance of the source may be varied continuously. The camera signals from such a source may be plotted against the source luminance to yield a light transfer characteristic curve. When such calibration is repeated for each color filter in the camera, light transfer characteristics result for the eclipse image area, as shown in Fig. 6. Vidicon shading defined as variation in sensitivity across the image format, is also recorded with this source. As is seen in the figure, the filter transmissions are not equal for a source approximating the sun.

The nonlinear transfer characteristics give rise to an interesting effect in the chromaticity diagram. For example, in Fig. 6, if the camera signals through the red and green filters are on the semilinear portion of the transfer characteristic, but the blue is close to the toe, then the uncertainty in the blue signal will be reflected in its tristimulus value. Furthermore, if the chromaticities determined from Eqs. (1) and (2) are calculated, keeping the blue R_z and the green R_y signals constant and allowing the uncertainty of the red R_x signal to vary, then a series of dots results on the chromaticity diagram. Figure 7 shows these dots lying along line 1 that, if extended, intersects the end of the diagram at $x = 1.0$ and $y = 0.0$ (the intersection of the X primary and the chromaticity diagram). Similarly, other lines are formed

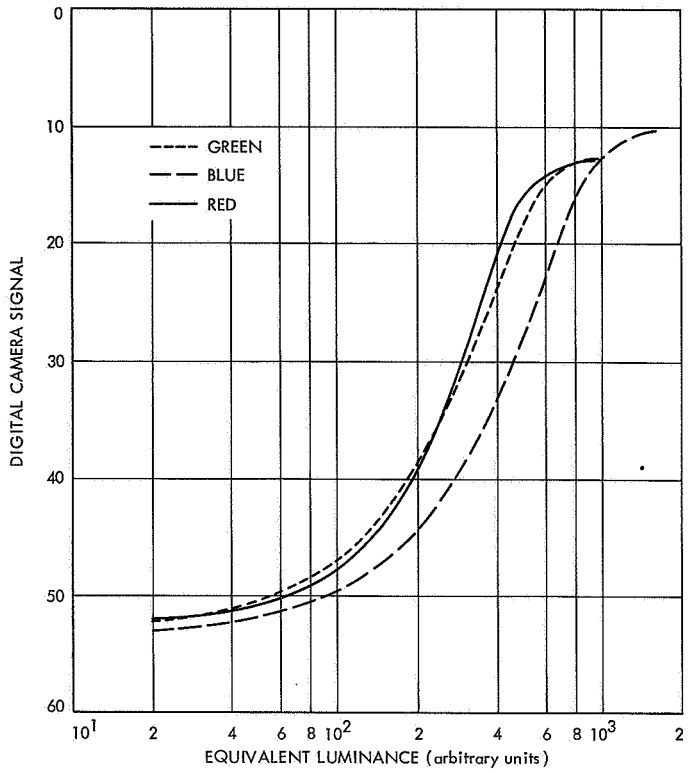

Fig. 6. Light transfer characteristics of eclipse image area through three filters

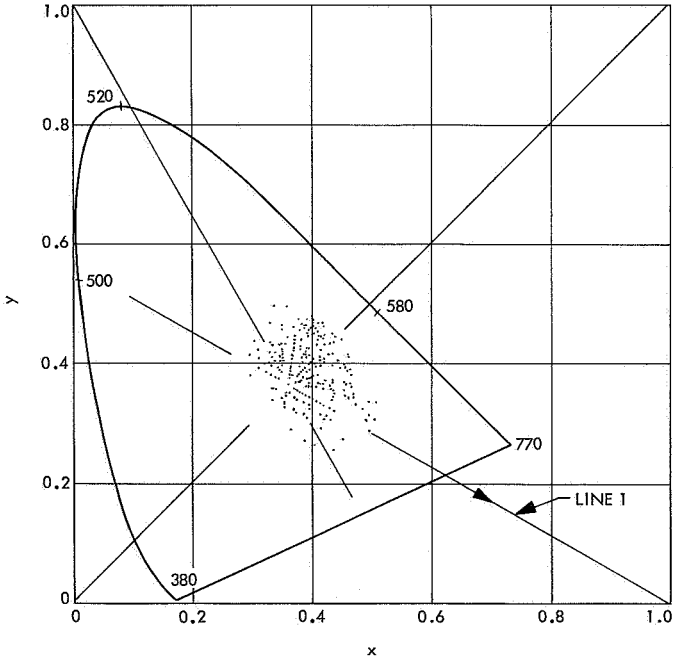

Fig. 7. Chromaticity errors resulting from uncertainty in one or two camera signals

when either one or two of the three camera signals are varied and the other(s) held constant. Thus a star-like appearance occurs in the diagram and is very symptomatic of nonlinearity errors in the respective camera signals. Such a diagram was first seen in the early reduction of the *Surveyor III* eclipse frames. The cause of this erroneous data was not determined until after the completion of the *Surveyor* missions; this cause will be explained in the next section.

IV. Data Reduction

A. Frame Digitization

The data reduction of the eclipse frames involved digital conversion of the analog video tapes. The video signal was digitized to six bits (0–63). The transfer characteristics shown in Fig. 6 were used to convert the digital values to equivalent luminances, and Eqs. (1) and (2) were then used to compute the chromaticities. The image was broken into 600 lines by 684 elements. The greater width of the frame is a function of the communications bandwidth. Each picture element (called a pixel) thus yielded a chromaticity. The chromaticities were then plotted on the diagram and gave a result similar to Fig. 7. The search for the error was then directed along other lines.

B. Image Spread and Expected Image Size

During the *Surveyor* program, it was suspected that image bleed or spread of point images would occur. This effect was observed in early tests using stellar images. The magnitude of this effect was not measured, at any time, on the actual flight vidicons. It thus remained the province of post-mission analysis to quantitatively describe the spread.

A special test was devised using a rear-illuminated slit and an extra flight-type camera. The slit dimensions were chosen so that its width subtended less than one-third of a picture element under ideal conditions of image formation. The measurement of the spread of this slit was thus a combination of the lens line spread function and a spread function associated with the vidicon.

Figure 8 shows what happens when the luminance behind the slit is increased. The image width is measured at one-tenth of its peak value. Comparison with the light transfer characteristic curve shows that an image spread effect begins to occur when the signal is 85% of the saturation level. From that point on the

spread follows the equation

$$x = -13.61 + 5.05 \ (\log L)$$

where x is the number of picture elements and L is the source luminance. Examination of stellar images that have been computer processed indicate a slightly larger size than that given in Fig. 8.

The expected image size of the illuminated portion of the eclipse is found from the astronomical data. If the effective optical atmosphere of the earth is 65 km in height, then the width of the image (atmosphere thickness) is less than one-third of a picture element for the solar eclipse. For the earth, the image is only 50 elements in diameter. It is therefore necessary to assume the conditions of image spread.

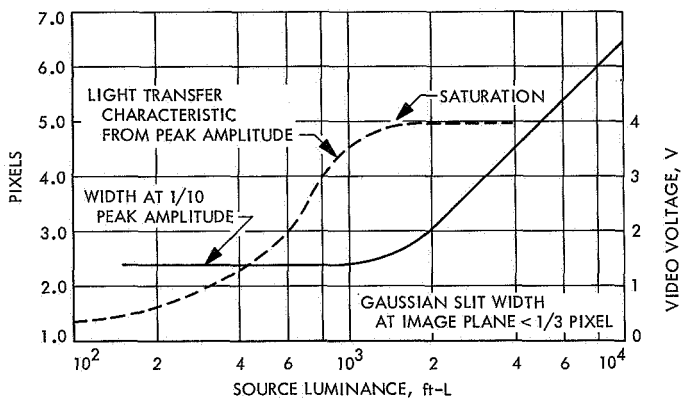

Fig. 8. Plot of image spread of an unresolved slit image as saturation is approached and exceeded

Cross sections of the first solar eclipse picture through the bright saturated cap and then through an area at approximately 43.5 deg N latitude is shown in Figs. 9 and 10, respectively. Both sections of each figure are plotted using uncorrected raw video and the corresponding equivalent luminances. In Fig. 9, the center of the cap reaches saturation. In Fig. 10, there still exists a spread of the image even in the presence of a nonsaturated video signal. This may be caused by the light scattering from lunar material present on the camera mirror.

In view of the unresolved differences, it thus appeared that the total video signal for an unresolved image would be equal to the integral

$$s = \int L \, dx \simeq \Sigma \, L \, \Delta x$$

where L and x have the same meaning as given previously.

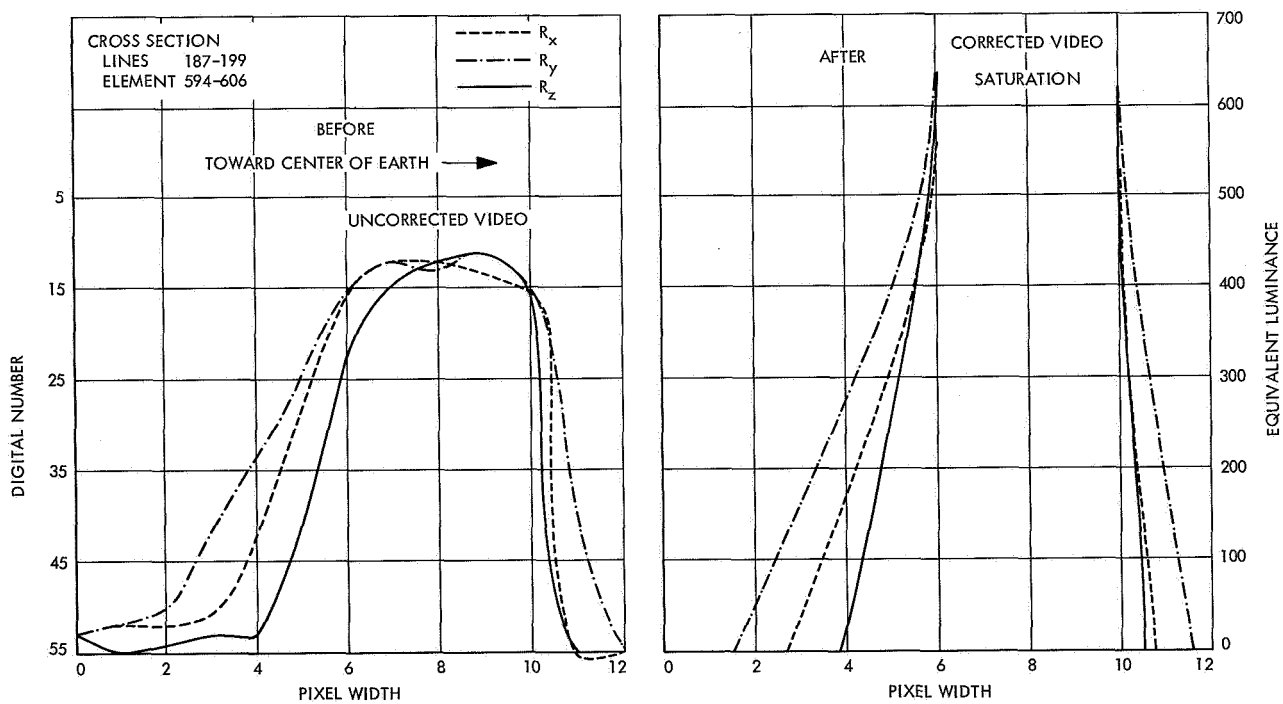

Fig. 9. Signal cross section through bright saturated cap (before and after correction for nonlinear transfer characteristics)

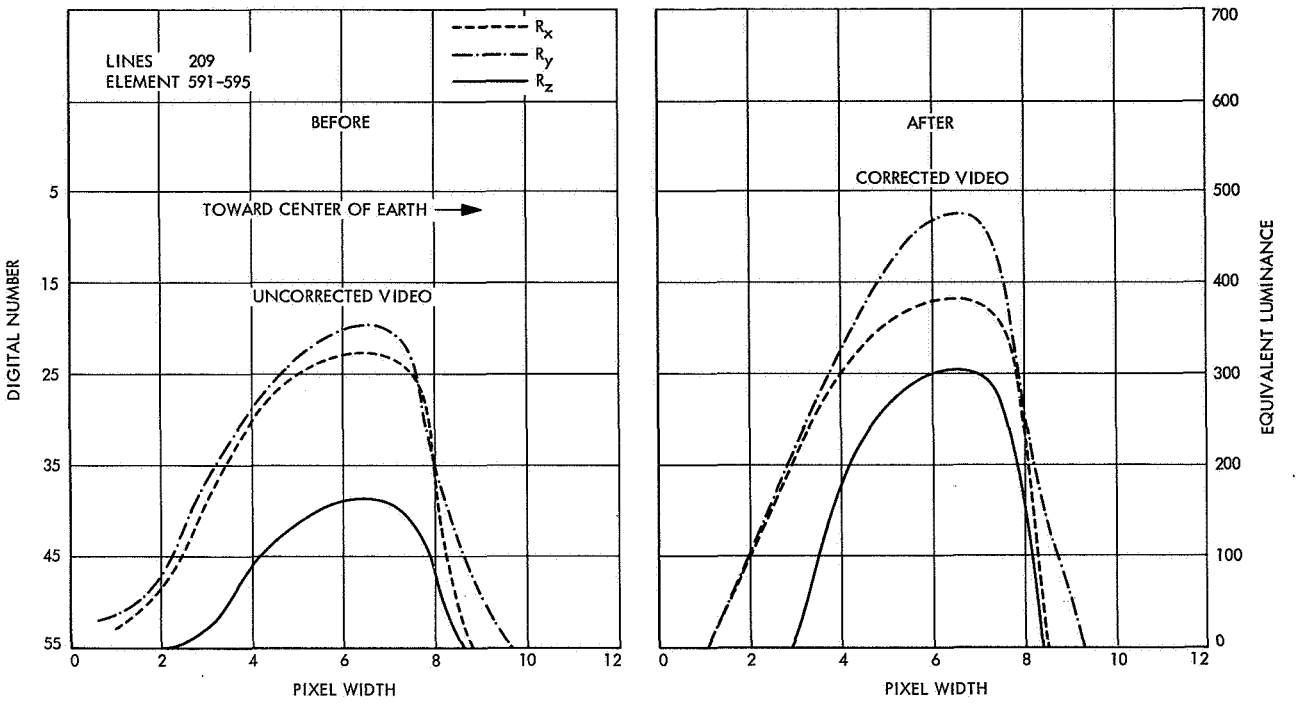

Fig. 10. Signal cross section at 43.5 deg N latitude (both before and after correction for nonlinear transfer characteristics)

C. Results

Using the above assumption, the eclipse frames chromaticity coordinates were computed for approximately every 10 deg in earth latitude. The results, numbering 35, are given in Table 1; corresponding points are shown on the chromaticity diagram of Fig. 11. Two points marked with crosses and labeled G denote the chromaticity measurements of bead G from the second series of eclipse pictures. Remaining portions of the image were sufficiently underexposed to cause large uncertainties in the measurements. For comparison, the chromaticity locus of a full radiator, radiating in accordance with Planck's law, is also plotted in Fig. 11. Four isotemperature lines at 3000, 3500, 4444, and 5000°K are likewise shown crossing the locus. The chromaticities in general are grouped close to these isotemperature lines.

The location (in relation to latitude) of the color measurements on a black and white frame is shown in Fig. 12. The prominent bead G is also marked on this figure.

The measurements of the earth, as was previously mentioned, were underexposed in the cloud-free areas. The average chromaticity of the clouds is also plotted in Fig. 11 and given in Table 1.

V. Conclusions

The colors of the eclipse as measured by *Surveyor III* show a fair degree of blue attenuation as the sunlight is refracted through the atmosphere. Calculations could be made to determine the expected chromaticities assuming various aerosols, but this effort was considered beyond the scope of this paper. It is sufficient to state that the color variations are undoubtedly caused by the degree of scattering in the cloudy vs clear areas, as well as particulate material in the aerosols. The colors, especially in the clear areas of the atmosphere, also increase in purity as the angular separation increases between these areas and the sun. This change is most apparent in bead G.*

The average earth chromaticity, determined largely by cloud cover, agrees well with the chromaticity of extraterrestrial sunlight. The clouds are thus fairly neutral reflectors in the visible spectral region. Most all land areas were cloud covered at the time of observation, and the clear ocean areas were sufficiently underexposed to render that data inaccurate.

*No detection of the solar corona was noted in the eclipse frames. Exposures for the corona, 1–2 earth radii distant, would have rendered the refracted sunlight unmeasurable.

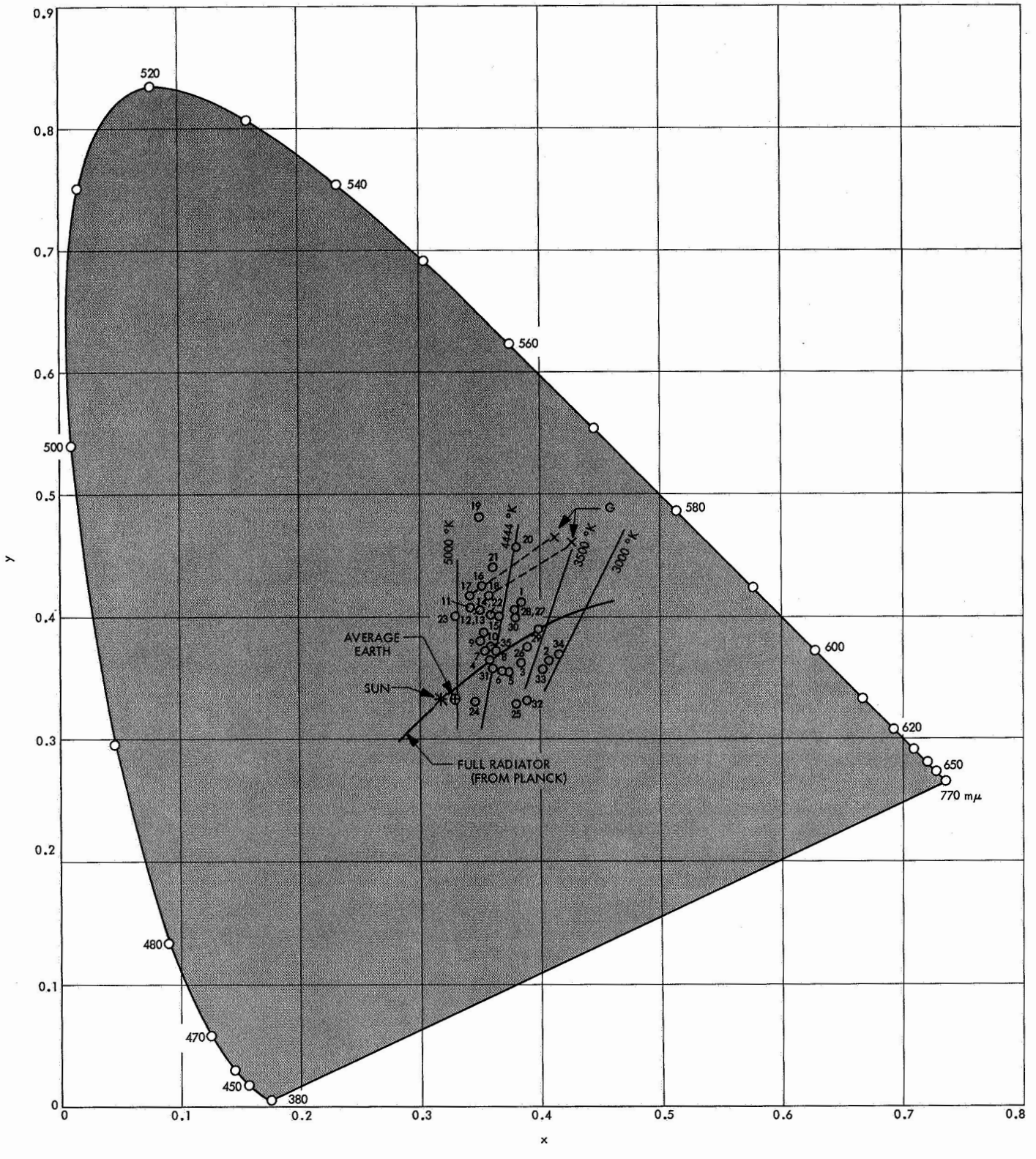

Fig. 11. Plot of the chromaticities of the eclipse and earth cloud cover based on 1931 CIE chromaticity diagram

Table 1. Eclipse frames chromaticity coordinates

Position	x	y	Position	x	y	Position	x	y
1	0.386	0.411	14	0.361	0.399	27	0.378	0.403
2	0.408	0.363	15	0.365	0.400	28	0.380	0.404
3	0.385	0.360	16	0.353	0.425	29	0.399	0.388
4	0.358	0.364	17	0.343	0.416	30	0.379	0.398
5	0.375	0.352	18	0.359	0.417	31	0.361	0.356
6	0.370	0.354	19	0.352	0.481	32	0.388	0.332
7	0.356	0.371	20	0.381	0.457	33	0.403	0.354
8	0.364	0.370	21	0.361	0.440	34	0.416	0.368
9	0.351	0.379	22	0.361	0.398	35	0.360	0.373
10	0.354	0.385	23	0.330	0.399	G[a]	0.429	0.460
11	0.344	0.407	24	0.347	0.328	G	0.414	0.467
12	0.352	0.403	25	0.372	0.327	⊕[b]	0.325	0.330
13	0.351	0.404	26	0.391	0.374			

[a]Chromaticity measurements of bead G.

[b]Average chromaticity of earth clouds.

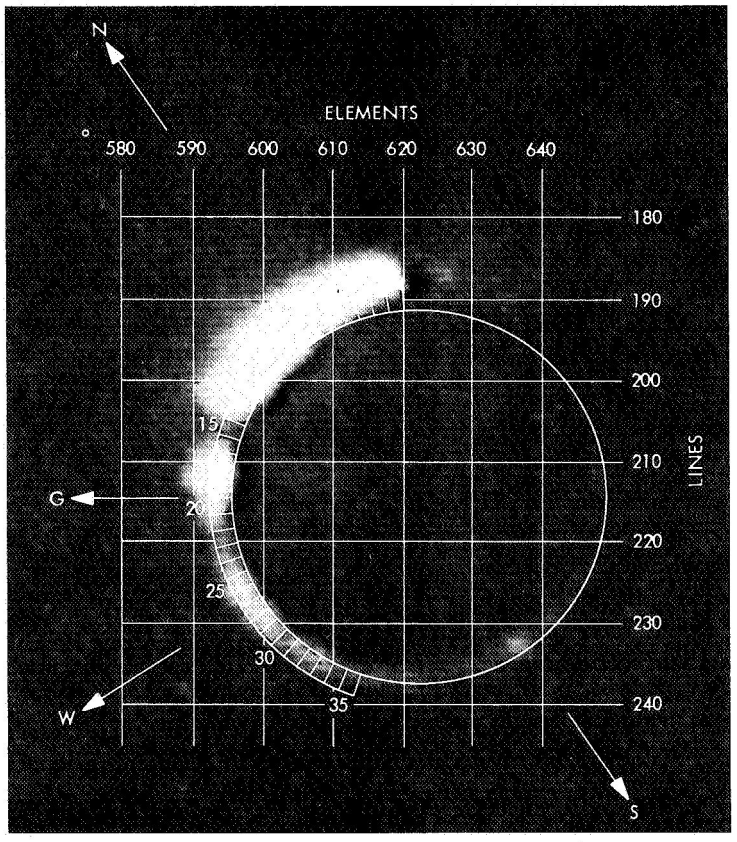

Fig. 12. A frame through green filter of first series of eclipse pictures on April 24, 1967, at 11:23:01 GMT

References

1. *Surveyor III Mission Report: Part II. Scientific Results*, Technical Report 32-1177. Jet Propulsion Laboratory, Pasadena, Calif., June 1, 1967.

2. Davies, W. E., and Wyszecki, G., "Physical Approximation of Color-Mixture-Functions," *J. Opt. Soc. Am.*, Vol. 52, No. 6, pp. 679–685, June 1962.

3. Rennilson, J. J., "A Television Colorimeter for Lunar Exploration," in *Proceedings of the 8th International Colour Meeting, Lucerne, Switzerland.* Centre d' Information de la Couleur, 23 Rue Notre-Dame-des-Victoire, Paris, France, pp. 498–506, June 1965.

NASA — JPL — Coml., L.A., Calif.